

# **Protein-Polymer Conjugate Arrays for Enhanced Biosensor Sensitivity and Selectivity**

by

Justin Michael Paloni

B. ChE., University of Delaware, 2016

Submitted to the Department of Chemical Engineering  
in partial fulfillment of the requirements for the degree of

**Doctor of Philosophy**

at the

**Massachusetts Institute of Technology**

May 2020

© 2020 Massachusetts Institute of Technology. All rights reserved.

Signature of Author: \_\_\_\_\_

Department of Chemical Engineering  
May 11, 2020

Certified by: \_\_\_\_\_

Bradley D. Olsen  
Professor of Chemical Engineering  
Thesis Supervisor

Accepted by: \_\_\_\_\_

Patrick S. Doyle  
Robert T. Haslam (1911) Professor  
Chairman, Committee for Graduate Students



# Protein-Polymer Conjugate Arrays for Enhanced Biosensor Sensitivity and Selectivity

Justin Michael Paloni

Submitted to the Department of Chemical Engineering on May 11, 2020 in partial fulfillment of the requirements of the degree of Doctor of Philosophy in Chemical Engineering

## Abstract

The capability of biosensors to provide highly sensitive and selective molecular detection has enabled development of rapid, inexpensive medical diagnostics. Despite significant advancements in sensor design over the past several decades, most biosensors experience significantly reduced sensitivity in common sensing fluids such as blood and urine. In these mixtures, off-target molecules nonspecifically bind to the sensor surfaces, blocking analyte binding sites and increasing background signal. The self-assembled structure of protein-polymer conjugates presents a potential solution to this issue, offering both biological functionality and a mechanism for excluding many non-analyte molecules in biosensing fluids. Therefore, this thesis explores the use of protein-polymer conjugate thin films as biosensors to minimize nonspecific binding effects during detection in complex mixtures.

The first part of this thesis focuses on protein engineering methods to improve the self-assembly of protein-polymer conjugates. It is first demonstrated that oligomerization of low-molecular weight protein blocks significantly enhances ordering quality of the corresponding conjugates. As the degree of oligomerization of the protein block increases, conjugates form ordered phases that display longer-range assembly. Another technique shown to improve protein-polymer conjugate self-assembly is fusion of complementary coiled-coil sequences to the protein block. When proteins bearing these sequences are mixed together in solution, a strongly associative coiled-coil forms, promoting a substantial ordering improvement. Both protein oligomerization and fusion to coiled-coil sequences retain the biological functionality of the protein block, and it is found that protein activity generally scales with conjugate ordering quality.

The second part of this thesis explores the capabilities of the polymer block in protein-polymer conjugate thin films to control diffusion into these films. By increasing the molecular weight of this polymer block, larger analyte molecules experience less restricted diffusion into the thin films. Transport studies performed in solutions of the polymer block indicate that most proteins display size-based diffusion following the Stokes-Einstein equation, but some proteins deviate significantly from this behavior due to a combination of protein-protein and protein-polymer interactions. When an analyte molecule is mixed with a protein that diffuses faster than the analyte in these polymer solutions, the sensitivity of the thin film conjugate biosensors towards the analyte is often significantly enhanced. This sensitivity improvement is also observed during detection in mixtures containing the analyte and several proteins, only some of which diffuse faster than the analyte. Accordingly, biosensing measurements using protein-polymer conjugate thin films performed in blood serum and urine solutions, which should contain a variety of proteins that diffuse faster than a given analyte, display a two order of magnitude improvement in sensitivity over traditional surface-based biosensor technologies. Thus, protein-polymer conjugate thin film biosensors can overcome nonspecific binding effects and demonstrate greater sensitivity during measurements performed in complex protein mixtures.

Thesis Supervisor: Bradley D. Olsen, Professor of Chemical Engineering



## Acknowledgements

While this thesis bears my name, it would be remiss to not recognize that many others played critical roles pertaining to both the development of the body of knowledge contained herein and my personal growth during my time at MIT.

First and foremost, I would like to thank my thesis advisor, Brad Olsen, for the great privilege of working with him over the past four years. In addition to providing excellent guidance and fostering an incredibly supportive group culture, Brad has consistently challenged me (in a good way). It is clear that Brad sees the best in each of his students and constantly pushes them to achieve that optimal state. It because of this constant source of encouragement and challenge that I have grown so much. Brad has also been highly supportive of my endeavors—academic, career-related, and otherwise—throughout my PhD experience. In fact, he played a very large role in me obtaining my job at a startup that I will be working at following graduation. To say that he has aided in my growth as a researcher and a person over these last few years would be an understatement, as Brad has easily been the largest contributor to my development in this time.

I am very thankful for the guidance provided by my thesis committee members, Professors Hadley Sikes and Michael Strano. Professor Sikes played an instrumental role during the early stages of my thesis by providing guidance about the design and issues associated with biosensors. Since nobody in the Olsen Lab had any real experience with biosensors, her guidance helped shape and refine the application-based projects in my thesis. I also thank Professor Strano for both his insightful comments and suggestions during my committee meetings in addition to being a great mentor while I was serving as a TA for his class.

The members of the Olsen lab have also provided instrumental guidance during my PhD. I am extremely grateful that in the months before I officially joined the Olsen lab, XueHui Dong, who was preparing to return to China for a faculty position at the time, always made time to teach me experimental techniques. Michelle Sing played perhaps the largest role in helping me adapt to the Olsen Lab, and I greatly appreciate her answering my incessant questions during my first few weeks in lab (I also apologize for this). Aaron Huang was an excellent mentor and discussion partner with regards to the self-assembly of protein-polymer conjugates. Eric Miller not only designed the genes for the first project I tackled in lab, helping jumpstart my research, but he also served as (and has continued to be) a great source to talk to about biosensors and their applications. Of course, I am greatly indebted to Carrie Mills as well, who not only taught me a variety of molecular biology protocols and helped me troubleshoot my cloning experiments, but also helped me rationalize many of the experimental trends I was observing (while writing her thesis at the same time). I also greatly appreciate having worked with Hursh, Helen, Irina, Celestine, Tzyy-Shyang, Tom, Rui, Angie, Reggie, Takuya, Zach, Daphne, Brian, Ameya, Akash, Weizhong, Wontae, Diego, Nuno, Yun Jung, Sieun, Nari, Haley, Sarah, Nathan, Danielle, Rogerio, and Melody, who have all helped me become acclimated to lab, given helpful guidance about my research, or been absolutely stellar people to spend time with each day.

Finally, I would like to thank those who have provided me with constant support. My girlfriend, Stephanie Kong, has truly helped keep me sane while dealing with the many stresses of research. By her unremitting compassion, choosing to work in lab at the same time as me when I would stay in lab late or work long days on weekends so we could still spend time “together”, and helping me maintain a work-life balance, Steph has been my rock since we started dating. I am also eternally grateful to my family, especially my parents, without whom I never would have been able to reach this point in my life.

## Table of Contents

Acknowledgements.....	5
List of Schemes.....	10
List of Tables.....	10
List of Figures.....	11
Chapter 1. Introduction.....	15
1.1 Motivation.....	15
1.2 Proteins.....	16
1.3 Protein Biosensors.....	19
1.4 Block Copolymer Self-Assembly.....	21
1.5 Protein-Polymer Conjugate Self-Assembly.....	23
1.6 Transport in Block Copolymer and Homopolymer Solutions.....	25
1.7 Thesis Overview.....	27
1.8 References.....	28
Chapter 2. Materials and Methods.....	39
2.1 Molecular Biology Protocols.....	39
2.1.1 Polymerase Chain Reaction (PCR).....	39
2.1.2 Agarose Gel Extraction.....	40
2.1.3 Digests and Dephosphorylations.....	40
2.1.4 Ligations.....	41
2.1.5 Transformations.....	42
2.1.6 Cell Outgrowth for DNA Purification.....	43
2.1.7 Design of Oligomerized rcSso7d.SA Genes.....	44
2.1.8 Design of 2x rcSso7d.SA Coiled-Coil Fusion Genes.....	46
2.1.8.1 Design of Gene with C-terminal Cysteine.....	46
2.1.8.2 Preparation of Genes for Insertion of Coiled-Coil Sequences.....	47
2.1.8.3 Cloning of Coiled-Coil Fusions.....	48
2.2 Protein Expression and Purification.....	49
2.2.1 General Techniques.....	49
2.2.1.1 Media Preparation.....	49
2.2.1.2 Cell Workup.....	50
2.2.1.3 Ni-NTA Purification.....	51
2.2.1.4 Dialysis.....	52
2.2.1.5 Protein Concentration Determination.....	52
2.2.2 rcSso7d.SA Oligomer and Coiled-Coil Fusion Expression and Purification.....	53
2.2.3 TEV Protease Expression and Purification.....	54
2.2.4 mSA2 Expression and Purification.....	55
2.2.5 GFP Variants.....	58
2.3 Polymer Synthesis.....	59
2.3.1 Synthesis of EMP.....	60
2.3.2 Synthesis of exo-3a,4,7,7a-Tetrahydro-2-(3-hydroxypropyl)-4,7-epoxy-14-isoindole-1,3(2 <i>H</i> )-dione (1).....	61
2.3.3 CTA Synthesis.....	62
2.3.4 RAFT Polymerization.....	63
2.4 Bioconjugate Synthesis.....	66

2.5 Fluorescent Labeling of Proteins.....	67
2.6 Structural and Biophysical Characterization Techniques .....	69
2.6.1 Small-angle X-ray Scattering (SAXS) .....	69
2.6.1.1 Sample Preparation.....	69
2.6.1.2 Experimental Procedure .....	71
2.6.2 Grazing-incidence Small-angle X-ray Scattering (GISAXS).....	73
2.6.2.1 Sample Preparation.....	73
2.6.2.2 Experimental Procedure .....	74
2.6.3 Turbidimetry and Depolarized Light Scattering (DPLS) .....	75
2.6.3.1 Sample Preparation.....	76
2.6.3.2 Experimental Procedure .....	77
2.6.4 Differential Scanning Calorimetry (DSC).....	78
2.6.4.1 Sample Preparation.....	78
2.6.4.2 Experimental Procedure .....	78
2.6.5 Circular Dichroism (CD).....	79
2.6.5.1 Sample Preparation.....	79
2.6.5.2 Experimental Procedure .....	79
2.6.6 Analytical Ultracentrifugation (AUC).....	80
2.6.6.1 Sample Preparation.....	80
2.6.6.2 Experimental Procedure .....	80
2.6.7 Dynamic Light Scattering (DLS) .....	81
2.6.7.1 Sample Preparation.....	81
2.6.7.2 Experimental Procedure .....	81
2.6.8 Fluorescence Recovery After Photobleaching (FRAP).....	81
2.6.8.1 Sample Preparation.....	81
2.6.8.2 Experimental Procedure .....	83
2.7 Biosensor Analytical Techniques .....	84
2.7.1 Monolayer Fabrication .....	84
2.7.2 Fluorescent Binding Assays .....	84
2.7.3 Thermal Stability Assays.....	85
2.7.4 Sandwich Assays .....	85
2.8 Data Fitting.....	86
2.8.1 SAXS .....	86
2.8.2 GISAXS.....	86
2.8.3 FRAP .....	87
2.8.4 Biosensor Assays.....	89
2.9 References .....	91
Chapter 3. Improved Ordering in Low Molecular Weight Protein-Polymer Conjugates Through Oligomerization of the Protein Block .....	93
3.1 Abstract .....	93
3.2 Introduction .....	93
3.3 Materials and Methods .....	97
3.3.1 Synthesis.....	97
3.3.2 Bioconjugation and Preparation of Bulk Samples.....	98
3.3.3 Solution-phase Sample Preparation and Characterization .....	99
3.3.4 Thin Film Preparation.....	99

3.3.5 Fluorescence Assays.....	100
3.4 Results and Discussion.....	101
3.4.1 Phase Behavior.....	101
3.4.2 Ordering Quality.....	107
3.4.2.1 Concentrated Solution.....	107
3.4.2.2 Highly Concentrated Solution.....	109
3.4.3 Biosensing Capabilities.....	112
3.5 Conclusions.....	118
3.6 References.....	118
Chapter 4. Coiled-Coil Domains for Self-Assembly and Sensitivity Enhancement of Protein-Polymer Conjugate Biosensors.....	124
4.1 Abstract.....	124
4.2 Introduction.....	125
4.3 Materials and Methods.....	128
4.3.1 Gene Cloning.....	128
4.3.1.1 Design of Gene with C-terminus Cysteine.....	128
4.3.1.2 Preparation of Genes for Insertion of Coiled-Coil Sequences.....	128
4.3.1.3 Cloning of Coiled-Coil Fusions.....	129
4.3.2 Synthesis.....	129
4.3.2.1 PNIPAM Synthesis.....	129
4.3.2.2 Protein Expression.....	130
4.3.2.3 Bioconjugation.....	131
4.3.3 Characterization.....	132
4.3.3.1 Circular Dichroism (CD) Single Temperature Measurements.....	132
4.3.3.2 Analytical Ultracentrifugation.....	133
4.3.3.3 CD Melting Curve Measurements.....	133
4.3.3.4 Additional Characterization Methods.....	133
4.4 Results and Discussion.....	134
4.4.1 Conjugate Design.....	134
4.4.2 Coiled-Coil Folding and Stability.....	135
4.4.3 Self-Assembly.....	138
4.4.3.1 Phase Behavior.....	138
4.4.3.2 Ordering Quality.....	142
4.4.4 Thin Film Activity Assays.....	144
4.5 Conclusions.....	145
4.6 References.....	147
Chapter 5. Protein-Polymer Block Copolymer Thin Films for Highly Sensitive Detection of Small Proteins in Biological Fluids.....	152
5.1 Abstract.....	152
5.2 Introduction.....	152
5.3 Materials and Methods.....	155
5.3.1 Materials.....	155
5.3.2 Polymer Synthesis and Protein Expression and Bioconjugation.....	155
5.3.3 Thin Film Preparation.....	156
5.3.4 Fluorescence Assays.....	156
5.3.5 Sandwich Assays.....	157

5.4 Results and Discussion.....	158
5.4.1 Characterizing Diffusion into Biosensor Thin Films .....	158
5.4.2 Biosensing Capabilities .....	163
5.4.2.1 Sensing in Buffer.....	163
5.4.2.2 Sensing in Biological Fluids.....	166
5.4.2.3 Sensor Stability.....	170
5.4.3 Sandwich Assay Demonstration.....	170
5.5 Conclusions .....	173
5.6 References .....	174
Chapter 6. Polymer Domains Control Diffusion in Protein-Polymer Conjugate Biosensors.....	178
6.1 Abstract .....	178
6.2 Introduction .....	178
6.3 Materials and Methods .....	182
6.3.1 Materials.....	182
6.3.2 PNIPAM Synthesis.....	182
6.3.3 Protein Expression and Bioconjugation .....	183
6.3.4 Fluorescence Recovery After Photobleaching (FRAP) Sample Preparation .....	183
6.3.5 FRAP Experiments.....	185
6.3.6 Thin Film Preparation.....	186
6.3.7 Fluorescence Assays.....	186
6.3.8 Additional Characterization Methods.....	187
6.4 Results and Discussion.....	187
6.4.1 Overview of Diffusion Experiments .....	187
6.4.2 Thin Film Characterization.....	188
6.4.3 Diffusion Measurements .....	190
6.4.3.1 FRAP Data Fitting.....	190
6.4.3.2 Crosslinked 3xSso Gels.....	194
6.4.3.3 PNIPAM Solutions.....	196
6.4.4 Thin Film Binding Experiments.....	199
6.5 Conclusions .....	203
6.6 References .....	204
Chapter 7. Conclusions .....	210
7.1 Summary .....	210
7.2 Outlook.....	213
7.3 References .....	215
Appendix A. Supporting Information for Chapter 2.....	218
A.1 DNA and Amino Acid Sequences for Proteins Recombinantly Expressed in Thesis.....	218
A.1.1 Oligomers of rcSso7d.SA .....	220
A.1.1.1 1x rcSso7d.SA .....	220
A.1.1.2 2x rcSso7d.SA .....	221
A.1.1.3 3x rcSso7d.SA .....	221
A.1.1.4 4x rcSso7d.SA .....	221
A.1.2 Intermediate Genes Designed for Coiled-Coil fusions of 2x rcSso7d.SA .....	222
A.1.2.1 2x C-Cys.....	222
A.1.2.2 2x N-Cys_C-BsaI .....	222
A.1.2.3 2x C-Cys_N-BsaI .....	222

A.1.3 Coiled-Coil Fusions of 2x rcSso7d.SA.....	222
A.1.3.1 2xZEC.....	222
A.1.3.2 2xZRC .....	223
A.1.3.3 2xZEN .....	223
A.2 PAGE Gels and CD Spectra for Proteins Recombinantly Expressed in Thesis.....	225
A.2.1 Oligomers of rcSso7d.SA .....	225
A.2.2 Coiled-Coil Fusions of 2x rcSso7d.SA.....	226
A.3 <sup>1</sup> H-NMR Spectra .....	229
A.3.1 EMP .....	229
A.3.2 exo-3a,4,7,7a-Tetrahydro-2-(3-hydroxypropyl)-4,7-epoxy-14-isoindole-1,3(2 <i>H</i> )-dione (1) .....	230
A.3.3 CTA .....	231
A.4 Supporting Figures for Biosensor Measurements .....	232
A.5 Data Processing Code.....	233
A.5.1 SAXS Data Processing Code.....	233
A.5.2 FRAP Image Processing Code .....	236
A.5.3 FRAP Curve Fitting Code .....	239
Appendix B. Supporting Information for Chapter 3.....	243
Appendix C. Supporting Information for Chapter 4.....	263
Appendix D. Supporting Information for Chapter 5.....	287
Appendix E. Supporting Information for Chapter 6.....	295

## List of Schemes

Scheme 2-1. Synthetic scheme for the chain transfer agent (CTA) used in RAFT polymerizations.....	60
Scheme 2-2. Synthetic scheme for PNIPAM RAFT polymerization .....	64
Scheme 5-1. Bioconjugation of 3xSso containing an N-terminal cysteine residue to maleimide- functionalized PNIPAM.....	159
Scheme 6-1. Bioconjugation of 3xSso containing an N-terminal cysteine residue to maleimide- functionalized PNIPAM to form a 3xSP conjugate .....	189

## List of Tables

Table 2-1. Oligonucleotide sequences of primers used in oligomer generation .....	46
Table 2-2. Primers used for coiled-coil fusion gene cloning .....	49
Table 2-3. DNA sequences of ZE and ZR coiled-coil genes .....	49
Table 2-4. Buffer recipes tested for solubilization of coiled-coil fusions.....	54
Table 2-5. Proteins and dextran molecules purchased for diffusion experiments.....	59
Table 3-1. Composition of rcSso7d.SA oligomer-PNIPAM Conjugates.....	102
Table 3-2. Thermal Transitions for rcSso7d.SA Oligomer-PNIPAM Conjugates in Concentrated Solution.....	104
Table 3-3. Best-fit Parameter Values for Fits to Monomeric Streptavidin Binding Assays .	115
Table 4-1. Composition of Coiled-coil Fusion-PNIPAM Conjugates .....	135
Table 4-2. Percent Folding within Alpha Helical Region of Coiled-Coil Fusion Proteins...	136

Table 4-3.	Relative Activity of Coiled-Coil Fusion Conjugate Thin Films .....	145
Table 5-1.	Composition of 3xSso-PNIPAM Conjugates .....	159
Table 6-1.	Composition of 3xSP Conjugates .....	189
Table 6-2.	Thicknesses of Dry and Swollen 3xSP Conjugate Thin Films .....	190
Table 6-3.	Probe Molecules Used in FRAP Experiments .....	192
Table B-1.	Intermediate Values in Calculation of Relative Number of Binding Sites .....	262
Table C-1.	Activities and thicknesses of 2x and coiled-coil fusion conjugate thin films .....	263
Table D-1.	Comparison of Bulk and Thin Film Domain Spacings .....	289
Table D-2.	Best-fit Parameters for Buffer Binding Curves .....	291
Table D-3.	Best-fit Parameters for Biological Matrix Binding Curves .....	292
Table D-4.	Linear Range Approximations for Detection of mSA2 in Urine .....	292

## List of Figures

Figure 2-1.	Golden Gate assembly of the rcSso7d oligomers .....	46
Figure 2-2.	Agarose gel (1%) of gradient PCR experiments for formation of N-Cys and C-Cys variants of 2x rcSso7d.SA .....	48
Figure 2-3.	Representative standard curve generated for BSA standard using a reducing agent compatible BCA assay .....	53
Figure 2-4.	Denaturing protein gel (12% acrylamide) of TEV protease cleavage of mSA2-MBP at varying enzyme concentrations .....	57
Figure 2-5.	SEC purification of mSA2 .....	58
Figure 2-6.	TLC plate of crude product from EMP synthesis .....	61
Figure 2-7.	TLC plate of crude product from CTA synthesis .....	63
Figure 2-8.	Time series of GPC traces for PNIPAM polymerization .....	65
Figure 2-9.	Schematic of temperature-controlled 10-sample holder for SAXS experiments .....	71
Figure 2-10.	Added components to an existing turbidimetry/DPLS setup that allowed for automated data collection .....	76
Figure 2-11.	Schematic of temperature-controlled 5-sample holder for turbidimetry and DPLS experiments .....	77
Figure 2-12.	Comparison of representative fits to FRAP curves using equation (2-12) and equation (2-8) .....	89
Figure 3-1.	Representation and bioconjugation of rcSso7d.SA oligomers .....	101
Figure 3-2.	Phase diagrams of (a) 1xSP9.8k, (b) 2xSP17k, (c) 3xSP25k, and (d) 4xSP30k as a function of concentration and temperature .....	103
Figure 3-3.	SAXS curve displaying changes in conjugate phase behavior with (a) temperature and (b) concentration .....	106
Figure 3-4.	Ordering quality of rcSso7d.SA oligomer-PNIPAM conjugates indicated through (a) SAXS curves and (b) $\text{FWHM}^{-1}$ of the primary scattering peak .....	108
Figure 3-5.	Selected scattering data for 2xSP17k, 3xSP25k, and 4xSP30k .....	111
Figure 3-6.	Fluorescence binding assays with rcSso7d.SA oligomer conjugate thin films .....	114
Figure 4-1.	Coiled-coil fusion proteins and their bioconjugation .....	135
Figure 4-2.	Analytical ultracentrifugation continuous size distributions for coiled-coil fusion conjugates (a) 2xZEC, (b) 2xZRC, (c) 2xZEN, (d) 2xZEC-ZRC, and (e) 2xZEN-ZRC .....	137

Figure 4-3.	Melting curves for (a) 2x and 2xZEC-ZRC and component coiled-coil fusion proteins and (b) 2xZEN-ZRC and component coiled-coil fusion proteins.....	138
Figure 4-4.	Representative SAXS traces for 2xZEC conjugates.....	139
Figure 4-5.	Phase diagrams of the protein-PNIPAM conjugates (a) 2xZEC, (b) 2xZRC, (c) 2xZEN, (d) 2xZEC-ZRC, and (e) 2xZEN-ZRC as a function of concentration and temperature .....	140
Figure 4-6.	Ordering quality of coiled-coil fusion conjugates in aqueous solution .....	144
Figure 4-7.	Streptavidin binding curves for 2x and coiled-coil fusion conjugate thin film assays .....	145
Figure 5-1.	GISAXS data for synthesized 3xSP conjugates.....	159
Figure 5-2.	Fluorescent assays indicating the diffusion of (a) SA and (b) mSA2 into bioconjugate thin films over time .....	161
Figure 5-3.	Diagram of SA (red) and mSA2 (blue) diffusion into 3xSP conjugate thin films .....	161
Figure 5-4.	Results of 30 minute fluorescent binding assays performed in bioconjugate thin films using (a, b) SA or (c, d) mSA2 as the analyte .....	163
Figure 5-5.	Binding curves for conjugate thin films exposed to (a) SA or (c) mSA2 in PBS for different periods of time.....	165
Figure 5-6.	Binding curves for conjugate thin films exposed to (a, b) SA or (c, d) mSA2 in (a, c) 50% urine or (b, d) 50% blood serum solutions for 4 hours.....	168
Figure 5-7.	Schematic of model sandwich assay performed in conjugate thin film biosensors .....	171
Figure 5-8.	Binding curves for sandwich assays performed with SA in PBS .....	172
Figure 6-1.	GISAXS linecuts and domain spacings for 3xSP conjugate thin films .....	189
Figure 6-2.	Representative fit to a normalized FRAP curve $f(t)$ .....	193
Figure 6-3.	Effective diffusion coefficients of (a) proteins and (b) dextran molecules in 0.2 volume fraction solutions of crosslinked 3xSso gels measured using FRAP.....	195
Figure 6-4.	Effective diffusion coefficients of proteins in 0.2 volume fraction solutions of PNIPAM measured using FRAP .....	197
Figure 6-5.	Effective diffusion coefficients of dextran molecules in 0.2 volume fraction solutions of PNIPAM measured using FRAP.....	199
Figure 6-6.	Relative fluorescence intensities of thin films exposed to mSA2 mixed with other proteins at 100x the concentration of mSA2.....	201
Figure 6-7.	Relative fluorescence intensities of thin films exposed to mSA2 mixed with other proteins at 10x the concentration of mSA2.....	202
Figure A-1.	Plasmid map for pET28b(+) vector used for all cloning experiment in this thesis .....	218
Figure A-2.	Protein gels of rcSso7d.SA oligomers and conjugates .....	225
Figure A-3.	CD spectra of rcSso7d.SA oligomers and conjugates .....	225
Figure A-4.	Protein gels of coiled-coil fusions and conjugates.....	226
Figure A-5.	CD spectra of coiled-coil fusions and conjugates.....	227
Figure A-6.	Protein gels of 3xSP conjugates used in chapter 5 .....	227
Figure A-7.	CD spectra of 3xSP conjugates.....	228
Figure A-8.	Protein gels of 3xSP conjugates used in chapter 6 .....	228
Figure A-9.	$^1\text{H-NMR}$ spectra for EMP.....	229

Figure A-10.	<sup>1</sup> H-NMR spectra for exo-3a,4,7,7a-Tetrahydro-2-(3-hydroxypropyl)-4,7-epoxy-14-isoindole-1,3(2H)-dione (1).....	230
Figure A-11.	<sup>1</sup> H-NMR spectra for CTA.....	231
Figure A-12.	Fluorescent intensity of BSA labeled with Alexa Fluor 488 retained in 3xSP77.6k thin film after various rinsing times.....	232
Figure B-1.	Normalized differential refractive index signals from gel permeation chromatography of PNIPAM samples.....	243
Figure B-2.	Radially averaged SAXS patterns for 1xSP9.8k.....	244
Figure B-3.	Radially averaged SAXS patterns for 2xSP17k.....	245
Figure B-4.	Radially averaged SAXS patterns for 3xSP25k.....	246
Figure B-5.	Radially averaged SAXS patterns for 4xSP30k.....	247
Figure B-6.	DPLS and turbidimetry heating/cooling cycles for 1xSP9.8k.....	248
Figure B-7.	DPLS and turbidimetry heating/cooling cycles for 1xSP17k.....	251
Figure B-8.	DPLS and turbidimetry heating/cooling cycles for 1xSP25k.....	254
Figure B-9.	DPLS and turbidimetry heating/cooling cycles for 1xSP30k.....	257
Figure B-10.	DSC curves of (a) 1xSP9.8k, (b) 2xSP17k, (c) 3xSP25k, and (d) 4xSP30k at varying concentrations.....	260
Figure B-11.	Effect of incubation time on ordering quality in 70 wt.% 3xSP25k samples.....	261
Figure B-12.	Comparison of binding curves obtained for each considered conjugate and rcSso7d.SA monolayer using streptavidin as the analyte.....	262
Figure C-1.	Normalized differential refractive index signal from gel permeation chromatography of the synthesized PNIPAM sample.....	263
Figure C-2.	Radially averaged SAXS patterns for 2xZEC conjugates.....	264
Figure C-3.	Radially averaged SAXS patterns for 2xZRC conjugates.....	265
Figure C-4.	Radially averaged SAXS patterns for 2xZEN conjugates.....	266
Figure C-5.	Radially averaged SAXS patterns for 2xZEC-ZRC conjugates.....	267
Figure C-6.	Radially averaged SAXS patterns for 2xZEN-ZRC conjugates.....	268
Figure C-7.	DPLS and turbidimetry heating/cooling cycles for 2xZEC conjugates.....	269
Figure C-8.	DPLS and turbidimetry heating/cooling cycles for 2xZRC conjugates.....	272
Figure C-9.	DPLS and turbidimetry heating/cooling cycles for 2xZEN conjugates.....	275
Figure C-10.	DPLS and turbidimetry heating/cooling cycles for 2xZEC-ZRC conjugates.....	278
Figure C-11.	DPLS and turbidimetry heating/cooling cycles for 2xZEN-ZRC conjugates.....	281
Figure C-12.	DSC curves of (a) 2xZEC, (b) 2xZRC, (c) 2xZEN, (d) 2xZEC-ZRC, and (e) 2xZEN-ZRC at varying concentrations.....	284
Figure C-13.	Transition temperatures for (a) macrophase separation and (b) PNIPAM desolvation for coiled-coil fusion conjugates as a function of concentration.....	285
Figure C-14.	Domain spacings of coiled-coil fusion conjugates in aqueous solution.....	285
Figure C-15.	FWHM <sup>-1</sup> of ordered phases in 45 weight percent 2xZRC samples as a function of temperature.....	286
Figure D-1.	Normalized differential refractive index signals from gel permeation chromatography of PNIPAM samples.....	287
Figure D-2.	Representative GISAXS vertical linecut from swollen thin films.....	288
Figure D-3.	Bulk SAXS curves for synthesized conjugates at ambient conditions.....	289
Figure D-4.	GISAXS horizontal linecuts of a 150 nm 3xSP56.1k film swollen in an environment maintained at 95% RH for different periods of time.....	290
Figure D-5.	Thin film stability as a function of time under ambient and humid conditions.....	293

Figure D-6.	Results of sequential fluorescent binding assays using (a) mSA2 and (b) SA as the analyte .....	294
Figure D-7.	Binding curves for sandwich assays performed with SA in (a) 50% urine and (b) 50% blood serum .....	294
Figure E-1.	Normalized differential refractive index signals from gel permeation chromatography of PNIPAM samples .....	294
Figure E-2.	GISAXS patterns of crosslinked 3xSP thin films .....	296
Figure E-3.	Radially averaged SAXS patterns for 3x rcSso7d.SA conjugates in the bulk state .....	296
Figure E-4.	Fits to SANS patterns for (a) CytC and (b) mSA2 in deuterated PBS .....	297
Figure E-5.	CD curves for proteins in PBS with and without 10 wt.% PNIPAM 77k added.	297
Figure E-6.	DLS size histograms for PNIPAM 117k in PBS and proteins in PBS with and without 1 wt.% PNIPAM 117k added .....	298
Figure E-7.	Relative fluorescence intensities of mSA2 mixed with various proteins .....	299

## **Chapter 1. Introduction**

### **1.1 Motivation**

Biosensors, devices used to identify the presence or concentration of a target biomolecule, have become a pervasive tool in medical diagnostics.<sup>1-3</sup> Because these sensors see frequent use in early-stage detection of cancer and diseases, applications for which the concentration or change in normal body concentration of the intended analyte is low,<sup>4-5</sup> it is critical that biosensors have a high sensitivity for the target molecule. Additionally, these devices are commonly used at the point-of-care, where rapid, simple, and inexpensive testing is a necessity.<sup>4-6</sup> Despite the need for biosensors that can provide rapid and accurate readings directly on samples acquired from patients, most sensors display limited success at this feat. One of the most common issues is reduction in sensitivity due to nonspecific binding effects.<sup>7-8</sup> Because biosensing fluids usually contain off-target molecules millions of times more concentrated than the intended analyte, the large number of off-target molecules bind to sensor surfaces, blocking analyte receptor sites and reducing device sensitivity.<sup>9-10</sup> Some techniques have been developed to overcome these nonspecific binding issues, but these methods rely on time-consuming or expensive sample pre-treatment.<sup>11-12</sup>

Therefore, this thesis aims to develop a freestanding biosensor platform that can achieve high sensitivity and selectivity for a target analyte in biological fluids and other complex mixtures. The remainder of this chapter will provide a literature review of concepts and methods utilized in the design of this biosensing platform. Beginning with a comprehensive summary of the active components in biosensors, topics will gradually become increasingly focused on the selected biosensor design. The chapter will conclude with a presentation of the material selected for biosensor development and an overview of the research projects undertaken to develop and optimize this biosensor.

## 1.2 Proteins

The most fundamental components of biosensors that give these devices sensing capabilities, proteins are a diverse set of biological macromolecules consisting of one or more amino acid chains folded into complex 3D architectures. The process of protein folding, though occurring over times as short as microseconds,<sup>13</sup> is incredibly complex and allows a sequence of amino acids to fold into a unique structure. During folding, nearby amino acids first sample different conformations by forming local metastable structures through hydrogen bonding and other specific intramolecular interactions.<sup>13</sup> As the folding process progresses, many of these higher-energy metastable structures unfold while more stable regions grow and combine with adjacent structures until the peptide chain ultimately folds into its native state.<sup>13-14</sup> Though the number of intramolecular interactions that govern protein folding is rather limited, hundreds of different classes of local chain topologies exist in native protein structures,<sup>15</sup> and 5 million unique proteins are estimated to exist on Earth.<sup>16</sup> This great diversity of structures has given rise to proteins with a wide range of functions, enabling use of these biomolecules in a myriad of processes and products, including food processing and packaging,<sup>17-20</sup> pulp and paper bleaching,<sup>21</sup> detergents,<sup>17, 22</sup> and therapeutics.<sup>23-24</sup>

In many cases, the structure of a protein allows it to bind with high specificity to a substrate. Proteins have been found to bind to a variety of molecules, including small molecules,<sup>25-27</sup> DNA/RNA,<sup>28-30</sup> and other proteins.<sup>31-32</sup> Traditional models for protein-substrate binding mechanisms have either assumed that the protein structure is completely rigid and the substrate fits neatly into some binding site on the protein surface (i.e., the lock-and-key model)<sup>33</sup> or that the binding site is somewhat pliable and the substrate is able to slightly distort the binding site to fit the structure of the substrate (i.e., the induced fit model).<sup>34</sup> While many proteins do bind substrates

according to these models that assume a completely or almost completely rigid protein structure, studies within the past two decades have revealed that numerous proteins contain disordered regions of at least 10 amino acids in length, yielding more dynamic protein structures.<sup>35</sup> These disordered regions can allow a protein to adopt one or several conformations to achieve high-specificity binding to substrates.<sup>36-37</sup> For example, ubiquitin contains a large, highly dynamic region within its sequence, and this protein is known to form over 50 unique structures, each of which can bind to a distinct protein.<sup>37-39</sup> An extreme case of dynamism, intrinsically disordered proteins (IDPs) are proteins with little or no well-defined, persistent structure.<sup>40-41</sup> Despite having no true structure, IDPs can partially fold and form a strong bond in the presence of a substrate or other binding partner,<sup>40-41</sup> though no single hypothesis has emerged regarding the mechanism of this folding.<sup>42-44</sup>

Enzymes are another class of proteins that not only bind to a substrate, but facilitate a change in the structure of the substrate by catalyzing a chemical reaction. This catalysis is primarily achieved through interactions between specific residues in the active site, the region in the enzyme in which the chemical reaction occurs, and the substrate.<sup>45</sup> For instance, one very common set of residues that combine to provide catalytic activity is the catalytic triad, which is composed of a nucleophilic residue (e.g., serine), a basic residue (e.g., aspartate), and an acidic residue (e.g., histidine). Mechanisms involving this catalytic triad proceed by the base deprotonating the nucleophile, the acid stabilizing the resulting salt of the base, and the activated nucleophile attacking an electrophilic site on the substrate.<sup>46</sup> Though a wide variety of other catalytic series of residues exist, including unconventional modifications to the catalytic triad,<sup>47</sup> the interactions between the residues usually provide either charge, and acid/base, a nucleophile, or tautomerization.<sup>45</sup> In some enzymes, cofactors such as metal ions and small organic molecules are

also required for reaction to occur, typically to either stabilize the structure of the enzyme or the transition state in the chemical reaction.<sup>48-50</sup> While residues and cofactors within the active site directly catalyze the chemical reaction, recent studies have found that even residues far from this site affect catalysis rates.<sup>51-53</sup> Due to the non-static nature of the structure of enzymes and other proteins, it is believed that dynamic fluctuations, such as those caused by solvent molecules, affect the motion of individual residues, and this vibration is propagated to the active site, resulting in conformational changes.<sup>54-56</sup>

With the rapidly growing understanding of protein structure and function, many proteins can now be engineered for specific applications. One method to achieve unique protein functionality is through installing non-canonical amino acids by providing cells with modified tRNA molecules during recombinant protein expression.<sup>57</sup> Using this technique, proteins have been designed to understand protein structure and function,<sup>58</sup> provide new spectroscopic properties,<sup>59</sup> install site-specific groups for post-functionalization,<sup>60</sup> and modulate the clearance time of bacteriophages in plasma.<sup>61</sup> Protein scaffolds, proteins with well-defined binding faces that can easily be modified to display specificity for an arbitrary substrate, have also been identified for engineering novel proteins. From just a small number of scaffolds, proteins have been developed for therapeutic applications,<sup>62-64</sup> with enhanced thermal stability,<sup>65</sup> and to direct self-assembly of other molecules.<sup>66</sup> When an enzyme is desired for a specific reaction but it is not clear what mutations need to be made to an existing protein to achieve the desired functionality, directed evolution can be used. In this method, the gene sequence of an enzyme is subjected to successive rounds of mutagenesis. The activity of the mutants for the desired reaction is then measured and, in a manner similar to natural selection, used to direct future mutations towards the desired enzyme function.<sup>67-68</sup> This technique, though requiring no knowledge of what the final structure of the

engineered protein should be, has allowed development of numerous enzymes with industrially relevant applications.<sup>69-70</sup> Clearly, the breadth of protein function is expansive, and this diversity is continuously increasing.

### **1.3 Protein Biosensors**

One of the largest applications for binding proteins is in protein biosensors. Biosensors are devices used to detect the presence or concentration of one or more biological analytes. In general, these sensors contain three primary components: an element that selectively recognizes the target analyte(s), typically through a binding event, a part that converts this recognition event into a measurable signal, and a method for either quantifying the measurable signal or converting this signal into a useful and more easily understood form.<sup>71</sup> As an example, one of the earliest developed biosensors was a blood glucose sensor containing a thin film of glucose oxidase coated on an oxygen electrode.<sup>72</sup> A patient's blood was passed through the machine, where glucose oxidase catalyzed the consumption of glucose and oxygen. The corresponding drop in dissolved oxygen was detected at the electrode, and the change in potential was compared against a standard curve to provide a blood glucose concentration. While the technology used in this blood glucose sensor was simple, the design principles formed the foundation for the now burgeoning field of biosensors.<sup>1-3</sup>

Today, there are a wide variety of biosensor formats that use surface-immobilized proteins as the molecular recognition elements. Surface plasmon resonance (SPR) biosensors are widely used designs that consist of receptor proteins for a target analyte immobilized on a gold surface.<sup>73-75</sup> When analyte molecules bind to these capture proteins, the refractive index at the surface of the sensor changes, affecting the propagation rate of surface plasma waves that are generated when the surface is exposed to plane-polarized light. Changes in this propagation rate can be indirectly

measured to infer protein binding to the surface, but changes in signal can also be caused by binding of off-target proteins to the sensor surface or changes in refractive index due to temperature and concentration fluctuations.<sup>76</sup> Quartz crystal microbalance (QCM) biosensors have been designed that use piezoelectric effects to detect changes in mass corresponding to analyte binding.<sup>77-80</sup> Microcantilever biosensors operate on a similar principle, in which analyte binding to capture proteins on the surface of microcantilevers shifts the resonance frequency of the cantilever, allowing quantification of protein binding.<sup>81-85</sup> Yet another class of sensors, lateral flow assay (LFA) biosensors<sup>86-87</sup> and microfluidic biosensors<sup>88-89</sup> are typically paper-based devices that use capillary action to wick samples across regions where the analyte is sequentially labeled (e.g., with a dye) and bound to a capture protein. These biosensors offer a combination of low cost and high sensitivity that has prompted their use in point-of-care applications.<sup>90-92</sup>

Despite the diversity in their design, biosensors incorporating surface-immobilized proteins all have two major issues. First, capture proteins must be immobilized to the sensor surface with proper orientation such that the binding sites in the proteins are fully accessible.<sup>93-95</sup> Typical immobilization techniques produce a random orientation of proteins on the surface. While numerous procedures have been reported to achieve well-oriented protein monolayers,<sup>96-101</sup> these methods all require either pretreatment of the protein/surface or that the protein have a specific structure. Second, nonspecific binding from molecules present in the detection fluid along with the intended analyte increases the background signal for biosensors, reducing sensitivity by up to several orders of magnitude.<sup>9-10</sup> Due to this significant issue, a variety of both passive<sup>102</sup> and active<sup>103</sup> methods for reducing nonspecific binding have been developed. However, these methods either reduce sensor longevity or add complexity, making it challenging to use biosensors for simple and rapid analysis. Thus, the development of general methods for properly orienting capture

proteins and reducing nonspecific binding are of high priority for optimizing biosensor performance.

#### **1.4 Block Copolymer Self-Assembly**

To orient capture proteins, inspiration can be drawn from block copolymer self-assembly. Block copolymers provide a general framework for creating 3D arrays of densely packed and well-oriented materials. While a variety of block copolymer architectures have been developed, including nonlinear,<sup>104</sup> multiblock,<sup>105-106</sup> and tapered block copolymers,<sup>107-108</sup> the simplest and most well-studied design is the diblock copolymer. These copolymers, composed of two homopolymers linked together end-to-end, have been demonstrated to self-assemble into a variety of nanostructures including lamellae, hexagonally-packed cylinders, and gyroids.<sup>109-112</sup> Phase separation within diblock systems is driven by three parameters:  $\chi$ , the Flory-Huggins interaction parameter, which is an enthalpic term describing the degree of chemical dissimilarity between the two blocks,  $N$ , the overall degree of polymerization, which encompasses the entropic penalty of chain stretching, and  $f$ , the volume fraction of one of the blocks.<sup>109-111</sup> The onset of phase separation for symmetric diblocks is predicted to occur at  $\chi N = 10.5$ , at which point the entropic penalty associated with stretching chains in the ordered state is balanced by the decreased enthalpy as a result of decreased interfacial area.<sup>111</sup> Because the two blocks are connected by a covalent bond, macrophase separation does not occur, and the blocks instead separate at lengths scales on the order of 10-100 nm.<sup>110</sup>

In dilute aqueous solution, amphiphilic diblock copolymers primarily form micelles, structures in which hydrophobic blocks aggregate in solvent-poor phases surrounded by hydrophilic blocks extending into a solvent-rich phase. While individual block copolymer molecules are distributed throughout the solution and act as surfactants at low concentrations,

micelles spontaneously form above a critical micelle concentration (CMC).<sup>113</sup> Above the CMC, micelle stability is primarily controlled by the hydrophobic block, where longer and more hydrophobic chains significantly enhance stability.<sup>114-115</sup> Varying the relative length of the hydrophilic block yields a variety of morphologies, including bilayers, cylinders, wormlike micelles, and spheres;<sup>116-117</sup> the self-assembly of spherical micelles in particular has garnered significant attention in the literature.<sup>113, 118-120</sup>

In concentrated solution, diblock copolymers self-assemble into many of the same phases observed in the bulk state. Unlike in the bulk state, however, the solvent and therefore its selectivity for each block can be adjusted in concentrated solution, providing another variable by which phase behavior can be controlled.<sup>121-123</sup> Since a perfectly neutral solvent distributes equally between domains, it is assumed that the only effect of the solvent on segregation strength is to dilute monomer-monomer interactions in proportion to the polymer volume fraction, which is referred to as the dilution approximation.<sup>124</sup> Selective solvents not only dilute monomer-monomer interactions but also selectively partition into one phase, effectively changing the volume fraction of each block. When these solvent effects are mapped onto a bulk diblock copolymer phase diagram of  $\chi N$  vs.  $f$ , good qualitative agreement is shown with the bulk data, except that the region of disordered phases is expanded in solution.<sup>121, 125</sup> It has also been demonstrated in both theory<sup>126</sup> and experiments<sup>127</sup> that solvents that are good and nonselective for both blocks preferentially segregate to the interface, shielding the repulsive interactions between phases and causing a reduction in overall domain spacing.<sup>128</sup> This enhanced solvent distribution at the interface between phases is not observed in nonselective solvents,<sup>127</sup> where domain spacing trends with polymer volume fraction can vary greatly as a function of both temperature and the assembled nanophase.<sup>128</sup>

In block copolymer thin films, films thinner than approximately one micron, the small length scales cause morphology to be largely determined by confinement and interfacial effects. For example, block copolymer thin films that assemble into lamellae can be oriented either perpendicular or parallel to the underlying substrate. Because lamellae have a natural repeat spacing, parallel lamellae pay an energetic penalty due to chain stretching or compression if film thickness is not commensurate with this spacing, and perpendicular lamellae are favored.<sup>129-131</sup> However, if the surface energetics at the top and bottom interfaces of the film (e.g., the underlying substrate and the atmosphere) are different such that one block preferentially segregates to each interface, a parallel lamellar orientation is more stable.<sup>132</sup> These surface effects can be used to induce ordering that propagates hundreds of nanometers into thin films,<sup>133-134</sup> as has been realized in several robust methods for inducing order such as epitaxy<sup>135</sup> and solvent vapor annealing.<sup>136</sup> The interplay between confinement and surface energetics can result in thin films displaying islands/holes<sup>112, 137</sup> and morphologies that vary drastically with even small changes in film thickness.<sup>138</sup> As such, block copolymers offer a wealth of methods to achieve self-assembled materials.

### **1.5 Protein-Polymer Conjugate Self-Assembly**

Protein-polymer conjugates, block copolymers in which one block is a protein, exhibit the self-assembly properties of traditional block copolymers while also introducing biological functionality. In dilute solution, amphiphilic protein-polymer conjugates have been shown to self-assemble into micellar morphologies, as is observed in coil-coil diblock copolymers.<sup>139-141</sup> These micelles have primarily been used for drug and gene delivery applications,<sup>142-143</sup> where the proteins blocks can promote intracellular delivery,<sup>144</sup> enable stimuli-driven changes in micelle size and density,<sup>145</sup> and both bind and release payloads.<sup>146</sup> Furthermore, the protein block in protein-

polymer conjugates can enhance self-assembly if the protein itself forms or promotes well-defined structures such that hydrophobic collapse of one block is no longer required for self-assembly in aqueous solution. For instance, when peptides that form beta sheets are conjugated to polymers, these beta sheets promote fiber formation.<sup>147-149</sup> Similarly, coiled-coils, supercoiled bundles of alpha helices, have been conjugated to polymers to promote formation of aggregates with precise aggregation number<sup>150-151</sup> as well as rodlike and spherical micelles.<sup>152</sup> When several of these coils are incorporated in the protein block of protein-polymer block copolymers, hydrogels can spontaneously form from association of coiled-coil domains.<sup>153-156</sup>

In bulk and concentrated solution, the self-assembly of proteins conjugated to a fully-folded protein block shares some similarities with that of coil-coil diblock copolymers. Like traditional diblock copolymers, protein-polymer conjugates can access a wide range of morphologies, including lamellae, hexagonally packed cylinders, and gyroids.<sup>157-159</sup> These periodic structures with regions of densely packed protein enhance protein activity, as realized in biocatalysts and biosensors with significantly improved performance compared to devices with surface-immobilized proteins.<sup>160-161</sup> Unlike traditional coil-coil block copolymers, however, protein-polymer conjugates display lamellar ordering over a wide compositional range, asymmetric phase diagrams, and re-entrant order-disorder transition (ODT) behavior.<sup>162-163</sup> Though the cause of these behaviors is not fully understood, recent work has demonstrated that the identities and ordering qualities of observed protein-polymer nanophases are highly dependent upon coarse-grained properties of the protein block (i.e., size and structure) and attributed entanglement effects from the polymer block.<sup>164</sup> Despite an incomplete understanding of the self-assembly of protein-polymer conjugates in concentrated solution, the enhanced activity and

sensitivity exhibited by these materials provides significant motivation to study their use in biotechnological applications.

## **1.6 Transport in Block Copolymer and Homopolymer Solutions**

While the self-assembly properties of protein-polymer conjugates can be utilized to orient capture proteins in biosensors, the transport properties of these block copolymers can also allow minimization of nonspecific binding. To date, the diffusion in ordered block copolymer solutions has primarily been studied for two classes of diffusants: block copolymers (self-diffusion) and ions. For diblock copolymer self-diffusion in lamellae, diffusion can occur either along the interfaces between domains (parallel diffusion), in which each block of the copolymer remains within its own phase, or through the lamellar layers (perpendicular diffusion), where blocks must pass through domains of the opposite phase. Clearly, perpendicular diffusion is expected to pose a much greater resistance to diffusion of the diblock copolymer, as it requires enthalpically unfavorable movement of the blocks of the copolymer into chemically dissimilar domains. Indeed, early diffusion experiments in disordered and lamellar block copolymers without macroscale orientation showed that the diffusion of Rouse chains was essentially unaffected by ordering, whereas reptating chains exhibited significantly reduced diffusion in the ordered state.<sup>165-167</sup> Direct measurements of these two methods of diffusion were later used to confirm that the diffusion coefficient for parallel diffusion is over an order of magnitude greater than that for perpendicular diffusion in lamellae.<sup>168</sup> Similar asymmetries have also been measured in other block copolymer morphologies.<sup>169</sup>

For ion diffusion in block copolymers, diffusion is considered to occur within a single domain of the system. As such, diffusion through randomly oriented grains of morphologies in which diffusion primarily occurs along one or two of the principle directions, such as cylinders

and lamellae, is expected to be reduced by a factor of 1/3 or 2/3, respectively, compared to bulk diffusion. These morphology-dependent factors for diffusion reduction have been supported by both theory<sup>170</sup> and experiments.<sup>171-173</sup> Morphologies with more complex symmetries such as gyroids instead reduce diffusion by a factor intermediate to 1/3 and 2/3, for which the exact reduction is dependent on the relative volume fraction of each phase.<sup>174</sup>

While self-diffusion and ion transport in block copolymer solutions have been well-studied, the diffusion of nanoparticles and proteins in these solutions is almost completely unexplored. At the time of writing, only one study has reported on this topic, in which it was demonstrated that protein diffusivity in micelle crystals was reduced by up to four orders of magnitude compared to diffusivity measurements in aqueous solution.<sup>175</sup> Instead of focusing on diffusion in block copolymers, most research has considered diffusion of nanoparticles and proteins in homopolymer solutions and gels. For nanoparticles, it has been found that the diffusivity of the particle is dependent upon the size of the particle relative to the radius of gyration ( $R_g$ ) of the polymer.<sup>176</sup> While diffusion follows the Stokes-Einstein relation if the nanoparticle is larger than the polymer  $R_g$ , the particle diffuses much faster than is predicted by this equation if the particle is smaller than the polymer  $R_g$ .<sup>177-179</sup> Theories have been developed to rationalize this phenomenon, which have assumed diffusion mechanisms including nanoparticle hopping between entanglements<sup>180</sup> and fast diffusion within a confined depletion region at small length scales.<sup>181-182</sup>

Unlike nanoparticles, which are assumed to not interact with polymer chains, proteins can and do interact with polymers, leading to more complex transport phenomena. Polymers such as dextran that interact with proteins increase the effective hydrodynamic diameter of the protein, causing negative deviations in translational diffusion from Stokes-Einstein predictions.<sup>183-186</sup> Rotational diffusion also is lower than expected, though different studies find that the decrease in

rotational diffusion can either be greater than or less than that of translational diffusion.<sup>184-186</sup> Even polymers that do not interact with proteins, however, can still affect diffusion by indirectly controlling protein-protein association. When these non-interacting polymers are in the dilute regime, the polymers induce preferential hydration of the proteins, reducing the likelihood of aggregation.<sup>185, 187</sup> In the semidilute regime, association rates are enhanced, while in the concentrated regime, protein-protein association is again diminished, which has been attributed to depletion effects.<sup>187</sup> Thus, diffusion of proteins in polymer solutions is incredibly complex, depending upon the identity and concentration of both the protein and polymer.

## **1.7 Thesis Overview**

Due to their potential to orient capture proteins and control molecular transport, protein-polymer conjugates were selected as an ideal material for biosensor fabrication. Thus, the goal of this thesis is to develop strategies to design protein-polymer conjugate biosensors with enhanced sensitivity and selectivity in complex sensing mixtures. To accomplish this objective, techniques to improve conjugate self-assembly will be presented, and factors governing transport within these the fabricated biosensors will be studied. In this document, chapter 2 provides detailed methodologies for the synthesis, data collection, and data processing used in the thesis. Chapters 3 and 4 discuss methodologies for enhancing ordering quality of protein-polymer conjugates through genetic engineering of the protein block. In chapter 3, oligomerization of the protein block is explored as a method to promote better assembly of otherwise weakly ordered conjugates with low molecular weight protein blocks. Chapter 4 presents a more general ordering technique of fusing associative heterodimeric coiled-coil sequences to the protein block. In chapter 5, the biosensing capabilities of bioconjugate thin films are measured and compared to those of traditional surface-immobilized protein biosensors. Performance, including ability to prevent nonspecific binding during sensing

in biological fluids, is also measured as a function of the molecular weight of the polymer block in the protein-polymer conjugate. Finally, chapter 6 explores factors affecting size-based transport of proteins in conjugate thin films. Diffusion coefficients for a panel of proteins is measured in protein and polymer solutions individually, and the results are compared to diffusion measurements in the thin films, providing insight into the relative diffusional resistance applied by each block.

## 1.8 References

1. Asal, M.; Özen, Ö.; Şahinler, M.; Polatoğlu, İ., Recent Developments in Enzyme, DNA and Immuno-Based Biosensors. *Sensors* **2018**, *18* (6).
2. Grieshaber, D.; MacKenzie, R.; Vörös, J.; Reimhult, E., Electrochemical Biosensors - Sensor Principles and Architectures. *Sensors* **2008**, *8* (3).
3. Vigneshvar, S.; Sudhakumari, C. C.; Senthilkumaran, B.; Prakash, H., Recent Advances in Biosensor Technology for Potential Applications – An Overview. *Front. Bioeng. Biotechnol.* **2016**, *4* (11).
4. Miller, E.; Sikes, H. D., Addressing Barriers to the Development and Adoption of Rapid Diagnostic Tests in Global Health. *Nanobiomedicine* **2015**, *2*, 6.
5. Wang, J., Electrochemical biosensors: Towards point-of-care cancer diagnostics. *Biosens. Bioelectron.* **2006**, *21* (10), 1887-1892.
6. Roda, A.; Michelini, E.; Zangheri, M.; Di Fusco, M.; Calabria, D.; Simoni, P., Smartphone-based biosensors: A critical review and perspectives. *TrAC, Trends Anal. Chem.* **2016**, *79*, 317-325.
7. Blawas, A. S.; Reichert, W. M., Protein patterning. *Biomaterials* **1998**, *19* (7), 595-609.
8. Nedelkov, D.; Nelson, R. W., Analysis of native proteins from biological fluids by biomolecular interaction analysis mass spectrometry (BIA/MS): exploring the limit of detection, identification of non-specific binding and detection of multi-protein complexes. *Biosens. Bioelectron.* **2001**, *16* (9), 1071-1078.
9. Masson, J.-F., Surface Plasmon Resonance Clinical Biosensors for Medical Diagnostics. *ACS Sensors* **2017**, *2* (1), 16-30.
10. Arlett, J. L.; Myers, E. B.; Roukes, M. L., Comparative advantages of mechanical biosensors. *Nat. Nano.* **2011**, *6* (4), 203-215.
11. Bunyakul, N.; Baeumner, A. J., Combining Electrochemical Sensors with Miniaturized Sample Preparation for Rapid Detection in Clinical Samples. *Sensors* **2015**, *15* (1), 547-564.
12. Zanolli, L. M.; Spoto, G., Isothermal Amplification Methods for the Detection of Nucleic Acids in Microfluidic Devices. *Biosensors* **2013**, *3* (1), 18-43.
13. Dill, K. A.; Ozkan, S. B.; Shell, M. S.; Weikl, T. R., The Protein Folding Problem. *Annu. Rev. Biophys.* **2008**, *37* (1), 289-316.
14. Englander, S. W.; Mayne, L., The nature of protein folding pathways. *Proc. Natl. Acad. Sci. U.S.A.* **2014**, *111* (45), 15873-15880.

15. Cyrus Chothia; Tim Hubbard; Steven Brenner; Hugh Barns, a.; Murzin, A., PROTEIN FOLDS IN THE ALL- $\beta$  AND ALL- $\alpha$  CLASSES. *Annu. Rev. Biophys. Biomol. Struct.* **1997**, *26* (1), 597-627.
16. Perez-Iratxeta, C.; Palidwor, G.; Andrade-Navarro, M. A., Towards completion of the Earth's proteome. *EMBO reports* **2007**, *8* (12), 1135-1141.
17. Gupta, R.; Beg, Q.; Lorenz, P., Bacterial alkaline proteases: molecular approaches and industrial applications. *Appl. Microbiol. Biotechnol.* **2002**, *59* (1), 15-32.
18. Houde, A.; Kademi, A.; Leblanc, D., Lipases and their industrial applications. *Appl. Biochem. Biotechnol.* **2004**, *118* (1), 155-170.
19. Souza, P. M. d.; Magalhães, P. r. d. O. e., Application of microbial  $\pm$ -amylase in industry - A review. *Braz. J. Microbiol.* **2010**, *41*, 850-861.
20. Bhosale, S. H.; Rao, M. B.; Deshpande, V. V., Molecular and industrial aspects of glucose isomerase. *Microbiol. Rev.* **1996**, *60* (2), 280-300.
21. Walia, A.; Guleria, S.; Mehta, P.; Chauhan, A.; Parkash, J., Microbial xylanases and their industrial application in pulp and paper biobleaching: a review. *3 Biotech* **2017**, *7* (1), 11.
22. Kuhad, R. C.; Gupta, R.; Singh, A., Microbial cellulases and their industrial applications. *Enzyme Res* **2011**, *2011*, 280696-280696.
23. Leader, B.; Baca, Q. J.; Golan, D. E., Protein therapeutics: a summary and pharmacological classification. *Nat. Rev. Drug Discov.* **2008**, *7* (1), 21-39.
24. Chames, P.; Van Regenmortel, M.; Weiss, E.; Baty, D., Therapeutic antibodies: successes, limitations and hopes for the future. *Br. J. Pharmacol.* **2009**, *157* (2), 220-233.
25. Gao, M.; Skolnick, J., A Comprehensive Survey of Small-Molecule Binding Pockets in Proteins. *PLoS Comp. Biol.* **2013**, *9* (10), e1003302.
26. Lee, G. U.; Kidwell, D. A.; Colton, R. J., Sensing Discrete Streptavidin-Biotin Interactions with Atomic Force Microscopy. *Langmuir* **1994**, *10* (2), 354-357.
27. Ong, S.-E.; Schenone, M.; Margolin, A. A.; Li, X.; Do, K.; Doud, M. K.; Mani, D. R.; Kuai, L.; Wang, X.; Wood, J. L.; Tolliday, N. J.; Koehler, A. N.; Marcaurelle, L. A.; Golub, T. R.; Gould, R. J.; Schreiber, S. L.; Carr, S. A., Identifying the proteins to which small-molecule probes and drugs bind in cells. *Proc. Natl. Acad. Sci. U.S.A.* **2009**, *106* (12), 4617-4622.
28. Luscombe, N. M.; Austin, S. E.; Berman, H. M.; Thornton, J. M., An overview of the structures of protein-DNA complexes. *Genome Biol.* **2000**, *1* (1), reviews001.1.
29. Hudson, W. H.; Ortlund, E. A., The structure, function and evolution of proteins that bind DNA and RNA. *Nat. Rev. Mol. Cell Biol.* **2014**, *15* (11), 749-760.
30. Lunde, B. M.; Moore, C.; Varani, G., RNA-binding proteins: modular design for efficient function. *Nat. Rev. Mol. Cell Biol.* **2007**, *8* (6), 479-490.
31. De Las Rivas, J.; Fontanillo, C., Protein-Protein Interactions Essentials: Key Concepts to Building and Analyzing Interactome Networks. *PLoS Comp. Biol.* **2010**, *6* (6), e1000807.
32. Pollard, T. D., Actin and Actin-Binding Proteins. *Cold Spring Harb. Perspect. Biol.* **2016**, *8* (8).
33. Fischer, E., Einfluss der Configuration auf die Wirkung der Enzyme. *Ber. Dtsch. Chem. Ges.* **1894**, *27* (3), 2985-2993.
34. Koshland, D. E., Application of a Theory of Enzyme Specificity to Protein Synthesis. *Proc. Natl. Acad. Sci. U.S.A.* **1958**, *44* (2), 98-104.
35. Gall, T. L.; Romero, P. R.; Cortese, M. S.; Uversky, V. N.; Dunker, A. K., Intrinsic Disorder in the Protein Data Bank. *J. Biomol. Struct. Dyn.* **2007**, *24* (4), 325-341.

36. Levy, Y.; Wolynes, P. G.; Onuchic, J. N., Protein topology determines binding mechanism. *Proc. Natl. Acad. Sci. U.S.A.* **2004**, *101* (2), 511-516.
37. Mannige, R. V., Dynamic New World: Refining Our View of Protein Structure, Function and Evolution. *Proteomes* **2014**, *2* (1), 128-153.
38. Akutsu, M.; Dikic, I.; Bremm, A., Ubiquitin chain diversity at a glance. *J. Cell Sci.* **2016**, *129* (5), 875-880.
39. Lange, O. F.; Lakomek, N.-A.; Farès, C.; Schröder, G. F.; Walter, K. F. A.; Becker, S.; Meiler, J.; Grubmüller, H.; Griesinger, C.; de Groot, B. L., Recognition Dynamics Up to Microseconds Revealed from an RDC-Derived Ubiquitin Ensemble in Solution. *Science* **2008**, *320* (5882), 1471-1475.
40. Oldfield, C. J.; Dunker, A. K., Intrinsically Disordered Proteins and Intrinsically Disordered Protein Regions. *Annu. Rev. Biochem.* **2014**, *83* (1), 553-584.
41. Wright, P. E.; Dyson, H. J., Intrinsically unstructured proteins: re-assessing the protein structure-function paradigm. *J. Mol. Biol.* **1999**, *293* (2), 321-331.
42. Schneider, R.; Blackledge, M.; Jensen, M. R., Elucidating binding mechanisms and dynamics of intrinsically disordered protein complexes using NMR spectroscopy. *Curr. Opin. Struct. Biol.* **2019**, *54*, 10-18.
43. Espinoza-Fonseca, L. M., Reconciling binding mechanisms of intrinsically disordered proteins. *Biochem. Biophys. Res. Commun.* **2009**, *382* (3), 479-482.
44. Mollica, L.; Bessa, L. M.; Hanouille, X.; Jensen, M. R.; Blackledge, M.; Schneider, R., Binding Mechanisms of Intrinsically Disordered Proteins: Theory, Simulation, and Experiment. *Front. Mol. Biosci.* **2016**, *3* (52).
45. Gutteridge, A.; Thornton, J. M., Understanding nature's catalytic toolkit. *Trends Biochem. Sci* **2005**, *30* (11), 622-629.
46. Dodson, G.; Wlodawer, A., Catalytic triads and their relatives. *Trends Biochem. Sci* **1998**, *23* (9), 347-352.
47. Ekici, Ö. D.; Paetzel, M.; Dalbey, R. E., Unconventional serine proteases: Variations on the catalytic Ser/His/Asp triad configuration. *Protein Sci.* **2008**, *17* (12), 2023-2037.
48. Richter, M., Functional diversity of organic molecule enzyme cofactors. *Nat. Prod. Rep.* **2013**, *30* (10), 1324-1345.
49. Schwarz, G.; Mendel, R. R.; Ribbe, M. W., Molybdenum cofactors, enzymes and pathways. *Nature* **2009**, *460* (7257), 839-847.
50. Robinson, P. K., Enzymes: principles and biotechnological applications. *Essays Biochem.* **2015**, *59*, 1-41.
51. Ishida, T., Effects of Point Mutation on Enzymatic Activity: Correlation between Protein Electronic Structure and Motion in Chorismate Mutase Reaction. *J. Am. Chem. Soc.* **2010**, *132* (20), 7104-7118.
52. Mendonça, L. M. F.; Marana, S. R., Single mutations outside the active site affect the substrate specificity in a  $\beta$ -glycosidase. *Biochim. Biophys. Acta* **2011**, *1814* (12), 1616-1623.
53. Tyukhtenko, S.; Rajarshi, G.; Karageorgos, I.; Zvonok, N.; Gallagher, E. S.; Huang, H.; Vemuri, K.; Hudgens, J. W.; Ma, X.; Nasr, M. L.; Pavlopoulos, S.; Makriyannis, A., Effects of Distal Mutations on the Structure, Dynamics and Catalysis of Human Monoacylglycerol Lipase. *Sci. Rep.* **2018**, *8* (1), 1719.
54. Agarwal, P. K., Enzymes: An integrated view of structure, dynamics and function. *Microbial Cell Factories* **2006**, *5* (1), 2.

55. Luk, L. Y. P.; Loveridge, E. J.; Allemann, R. K., Protein motions and dynamic effects in enzyme catalysis. *PCCP* **2015**, *17* (46), 30817-30827.
56. Merlino, A.; Mazzearella, L.; Carannante, A.; Fiore, A. D.; Donato, A. D.; Notomista, E.; Sica, F., The Importance of Dynamic Effects on the Enzyme Activity: X-RAY STRUCTURE AND MOLECULAR DYNAMICS OF ONCONASE MUTANTS. *J. Biol. Chem.* **2005**, *280* (18), 17953-17960.
57. Link, A. J.; Mock, M. L.; Tirrell, D. A., Non-canonical amino acids in protein engineering. *Curr. Opin. Biotechnol.* **2003**, *14* (6), 603-609.
58. Xiu, X.; Puskar, N. L.; Shanata, J. A. P.; Lester, H. A.; Dougherty, D. A., Nicotine binding to brain receptors requires a strong cation- $\pi$  interaction. *Nature* **2009**, *458* (7237), 534-537.
59. Lepthien, S.; Hoesl, M. G.; Merkel, L.; Budisa, N., Azatryptophans endow proteins with intrinsic blue fluorescence. *Proc. Natl. Acad. Sci. U.S.A.* **2008**, *105* (42), 16095-16100.
60. Teeuwen, R. L. M.; van Berkel, S. S.; van Dulmen, T. H. H.; Schoffelen, S.; Meeuwissen, S. A.; Zuilhof, H.; de Wolf, F. A.; van Hest, J. C. M., "Clickable" elastins: elastin-like polypeptides functionalized with azide or alkyne groups. *Chem. Commun.* **2009**, (27), 4022-4024.
61. Prasuhn, D. E.; Singh, P.; Strable, E.; Brown, S.; Manchester, M.; Finn, M. G., Plasma Clearance of Bacteriophage Q $\beta$  Particles as a Function of Surface Charge. *J. Am. Chem. Soc.* **2008**, *130* (4), 1328-1334.
62. Nuttall, S. D.; Walsh, R. B., Display scaffolds: protein engineering for novel therapeutics. *Curr. Opin. Pharmacol.* **2008**, *8* (5), 609-615.
63. Saeed, A. F. U. H.; Wang, R.; Ling, S.; Wang, S., Antibody Engineering for Pursuing a Healthier Future. *Front. Microbiol.* **2017**, *8* (495).
64. WEIDLE, U. H.; AUER, J.; BRINKMANN, U.; GEORGES, G.; TIEFENTHALER, G., The Emerging Role of New Protein Scaffold-based Agents for Treatment of Cancer. *Cancer Genom. Proteom.* **2013**, *10* (4), 155-168.
65. Gera, N.; Hussain, M.; Wright, R. C.; Rao, B. M., Highly Stable Binding Proteins Derived from the Hyperthermophilic Sso7d Scaffold. *J. Mol. Biol.* **2011**, *409* (4), 601-616.
66. Grinkova, Y. V.; Denisov, I. G.; Sligar, S. G., Engineering extended membrane scaffold proteins for self-assembly of soluble nanoscale lipid bilayers. *Protein Eng. Des. Sel.* **2010**, *23* (11), 843-848.
67. Arnold, F. H., Design by Directed Evolution. *Acc. Chem. Res.* **1998**, *31* (3), 125-131.
68. Romero, P. A.; Arnold, F. H., Exploring protein fitness landscapes by directed evolution. *Nat. Rev. Mol. Cell Biol.* **2009**, *10* (12), 866-876.
69. Rigoldi, F.; Donini, S.; Redaelli, A.; Parisini, E.; Gautieri, A., Review: Engineering of thermostable enzymes for industrial applications. *APL Bioeng.* **2018**, *2* (1), 011501.
70. Porter, J. L.; Rusli, R. A.; Ollis, D. L., Directed Evolution of Enzymes for Industrial Biocatalysis. *ChemBioChem* **2016**, *17* (3), 197-203.
71. Altintas, Z., *Biosensors and Nanotechnology: Applications in Health Care Diagnostics*. John Wiley & Sons, Inc.: United States of America, 2018.
72. Clark Jr, L. C.; Lyons, C., ELECTRODE SYSTEMS FOR CONTINUOUS MONITORING IN CARDIOVASCULAR SURGERY. *Ann. N.Y. Acad. Sci.* **1962**, *102* (1), 29-45.
73. Nguyen, H. H.; Park, J.; Kang, S.; Kim, M., Surface Plasmon Resonance: A Versatile Technique for Biosensor Applications. *Sensors* **2015**, *15* (5).

74. Piliarik, M.; Vaisocherová, H.; Homola, J., Surface Plasmon Resonance Biosensing. In *Biosensors and Biodetection*, Rasooly, A.; Herold, K. E., Eds. Humana Press: Totowa, NJ, 2009; pp 65-88.
75. Hoa, X. D.; Kirk, A. G.; Tabrizian, M., Towards integrated and sensitive surface plasmon resonance biosensors: A review of recent progress. *Biosens. Bioelectron.* **2007**, *23* (2), 151-160.
76. Homola, J., Present and future of surface plasmon resonance biosensors. *Anal. Bioanal. Chem.* **2003**, *377* (3), 528-539.
77. Alassi, A.; Benammar, M.; Brett, D., Quartz Crystal Microbalance Electronic Interfacing Systems: A Review. *Sensors* **2017**, *17* (12).
78. Shen, Z.; Huang, M.; Xiao, C.; Zhang, Y.; Zeng, X.; Wang, P. G., Nonlabeled Quartz Crystal Microbalance Biosensor for Bacterial Detection Using Carbohydrate and Lectin Recognitions. *Anal. Chem.* **2007**, *79* (6), 2312-2319.
79. Park, H. J.; Lee, S. S., A quartz crystal microbalance-based biosensor for enzymatic detection of hemoglobin A1c in whole blood. *Sensors Actuators B: Chem.* **2018**, *258*, 836-840.
80. Lai, Y.-T.; Ogi, H.; Noi, K.; Kato, F., Viscoelasticity Response during Fibrillation of Amyloid  $\beta$  Peptides on a Quartz-Crystal-Microbalance Biosensor. *Langmuir* **2018**, *34* (19), 5474-5479.
81. Hansen, K. M.; Thundat, T., Microcantilever biosensors. *Methods* **2005**, *37* (1), 57-64.
82. Buchapudi, K. R.; Huang, X.; Yang, X.; Ji, H.-F.; Thundat, T., Microcantilever biosensors for chemicals and bioorganisms. *Analyst* **2011**, *136* (8), 1539-1556.
83. Huang, L.-S.; Pheanpanitporn, Y.; Yen, Y.-K.; Chang, K.-F.; Lin, L.-Y.; Lai, D.-M., Detection of the antiepileptic drug phenytoin using a single free-standing piezoresistive microcantilever for therapeutic drug monitoring. *Biosens. Bioelectron.* **2014**, *59*, 233-238.
84. Kim, H. H.; Jeon, H. J.; Cho, H. K.; Cheong, J. H.; Moon, H. S.; Go, J. S., Highly sensitive microcantilever biosensors with enhanced sensitivity for detection of human papilloma virus infection. *Sensors Actuators B: Chem.* **2015**, *221*, 1372-1383.
85. Li, C.; Ma, X.; Guan, Y.; Tang, J.; Zhang, B., Microcantilever Array Biosensor for Simultaneous Detection of Carcinoembryonic Antigens and  $\alpha$ -Fetoprotein Based on Real-Time Monitoring of the Profile of Cantilever. *ACS Sensors* **2019**, *4* (11), 3034-3041.
86. Koczula, Katarzyna M.; Gallotta, A., Lateral flow assays. *Essays Biochem.* **2016**, *60* (1), 111-120.
87. Quesada-González, D.; Merkoçi, A., Nanoparticle-based lateral flow biosensors. *Biosens. Bioelectron.* **2015**, *73*, 47-63.
88. Carrell, C.; Kava, A.; Nguyen, M.; Menger, R.; Munshi, Z.; Call, Z.; Nussbaum, M.; Henry, C., Beyond the lateral flow assay: A review of paper-based microfluidics. *Microelectron. Eng.* **2019**, *206*, 45-54.
89. Luka, G.; Ahmadi, A.; Najjaran, H.; Alocilja, E.; DeRosa, M.; Wolthers, K.; Malki, A.; Aziz, H.; Althani, A.; Hoorfar, M., Microfluidics Integrated Biosensors: A Leading Technology towards Lab-on-a-Chip and Sensing Applications. *Sensors* **2015**, *15* (12).
90. Li, C.-z.; Vandenberg, K.; Prabhulkar, S.; Zhu, X.; Schneper, L.; Methee, K.; Rosser, C. J.; Almeida, E., Paper based point-of-care testing disc for multiplex whole cell bacteria analysis. *Biosens. Bioelectron.* **2011**, *26* (11), 4342-4348.
91. Choi, S.; Goryll, M.; Sin, L. Y. M.; Wong, P. K.; Chae, J., Microfluidic-based biosensors toward point-of-care detection of nucleic acids and proteins. *Microfluid. Nanofluid.* **2011**, *10* (2), 231-247.

92. Pandey, C. M.; Augustine, S.; Kumar, S.; Kumar, S.; Nara, S.; Srivastava, S.; Malhotra, B. D., Microfluidics Based Point-of-Care Diagnostics. *Biotechnol. J.* **2018**, *13* (1), 1700047.
93. Cracknell, J. A.; Vincent, K. A.; Armstrong, F. A., Enzymes as Working or Inspirational Electrocatalysts for Fuel Cells and Electrolysis. *Chem. Rev.* **2008**, *108* (7), 2439-2461.
94. Makaraviciute, A.; Ramanaviciene, A., Site-directed antibody immobilization techniques for immunosensors. *Biosens. Bioelectron.* **2013**, *50* (Supplement C), 460-471.
95. Squires, T. M.; Messinger, R. J.; Manalis, S. R., Making it stick: convection, reaction and diffusion in surface-based biosensors. *Nat. Biotechnol.* **2008**, *26* (4), 417-426.
96. Boozer, C.; Ladd, J.; Chen, S.; Jiang, S., DNA-Directed Protein Immobilization for Simultaneous Detection of Multiple Analytes by Surface Plasmon Resonance Biosensor. *Anal. Chem.* **2006**, *78* (5), 1515-1519.
97. Wasserberg, D.; Cabanas-Danés, J.; Prangma, J.; O'Mahony, S.; Cazade, P.-A.; Tromp, E.; Blum, C.; Thompson, D.; Huskens, J.; Subramaniam, V.; Jonkheijm, P., Controlling Protein Surface Orientation by Strategic Placement of Oligo-Histidine Tags. *ACS Nano* **2017**, *11* (9), 9068-9083.
98. Ho, J.-a. A.; Hsu, W.-L.; Liao, W.-C.; Chiu, J.-K.; Chen, M.-L.; Chang, H.-C.; Li, C.-C., Ultrasensitive electrochemical detection of biotin using electrically addressable site-oriented antibody immobilization approach via aminophenyl boronic acid. *Biosens. Bioelectron.* **2010**, *26* (3), 1021-1027.
99. Miller, E. A.; Baniya, S.; Osorio, D.; Al Maalouf, Y. J.; Sikes, H. D., Paper-based diagnostics in the antigen-depletion regime: High-density immobilization of rcSso7d-cellulose-binding domain fusion proteins for efficient target capture. *Biosens. Bioelectron.* **2018**, *102*, 456-463.
100. Liu, Y.; Yu, J., Oriented immobilization of proteins on solid supports for use in biosensors and biochips: a review. *Microchimica Acta* **2016**, *183* (1), 1-19.
101. Hernandez, K.; Fernandez-Lafuente, R., Control of protein immobilization: Coupling immobilization and site-directed mutagenesis to improve biocatalyst or biosensor performance. *Enzyme Microb. Technol.* **2011**, *48* (2), 107-122.
102. Contreras-Naranjo, E. J.; Aguilar, O., Suppressing Non-Specific Binding of Proteins onto Electrode Surfaces in the Development of Electrochemical Immunosensors. *Biosensors* **2019**, *9* (1).
103. Lichtenberg, Y. J.; Ling, Y.; Kim, S., Non-Specific Adsorption Reduction Methods in Biosensing. *Sensors* **2019**, *19* (11).
104. Pitsikalis, M.; Pispas, S.; Mays, J. W.; Hadjichristidis, N., Nonlinear Block Copolymer Architectures. In *Blockcopolymers - Polyelectrolytes - Biodegradation*, Bellon-Maurel, V.; Calmon-Decriaud, A.; Chandrasekhar, V.; Hadjichristidis, N.; Mays, J. W.; Pispas, S.; Pitsikalis, M.; Silvestre, F., Eds. Springer Berlin Heidelberg: Berlin, Heidelberg, 1998; pp 1-137.
105. Zheng, W.; Wang, Z.-G., Morphology of ABC Triblock Copolymers. *Macromolecules* **1995**, *28* (21), 7215-7223.
106. Bates, F. S.; Hillmyer, M. A.; Lodge, T. P.; Bates, C. M.; Delaney, K. T.; Fredrickson, G. H., Multiblock Polymers: Panacea or Pandora's Box? *Science* **2012**, *336* (6080), 434-440.
107. Hodrokoukes, P.; Floudas, G.; Pispas, S.; Hadjichristidis, N., Microphase Separation in Normal and Inverse Tapered Block Copolymers of Polystyrene and Polyisoprene. 1. Phase State. *Macromolecules* **2001**, *34* (3), 650-657.

108. Luo, M.; Brown, J. R.; Remy, R. A.; Scott, D. M.; Mackay, M. E.; Hall, L. M.; Epps, T. H., Determination of Interfacial Mixing in Tapered Block Polymer Thin Films: Experimental and Theoretical Investigations. *Macromolecules* **2016**, *49* (14), 5213-5222.
109. Bates, F. S.; Fredrickson, G. H., Block Copolymer Thermodynamics: Theory and Experiment. *Annu. Rev. Phys. Chem.* **1990**, *41* (1), 525-557.
110. Bates, F. S.; Fredrickson, G. H., Block Copolymers—Designer Soft Materials. *Phys. Today* **1999**, *52* (2), 32-38.
111. Hamley, I. W., *The physics of block copolymers*. Oxford Univ. Press: New York, 1998.
112. Segalman, R. A., Patterning with block copolymer thin films. *Mater. Sci. Eng. R Rep.* **2005**, *48* (6), 191-226.
113. Owen, S. C.; Chan, D. P. Y.; Shoichet, M. S., Polymeric micelle stability. *Nano Today* **2012**, *7* (1), 53-65.
114. Yang, Y.-W.; Deng, N.-J.; Yu, G.-E.; Zhou, Z.-K.; Attwood, D.; Booth, C., Micellization of Diblock and Triblock Copolymers in Aqueous Solution. New Results for Oxyethylene/Oxybutylene Copolymers E38B12 and E21B11E21. Comparison of Oxyethylene/Oxybutylene, Oxyethylene/Oxypropylene, and Oxyethylene/Alkyl Systems. *Langmuir* **1995**, *11* (12), 4703-4711.
115. Van Domeselaar, G. H.; Kwon, G. S.; Andrew, L. C.; Wishart, D. S., Application of solid phase peptide synthesis to engineering PEO-peptide block copolymers for drug delivery. *Colloids Surf. B. Biointerfaces* **2003**, *30* (4), 323-334.
116. Jain, S.; Bates, F. S., On the Origins of Morphological Complexity in Block Copolymer Surfactants. *Science* **2003**, *300* (5618), 460-464.
117. Zhulina, E. B.; Adam, M.; LaRue, I.; Sheiko, S. S.; Rubinstein, M., Diblock Copolymer Micelles in a Dilute Solution. *Macromolecules* **2005**, *38* (12), 5330-5351.
118. Hamley, I. W., *Block copolymers in solution : fundamentals and applications*. Wiley: Hoboken, NJ, 2005.
119. Leibler, L., Theory of Microphase Separation in Block Copolymers. *Macromolecules* **1980**, *13* (6), 1602-1617.
120. Blanz, A.; Armes, S. P.; Ryan, A. J., Self-Assembled Block Copolymer Aggregates: From Micelles to Vesicles and their Biological Applications. *Macromol. Rapid Commun.* **2009**, *30* (4-5), 267-277.
121. Hanley, K. J.; Lodge, T. P.; Huang, C.-I., Phase Behavior of a Block Copolymer in Solvents of Varying Selectivity. *Macromolecules* **2000**, *33* (16), 5918-5931.
122. Lodge, T. P.; Pudil, B.; Hanley, K. J., The Full Phase Behavior for Block Copolymers in Solvents of Varying Selectivity. *Macromolecules* **2002**, *35* (12), 4707-4717.
123. Lodge, T. P.; Hanley, K. J.; Pudil, B.; Alahapperuma, V., Phase Behavior of Block Copolymers in a Neutral Solvent. *Macromolecules* **2003**, *36* (3), 816-822.
124. Huang, C.-I.; Lodge, T. P., Self-Consistent Calculations of Block Copolymer Solution Phase Behavior. *Macromolecules* **1998**, *31* (11), 3556-3565.
125. Khandpur, A. K.; Foerster, S.; Bates, F. S.; Hamley, I. W.; Ryan, A. J.; Bras, W.; Almdal, K.; Mortensen, K., Polyisoprene-Polystyrene Diblock Copolymer Phase Diagram near the Order-Disorder Transition. *Macromolecules* **1995**, *28* (26), 8796-8806.
126. Fredrickson, G. H.; Leibler, L., Theory of block copolymer solutions: nonselective good solvents. *Macromolecules* **1989**, *22* (3), 1238-1250.
127. Lodge, T. P.; Hamersky, M. W.; Hanley, K. J.; Huang, C.-I., Solvent Distribution in Weakly-Ordered Block Copolymer Solutions. *Macromolecules* **1997**, *30* (20), 6139-6149.

128. Lai, C.; Russel, W. B.; Register, R. A., Scaling of Domain Spacing in Concentrated Solutions of Block Copolymers in Selective Solvents. *Macromolecules* **2002**, *35* (10), 4044-4049.
129. Fredrickson, G. H.; Helfand, E., Fluctuation effects in the theory of microphase separation in block copolymers. *J. Chem. Phys.* **1987**, *87* (1), 697-705.
130. Foster, M. D.; Sikka, M.; Singh, N.; Bates, F. S.; Satija, S. K.; Majkrzak, C. F., Structure of symmetric polyolefin block copolymer thin films. *J. Chem. Phys.* **1992**, *96* (11), 8605-8615.
131. Walton, D. G.; Kellogg, G. J.; Mayes, A. M.; Lambooy, P.; Russell, T. P., A Free Energy Model for Confined Diblock Copolymers. *Macromolecules* **1994**, *27* (21), 6225-6228.
132. Fasolka, M. J.; Banerjee, P.; Mayes, A. M.; Pickett, G.; Balazs, A. C., Morphology of Ultrathin Supported Diblock Copolymer Films: Theory and Experiment. *Macromolecules* **2000**, *33* (15), 5702-5712.
133. Yokoyama, H.; Kramer, E. J.; Rafailovich, M. H.; Sokolov, J.; Schwarz, S. A., Structure and Diffusion of Asymmetric Diblock Copolymers in Thin Films: A Dynamic Secondary Ion Mass Spectrometry Study. *Macromolecules* **1998**, *31* (25), 8826-8830.
134. Han, E.; Stuen, K. O.; Leolukman, M.; Liu, C.-C.; Nealey, P. F.; Gopalan, P., Perpendicular Orientation of Domains in Cylinder-Forming Block Copolymer Thick Films by Controlled Interfacial Interactions. *Macromolecules* **2009**, *42* (13), 4896-4901.
135. Ouk Kim, S.; Solak, H. H.; Stoykovich, M. P.; Ferrier, N. J.; de Pablo, J. J.; Nealey, P. F., Epitaxial self-assembly of block copolymers on lithographically defined nanopatterned substrates. *Nature* **2003**, *424* (6947), 411-414.
136. Sinturel, C.; Vayer, M.; Morris, M.; Hillmyer, M. A., Solvent Vapor Annealing of Block Polymer Thin Films. *Macromolecules* **2013**, *46* (14), 5399-5415.
137. Fasolka, M. J.; Mayes, A. M., Block Copolymer Thin Films: Physics and Applications. *Annual Review of Materials Research* **2001**, *31* (1), 323-355.
138. Knoll, A.; Horvat, A.; Lyakhova, K. S.; Krausch, G.; Sevink, G. J. A.; Zvelindovsky, A. V.; Magerle, R., Phase Behavior in Thin Films of Cylinder-Forming Block Copolymers. *Phys. Rev. Lett.* **2002**, *89* (3), 035501.
139. van Eldijk, M. B.; Smits, F. C. M.; Vermue, N.; Debets, M. F.; Schoffelen, S.; van Hest, J. C. M., Synthesis and Self-Assembly of Well-Defined Elastin-Like Polypeptide–Poly(ethylene glycol) Conjugates. *Biomacromolecules* **2014**, *15* (7), 2751-2759.
140. Chécot, F.; Brûlet, A.; Oberdisse, J.; Gnanou, Y.; Mondain-Monval, O.; Lecommandoux, S., Structure of Polypeptide-Based Diblock Copolymers in Solution: Stimuli-Responsive Vesicles and Micelles. *Langmuir* **2005**, *21* (10), 4308-4315.
141. Gebhardt, K. E.; Ahn, S.; Venkatachalam, G.; Savin, D. A., Rod-Sphere Transition in Polybutadiene–Poly(l-lysine) Block Copolymer Assemblies. *Langmuir* **2007**, *23* (5), 2851-2856.
142. Shu, J. Y.; Panganiban, B.; Xu, T., Peptide-Polymer Conjugates: From Fundamental Science to Application. *Annu. Rev. Phys. Chem.* **2013**, *64* (1), 631-657.
143. Osada, K.; Christie, R. J.; Kataoka, K., Polymeric micelles from poly(ethylene glycol)–poly(amino acid) block copolymer for drug and gene delivery. *Journal of The Royal Society Interface* **2009**, *6* (suppl\_3), S325-S339.
144. Holowka, E. P.; Sun, V. Z.; Kamei, D. T.; Deming, T. J., Polyarginine segments in block copolypeptides drive both vesicular assembly and intracellular delivery. *Nature Materials* **2007**, *6* (1), 52-57.

145. Sallach, R. E.; Wei, M.; Biswas, N.; Conticello, V. P.; Lecommandoux, S.; Dluhy, R. A.; Chaikof, E. L., Micelle Density Regulated by a Reversible Switch of Protein Secondary Structure. *J. Am. Chem. Soc.* **2006**, *128* (36), 12014-12019.
146. Constancis, A.; Meyrueix, R.; Bryson, N.; Huille, S.; Grosselin, J.-M.; Gulik-Krzywicki, T.; Soula, G., Macromolecular Colloids of Diblock Poly(amino acids) That Bind Insulin. *J. Colloid Interface Sci.* **1999**, *217* (2), 357-368.
147. Castelletto, V.; Cheng, G.; Furzeland, S.; Atkins, D.; Hamley, I. W., Control of strand registry by attachment of PEG chains to amyloid peptides influences nanostructure. *Soft Matter* **2012**, *8* (20), 5434-5438.
148. Collier, J. H.; Messersmith, P. B., Self-Assembling Polymer–Peptide Conjugates: Nanostructural Tailoring. *Adv. Mater.* **2004**, *16* (11), 907-910.
149. Burkoth, T. S.; Benzinger, T. L. S.; Jones, D. N. M.; Hallenga, K.; Meredith, S. C.; Lynn, D. G., C-Terminal PEG Blocks the Irreversible Step in  $\beta$ -Amyloid(10-35) Fibrillogenesis. *J. Am. Chem. Soc.* **1998**, *120* (30), 7655-7656.
150. Vandermeulen, G. W. M.; Tziatzios, C.; Duncan, R.; Klok, H.-A., PEG-Based Hybrid Block Copolymers Containing  $\alpha$ -Helical Coiled Coil Peptide Sequences: Control of Self-Assembly and Preliminary Biological Evaluation. *Macromolecules* **2005**, *38* (3), 761-769.
151. Vandermeulen, G. W. M.; Tziatzios, C.; Klok, H.-A., Reversible Self-Organization of Poly(ethylene glycol)-Based Hybrid Block Copolymers Mediated by a De Novo Four-Stranded  $\alpha$ -Helical Coiled Coil Motif. *Macromolecules* **2003**, *36* (11), 4107-4114.
152. Marsden, H. R.; Korobko, A. V.; van Leeuwen, E. N. M.; Pouget, E. M.; Veen, S. J.; Sommerdijk, N. A. J. M.; Kros, A., Noncovalent Triblock Copolymers Based on a Coiled-Coil Peptide Motif. *J. Am. Chem. Soc.* **2008**, *130* (29), 9386-9393.
153. Sahin, E.; Kiick, K. L., Macromolecule-Induced Assembly of Coiled-Coils in Alternating Multiblock Polymers. *Biomacromolecules* **2009**, *10* (10), 2740-2749.
154. Petka, W. A.; Harden, J. L.; McGrath, K. P.; Wirtz, D.; Tirrell, D. A., Reversible Hydrogels from Self-Assembling Artificial Proteins. *Science* **1998**, *281* (5375), 389-392.
155. Jing, P.; Rudra, J. S.; Herr, A. B.; Collier, J. H., Self-Assembling Peptide-Polymer Hydrogels Designed From the Coiled Coil Region of Fibrin. *Biomacromolecules* **2008**, *9* (9), 2438-2446.
156. Glassman, M. J.; Olsen, B. D., Structure and mechanical response of protein hydrogels reinforced by block copolymer self-assembly. *Soft Matter* **2013**, *9* (29), 6814-6823.
157. Thomas, C. S.; Glassman, M. J.; Olsen, B. D., Solid-State Nanostructured Materials from Self-Assembly of a Globular Protein–Polymer Diblock Copolymer. *ACS Nano* **2011**, *5* (7), 5697-5707.
158. Thomas, C. S.; Xu, L.; Olsen, B. D., Kinetically Controlled Nanostructure Formation in Self-Assembled Globular Protein–Polymer Diblock Copolymers. *Biomacromolecules* **2012**, *13* (9), 2781-2792.
159. Lam, C. N.; Olsen, B. D., Phase transitions in concentrated solution self-assembly of globular protein-polymer block copolymers. *Soft Matter* **2013**, *9* (8), 2393-2402.
160. Huang, A.; Qin, G.; Olsen, B. D., Highly Active Biocatalytic Coatings from Protein–Polymer Diblock Copolymers. *ACS Appl. Mater. Interfaces* **2015**, *7* (27), 14660-14669.
161. Dong, X.-H.; Obermeyer, A. C.; Olsen, B. D., Three-Dimensional Ordered Antibody Arrays Through Self-Assembly of Antibody–Polymer Conjugates. *Angew. Chem. Int. Ed.* **2017**, *56* (5), 1273-1277.

162. Thomas, C. S.; Olsen, B. D., Coil fraction-dependent phase behaviour of a model globular protein-polymer diblock copolymer. *Soft Matter* **2014**, *10* (17), 3093-3102.
163. Chang, D.; Lam, C. N.; Tang, S.; Olsen, B. D., Effect of polymer chemistry on globular protein-polymer block copolymer self-assembly. *Polymer Chemistry* **2014**, *5* (17), 4884-4895.
164. Huang, A.; Paloni, J. M.; Wang, A.; Obermeyer, A. C.; Sureka, H. V.; Yao, H.; Olsen, B. D., Predicting Protein-Polymer Block Copolymer Self-Assembly from Protein Properties. *Biomacromolecules* **2019**, *20* (10), 3713-3723.
165. Ehlich, D.; Takenaka, M.; Hashimoto, T., Forced Rayleigh scattering study of diffusion of block copolymers. 2. Self-diffusion of block copolymer chains in lamellar microdomains and disordered melts. *Macromolecules* **1993**, *26* (3), 492-498.
166. Dalvi, M. C.; Eastman, C. E.; Lodge, T. P., Diffusion in microstructured block copolymers: Chain localization and entanglements. *Phys. Rev. Lett.* **1993**, *71* (16), 2591-2594.
167. Lodge, T. P.; Dalvi, M. C., Mechanisms of Chain Diffusion in Lamellar Block Copolymers. *Phys. Rev. Lett.* **1995**, *75* (4), 657-660.
168. Hamersky, M. W.; Tirrell, M.; Lodge, T. P., Anisotropy of Diffusion in a Lamellar Styrene-Isoprene Block Copolymer. *Langmuir* **1998**, *14* (24), 6974-6979.
169. Yokoyama, H., Diffusion of block copolymers. *Mater. Sci. Eng. R Rep.* **2006**, *53* (5), 199-248.
170. Sax, J.; Ottino, J. M., Modeling of transport of small molecules in polymer blends: Application of effective medium theory. *Polymer Engineering & Science* **1983**, *23* (3), 165-176.
171. Chintapalli, M.; Le, T. N. P.; Venkatesan, N. R.; Mackay, N. G.; Rojas, A. A.; Thelen, J. L.; Chen, X. C.; Devaux, D.; Balsara, N. P., Structure and Ionic Conductivity of Polystyrene-block-poly(ethylene oxide) Electrolytes in the High Salt Concentration Limit. *Macromolecules* **2016**, *49* (5), 1770-1780.
172. Mullin, S. A.; Stone, G. M.; Panday, A.; Balsara, N. P., Salt Diffusion Coefficients in Block Copolymer Electrolytes. *J. Electrochem. Soc.* **2011**, *158* (6), A619.
173. Panday, A.; Mullin, S.; Gomez, E. D.; Wanakule, N.; Chen, V. L.; Hexemer, A.; Pople, J.; Balsara, N. P., Effect of Molecular Weight and Salt Concentration on Conductivity of Block Copolymer Electrolytes. *Macromolecules* **2009**, *42* (13), 4632-4637.
174. Shen, K.-H.; Brown, J. R.; Hall, L. M., Diffusion in Lamellae, Cylinders, and Double Gyroid Block Copolymer Nanostructures. *ACS Macro Lett.* **2018**, *7* (9), 1092-1098.
175. Cheng, V. A.; Walker, L. M., Transport of nanoparticulate material in self-assembled block copolymer micelle solutions and crystals. *Faraday Discuss.* **2016**, *186* (0), 435-454.
176. Kohli, I.; Mukhopadhyay, A., Diffusion of Nanoparticles in Semidilute Polymer Solutions: Effect of Different Length Scales. *Macromolecules* **2012**, *45* (15), 6143-6149.
177. Chen, T.; Qian, H.-J.; Lu, Z.-Y., Note: Chain length dependent nanoparticle diffusion in polymer melt: Effect of nanoparticle softness. *J. Chem. Phys.* **2016**, *145* (10), 106101.
178. Pryamitsyn, V.; Ganesan, V., Noncontinuum effects on the mobility of nanoparticles in unentangled polymer solutions. *J. Polym. Sci., Part B: Polym. Phys.* **2016**, *54* (21), 2145-2150.
179. Poling-Skutvik, R.; Krishnamoorti, R.; Conrad, J. C., Size-Dependent Dynamics of Nanoparticles in Unentangled Polyelectrolyte Solutions. *ACS Macro Lett.* **2015**, *4* (10), 1169-1173.
180. Cai, L.-H.; Panyukov, S.; Rubinstein, M., Hopping Diffusion of Nanoparticles in Polymer Matrices. *Macromolecules* **2015**, *48* (3), 847-862.

181. Ochab-Marcinek, A.; Hołyst, R., Scale-dependent diffusion of spheres in solutions of flexible and rigid polymers: mean square displacement and autocorrelation function for FCS and DLS measurements. *Soft Matter* **2011**, *7* (16), 7366-7374.
182. Tuinier, R.; Fan, T.-H., Scaling of nanoparticle retardation in semi-dilute polymer solutions. *Soft Matter* **2008**, *4* (2), 254-257.
183. Banks, D. S.; Fradin, C., Anomalous Diffusion of Proteins Due to Molecular Crowding. *Biophys. J.* **2005**, *89* (5), 2960-2971.
184. Wang, Y.; Li, C.; Pielak, G. J., Effects of Proteins on Protein Diffusion. *J. Am. Chem. Soc.* **2010**, *132* (27), 9392-9397.
185. Feng, X.; Chen, A.; Wang, J.; Zhao, N.; Hou, Z., Understanding Protein Diffusion in Polymer Solutions: A Hydration with Depletion Model. *J. Phys. Chem. B* **2016**, *120* (38), 10114-10123.
186. Li, C.; Wang, Y.; Pielak, G. J., Translational and Rotational Diffusion of a Small Globular Protein under Crowded Conditions. *J. Phys. Chem. B* **2009**, *113* (40), 13390-13392.
187. Kozer, N.; Kuttner, Y. Y.; Haran, G.; Schreiber, G., Protein-Protein Association in Polymer Solutions: From Dilute to Semidilute to Concentrated. *Biophys. J.* **2007**, *92* (6), 2139-2149.

## **Chapter 2. Materials and Methods**

### **2.1 Molecular Biology Protocols**

#### **2.1.1 Polymerase Chain Reaction (PCR)**

PCR was performed following the procedures outlined in the thesis of Dr. Carolyn Mills.<sup>1</sup> In brief, PCR primers were simultaneously designed with complementary sequences of 12-24 nucleotides such that the melting temperatures of the complementary regions (calculated using the NEB  $T_m$  calculator, <https://tmcalculator.neb.com/>) were within 5 °C of each other and primer dimers or hairpin loops could not form (determined using the ThermoFisher Multiple Primer Analyzer, <https://www.thermofisher.com/us/en/home/brands/thermo-scientific/molecular-biology/molecular-biology-learning-center/molecular-biology-resource-library/thermo-scientific-web-tools/multiple-primer-analyzer.html>). When primers were designed to install new restriction sites to the amplified gene, six non-repetitive base pairs were added upstream of the restriction site to ensure that the restriction enzyme could bind to the amplified DNA sequence. Annealing temperatures were selected by first performing gradient PCR with 35 cycles in eight reactions. The temperatures in these reactions were evenly spaced within the range 5 °C above and below the average melting temperature of the forward and reverse primer. An optimal anneal temperature was selected so that the relative yield of desired PCR products to undesired PCR products was maximized. In cases where this ratio was approximately equal at all temperatures, a temperature 2-3 °C above the average melting temperature of the two primers was used as the annealing temperature.

When performing the final PCR amplification, six 50  $\mu$ L reactions were run in parallel with 25 cycles to minimize formation of undesired PCR products. When significant formation of off-target products was observed at all temperatures in the gradient PCR experiment, PCR was

performed with 35 cycles to increase the mass of desired PCR product produced. The six reactions were then combined into two larger mixtures, one from four of the PCR mixture and the other from two of the PCR mixtures. The DNA from each of these two larger mixtures was then isolated and concentrated to 30  $\mu$ L using a PCR Cycle Pure Kit (Omega BioTek). DNA corresponding to the desired PCR sequence was purified using gel extraction (see section **2.1.2**), and the sequence was confirmed using Sanger sequencing.

### **2.1.2 Agarose Gel Extraction**

DNA agarose gel formation and gel electrophoresis were performed by directly following the procedures outlined in the thesis of Dr. Carolyn Mills.<sup>1</sup> To extract DNA, the gel was directly placed onto the imaging stage of a gel imager. Yellow polycarbonate safety glasses (optical density = 3 for UVA and UVB rays) were worn while exposing the gel to light from a UV transilluminator. Bright green regions corresponding to DNA of the expected length were then excised using a scalpel, and the extracted regions were placed into pre-weighed Eppendorf tubes. The mass of the excised fraction was minimized (by cutting as close to the bright DNA band as possible) to prevent agarose from interfering with purification steps. DNA was purified from the gel fragments using a Gel Extraction Kit (Qiagen), and the DNA concentration was measured using a nanodrop spectrophotometer.

### **2.1.3 Digests and Dephosphorylations**

Restriction enzymes and buffers used in DNA digests were purchased from New England Biolabs (NEB). For all digests, 1-2  $\mu$ g of DNA (for desired digest products > 1 kb) or 2-5  $\mu$ g of DNA (for desired digest products < 1 kb) was added to 3  $\mu$ L of 10x CutSmart buffer along with 1  $\mu$ L of each required restriction enzyme into a PCR tube. Freshly filtered MilliQ water was then added to a final volume of 30  $\mu$ L. The solution was mixed by quickly pipetting up and down at least 10 times,

after which all material was collected on the bottom of the tube using a benchtop centrifuge (~5 second centrifugation time). Digests were run in a thermal cycler at 37 °C overnight (for ~16 hours), after which the mixtures were heated to 65 °C for 20 minutes to deactivate the restriction enzymes.

Digest mixtures containing shorter DNA fragments (e.g., those that would be ligated into a vector) were then stored at 4 °C, while mixtures containing larger DNA fragments (e.g., a digested vector) were dephosphorylated. For the latter mixtures, 4 µL of freshly filtered MilliQ water, 4 µL of 10x Antarctic Phosphatase buffer, and 2 µL of Antarctic Phosphatase were directly added to the digest mixture. Dephosphorylation was performed by heating the mixture in a thermal cycler at 37 °C for 30 minutes, followed by enzyme deactivation at 80 °C for 2 minutes. The desired DNA fragments from all initial digest reactions were then isolated and purified using gel extraction (see section 2.1.2). Typical concentrations of DNA in a final volume of 30 µL were ~10 ng/µL for DNA fragments < 1 kb and  $\geq 15$  ng/µL for DNA fragments > 1 kb.

#### **2.1.4 Ligations**

All enzymes and buffers used in DNA ligations were purchased from NEB. Ligations were performed using a 3:1 insert:vector molar ratio such that the total mass of the desired plasmid (assuming 100% yield) was 100 ng. The volumes of insert and vector that satisfied these constraints were added to a PCR tube along with 1 µL of 10x T4 DNA Ligase buffer and 0.5 µL of T4 DNA ligase at a concentration of 2,000,000 units/mL. It is critical to use T4 DNA ligase at this concentration, as ligations performed using lower-concentration T4 DNA ligase were found to be successful < 10% of the time, while ligations performed using this higher-concentration enzyme almost always yielded successful ligations (> 90% success rate). Freshly filtered MilliQ water was then added to the mixture to a final volume of 10 µL. Ligations run at higher volumes

almost never gave the desired ligation product (< 10% success rate). The solution was mixed by quickly pipetting up and down at least 10 times, after which all material was collected on the bottom of the tube using a benchtop centrifuge (~5 second centrifugation time). In addition to this ligation reaction, a control reaction was run in parallel in which the insert DNA was replaced with an equal volume of MilliQ water. Both ligations were run in a thermal cycler at 16 °C for 16 hours. After this time, the ligations were stored at 4 °C until the ligated plasmids were transformed into NEB5α *Escherichia coli* cells and grown on agar plates with the appropriate antibiotic resistance(s) (see section 2.1.5). If the plate on which the control ligation transformants were grown contained significantly fewer (at least 10x fewer, but usually ~100x fewer) colonies than the plate on which the full ligation transformants were grown, four of the colonies from the latter plate were picked and grown in an overnight culture. The plasmid DNA was extracted from these cells, and the sequence of the insert gene was confirmed using Sanger sequencing.

### **2.1.5 Transformations**

An Eppendorf tube containing 50 µL of chemically competent *E. coli* cells purchased from NEB (competency was checked by running a parallel transformation using the supplier-provided control vector using the same procedure described hereafter) was removed from storage at -80 °C and thawed on ice. If *E. coli* were stored at a volume larger than 50 µL, the cells were first thawed on ice, then pipetted into Eppendorf tubes as 50 µL aliquots, and any tubes that were not used immediately were stored at -80 °C for future use. Plasmid DNA cooled on ice (1 µL) was then added to the cells by pipetting up and down several times to ensure all of the DNA was dispensed. The Eppendorf tube was then gently flicked to ensure the cells were suspended and the DNA was sufficiently mixed, and the tube was placed on ice for 30 minutes. DNA was transformed into the cells by transferring the chilled Eppendorf tube to a water bath maintained at 42 °C for 30 seconds,

after which the tube was cooled on ice for 5 minutes. Super Optimal broth with Catabolite suppression (SOC) (950  $\mu$ L) was added to the Eppendorf tube, and the tube was shaken in an incubator at 37 °C and 220 rpm for 1 hour. During this time, agar plates containing the appropriate antibiotic(s) were also pre-warmed in the incubator. Cells were added to the plates by pipetting 100  $\mu$ L of the SOC media solution directly onto the surface of the agar plate. Sterile glass beads (4-6) were then gently added to the plate by opening the plate lid just enough to allow the beads to enter. The plates were shaken for 1 minute to spread the cells, ensuring that the beads never became stuck against the side of the plate while shaking. The glass beads were removed from the plate by tilting the plate sideways, opening the lid just enough to allow the beads to leave the plate, and gently tapping the plate until all beads were removed. Approximately 1/2-2/3 of the plate was then wrapped in parafilm, and the plates were stored in an incubator at 37 °C for 16-20 hours. After this time, the plates were removed from the incubator, fully wrapped in parafilm, and stored at 4 °C for up to one month until future use.

#### **2.1.6 Cell Outgrowth for DNA Purification**

To a sterile culture tube containing 5 mL of lysogeny broth (LB) was added the appropriate antibiotic(s) for the plasmid to be grown in the media. A P1000 pipette tip was then used to collect a single bacterial colony from an agar plate and added to the media. The tube was shaken in an incubator at 37 °C and 220 rpm for ~16 hours. Longer incubation times were avoided, as significant cell death began to occur after this time. While the cell density was never measured as a function of time, it was found that the yield of plasmid DNA (usually ~4-8  $\mu$ g per 5 mL culture) was approximately halved if incubation time was increased to 20 hours. DNA was extracted from the cells after this time using a Miniprep Kit (Omega BioTek), and the DNA concentration was measured using a nanodrop spectrophotometer. If this was the first time the given plasmid was

transformed into the given cell line, an additional 5 mL culture was grown overnight, and 750  $\mu$ L of the culture was added to an Eppendorf tube containing 750  $\mu$ L of a 1:1 (v/v) mixture of glycerol in MilliQ water. This tube was stored at -80 °C and used as the seed cells for future agar plates of this plasmid/cell line combination.

### **2.1.7 Design of Oligomerized rcSso7d.SA Genes**

Genetic constructs encoding oligomers of rcSso7d.SA<sup>2</sup> were produced via Golden Gate assembly, using the Type IIS restriction endonuclease BsaI to create a diverse library of scarless oligomers (i.e., genes without any undesired DNA sequences added as a result of cloning) in a single reaction (**Figure 2-1a**). An acceptor plasmid was first generated by appending a pair of opposing BsaI sites with unique overhang motifs to the 3' side of the monomeric rcSso7d.SA gene. This was done via standard PCR (see section **2.1.1**), conducted using the **N-Cys-rcSso-for** and **rcSso-Mult-Acc-rev** primers (**Table 2-1**) at an annealing temperature of 59.2 °C. This construct was then integrated into a pET28b(+) vector via an NdeI/XhoI double digest and overnight ligation, as previously described (see section **2.1.4**).<sup>2</sup>

In a separate reaction, an insertion product was produced by modifying the rcSso7d.SA gene with a 5'-(G<sub>4</sub>S)<sub>2</sub> flexible linker sequence. BsaI sites with cleavage overhangs complementary to those in the acceptor plasmid were appended on either end of the insertion product. PCR was conducted using the **rcSso-Mult-Ins-for** and **rcSso-Mult-Ins-rev** primers at an annealing temperature of 61 °C (see section **2.1.1**).

Following preparative-scale 1% agarose gel electrophoresis and gel extraction (see section **2.1.2**), each of these constructs was incubated for one hour at 37°C in a separate BsaI restriction digest reaction (see section **2.1.3**), followed by an hour-long incubation with Antarctic phosphatase and a ten-minute 65 °C hold for enzymatic inactivation. The products were once again gel-purified

and extracted, and a 20  $\mu\text{L}$  ligation reaction was prepared using 40 ng of digested acceptor plasmid, with the digested insertion product comprising the remainder of the available reaction volume. This ligation reaction was incubated overnight at 16  $^{\circ}\text{C}$  (see section **2.1.4**) and was purified using a Clean and Concentrator kit (Zymoprep). Purified ligation product was eluted in 12  $\mu\text{L}$  of MilliQ water, and 4  $\mu\text{L}$  of this ligation mixture was transformed into DH5 $\alpha$  *E. coli* (see section **2.1.5**).

To screen the resultant library of clones for the desired oligomer products, selected colonies were subjected to colony PCR. Flanking primers were used rather than rcSso7d-specific primers, because rcSso7d-specific primers would primarily yield monomeric product bands, regardless of the actual degree of oligomerization. Individual colonies were re-suspended in 50  $\mu\text{L}$  of molecular-grade water, and 1  $\mu\text{L}$  of each cell suspension was taken for the PCR mixture. Each PCR mix also contained 2  $\mu\text{L}$  of 5x Phusion HF polymerase buffer, 0.25  $\mu\text{L}$  of dNTP mix (10 mM of each base), 0.6  $\mu\text{L}$  each of the **T7-for** and **T7-rev** primers at a concentration of 10  $\mu\text{M}$ , 0.2  $\mu\text{L}$  of Phusion HF polymerase, and 5.35  $\mu\text{L}$  of molecular-grade water, for a final reaction volume of 10  $\mu\text{L}$ . The thermocycling profile featured an initial denaturation at 95  $^{\circ}\text{C}$  for 6 minutes, followed by 35 cycles of (i) denaturation at 95  $^{\circ}\text{C}$  for 30 seconds, (ii) primer annealing at 41  $^{\circ}\text{C}$  for 30 seconds, and (iii) extension at 72  $^{\circ}\text{C}$  for 30 seconds, with a final extension step at 72  $^{\circ}\text{C}$  for 10 minutes. Following PCR, the reaction mixtures were visualized via analytical-scale 1% agarose gel electrophoresis (**Figure 2-1b**). Colonies corresponding to PCR products at the predicted amplicon lengths were sequence-verified using the **T7-for** and **T7-rev** sequencing primers. Verified DNA and amino acid sequences for the four oligomer genes can be found in **Appendix A1**.

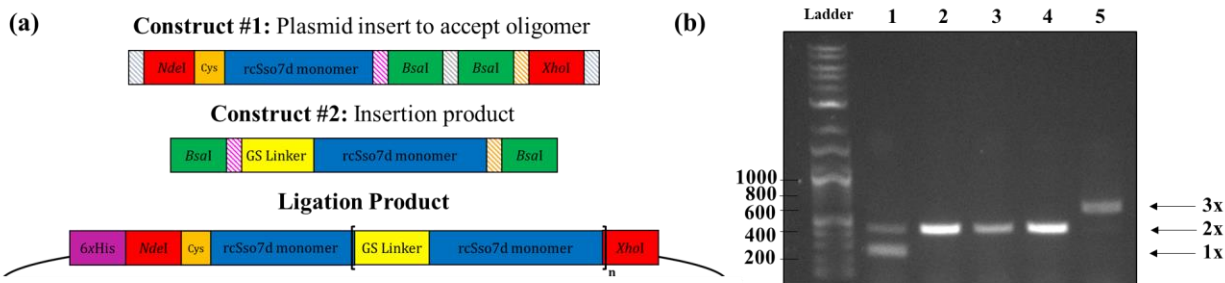


**Figure 2-1.** (a) Schematic representation of the Golden Gate assembly of the rcSso7d oligomers. Construct #1, bearing a codon encoding an N-terminal cysteine and opposing *BsaI* sites, was stably incorporated into an acceptor plasmid. Construct #2, featuring an N-terminal GS linker, was incorporated into this acceptor plasmid in a stochastic manner to yield the library of ligation products. (b) Representative colony PCR gel with selected clones from the resulting library. Labels at left represent the DNA product size, and labels at right represent the degree of oligomerization yielding bands at this product size.

**Table 2-1.** Oligonucleotide sequences of primers used in oligomer generation.

Oligo Name	DNA Sequence, 5'-3' ( <b>NdeI</b> , <b>XhoI</b> , and <b>BsaI</b> sites)	Annealing Temperature (°C)
N-Cys rcSso7d-for	AGGCAGTCT <b>CATATG</b> TGTGCAACCGTGAAATTCAC	64.2
rcSso-Mult-Acc-rev	ATTGAC <b>CTCGAGT</b> TATCCACCC <b>GAGACC</b> ACTG <b>GGTCTC</b> ACACCTTGCTTTTCCAGCATCT	71.7
rcSso-Mult-Ins-for	ATTTAA <b>GGTCTC</b> CGGTGGTGGTGGTAGCGGTGGTGGCG GTTCAATGGCAACCGTGAAATT	73.2
rcSso-Mult-Ins-rev	ATTTAA <b>GGTCTC</b> ACACCTTGCTTTTCCAGCATCTGCAGC	66
T7-for	TAATACGACTCACTATAGGG	47.5
T7-rev	GCTAGTTATTGCTCAGCGG	53.4

## 2.1.8 Design of 2x rcSso7d.SA Coiled-Coil Fusion Genes

### 2.1.8.1 Design of Gene with C-terminal Cysteine

Fusion genes were constructed using the previously-designed rcSso7d.SA dimer (2x) gene, which contains an N-terminal cysteine. Removal of the N-terminal cysteine and insertion of a C-terminal cysteine was accomplished using a QuikChange Multi Site-Directed Mutagenesis Kit (Agilent). In brief, two primers were designed to remove/insert a cysteine at the desired positions, **Del\_N-Cys** and **Ins\_C-Cys** (Table 2-2). The desired gene (2x C-Cys) was generated by running PCR amplification of the two primers with the template sequence in a pET28b(+) vector (see section

**2.1.1).** The template DNA was then digested using DpnI, and the resulting ssDNA was transformed into XL10 Gold ultracompetent cells (see section **2.1.5**). Proper deletion and insertion were verified using Sanger sequencing. A verified DNA sequence for the gene **2x C-Cys** can be found in **Appendix A1**.

### **2.1.8.2 Preparation of Genes for Insertion of Coiled-Coil Sequences**

For both the N-Cys and C-Cys variants of 2x in pET28b(+), a pair of primers was designed to extract the 2x gene with an N-terminal NdeI restriction site and a C-terminal XhoI restriction site, **N-Cys\_fwd** and **N-Cys\_rev** for the N-Cys variant, and **C-Cys\_fwd** and **C-Cys\_rev** for the C-Cys variant (**Table 2-2**). In addition, the primers added a BsaI restriction site and recognition sequence on the side of the gene opposite from the cysteine residue to allow scar-free insertion of coiled-coil gene sequences. Annealing temperature for the two final PCR amplifications were selected by first running gradient PCR (**Figure 2-2**). Because off-target PCR products were observed at all tested temperatures, an annealing temperature of 66 °C was selected for both reactions, a temperature just above the average melting temperature of the two primers. Each template plasmid was PCR amplified with the appropriate primers (see section **2.1.1**), and the desired DNA fragments were purified by gel extraction (see section **2.1.2**). Sanger sequencing was used to confirm the sequences of the extracted fragments. The DNA fragments and pET28b(+) were then digested with NdeI/XhoI (see section **2.1.3**), purified by gel extraction (see section **2.1.2**), and ligated using a 3:1 insert to vector molar ratio (see section **2.1.4**). Ligated plasmids were transformed into chemically competent NEB5 $\alpha$  cells (see section **2.1.5**). Sequences of the two 2x genes (one with an N-terminal Cys and a C-terminal BsaI/XhoI cloning site—**2x N-Cys\_C-BsaI**—and the other with an N-terminal NdeI/BsaI cloning site and a C-terminal Cys—**2x C-Cys\_N-**

**BsaI**) were confirmed using Sanger sequencing. Verified DNA sequences for the genes **2x N-Cys\_C-BsaI** and **2x C-Cys\_N-BsaI** can be found in **Appendix A1**.

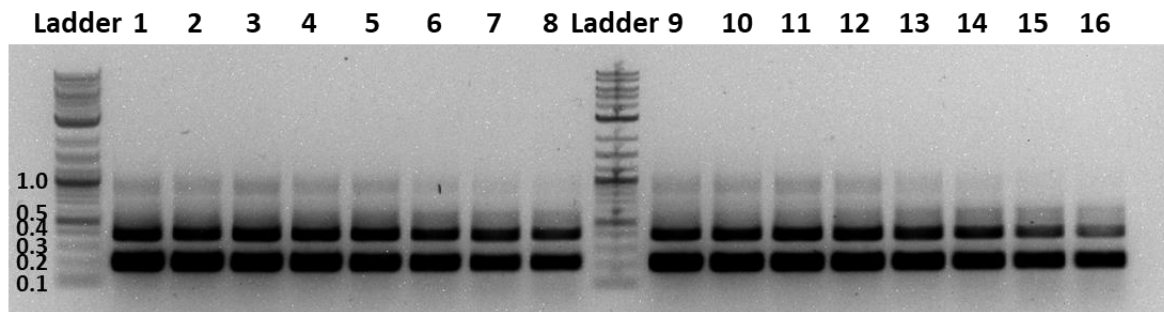


**Figure 2-2.** Agarose gel (1%) of gradient PCR experiments for formation of N-Cys and C-Cys variants of 2x rcSso7d.SA. Lanes 1-8 and 9-16 represent the products of 35 cycle PCR experiments with annealing temperatures linearly spaced between 59 °C (left-most) and 69 °C (right-most) for the N-Cys and C-Cys variants, respectively. Both ladders represent DNA length in kb. The bottom row of dark bands represents amplified 1x rcSso7d.SA sequences, and the above row of dark bands represents the desired 2x rcSso7d.SA variants.

### 2.1.8.3 Cloning of Coiled-Coil Fusions

Genes encoding coiled-coil sequences ZE and ZR<sup>3</sup> were synthesized and cloned into pUC57 by GenScript USA (**Table 2-3**). The plasmids containing ZE, ZR, and the variant of 2x with an N-terminal Cys were digested with BsaI/XhoI (see section **2.1.3**) and purified by gel extraction (see section **2.1.2**). Each digested coiled-coil gene was separately ligated with the digested 2x plasmid using a 3:1 insert to vector molar ratio (see section **2.1.4**). Ligated plasmids were transformed into chemically competent NEB5 $\alpha$  cells (see section **2.1.5**). Gene sequences were confirmed using Sanger sequencing and then transformed into BL21(DE3) cells. The same procedure was used for inserting the ZE coiled-coil sequence into the N-terminus of the 2x gene with a C-terminal Cys, except the initial digest was performed with NdeI/BsaI. Verified DNA sequences and amino acid sequences for the fusion proteins can be found in **Appendix A1**.

**Table 2-2.** Primers used for coiled-coil fusion gene cloning.

Primer	DNA Sequence, 5'-3'	Melting Temperature (°C)
Del_N-Cys	CGCGGCAGCCATATGGCAACCGTGAAATTC	78.9
Ins_C-Cys	CTGCAGATGCTGGAAAAGCAATGTGGTGGATAACTCGA	79.2
N-Cys_fwd	GGCAGC <b>CATATG</b> TGTGCAAC	64.3
N-Cys_rev	GTGTCA <b>CTCGAG</b> <b>GAGACC</b> <b>TCACC</b> TCCACCTTGCTTTTCCAGCATC	64.8
C-Cys_fwd	TGTCAG <b>CATATG</b> <b>GGTCTC</b> <b>CAATG</b> GCAACCGTGAAATTCAC	63.7
C-Cys_rev	GTGGTG <b>CTCGAG</b> TTATCCAC	64.8

**Table 2-3.** DNA sequences of ZE and ZR coiled-coil genes.

Gene	DNA Sequence, 5'-3'
ZE_N-Cys	<b>GGTCTC</b> <b>AGGTC</b> GTAGCGGTGGTGGCGGTTCA <b>CTGGAGATCGAAGCGGCGGCGCTGGAG</b> <b>CAGGAAAACACCGCGCTGGAAACCGAGGTGGCGGAGCTGGAACAGGAAGTGCAACGTC</b> <b>TGGAAAACATTGTGAGCCAATACCGTACCCGTTATGGTCCGCTG</b> TAA <b>CTCGAG</b>
ZR_N-Cys	<b>GGTCTC</b> <b>AGGTC</b> GTAGCGGTGGTGGCGGTTCA <b>CTGGAGATCCGTGCGGCGGCGCTGCGT</b> <b>CGTCGTAACACCGCGCTGCGTACCCGTGTGGCGGAACTGCGTCAGCGTGTTC AACGTC</b> <b>TGCGTAACGAGGTGAGCCAGTACGAAACCCGTTATGGTCCGCTG</b> TAA <b>CTCGAG</b>
ZE_C-Cys	<b>CATATG</b> <b>CTGGAGATCGAAGCGGCGGCGCTGGAGCAGGAAAACACCGCGCTGGAAACCG</b> <b>AGGTGGCGGAGCTGGAACAGGAAGTGCAACGTC</b> <b>TGGAAAACATTGTGAGCCAATACCG</b> <b>TACCCGTTATGGTCCGCTG</b> <b>GGTGGTGGTGGTAGCGGTGGTGGCGGTTCA</b> <b>AATGC</b> <b>GAGAC</b> <b>C</b>

**For Tables 2-2 and 2-3:**

- = NdeI restriction site
- = XhoI restriction site
- = BsaI recognition sequence
- = BsaI restriction site
- = Flexible (Gly<sub>4</sub>Ser)<sub>2</sub> linker sequence fragment
- = Coiled-coil sequence

## 2.2 Protein Expression and Purification

### 2.2.1 General Techniques

#### 2.2.1.1 Media Preparation

Expressions were carried out in Lysogeny Broth (LB) or Terrific Broth (TB). All media were prepared with freshly filtered MilliQ water and sterilized by autoclaving. Expressions were performed under antibiotic selection using 50 µg/mL kanamycin or 200 µg/mL ampicillin. Antibiotic stocks were prepared at 1000x concentration (50 mg/mL kanamycin or 200 mg/mL ampicillin) in MilliQ water, sterile filtered using a syringe (0.2 µm pore size), and stored at -20

°C. To prepare antibiotic-supplemented media, concentrated antibiotics were added to autoclaved media after cooling below 60 °C at a dilution of 1000:1. Isopropyl  $\beta$ -D-1-thiogalactopyranoside (IPTG) used to induce expressions was prepared at 1000x concentration (1 M) in freshly filtered MilliQ water, sterile filtered, and stored at -20 °C.

### **2.2.1.2 Cell Workup**

Cells were separated from media by centrifuging at 4 °C and 4000 x g for 15 minutes, after which time media was removed from cells by decanting. Media was portioned such that after centrifugation was completed, each container held cells from 1 L of expression media. Cells were then resuspended under native conditions by adding 35 mL of lysis buffer (50 mM  $\text{NaH}_2\text{PO}_4$ , 300 mM NaCl, 10 mM imidazole, 10 mM  $\beta$ -mercaptoethanol (BME), pH 8.0) to each container. The cells were then moved to an appropriate-sized freeze-resistant container (125 mL for 1 L expressions, or 250 mL for 4 L expression, in which all cells were combined into a single container). To assist with later mechanical lysis steps, additional lysis buffer was added to the freeze-resistant container such that the container was approximately 80% full. Containers were then stored at -80 °C for at least one hour, but usually overnight. After thawing with constant shaking in an incubator at 37 °C (takes 1-2 hours, depending on the amount of time kept at -80 °C and the volume of solution being thawed), lysozyme was added to solutions at a concentration of 1 mg/mL. Solutions were then vigorously shaken by hand to ensure sufficient dispersion of lysozyme throughout the cell mixture. The mixture was incubated at 4 °C on a rocking platform for 1 hour to begin enzymatic cell lysis. Mechanical lysis was then performed by sonicating for 15 cycles of 30 seconds on/30 seconds off at 50% power and 50% duty cycle using a Branson sonifier with a 12.7 mm diameter tip. Lysate was added to 50 mL conical tubes at a volume of 35-40 mL per tube. Lysed cells were separated from buffer by centrifuging the tubes at 13,000 rpm and 4 °C

using a fixed-angle rotor (34°) until complete separation was observed (usually 1 hour). Buffer containing proteins was collected by decanting.

### **2.2.1.3 Ni-NTA Purification**

An appropriate volume of Ni-NTA resin suspended in lysis buffer was added to the lysis buffer containing proteins. When unsure what this volume should be, 5 mL of resin solution (purchased from Thermo Scientific as a 50% slurry in 20% ethanol) was added per 1 L of initial expression (which ended up being appropriate for all His-tagged proteins expressed in this thesis). To optimize the volume of resin used for purification, the volume of Ni-NTA added in future expressions should be increased if virtually no impurities are observed in SDS-PAGE following Ni-NTA purification and/or a low protein yield is obtained, as determined after performing several expressions. Conversely, the volume of added Ni-NTA should be decreased if significant impurities are observed in SDS-PAGE. The buffer was incubated at 4 °C on a rocking platform for at least 3 hours (usually overnight), after which time the mixture was filtered by pouring the slurry into a column with a glass frit filter. During this and future filtering steps, it was ensured that the Ni-NTA resin never ran dry, which could be guaranteed by only using gravity filtration. When pressure was used to increase the speed of filtering, the filtering method was switched to gravity filtration when the solution line was approximately 1 cm above the top of the resin. After filtering the initial slurry, 15 column volumes (CV) of equilibrium buffer (50 mM Tris buffer, 300 mM NaCl, 10 mM imidazole, 10 mM BME, pH 7.4) was gently added to the resin by tilting the column at an approximately 20° angle and adding buffer directly to the walls of the column. Then, 3 CV of elution buffer (50 mM Tris buffer, 300 mM NaCl, 500 mM imidazole, 10 mM BME, pH 7.4) was gently added to the resin, and the filtrate was collected. Ni-NTA resin was then cleaned by washing with 10 CV of 0.5 M NaOH (allowing the first 5 CV to pass through the resin and letting

the resin sit in the remaining solution for 30 minutes before filtering). The resin was then washed with 20 CV of water and stored at 4 °C in 30% ethanol in water (v/v) for future use when purifying the same protein.

#### **2.2.1.4 Dialysis**

Dialysis was performed by adding solution containing a purified protein or bioconjugate into dialysis tubing with a molecular weight cutoff (MWCO) smaller than that of the purified molecule (at least two times smaller, when possible). If the volume of the sample was less than 30 mL, the solution was dialyzed against 1.8 L of dialysis solution, and a dialysis solution of 5 L was used for larger sample volumes. Proteins were dialyzed against buffer solutions (4 total dialysis solution exchanges), and bioconjugates were dialyzed against MilliQ water (10 total dialysis solution exchanges). The sample and dialysis solution were allowed to equilibrate for at least 3 hours between each exchange.

#### **2.2.1.5 Protein Concentration Determination**

After Ni-NTA purification and dialysis, the concentration of all proteins used in this thesis was determined using a reducing agent compatible Pierce Microplate BCA Assay Kit (ThermoFisher). If the buffer in which the protein was being measured did not contain a reducing agent, the steps involving reducing agent compatibilization were skipped. Three replicate wells were run for all samples and references. Standard curves were generated by fitting a quadratic curve to the data collected using a bovine serum albumin (BSA) standard. In all cases, the R squared value for this curve was > 0.999. A representative standard curve is shown in **Figure 2-3**.

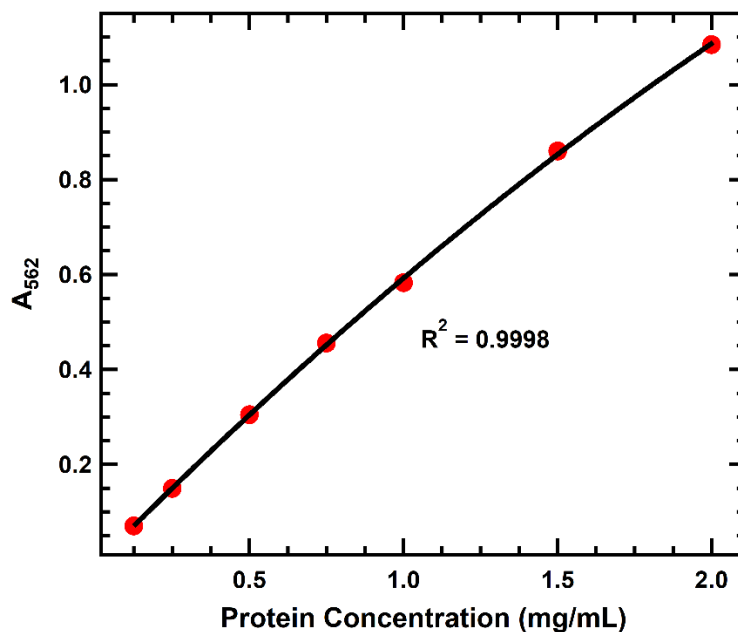


**Figure 2-3.** Representative standard curve generated for BSA standard using a reducing agent compatible BCA assay.

### 2.2.2 rcSso7d.SA Oligomer and Coiled-Coil Fusion Expression and Purification

Monomeric through tetrameric rcSso7d.SA (1x rcSso7d.SA, 2x rcSso7d.SA, 3x rcSso7d.SA, and 4x rcSso7d.SA, respectively), 2x rcSso7d.SA with a C-terminal ZE (2xZEC) or ZR (2xZRC), and 2x with a N-terminal ZE (2xZE) were expressed in BL21(DE3) *E. coli* cells. Each protein was expressed in 1 L of TB containing kanamycin at 37 °C inoculated with 5 mL of overnight culture and induced with 1 mM IPTG at an OD<sub>600</sub> of 0.8-1.0 (usually takes 3 hours). After induction, the cells were cultured at 20 °C for 18-20 hours and harvested. The cells were resuspended in lysis buffer and frozen at -80 °C overnight. Lysozyme was then added to the cells, after which the cells were lysed by ultrasonication (see section 2.2.1.2). The lysate was clarified by centrifugation, and the protein was purified using Ni-NTA metal affinity chromatography (see section 2.2.1.3). Elution fractions containing purified protein were immediately exchanged into Sso resuspension buffer (50 mM Tris buffer, 100 mM NaCl, 0.25 mM tris(2-carboxyethyl)phosphine (TCEP), pH 7.4) for all four rcSso7d.SA oligomers, ZE resuspension buffer (50 mM Tris buffer, 500 mM NaCl,

0.25 mM TCEP, pH 8.0) for 2xZEC and 2xZEN, or ZR resuspension buffer (50 mM Tris buffer, 500 mM NaCl, 0.25 mM TCEP, pH 7.0) for 2xZRC using dialysis (see section 2.2.1.4). Buffer recipes were developed by testing a range of salt concentrations and pH values that resulted in greatest solubility, as determined by visual inspection (Table 2-4). The purity of the protein was confirmed by denaturing gel electrophoresis (SDS-PAGE) (Figures A-2a, A-4a). Protein concentration was determined by performing a reducing-agent compatible BCA assay (see section 2.2.1.5), and proper secondary structure folding of the proteins was assessed using circular dichroism (CD) (Figures A-3a, A-5a). The typical yields of purified protein for 1x rcSso7d.SA, 2x rcSso7d.SA, 3x rcSso7d.SA, 4x rcSso7d.SA, 2xZEC, 2xZRC, and 2xZEN were 120, 160, 75, 40, 100, 180, and 20 mg per liter of culture, respectively.

**Table 2-4.** Buffer recipes tested for solubilization of coiled-coil fusions.<sup>a</sup>

2xZRC	pH 7	pH 8
50 mM NaCl		
100 mM NaCl		
500 mM NaCl	X	
2xZEC/2xZEN	pH 7	pH 8
50 mM NaCl		
100 mM NaCl		
500 mM NaCl		X

<sup>a</sup>Cell colors represent conditions in which the fusion proteins were insoluble (red), mostly soluble (orange), or completely soluble (green). Selected buffers are marked with an X.

### 2.2.3 TEV Protease Expression and Purification

The gene for an S219V mutant of tobacco etch virus (TEV) protease containing an N-terminal 6xHis tag, was a gift from David Waugh (Addgene plasmid # 8827).<sup>4</sup> TEV protease was transformed into BL21(DE3) *E. coli* cells for expression (see section 2.1.5). The protein was expressed in 1 L of TB containing kanamycin at 37 °C inoculated with 5 mL of overnight culture

and induced with 1 mM IPTG at an OD<sub>600</sub> of 0.8-1.0 (usually takes 3 hours). After induction, the cells were cultured at 30 °C for 16-18 hours and harvested. The cells were resuspended in lysis buffer and frozen at -80 °C overnight. Lysozyme was then added to the cells, after which the cells were lysed by ultrasonication (see section **2.2.1.2**). The lysate was clarified by centrifugation, and the protein was purified using Ni-NTA metal affinity chromatography (see section **2.2.1.3**). Elution fractions containing purified protein were immediately exchanged into TEV resuspension buffer (50 mM Tris buffer, 1 mM ethylenediaminetetraacetic acid (EDTA), 5 mM dithiothreitol (DTT), pH 7.5) using dialysis (see section **2.2.1.4**). After the final dialysis exchange, the protein solution was diluted with glycerol (50% v/v) and Triton X-100 (0.1% v/v), aliquoted into 200 µL portions in Eppendorf tubes, flash frozen in liquid nitrogen, and stored at -80 °C for future use. The typical yield of purified protein was 10 mg per liter of culture. An SDS-PAGE gel showing purified TEV protease can be found in **Figure 2-4**.

#### **2.2.4 mSA2 Expression and Purification**

The gene for mSA2 containing a C-terminal FLAG tag and N-terminal 6xHis and MBP tags separated from the mSA2 sequence by a TEV protease recognition site, mSA2-MBP, was a gift from Sheldon Park (Addgene plasmid # 52319). Prior to expression, the plasmid was transformed into BL21(DE3) *E. coli* cells (see section **2.1.5**). The protein was expressed in 1 L of Terrific Broth at 37 °C inoculated with 5 mL of overnight culture and induced with 1 IPTG at an OD<sub>600</sub> of 0.8-1.0. After induction the cells were cultured at 20 °C for 18-20 hours and harvested. The cells were resuspended in lysis buffer and frozen at -80 °C overnight. After thawing, the cells were subjected to two more freeze-thaw cycles (minimum freeze time of 1 hour). The cells were then lysed by ultrasonication (see section **2.2.1.2**). The lysate was clarified by centrifugation, and the protein was purified using Ni-NTA metal affinity chromatography (see section **2.2.1.3**). Elution fractions

containing purified mSA2-MBP were dialyzed against 50 mM Tris buffer (pH 8.5) (see section **2.2.1.4**). The typical yield of mSA2-MBP was 60 mg per liter of culture.

The N-terminal 6xHis and MBP tags were cleaved using either AcTEV protease (Invitrogen) or recombinant TEV protease. For a cleavage reaction involving 100 mg of target protein, 0.75 mL of 20x TEV buffer (1 M Tris, pH 8.0) and 50  $\mu$ L of TEV protease from the stock solution were added to the protein solution. MilliQ water was then added to a final volume of 15 mL. Reactions were allowed to run at room temperature on an orbital shaker for 2 hours, during which time white precipitates began to form. These precipitates were removed using centrifugation (15 minutes at 4000 x g, 20 °C) before proceeding to purification. Prior to running a full-scale enzymatic cleavage, 100  $\mu$ L test reactions were run for 2 hours in which the concentration of TEV protease was varied from the full concentration of the stock solution to a 1000x dilution of the stock solution. The reaction mixtures from these reactions were directly run on an SDS-PAGE gel (see sample gel in **Figure 2-4**). The condition with the lowest concentration of TEV protease that showed complete cleavage of the target protein was selected for the full-scale cleavage reaction. If all conditions showed only partial cleavage of the target protein, the full-scale reaction used volumes of TEV protease directly taken from the full concentration stock.

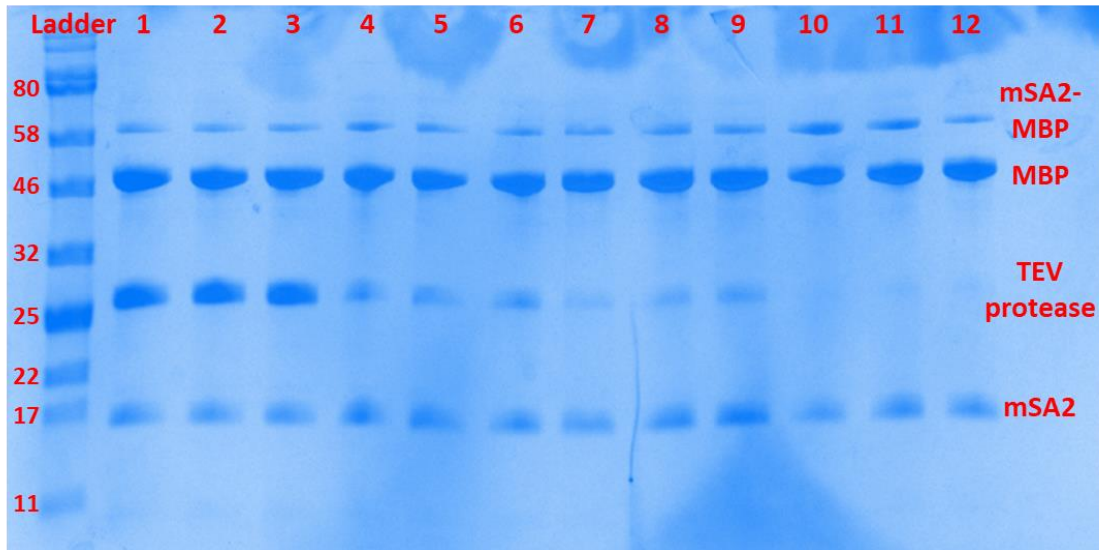


**Figure 2-4.** Denaturing protein gel (12% acrylamide) of TEV protease cleavage of mSA2-MBP at varying enzyme concentrations. The concentration of TEV protease was decreased logarithmically between the full concentration of the stock solution used (lane 1) to a 1000x dilution of the full concentration (lane 12). The ladder represents molecular weight in kDa. In this (typical) gel, only partial cleavage of mSA2-MBP was achieved under all conditions, so TEV protease at the full concentration of the stock solution was used for the full-scale cleavage reaction.

For full-scale reactions, the centrifuged cleavage mixture was incubated with an excess of Ni-NTA (at least 2.5 mL of dry resin per 100 mg of initial protein) on a rocking platform at 4 °C overnight. The mixture was loaded into a column, and the filtrate was collected, as the only protein in the mixture without a 6xHis tag was cleaved mSA2. The resin was rinsed with 15 CV of equilibrium buffer (50 mM Tris buffer, 300 mM NaCl, 10 mM imidazole, 10 mM BME, pH 7.4). The elution fractions were combined with the initial filtrate and dialyzed against mSA2 SEC buffer (50 mM sodium phosphate, 150 mM NaCl, pH 7.2) (see section 2.2.1.4). The solution was concentrated to the smallest volume possible (for a 4 L expression, this volume was usually 0.5-1 mL) using Amicon Ultra 15 centrifugal filters (molecular weight cutoff of 3 kDa, Millipore Sigma). The resulting viscous, opaque yellow mixture was centrifuged for at least two hours at 13,000 rpm and 4 °C to yield a clear, yellow solution. This solution was then purified using a HiLoad 16/600 Superdex 75 pg size exclusion chromatography (SEC) column (GE Healthcare) by

eluting with mSA2 SEC buffer. A representative SEC run is shown in **Figure 2-5**. Fractions containing pure mSA2 were combined, dialyzed against PBS (pH 7.4) (see section 2.2.1.4), and stored at 4 °C until further use. The typical yield of mSA2 was < 5 mg per liter of culture.

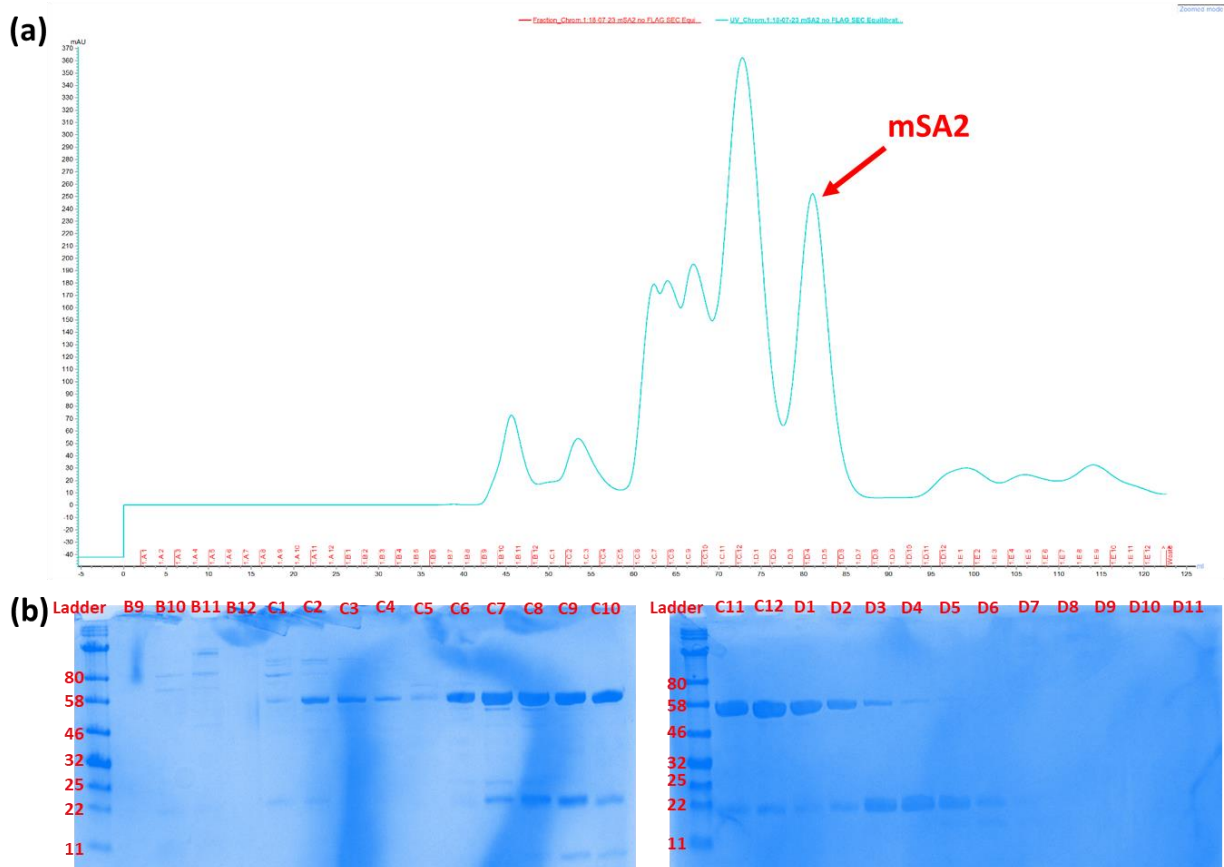


**Figure 2-5.** (a) A280 trace overlaid with elution fractions (eluted with 50 mM sodium phosphate, 150 mM NaCl, pH 7.2) for SEC of mSA2, and (b) corresponding denaturing protein gels (12% acrylamide). For this run, fractions D5-D7 were collected, which corresponded to the noted peak of the A280 trace in (a).

## 2.2.5 GFP Variants

Variants of Superfolder GFP with net charges of 0, -8, and -21, GFP(0), GFP(-8), and GFP(-21), respectively, were expressed and purified by directly following the protocols outlined in the thesis of Dr. Christopher Lam.<sup>5</sup> No significant deviations in performance from the reported procedure were observed. Typical yields were similar to the reported yields (reported yields listed in

parentheses): 80 mg per liter of culture for GFP(0) (60 mg/L), 90 mg per liter of culture for GFP(-8) (70 mg/L), and 10 mg per liter of culture for GFP(-21) (15 mg/L).

### 2.2.6 Proteins Used for Diffusion Experiments and Biosensor Assays

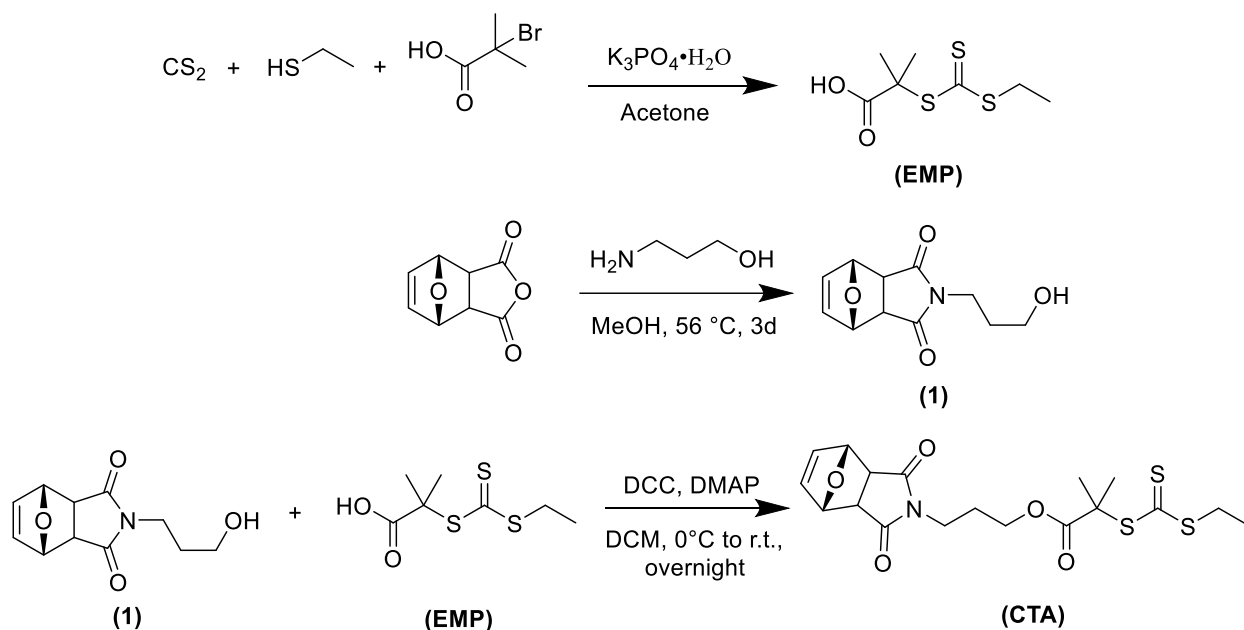
All other proteins and dextran molecules in this thesis were purchased from commercial vendors and used without further purification. A full list of these molecules can be found in **Table 2-5**.

**Table 2-5.** Proteins and dextran molecules purchased for diffusion experiments. Dextran molecules are distinguished by their average molecular weights.

Molecule	Vendor
Cytochrome C	Lee Biosolutions
Lysozyme	Millipore Sigma
Streptavidin	New England Biolabs
Bovine serum albumin	Millipore Sigma
Transferrin	Lee Biosolutions
Glucose oxidase	Millipore Sigma
Catalase	Millipore Sigma
Dextran 10k	Thermo Fisher
Dextran 40k	Thermo Fisher
Dextran 70k	Thermo Fisher
Dextran 500k	Thermo Fisher

### 2.3 Polymer Synthesis

Poly(*N*-isopropylacrylamide) (PNIPAM) with low dispersity was synthesized using reversible addition-fragmentation chain-transfer (RAFT) polymerization. The chain transfer agent (CTA) for RAFT polymerizations was synthesized to contain a maleimide end group, thereby allowing thiol-maleimide coupling between PNIPAM and cysteine-bearing proteins. However, this maleimide group is capable of undergoing a [2+2] cycloaddition during polymerization (resulting in dimerized PNIPAM), so a furan-protected maleimide group was used, which could easily be deprotected by post-polymerization modification via a retro Diels-Alder reaction. The full synthetic scheme for this CTA is shown in **Scheme 2-1**.



**Scheme 2-1.** Synthetic scheme for the chain transfer agent (CTA) used in RAFT polymerizations.

### 2.3.1 Synthesis of EMP

This following procedure was adapted from that of Thomas et al.<sup>6</sup> To a 1000 mL round-bottom flask charged with a magnetic stir bar was added ethanethiol (3.73 g, 60 mmol, 1.15 equiv),  $\text{K}_3\text{PO}_4 \cdot \text{H}_2\text{O}$  (12.67 g, 55 mmol, 1.05 equiv), and acetone (180 mL). The mixture was stirred for 20 minutes in an ice bath, by which point the solution had become mostly opaque. Carbon disulfide (11.42 g, 150 mmol, 2.9 equiv) was then added dropwise over 2 hours, over which time the solution became bright yellow then orange. Then, 2-bromo-2-methylbutanoic acid (8.7 g, 52.1 mmol, 1 equiv) was added dropwise over 20 minutes. The mixture was then allowed to warm to room temperature (by leaving the flask in the ice bath and allowing the bath to naturally warm to room temperature) and stirred for an additional 22 hours. When the reaction was checked again after 16 hours, the mixture had become very viscous with white precipitates in an orange solution, so the stirring rate was increased. After the full 22 hours had elapsed, ice was added to the water bath, and 1 M HCl (610 mL) was added portion-wise to the flask, being careful to add very slowly in the beginning due to the reaction being highly exothermic. The reaction mixture was then added directly to a separatory

funnel and extracted with DCM (3 x 200 mL). The combined organic extracts were rinsed with H<sub>2</sub>O (1 x 250 mL) and brine (1 x 250 mL), dried over Na<sub>2</sub>SO<sub>4</sub>, and filtered. The filtrate was concentrated *in vacuo* to give 11.32 g of an orange oil. A TLC of this crude product showed almost no impurities (**Figure 2-6**). The crude product was purified by column chromatography on silica gel. Column chromatography was performed on a Biotage Isolera automated flash column system using a 100 g KP-Sil cartridge. The product was eluted with the following series of solvents: 5 column volumes (CVs) of the initial solvent mixture (pure hexanes), a linear gradient across 15 CV between this initial mixture and the final solvent mixture (hexanes:ethyl acetate 2:1), and 2 CVs of the final solvent mixture. The fractions containing product (as referenced against the major spot in **Figure 2-6**) were combined and concentrated *in vacuo* to give the product as an orange oil (10.15 g, 79% yield). <sup>1</sup>H-NMR spectra of the purified product is shown in **Figure A-9**. <sup>1</sup>H-NMR (300 MHz, CDCl<sub>3</sub>, δ): 3.30 (q, *J* = 7.4 Hz, 2H), 1.73 (s, 6H), 1.33 (t, *J* = 7.4 Hz, 3H).

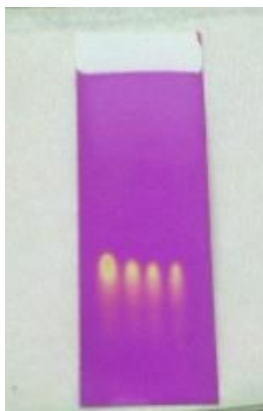


**Figure 2-6.** TLC plate of crude product from EMP synthesis. The TLC was run on silica gel, developed with hexanes:ethyl acetate (2:1), and visualized with KMnO<sub>4</sub> stain. The major spot appears at *R*<sub>f</sub> = 0.33.

### 2.3.2 Synthesis of *exo*-3a,4,7,7a-Tetrahydro-2-(3-hydroxypropyl)-4,7-epoxy-14-isoindole-1,3(2*H*)-dione (1)

This following procedure was adapted from that of Thomas et al.<sup>6</sup> To an oven-dried, nitrogen-flushed 500 mL round-bottom flask charged with a magnetic stir bar was added *exo*-3,6-epoxy-

1,2,3,6-tetrahydrophthalic anhydride (4.50 g, 27.1 mmol, 1 equiv) and dry methanol (250 mL). To the stirred suspension was added 3-amino-1-propanol (2.03 g, 27.1 mmol, 1 equiv) dropwise over 10 minutes at room temperature, resulting in complete solubilization of the solid. Then, a reflux condenser was added, and the mixture was stirred at 56 °C for three days. The solution was concentrated *in vacuo* to give a white solid, which was dissolved in DCM (100 mL) and washed with brine (3 x 100 mL). The initially opaque organic layer became clear upon the rinses with brine. The organic layer was then dried over Na<sub>2</sub>SO<sub>4</sub>, filtered, and concentrated *in vacuo*. The resulting residue began to crystallize into a solid after cooling after rotary evaporation. This residue was then dried in a vacuum oven overnight at room temperature to give the product as a white, crystalline solid (1.57 g, 26%). <sup>1</sup>H-NMR spectra of the purified product is shown in **Figure A-10**. <sup>1</sup>H-NMR (300 MHz, CDCl<sub>3</sub>, δ): 6.53 (t, *J* = 1.0 Hz, 2H), 5.28 (t, *J* = 1.0 Hz, 2H), 3.66 (t, *J* = 6.1 Hz, 2H), 3.52 (t, *J* = 5.7 Hz, 2H), 2.88 (s, 2H), 2.48 (s, 1H), 1.77 (dt, *J* = 6.1, 5.7 Hz, 2H).

### 2.3.3 CTA Synthesis

This following procedure was adapted from that of Thomas et al.<sup>6</sup> To an oven-dried, nitrogen-flushed 50 mL round-bottom flask charged with a magnetic stir bar was added (1) (1.70 g, 7.62 mmol, 1.1 equiv), EMP (1.55 g, 6.92 mmol, 1 equiv), DMAP (0.085 g, 0.69 mmol, 0.1 equiv), and dry DCM (10 mL). The mixture was added to an ice bath and cooled to 0 °C, at which point DCC (1.57 g, 7.62 mmol, 1.1 equiv) was added portion-wise, causing the reaction to become dark orange (initially clear, but slowly became opaque). The mixture was stirred at 0 °C for an additional hour and then allowed to warm to room temperature and stirred overnight for 16 hours. After approximately 1.5 hours, the mixture had become brown. When the reaction was stopped, the mixture had become highly viscous. This mixture was filtered, giving an amber-brown filtrate and a white solid. The filtrate was diluted with DCM (200 mL) and rinsed with 1 M HCl (3 x 100 mL),

which yielded an orange organic phase, saturated sodium bicarbonate (3 x 100 mL), which yielded a dark orange organic phase, and brine (100 mL). The organic layer was dried over Na<sub>2</sub>SO<sub>4</sub>, filtered, and concentrated *in vacuo* to give a brown solid. A TLC of this crude product is shown in **Figure 2-7**. The crude product was purified by column chromatography on silica gel. Column chromatography was performed on a Biotage Isolera automated flash column system using a 25 g KP-Sil cartridge. The product was eluted with 15 CVs of hexanes:ethyl acetate (1:1). The fractions containing product (as referenced against the major spot in **Figure 2-7**) were combined and concentrated *in vacuo* (the product began precipitating in solution during rotary evaporation) to give the product as a yellow powder (2.21 g, 75% yield). <sup>1</sup>H-NMR spectra of the purified product is shown in **Figure A-11**. <sup>1</sup>H-NMR (300 MHz, CDCl<sub>3</sub>, δ): 6.51 (t, *J* = 1.0 Hz, 2H), 5.26 (t, *J* = 1.0 Hz, 2H), 4.08 (t, *J* = 6.2 Hz, 2H), 3.56 (t, *J* = 7.0 Hz, 2H), 3.28 (q, *J* = 7.4 Hz, 2H), 2.85 (s, 2H), 1.92 (p, *J* = 6.5 Hz, 2H), 1.71 (s, 6H), 1.32 (t, *J* = 7.4 Hz, 3H).

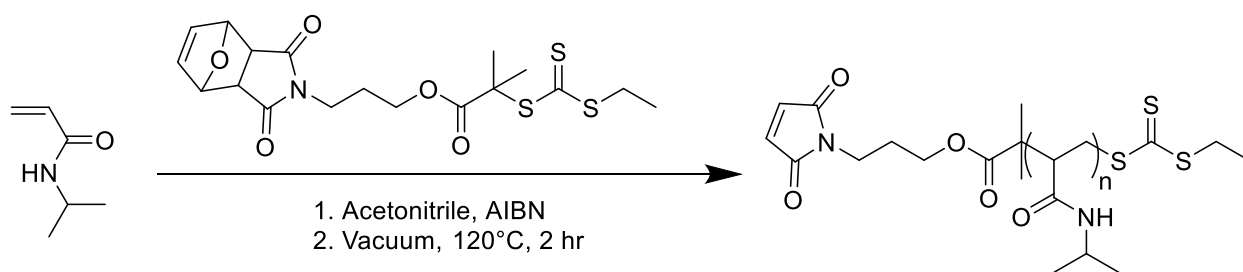


**Figure 2-7.** TLC plate of crude product from CTA synthesis. The TLC was run on silica gel, developed with hexanes:ethyl acetate (1:1), and visualized with KMnO<sub>4</sub> stain. Minor impurities appear at the baseline and at R<sub>f</sub> = 0.58 (EMP). The desired product corresponds to the brightest spot at R<sub>f</sub> = 0.18.

### 2.3.4 RAFT Polymerization

In a typical RAFT polymerization of PNIPAM (**Scheme 2-2**), *N*-isopropylacrylamide (NIPAM, sublimated at 65 °C, 2.5 equiv) was added to HPLC-grade acetonitrile (such that the concentration

of NIPAM was 2 M) in a polymerization flask (oven dried, flushed with nitrogen) that was at least twice the volume of the added acetonitrile. Then, CTA (1 equiv) and AIBN (recrystallized twice from methanol, 0.2 equiv) were added, and the solution was stirred until all solids were completely dissolved. The solution was then degassed by three freeze-pump-thaw cycles. During the final pump cycle, the system was given sufficient time to reach within 5 mTorr of the full vacuum level of the synthesis line being used (usually between 60 and 80 mTorr). After achieving this pressure, the system was back-filled with nitrogen and subsequently pumped down to within 5 mTorr of full vacuum level. This process was repeated three times total, but after back-filling with nitrogen a third time, the reaction was allowed to warm to room temperature without degassing.



**Scheme 2-2.** Synthetic scheme for PNIPAM RAFT polymerization.

Once all solids had re-dissolved, the reaction was added to an oil bath heated to 50 °C (when the desired PNIPAM  $M_n$  was < 50 kDa) or 55 °C (when the desired PNIPAM  $M_n$  was > 50 kDa). Throughout the polymerization, polymer molecular weight and dispersity were characterized by gel permeation chromatography (GPC) performed on an Agilent 1260 LC system equipped with two columns (ResiPore, 300 × 7.5 mm, up to 500 kDa, Agilent Technologies, CA) in series, a Wyatt miniDAWN TREOS multi-angle light scattering detector, and a Wyatt Optilab T-rEX diffractometer. DMF with 0.02 M LiBr was used as the mobile phase with a flow rate of 1 mL/min at 70 °C. The reaction progress was monitored by GPC at least every hour, but GPC sampling became more frequent as the PNIPAM approached the target  $M_n$ . It was found that chain length grew roughly linearly after the first 1-2 hours. A sample time series of GPC traces is

provided in **Figure 2-8**. At the time that this linear projection predicted the polymerization would reach the desired  $M_n$  (provided that a GPC sample had been collected within the past 30 minutes), the reaction was terminated by removing the flask from the oil bath, removing the septa from the flask, and using an empty 60 mL syringe to pump air into the flask. The septum was then replaced, and the flask was stored at  $-20\text{ }^\circ\text{C}$  overnight.

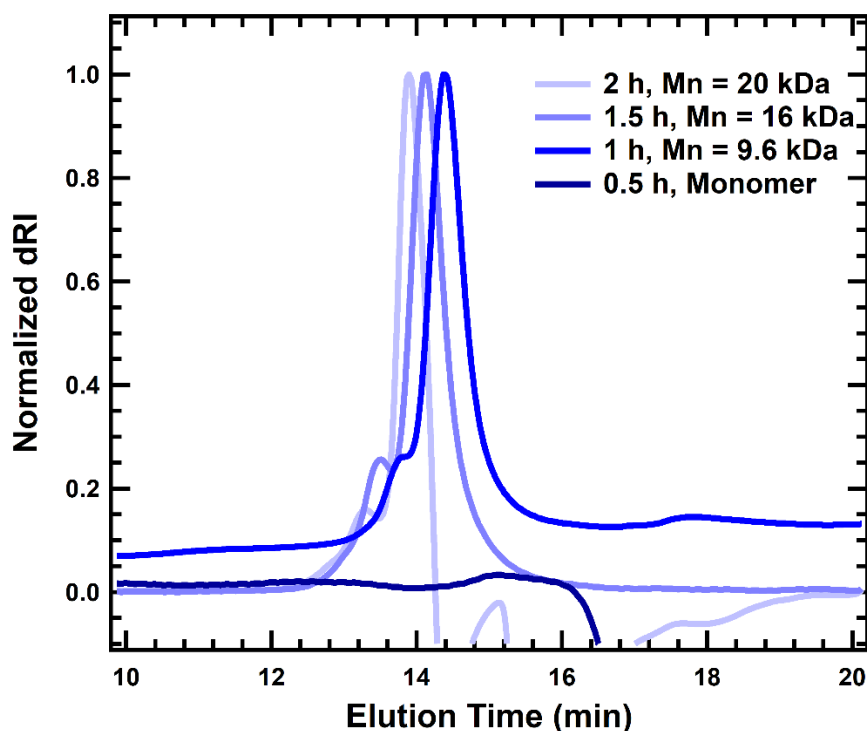


**Figure 2-8.** Time series of GPC traces for PNIPAM polymerization with target  $M_n$  of 22 kDa. Samples were collected every 30 minutes, as the target PNIPAM  $M_n$  was relatively low ( $< 30$  kDa). Negative dRI values are caused by the presence of NIPAM monomer. No PNIPAM peak is observed at 0.5 h, as the solution is primarily NIPAM monomer and oligomers.

The following day, the polymer was precipitated by pipetting dropwise into a stirred solution of diethyl ether (10x the reaction volume) in an ice bath. The precipitates were collected by filtering using a Buchner funnel, and the slightly wet solid was dried under vacuum. Once the solid was dry, it was placed in a vacuum oven preheated to  $120\text{ }^\circ\text{C}$  for two hours to remove the furan group protecting the maleimide (during which time any residual NIPAM in the solid sublimated and collected in the cold trap). The product was collected as a solid with a color that

ranged from bright yellow ( $M_n < 10$  kDa) to a very pale yellow ( $M_n > 100$  kDa) that was stored at  $-20$  °C for future use.

## 2.4 Bioconjugate Synthesis

Bioconjugations between cysteine-bearing proteins and maleimide-functionalized PNIPAM were performed in Sso resuspension buffer for bioconjugations involving rcSso7d.SA oligomers or ZE resuspension buffer for bioconjugations involving coiled-coil fusions. Solutions of the proteins were diluted to approximately 1 mg/mL, and a 5x molar excess of PNIPAM was added. After complete dissolution of PNIPAM, samples were incubated at room temperature on an orbital shaker for 24 h. Ammonium sulfate (3 M, in MilliQ water) was then added to a concentration of 1 M to remove unconjugated protein. Following centrifugation for 30 minutes at 13,000 rpm and room temperature, the supernatant was discarded, and the precipitates were resuspended in the appropriate resuspension buffer to approximately 1 mg/mL. Two additional ammonium sulfate precipitations were performed, after which the solution was incubated with Ni-NTA (the same volume of resin that would have been used to purify the initial quantity of unconjugated protein) overnight at 4 °C on a rocking platform.

The mixture was purified by Ni-NTA chromatography to remove unconjugated PNIPAM (see section **2.2.1.3**). To ensure that all PNIPAM was removed, the last CV of the 15 CV of equilibrium buffer used to wash the resin was collected and stored at 37 °C for 10 minutes. If the solution did not become turbid, the affinity chromatography was continued following the standard procedure by eluting the bound conjugate with elution buffer. Otherwise, additional equilibrium buffer was added, 5 CV at a time, until the last CV of added buffer did not become turbid when stored at 37 °C. Purified protein-PNIPAM conjugates were dialyzed against MilliQ water (see section **2.2.1.4**). Bioconjugate purity was confirmed using SDS-PAGE and native PAGE (**Figures**

**A-2b, c; A-4b, c; A-6; and A-8**), and retention of protein secondary structure was assessed using CD (**Figures A-3b, A-5b, and A-7a**).

Conjugate solution was concentrated to approximately 100 mg/mL using Amicon Ultra 15 centrifugal filters (molecular weight cutoff of 10 kDa, Millipore Sigma). Bulk solid samples were prepared by drop-casting aliquots of this concentrated solution onto Teflon sheets and drying under vacuum to a final pressure of 5 Torr (ramp rate 50 Torr/h) at room temperature. The volume of the aliquots varied between 20  $\mu$ L (for highly viscous samples) and 50  $\mu$ L (for samples with water-like viscosity). Samples were then collected and stored at 4 °C until future use. Dried samples could be stored at 4 °C for at least one year without any noticeable change in conjugate morphology or protein secondary structure. Typical yields after purification for all conjugates ranged from 50% (for conjugation to low- $M_n$  PNIPAM) to 20% (for conjugation to high- $M_n$  PNIPAM).

To form heterodimer coiled-coil bioconjugates, dried bioconjugate samples were dissolved at a concentration of 0.1 mg/mL in MilliQ water at 4 °C. Then, the solutions of either 2xZEC and 2xZRC (to form 2xZEC-ZRC) or 2xZEN and 2xZRC (to form 2x ZEN-ZRC) were mixed in an equimolar ratio and incubated at 4 °C overnight. Bulk samples were prepared by concentrating and drying as described previously. Samples were stored at 4 °C until future use.

## **2.5 Fluorescent Labeling of Proteins**

In a typical fluorescent labeling reaction, 1 mg of protein in 500  $\mu$ L of PBS (pH 7.4) was added to an Eppendorf tube wrapped in aluminum foil. For conjugations to fluorescein isothiocyanate (FITC), 10  $\mu$ L of freshly-prepared 50x sodium carbonate buffer (final concentration = 100 mM, pH = 9.0) was added to the protein solution. For conjugations to Alexa Fluor 647 or Alexa Fluor 488 (both of which contained an NHS ester functionality), 30  $\mu$ L of a freshly-prepared sodium bicarbonate solution (84 mg of sodium bicarbonate dissolved in 1 mL of MilliQ water) was added

to the protein solution. Immediately prior to conjugation, the dye molecule was dissolved in amine-free, anhydrous DMF at a concentration of 2 mg/mL (for FITC) or 10 mg/mL (for Alexa Fluor 647 or 488). An appropriate volume of dye in DMF was then added to the Eppendorf tube, and the solution was mixed by pipetting up and down several times. While the exact amount of dye that needed to be added to achieve a suitable degree of labeling varied from protein-to-protein, the following guidelines served as a good starting point: 5 equivalents of dye for proteins with MW < 30 kDa, 10 equivalents of dye for proteins with 30 kDa < MW < 100 kDa, 20 equivalents of dye for proteins with MW > 100 kDa. After the dye was added, the Eppendorf tube was quickly closed, fully covered in aluminum foil, and incubated at 4 °C for 16 hours on a rocking platform. If FITC was being used as the dye molecule, after this time had elapsed ammonium chloride was added to a final concentration of 50 mM (to react with any unreacted FITC), and the solution was incubated at 4 °C for an additional 2 hours on a rocking platform.

Removal of unbound dye molecules was carried out using a PD-10 column with Sephadex G-25 (GE Healthcare). The column was allowed to warm to room temperature, and the excess fluid was drained by gravity. Then, the column was filled with PBS and drained fully a total of 4 times. The dye/protein sample was then added directly to the top of the column (ensuring that no sample touched the walls of the plastic column) and allowed to enter the gel bed completely. Once the sample had fully entered the gel, 2 mL of PBS was added to the column. As this PBS passed through the column, two bright colored bands could be observed: a band that moved close to the bottom of the column (corresponding to dye-labeled protein) and a band that remained at the top of the column (corresponding to unlabeled dye). An Eppendorf tube wrapped in aluminum foil was then added beneath the column, and an additional 1.5 mL of PBS was added to the column to elute the dye-labeled protein. The collected sample was then concentrated using an Amicon Ultra

0.5 mL centrifugal filter (molecular weight cutoff of 10 kDa, Millipore Sigma) by centrifuging at 13000 rpm and 4 °C for 10 minutes. The collected filtrate was colorless, indicating complete removal of unconjugated dye. The concentrated sample was diluted to 0.4 mL, wrapped in aluminum foil, and stored at 4 °C.

To ensure appropriate dye loading, the degree of labeling (DOL) was determined for each protein. The DOL was calculated using the following formula:

$$DOL = \frac{A_{max} \times 150 \text{ kDa}}{[protein] \times \epsilon_{dye} \times l \times MW}, \quad (2-1)$$

where  $A_{max}$  is the absorbance of the labeled protein at the absorbance maximum of the dye, 150 kDa is the average molecular weight of an antibody,  $[protein]$  is the concentration of the protein (at the same dilution used to measure  $A_{max}$ ) in M,  $\epsilon_{dye}$  is the extinction coefficient of the dye at its absorbance maximum in  $M^{-1}cm^{-1}$ ,  $l$  is the path length of the cell used to measure  $A_{max}$ , and  $MW$  is the molecular weight of the protein in kDa. The wavelength corresponding to the maximum absorbance of the dye molecule and the dye extinction coefficient were found in Thermo Fisher's Amine-Reactive Probes guide.<sup>7</sup> Protein concentration was measured using a Pierce microplate BCA protein assay kit (Thermo Fisher) (see section 2.2.1.5). If the calculated DOL fell outside the optimal range of 3-7, the fluorescent labeling was repeated by doubling (if the DOL was too low) or halving (if the DOL was too high) the equivalents of dye reacted with the protein.

## 2.6 Structural and Biophysical Characterization Techniques

### 2.6.1 Small-angle X-ray Scattering (SAXS)

#### 2.6.1.1 Sample Preparation

Dried conjugate samples were added to 0.6 mL microcentrifuge tubes, and the samples were crushed using tweezers so the samples were as densely packed at the bottom of the tubes as possible. The mass of sample added to each tube was determined so that, once hydrated, samples

had a mass of at least 10 mg (e.g., for a desired 30 wt. % sample, at least 3 mg of dried conjugate was added to the microcentrifuge tube). MilliQ water was then added to the tube to achieve the desired conjugate concentration, and the tubes were centrifuged in a microcentrifuge at 14,800 rpm and 4 °C for 10 minutes. At this time, any dried conjugate not fully submerged in the water at the bottom of the tube was pushed into the water using a P10 pipette tip (usually only required for conjugate samples with concentrations > 40 wt. %). All samples were then centrifuged for an additional 10 minutes under the same conditions. While lower concentration conjugate samples were fully dissolved at this point, higher concentration samples needed to be incubated at 4 °C (without shaking) for at least 16 hours to achieve complete dissolution. All hydrated samples were used within a week of preparation (though most samples retained their morphology and protein secondary structure for at least one month).

Hydrated conjugate samples were loaded into 1 mm thick anodized aluminum washers with a 2-3 mm bore and sealed on both sides with Kapton tape. For solid conjugate samples, the thickest sample free of air bubbles was loaded into an aluminum washer in the same manner. Blank samples were prepared by sealing a washer with Kapton tape without loading any sample into the bore. These washers were then loaded into a brass 10-sample holder (schematic shown in **Figure 2-9**) connected to a water circulator when running SAXS experiments. Images of sample loading can be found in the thesis of Dr. Carolyn Mills.<sup>1</sup>

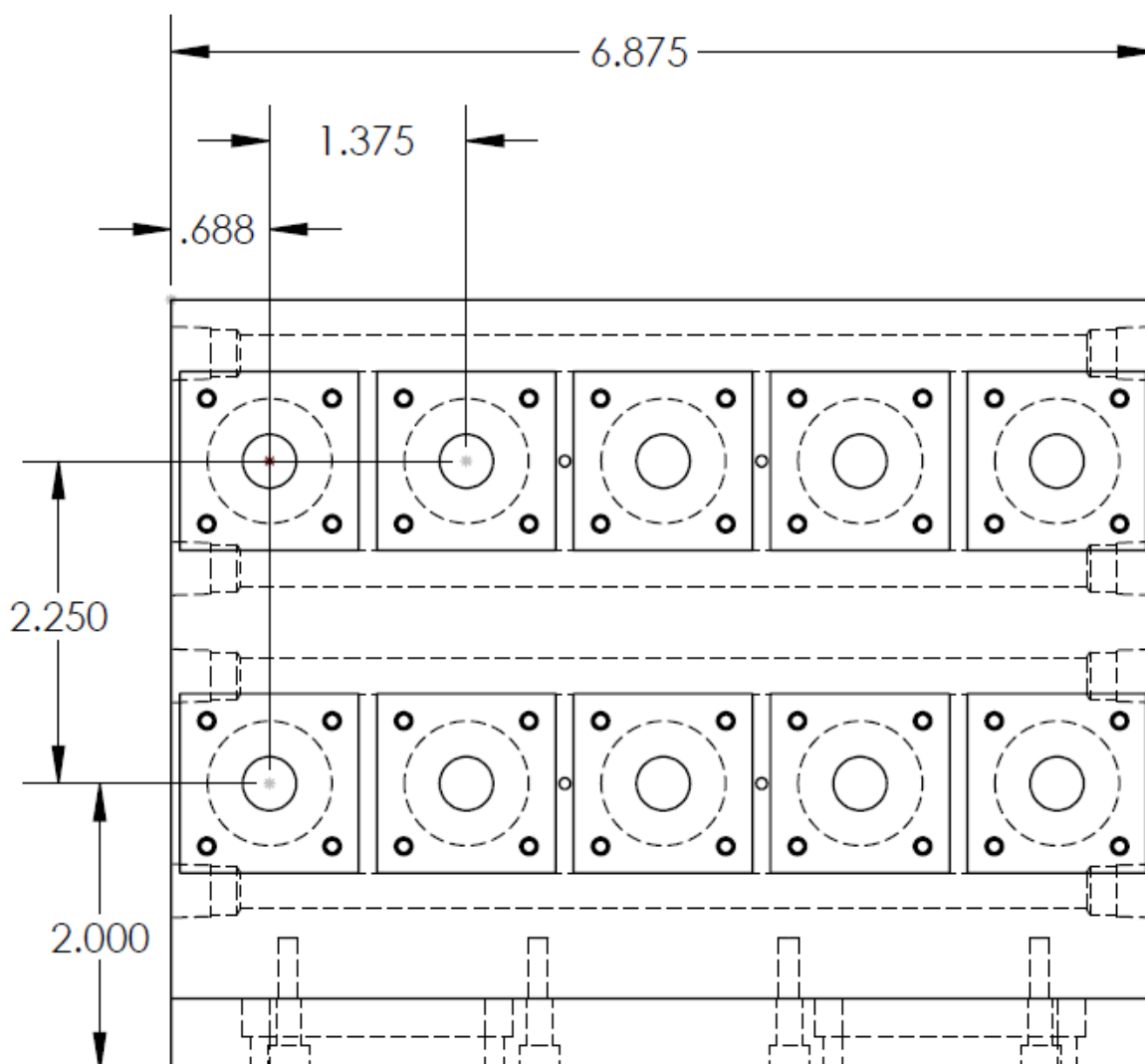


**Figure 2-9.** Schematic of temperature-controlled 10-sample holder for SAXS experiments. All lengths are in inches.

### 2.6.1.2 Experimental Procedure

All synchrotron SAXS samples for this thesis were measured at the National Synchrotron Light Source II (NSLS-II) at Beamline 11-BM using X-rays with energy 14.000 keV. Most SAXS samples required scattering at 5 °C temperature intervals in the range of 10-40 °C. For these samples, the sample holder was initially equilibrated to within 0.5 °C of 10 °C by setting the attached water circulator to an appropriate temperature (usually several degrees lower than 10 °C).

Temperature of the holder was measured using a resistance temperature detector (RTD) provided at the beamline. Once the temperature of the sample holder became steady around 10 °C, the samples were equilibrated in the holder for 10 minutes. The samples were then quickly scanned (usually for 0.1-1 s, each) to ensure that all samples were properly aligned and not shear-aligned (as evidenced by an asymmetric 2D SAXS pattern). The sampling point within each sample was then adjusted as necessary to ensure an appropriate region was being measured. A full scan of the samples was then performed. To ensure no X-ray beam damage was caused to the samples, SAXS patterns were collected for one sample after beam exposure times of 1 s, 10 s, 30 s, 1 min, 2 min, and 3 min. In all cases, no noticeable difference between the SAXS patterns was observed after 1 minute, and in most cases, little if any differences were observed after 3 minutes. Sampling times were selected to be long enough to obtain sufficient data counts (this minimum count value was always provided by the beamline scientists) yet short enough to be at least an order of magnitude less than the time required to cause beam damage. In general, sampling times ranged between 1 and 10 s. The temperature of the water circulator was then raised so that the holder achieved a stable temperature within 0.5 °C of 15 °C, and the samples were allowed to equilibrate at this steady temperature for 10 minutes. SAXS patterns collected after a 20 minute equilibration at the steady temperature were essentially identical to those collected after 10 minutes, indicating that the 10 minute equilibration time was sufficient. Sample alignment and a full scan were then performed as described previously, and this process of temperature adjustment and alignment/measurement was repeated for all temperatures of interest. For SAXS samples that only required scattering at a single temperature, samples were allowed to reach equilibrium at this temperature for 10 minutes in the pre-equilibrated 10-sample holder. Sample alignment and a full scan were then performed as described previously.

Two-dimensional SAXS patterns were reduced to one-dimensional curves by taking an azimuthal average of the full 2D data. This reduction was performed automatically using processing routines developed at the beamline. Since the data processing software at the beamline automatically corrected for dark field, fiber optic distortion, and non-uniformity of beam flux, data only needed to be corrected by subtracting the scattering of a blank cell (2 layers of Kapton tape) from that of each sample at the corresponding temperature. MATLAB code used to perform this data processing is provided in **Appendix A5**.

## **2.6.2 Grazing-incidence Small-angle X-ray Scattering (GISAXS)**

### **2.6.2.1 Sample Preparation**

Dried conjugate samples were hydrated to a final concentration of 10 wt. % following the same procedure outlined in the SAXS sample preparation section. Silicon wafers (Wafer World, P-type Silicon with boron as dopant, (100) orientation, single-side polished) cut into rectangular sections or quartz slides (Ted Pella, Inc., only used in experiments for which binding intensity was measured as a function of film thickness) were sequentially rinsed with acetone, methanol, and DI water, making sure to rinse both sides of the substrate during the final water rinse. Substrates were then dried under a filtered air flow and treated with oxygen plasma for 3 minutes. Immediately following plasma cleaning (which made the surface more wettable for film casting), conjugate samples rehydrated to 10 wt. % in MilliQ water (following the same procedure outlined in the SAXS sample preparation section, except volumes of at least 100  $\mu\text{L}$  were prepared) were flow coated onto the substrates in a chamber maintained at 60% relative humidity, as described previously.<sup>8</sup> To stabilize thin films against dissolution in water, a 1.4 wt. % aqueous solution of glutaraldehyde was prepared at 40 °C. Films were preheated by directly placing the film on the hotplate used to heat the glutaraldehyde for 5 seconds and then immediately submerging the film

in the glutaraldehyde solution for 20 s to lightly crosslink the protein nanodomains. Immediately following immersion, the thin films were thoroughly rinsed with DI water until the surfaces became hydrophilic, indicating complete removal of unlinked glutaraldehyde. Films were dried under filtered air and stored at ambient conditions until use. Film thickness was determined using a Woolam M-2000D spectroscopic ellipsometer using a single incidence angle of  $70^\circ$ . Curves were fit using a three-layer model consisting of a 0.4 mm bottom silicon substrate, a native silicon oxide layer of 1.8 nm, and a top conjugate layer fit using a Cauchy model.

### **2.6.2.2 Experimental Procedure**

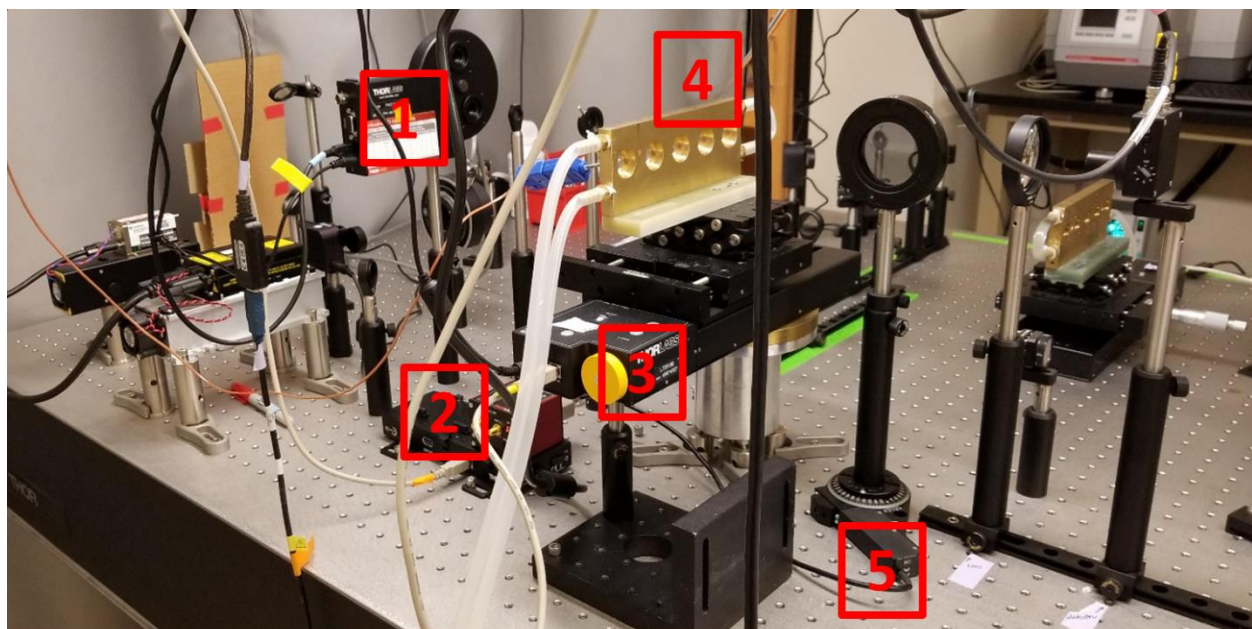
GISAXS experiments were conducted at beamline 8-ID-E of the Argonne National Laboratory using X-rays with energy 10.915 keV. Samples were measured at incident angles of  $0.105^\circ$  for analysis of surface morphology and  $0.140^\circ$  for bulk morphology. All measurements for a given sample were collected at the same position on the film, which was exposed to X-rays for a time totaling no more than 30 seconds to prevent beam damage. In all cases, no beam damage was observed after 1 minute of X-ray exposure, and the same procedure for determining the time required for beam damage in SAXS experiments (see section **2.6.1.2**) was followed. Films were loaded into a sealed Teflon chamber provided at the beamline and exposed to dry, room temperature nitrogen. Film thickness was continuously measured using a Filmetrics F20-UV thin film analyzer. Once the film thickness readings reached a constant value (usually took  $\sim 10$  minutes), the dry film thickness was recorded, and the chamber was filled with room temperature air at 95% relative humidity (RH). GISAXS measurements of swollen films were collected after 15 minutes of exposure to 95% RH air, at which time the air within the chamber had reached 95% RH and the film thickness had stabilized.

Image analysis and data processing were performed using the beamline-provided GIXSGUI software package for MATLAB. All horizontal linecuts were generated as 100 points between  $q_y$  values of 0.05 and 0.45  $\text{nm}^{-1}$  representing the average value along the  $q_z$  axis within the range 0.24-0.30  $\text{nm}^{-1}$  for the given  $q_y$  value. Vertical linecuts were generated as 100 points between  $q_z$  values of 0.70 and 2.5  $\text{nm}^{-1}$  representing the average value along the  $q_y$  axis within the range 0.00-0.05  $\text{nm}^{-1}$  for the given  $q_z$  value.

### **2.6.3 Turbidimetry and Depolarized Light Scattering (DPLS)**

For turbidimetry and DPLS measurements, an existing setup<sup>5</sup> was modified to enable automated data collection of five samples in series (**Figure 2-10**). During beam alignment and instrument maintenance, the ND filter wheel permitted easy adjustment of the incident beam intensity such that output voltage of the photodetector when exposed to this open beam was within the optimal range of ~3-6 V. This range ensured sufficient signal for identification of weakly-birefringent samples while also avoiding detector damage that would be caused by operating too close to the maximum output voltage of the photodetector (10 V). Noise in the collected data was minimized by adjusting the ND filter wheel rather than the detector gain (which was always set to a value of 0 decibels) to achieve an output voltage within the optimal range. The linear translation stage permitted motorized movement of the 5-sample holder such that the beam could access all 5 samples. If it is ever desired to analyze additional samples by extending the sample holder, either a longer translation stage would need to be purchased (if the sample holder were simply elongated) or a motorized z-stage would need to be installed (if another row were added to the sample holder). The motorized rotation stage underneath the rear polarizer, positioned such that the center of the polarizer was slightly out of the direct beam path, allowed the polarizer to be inserted and removed from the beam path through 90° rotations. LabVIEW codes were written to interface with these

devices and automatically collect data for the loaded samples, and these codes are summarized in section 2.6.3.2 and the Olsen Lab SOP for Birefringence/DPLS.



**Figure 2-10.** Added components to an existing turbidimetry/DPLS setup that allowed for automated data collection. Labels correspond to the following parts (Thorlabs part numbers in parentheses): (1) 12-position motorized ND filter wheel (FW212CNEB), (2) K-cube piezo controller for motorized rotation stage (KPZ101) on USB controller hub (KCH301), (3) 150 mm linear translation stage with integrated controller (LTS150), (4) 5-sample holder (see **Figure 2-11**), and (5) motorized rotation stage (PRM1Z8).

### 2.6.3.1 Sample Preparation

Dried conjugate samples were hydrated to final concentrations ranging from 20 wt. % to 70 wt. % following the same procedure outlined in the SAXS sample preparation section. Turbidimetry and DPLS<sup>9-10</sup> were performed on samples loaded into a 1 mm thick Teflon spacer with a 2-3 mm bore, sealed between two quartz disks, and loaded into a brass holder. The optics setup for these experiments consisted of the sample in a 5-sample temperature-controlled stage (**Figure 2-11**) between a forward and an optional rear polarizer. For turbidimetry measurements, the rear polarizer was removed from the beam path, while the rear polarizer was placed within the beam path for DPLS measurements.

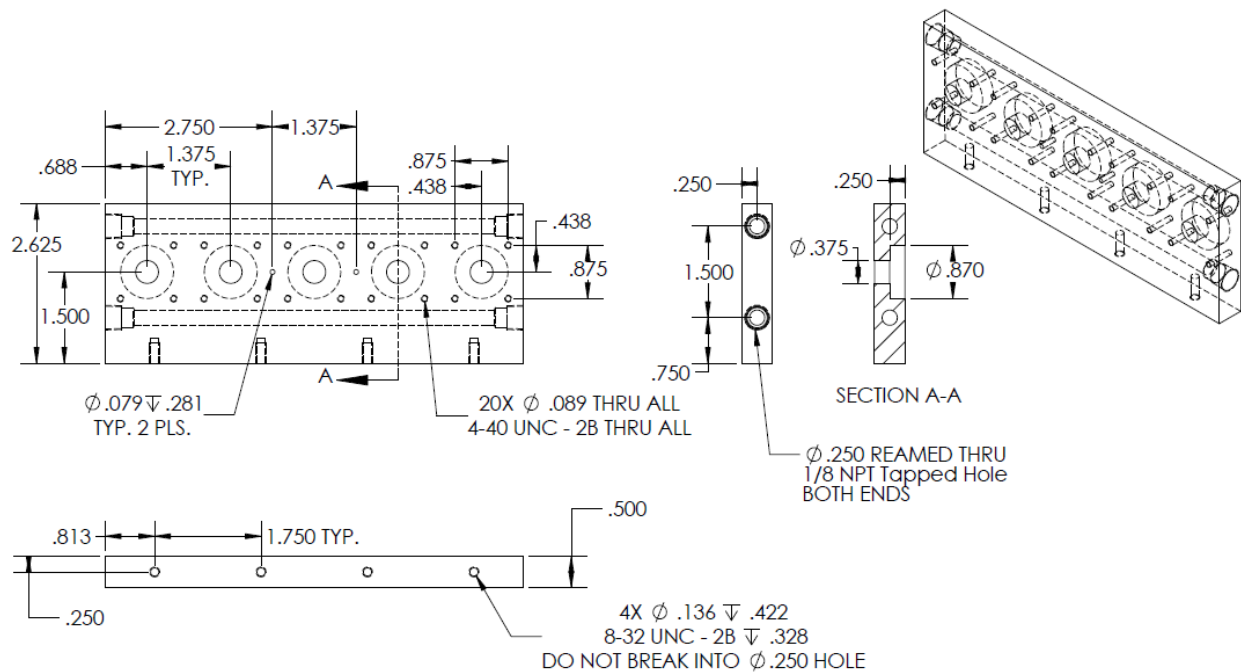


**Figure 2-11.** Schematic of temperature-controlled 5-sample holder for turbidimetry and DPLS experiments. All lengths are in inches.

### 2.6.3.2 Experimental Procedure

A Coherent OBIS LX660 laser was used with wavelength  $\lambda = 662$  nm and continuous wave output power 10 mW. Using the LabVIEW code *DPLS Main Code.vi*, samples were equilibrated at 10 °C for 10 minutes and then heated at 1 °C/min to 40 °C, allowed to equilibrate for 10 minutes, and then cooled at 1 °C/min to 10 °C. Prior to loading samples, three measurements were performed to allow for data correction using the LabVIEW code *Parameter Collection.vi*. Each measurement was run for 1 minute, and the value for each correction parameter was taken as the average value over the measurement period. First, the background signal  $I_{dark}$  was determined by collecting data with the laser off. The 100% transmission laser intensity  $I_{open}$  was then collected by running measurements with the laser on and with the rear polarizer out of the beam path. The rear polarizer was then re-positioned into the beam path to determine the laser signal through the rear polarizer  $I_{cross}$ .

Macrophase separation transitions were defined as the temperatures  $T_t$  corresponding to a 10% reduction in the initial sample transmittance, according to literature methods.<sup>11</sup> Transitions were reproducible for at least 5 repeated heating/cooling cycles, and data analysis was performed on the first heating cycle. The static depolarized light scattering signal was corrected for transmission and dark field background. Power fractions  $I_{PF}$  were calculated as the ratio of the birefringent intensity  $I$  to the laser intensity  $I_{open}$  as follows:

$$I = \frac{1}{T_S} (I_B - I_{dark}) - (I_{cross} - I_{dark}), \quad (2-2)$$

$$I_{PF} = \frac{I}{I_{open}}, \quad (2-3)$$

where  $T_S$  is sample transmission (the ratio of the measured transmission signal to  $I_{open}$ ) and  $I_B$  is the measured birefringent signal.

## 2.6.4 Differential Scanning Calorimetry (DSC)

### 2.6.4.1 Sample Preparation

Dried conjugate samples were hydrated to final concentrations ranging from 20 wt. % to 70 wt. % following the same procedure outlined in the SAXS sample preparation section. DSC samples were loaded into a hermetically sealed aluminum pan. The mass of the pan before and after loading with sample was recorded so the sample mass could be calculated.

### 2.6.4.2 Experimental Procedure

Data were acquired using a TA Instruments Discovery differential scanning calorimeter. Each sample was equilibrated at 5 °C for 5 minutes, followed by two cycles of ramping to 45 °C at 5 °C/min, holding isothermally for 2 minutes, cooling at 5 °C/min to 5 °C, and holding isothermally for 2 minutes. Both measurement cycles were found to overlap for all conjugates. Transition temperature values were extracted from the onset point in the initial heating cycle, as

determined using supplier-provided TRIOS software. The rate dependence of thermal transitions was never measured, as the optimized times for each step in the heating/cooling cycles listed in the thesis of Dr. Christopher Lam<sup>5</sup> were used.

## **2.6.5 Circular Dichroism (CD)**

### **2.6.5.1 Sample Preparation**

Protein samples were dialyzed against MilliQ water or the desired buffer (see section 2.2.1.4) and then diluted or concentrated to an appropriate concentration. Dried conjugate samples were hydrated to final concentrations such that the concentration of the protein in the conjugate was 0.1 mg/mL following the same procedure outlined in the SAXS sample preparation section. Samples were loaded into quartz cuvettes with path lengths of 1, 0.1, and 0.01 mm for measurements at concentrations of 0.1, 1, and 10 mg/mL, respectively. The volume of sample required to fill these three cuvettes was approximately 200, 26, and 4  $\mu$ L, respectively.

### **2.6.5.2 Experimental Procedure**

CD spectroscopy was performed using a JASCO Model J-1500 CD spectrometer to measure far UV CD spectroscopy between 195 and 250 nm. Single-temperature measurements were collected at 25 °C. Raw CD signal was smoothed and converted to molar ellipticity using literature methods.<sup>12</sup> For measurements of coiled-coil fusion proteins, the percentage of folding within coiled-coiled domains was estimated by first subtracting the molar ellipticity at 222 nm ( $[\theta]_{222}$ ) of 2x in MilliQ water from that of a 2x coiled-coil fusion in MilliQ water at the same concentration. This estimate of the  $[\theta]_{222}$  value corresponding to the coiled-coil region was then multiplied by the ratio of the molecular weights of the full fusion protein to that of the coiled-coil region to re-normalize the signal by the appropriate molecular weight. The resulting  $[\theta]_{222}$  value was then used to estimate percent folding of the coiled-coil using the following equation:<sup>13</sup>

$$\% \text{ Folded} = \frac{[\theta]_{222} - [\theta]_{222,\text{unfolded}}}{[\theta]_{222,\text{folded}} - [\theta]_{222,\text{unfolded}}} \times \frac{100}{\text{Frac Coil Residues}}, \quad (2-4)$$

where a value of  $-3,000 \text{ deg cm}^2 \text{ dmol}^{-1}$  was assumed for  $[\theta]_{222,\text{unfolded}}$ ,<sup>13</sup>  $[\theta]_{222,\text{folded}}$  was estimated to be  $-37,000 \text{ deg cm}^2 \text{ dmol}^{-1}$  using an approximation based on the number of residues in the helix,<sup>14</sup> and *Frac Coil Residues* was 0.81 for all samples, as each fusion protein had 53 residues in the non-2x region of the protein, 43 of which were part of the ZE or ZR coiled-coil.

For coiled-coil fusion protein temperature ramp experiments, melting curves were collected by continuously measuring  $[\theta]_{222}$  while heating samples from 10 to 90 °C at a rate of 1 °C/min. Samples were equilibrated at 10 °C for 10 minutes prior to starting the temperature ramp. All samples were measured at a concentration of 0.1 mg/mL in MilliQ water. Data were fit using a previously-derived thermodynamic model in which the equilibrium constant was assumed to exclusively describe the bimolecular reaction of coiled-coil monomers forming the intended homodimer or heterodimer.<sup>15</sup>

## 2.6.6 Analytical Ultracentrifugation (AUC)

### 2.6.6.1 Sample Preparation

Dried conjugate samples were hydrated in MilliQ water to desired concentrations between 0.1 and 1 mg/mL following the same procedure outlined in the SAXS sample preparation section. Samples were loaded into analytical ultracentrifugation cells with two windows that could fit into an AN-50 Ti rotor. One window was loaded with 250  $\mu\text{L}$  of conjugate sample, and the other window was loaded with 270  $\mu\text{L}$  of MilliQ water to ensure the meniscus in the conjugate sample could be easily detected after subtracting signal from the MilliQ water window.

### 2.6.6.2 Experimental Procedure

Sedimentation velocity experiments were run on a Beckman XL-I analytical ultracentrifuge equipped with an AN-50 Ti rotor. Samples were equilibrated at 10 °C for 1 hour, then spun at

42,000 rpm and 10 °C for 18 hours while constantly measuring absorbance at 280 nm. Data were fit with SEDFIT software<sup>16</sup> using a continuous size distribution.

## **2.6.7 Dynamic Light Scattering (DLS)**

### **2.6.7.1 Sample Preparation**

Proteins were either dissolved if received as a lyophilized powder or dialyzed (see section **2.2.1.4**) if the protein was received in solution into at least 500  $\mu$ L of PBS at an approximate concentration of 4 mg/mL. Samples were then centrifuged at 4 °C and 10,000 x g for 4.5 hours to pellet large aggregates and immediately used for measurements.

### **2.6.7.2 Experimental Procedure**

DLS measurements were performed on a Wyatt Möbiuζ DLS/zeta potential instrument with a 532 nm laser. At least 300  $\mu$ L of the centrifuged protein solutions were filtered through a 0.2  $\mu$ m pore size syringe filter to remove dust, pipetted into disposable polystyrene cuvettes with a 1 cm path length, and allowed to warm to room temperature. The cuvettes were then placed in the DLS instrument, which was equilibrated to 20 °C, and measured. Size distributions were produced by performing fits to autocorrelation curves in the Wyatt Dynamics software using a supplier-provided regularization algorithm.

## **2.6.8 Fluorescence Recovery After Photobleaching (FRAP)**

### **2.6.8.1 Sample Preparation**

To prepare crosslinked protein gels, a solution of 3x rcSso7d.SA dialyzed into sodium phosphate buffer (50 mM sodium phosphate, 150 mM NaCl, pH 7.2) (see section **2.2.1.4**) was concentrated to 20 wt. % (~200 mg/mL) in an Eppendorf tube. While most buffers would have been suitable for dialysis, it is important that amine-containing buffers (e.g., Tris) are not used to avoid unwanted crosslinking reactions in future steps. The concentrated protein solution was then heated to 40 °C,

and a 10x glutaraldehyde solution (final 1x concentration of 1.4 wt. % in MilliQ water) maintained at 40 °C was added to the protein solution by quickly pipetting up and down while stirring with the pipette tip. The mixture was then allowed to crosslink at 40 °C for 30 seconds, producing an amber-brown gel. Residual glutaraldehyde was removed by 5 cycles of: 1) adding MilliQ water to the gel to a final volume of 1 mL, 2) vigorously vortexing the mixture for 10 seconds, and 3) pouring off the supernatant. The gel was then stored at 4 °C for future use.

To prepare samples for microscopy, a small section from the gel (volume of < ca. 1 mm<sup>3</sup>, thickness of at least 10 µm) was cut using a scalpel and placed in the center of a small petri dish. A wax pencil was used to draw a small circle around the gel fragment (to prevent water from escaping this area), and 100-200 µL of a 1 µM solution of fluorescently labeled protein was added to the gel. The gel was allowed to equilibrate in the solution for 16 hours in the dark at 4 °C. Immediately before FRAP measurement were conducted, the fluorescent solution was pipetted off, and the gel was rinsed with 100 µL of MilliQ water (by pipetting up and down around the gel) to remove protein on the gel surface. The gel was then placed between a glass slide and a coverslip containing double-sided tape on two (opposite) edges to seal the gel in place. MilliQ water was then pipetted into the channel formed between the glass slide and coverslip, and the two open edges of the channel were sealed using Sally Hansen Hard as Nails hardener.

Samples for diffusion measurements in PNIPAM solutions were prepared by first dissolving PNIPAM samples of the desired molecular weights in MilliQ water to a final concentration of 20 wt. %. PNIPAM was dissolved by first incubating on a rocking platform at 4 °C for 2 days. After this time, the mixtures were briefly centrifuged to collect all material at the bottom of the containers. Samples were then stored upright at 4 °C for a time ranging from 1-2 days (for lower molecular weight PNIPAM) to 1-2 weeks (for high molecular weight PNIPAM)

to allow complete dissolution of PNIPAM. FITC-labeled protein samples in PBS were then concentrated to ~10  $\mu\text{M}$ , and 5  $\mu\text{L}$  of these solutions were added to PCR tubes containing 55  $\mu\text{L}$  of PNIPAM solution. A pipette tip was used to stir the solution until the color from the fluorescently-labeled protein was evenly distributed.

Microscope slides for diffusion measurements in PNIPAM solutions were prepared by adhering a Teflon spacer (No. 12 screw size, 0.25 in. ID, 0.5 in. OD, 0.06 in. thickness, McMaster-Carr) to the center of a glass microscope slide using Sally Hansen Hard as Nails hardener. The hardener was allowed to dry overnight. The top of the spacer was then coated with a thin, even layer of Sally Hansen Hard as Nails hardener, the PNIPAM solution containing fluorescently-labeled protein was pipetted into the spacer, and a microscope slide was placed on top of the spacer to seal the PNIPAM solution. The hardener was allowed to dry for 1 hour at room temperature in the dark and then stored at 4  $^{\circ}\text{C}$  in the dark for at least 16 hours.

### **2.6.8.2 Experimental Procedure**

Imaging was performed on a confocal laser scanning microscope (Zeiss LSM 710, W.M. Keck Microscopy Facility) equipped with an oil-immersion 40x objective lens (Plan Apochromat, NA 1.3). A circular region of interest was photobleached for 1 second using a 488 nm laser at full power, and fluorescence recovery was monitored by scanning the region of interest at low laser power (24%) every second for 1 min after bleaching. Images were also collected every second for 5 seconds prior to the bleaching event to obtain a pre-bleach intensity value within the bleached region.

FRAP curves were generated by using ImageJ software to process the full sequence of fluorescence images collected. For each image, fluorescence intensity values were adjusted to account for fluctuations in laser intensity by dividing the average fluorescence intensity within the

circular bleach region by the average intensity within a rectangular area far from the bleach region. These fluctuation-adjusted fluorescence values were then normalized between values of 0 (the fluctuation-adjusted fluorescence value immediately after bleaching) and 1 (the average of the fluctuation-adjusted fluorescence values in the 5 images collected prior to bleaching) prior to fitting FRAP curves. The Java macro used to perform this image processing is provided in **Appendix A5**.

## **2.7 Biosensor Analytical Techniques**

### **2.7.1 Monolayer Fabrication**

rcSso7d.SA (Sso) monolayers were prepared by coupling protein activated by 1-Ethyl-3-(3-dimethylaminopropyl)carbodiimide/N-hydroxysuccinimide (EDC/NHS) with amine-functionalized silicon wafers using literature methods.<sup>17</sup>

### **2.7.2 Fluorescent Binding Assays**

The binding capabilities of Sso monolayers and conjugate thin films were measured using AF647-labeled SA and mSA2. Samples were prepared by serial dilution of SA or mSA2 in PBS (pH 7.4), human urine (diluted to 50% v/v in PBS, pH 7.4), or blood serum (obtained as the supernatant by centrifuging whole blood at 1500 x g for 10 minutes, then diluted to 50% v/v in PBS, pH 7.4). These solutions were gently applied to the surface of a bioconjugate thin film (prepared as described in the GISAXS sample preparation section) or Sso monolayer as 0.5  $\mu$ L drops. Films were incubated for a specified period of time in a sealed chamber saturated with water vapor at room temperature to prevent drying of the applied fluorescent samples. Sealed chambers consisted of a large petri dish containing the inverted lid of a smaller petri dish in the center. Films coated with sample droplets were placed in the small petri dish lid, and the large petri dish was filled with a thin layer of MilliQ water. The chamber was sealed using the lid for the large petri dish, and the

entire chamber was covered in aluminum foil. The films were then rinsed with water for 10 seconds, a time determined to be sufficient to remove unbound molecules from the film (**Figure A-12**), dried under filtered air, and immediately analyzed for fluorescent signal. Fluorescence microscopy images were acquired at 4x magnification using a Cy5 filter set and exposure time of 5000 ms on an Olympus IX-81 inverted fluorescence microscope with an AxioCam HRC CCD camera. Fluorescent intensity was calculated using ImageJ software<sup>18</sup> by determining the average fluorescent signal in a rectangular area of the fluorescent image free of defects and occupying no less than half of the full sample application area. Corrected intensity was determined by subtracting the fluorescent intensity of a sample from that of an area on the substrate far away from regions exposed to fluorescent samples.

### **2.7.3 Thermal Stability Assays**

A long (> 6 cm) conjugate thin film was prepared as described in the GISAXS sample preparation section and cut into ~0.5 cm wide segments. Half of the segments were stored at ambient conditions (21 °C, 40% relative humidity, RH), and the remaining segments were stored in an environmental chamber at 60 °C, 60% RH. After specified periods of time, one ambient condition thin film segment and one environmental chamber thin film segment (allowed to cool to room temperature) were selected for fluorescent binding measurements. The same procedure used in the fluorescent binding assays section was followed.

### **2.7.4 Sandwich Assays**

Bioconjugate thin films and Sso monolayers were cut into 0.25 cm-by-0.25 cm pieces and securely fastened to the bottom of Falcon polystyrene 12-well plates using double-sided carbon tape. The film segments were fastened as close to the wall of the well as possible to prevent blocking of the detector during later plate reader analysis. Each well was submerged in 1 mL of 1% BSA in MilliQ

water, and the 12-well plate was incubated at 37 °C for 30 minutes. The wells were rinsed twice by adding 2 mL of MilliQ water and gently shaking the well plate at 70 rpm for 5 minutes. 1 mL of streptavidin diluted in PBS, urine, or blood serum (prepared as described in the fluorescent binding assays section) containing 0.1% BSA was then added to each well, and the well plate was shaken at 70 rpm for 4 hours at room temperature. Wells were rinsed twice with 2 mL of MilliQ water then twice with 2 mL of 0.1% BSA in MilliQ water by shaking at 70 rpm for 5 minutes. After rinsing, wells were submerged in 1 mL of 200 ng/mL biotin-HRP in MilliQ water containing 0.1% BSA, and the well plate was shaken at 70 rpm for 1 hour at room temperature. Wells were then rinsed with water and 0.1% BSA as described previously. 1 mL of solution from a Pierce TMB substrate kit (Thermo Fisher Scientific) was added to each well, and the well plate was shaken vigorously at 125 rpm for 15 minutes at room temperature. 1 mL of 2 M H<sub>2</sub>SO<sub>4</sub> was added to each well, and the absorbance at 450 nm was read using a Tecan Infinite M200 PRO plate reader.

## **2.8 Data Fitting**

### **2.8.1 SAXS**

The full width at half maximum (FWHM) of the primary scattering peak was calculated for each SAXS curve by individually fitting the peaks to a Lorentzian:

$$I(q) = I_0 \left[ \frac{\gamma^2}{(q - q_0)^2 + \gamma^2} \right], \quad (2-5)$$

where  $I_0$  is the peak height,  $q_0$  is the peak position, and  $2\gamma$  is the FWHM. Domain spacings were calculated by dividing  $2\pi$  by the value of  $q_0$  for each peak.

### **2.8.2 GISAXS**

GISAXS linecuts were fit using the following model:

$$I(q) = \{Aq^{-4} + Bq^{-2} + C\} + \left\{ I_0 \exp \left[ \frac{-(q - q_0)^2}{2\sigma^2} \right] \right\}, \quad (2-6)$$

where the first term in braces accounts for background scattering and the second term in braces represents a Gaussian fit to the observed peak where  $I_0$  is the peak height,  $q_0$  is the peak position, and  $2\sqrt{2\ln(2)}\sigma$  is the FWHM. For 3xSP77.6k linecuts in which two peaks were observed, the second peak was fit by adding an additional term to the previous equation:

$$I_{0,2} \exp \left[ \frac{-(q - 2q_0)^2}{2\sigma_2^2} \right], \quad (2-7)$$

where  $I_{0,2}$  represents the height of the second peak, the peak position is fixed at  $2q_0$ , and  $2\sqrt{2\ln(2)}\sigma_2$  is the FWHM of the second peak. Domain spacings were calculated by dividing  $2\pi$  by the value of  $q_0$  for each peak.

### 2.8.3 FRAP

FRAP curves were fit using a model that takes into account both reaction (e.g., binding to the matrix in which the fluorophores are diffusing) and diffusion effects:<sup>19</sup>

$$\bar{f}(s) = F_\infty \left\{ \frac{1}{s} - \frac{F_{eq}}{s} [1 - 2K_1(qw)I_1(qw)] \left( 1 + \frac{k_{on}}{s + k_{off}} \right) - \frac{C_{eq}}{s + k_{off}} \right\}, \quad (2-8)$$

$$F_{eq} = \frac{k_{off}}{k_{on} + k_{off}} \quad C_{eq} = \frac{k_{on}}{k_{on} + k_{off}}, \quad (2-9)$$

$$q^2 = \left( \frac{s}{D_f} \right) \left( 1 + \frac{k_{on}}{s + k_{off}} \right), \quad (2-10)$$

$$D_{eff} = \frac{D_f}{1 + \frac{k_{on}}{k_{off}}} \quad (2-11)$$

where  $\bar{f}$  is the mean relative fluorescence intensity within the bleach region (normalized by the mean fluorescence intensity in an area far from the bleach region),  $F_\infty$  is the equilibrium relative fluorescence intensity within the bleach region,  $s$  is the Laplace variable,  $I_1$  and  $K_1$  are the first-

order modified Bessel functions of the first and second kind, respectively,  $w$  is the radius of the bleach spot,  $k_{on}$  and  $k_{off}$  are the rate constants describing the rate of fluorophore binding to and release from the matrix, respectively,  $D_f$  is the diffusion coefficient of the fluorophore in the absence of binding, and  $D_{eff}$  is the effective diffusion coefficient that accounts for binding effects. To convert this equation from Laplace space to real space as function of time, a numerical Laplace inversion was performed using the Talbot algorithm.<sup>20</sup> Furthermore, when performing fits to the equation, a reduced data set was used to avoid over-fitting data at longer time points. Reduced data sets of roughly equally-spaced points were generated by selecting all data points from the first 10 seconds after bleaching and every third data point after this time interval.

Prior to fitting parameter values for the FRAP model, initial estimates for these values were determined. It was found that if initial parameter values were not close to their best-fit values, the curve fits would either return inaccurate parameter values or errors. First, initial estimates for  $F_\infty$  and  $D_f$  were obtained by fitting the curve to a FRAP model that only accounts for diffusion effects as a function of time  $t$ :<sup>19</sup>

$$f(t) = F_\infty e^{-w^2/2tD_f} \left[ I_0 \left( \frac{w^2}{2tD_f} \right) + I_1 \left( \frac{w^2}{2tD_f} \right) \right], \quad (2-12)$$

where  $I_0$  is the zeroth-order modified Bessel function of the first kind. These initial estimates were then used to fit the full FRAP equation (2-8) while testing fixed parameter values of  $k_{on}$  and  $k_{off}$ . The two rate constant values were independently varied between  $10^{-4}$  and  $10^4$  s<sup>-1</sup> (spaced logarithmically across 30 points), and the pair of these values along with the optimized values for  $F_\infty$  and  $D_f$  were used as the initial estimates in a full fit to equation (2-8) with none of these four parameters held constant. The code, provided in **Appendix A5**, usually required 10-15 minutes to fit a single FRAP curve.

Originally, FRAP curves were fit using equation (2-12) that only accounted for diffusional effects, but it was found that equation was not able to fit the curves well. As such, fits using equation (2-8) that also incorporated binding effects were attempted, and it was found that accounting for these binding effects yielded much better fits to the FRAP curves (**Figure 2-12**). Thus, all FRAP curves were fit using equation (2-12).

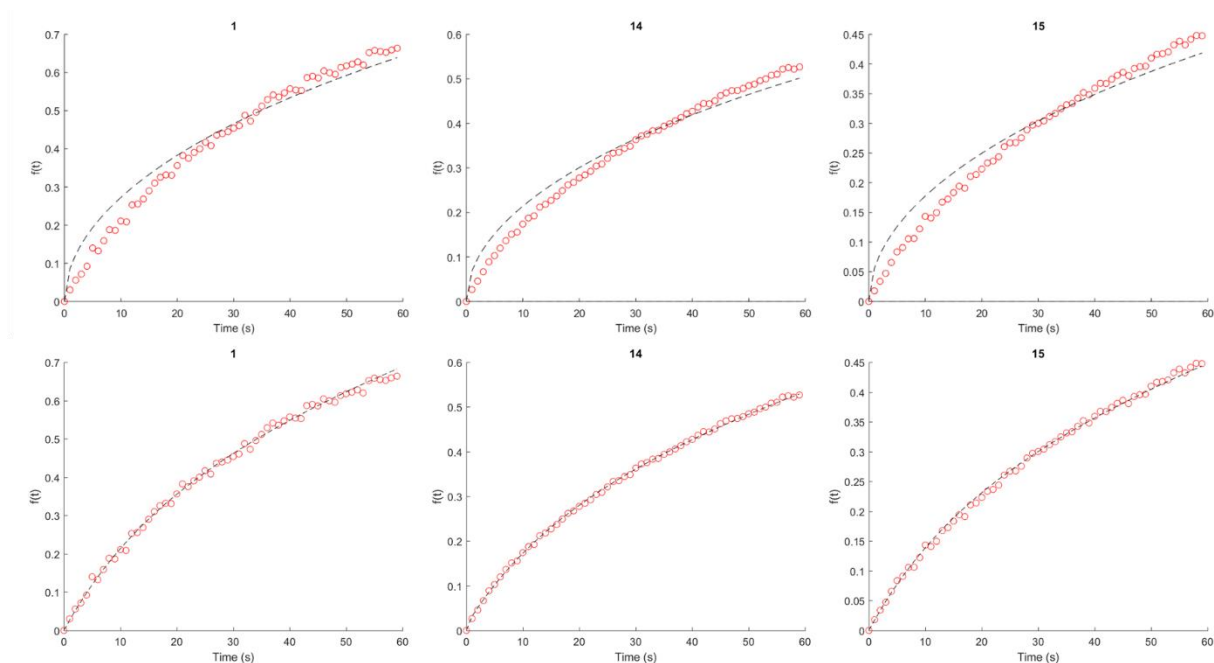


**Figure 2-12.** Comparison of representative fits to FRAP curves using equation (2-12) (top row) and equation (2-8) (bottom row).

### 2.8.4 Biosensor Assays

All binding curves were fit to the following derived equation. Consider a solution of analyte added to a thin film of protein-polymer conjugates. Since the analyte can exist either in solution with concentration  $[A]$  or bound to the protein-polymer conjugate with concentration  $[A-P]$ , a site balance can be written for the total concentration of the analyte  $[A]_T$  as follows:

$$[A] + [A - P] = [A]_T, \quad (2-12)$$

which can be solved for  $[A]$  to yield:

$$[A] = [A]_T - [A - P]. \quad (2-13)$$

The protein-polymer conjugate can also exist in either the unbound state with concentration  $[P]$  or bound to the analyte with concentration  $[A-P]$ , so a site balance can similarly be written for the total concentration of protein-polymer conjugate  $[P]_T$  as follows:

$$[P] + [A - P] = [P]_T, \quad (2-14)$$

which can be solved for  $[P]$  to yield:

$$[P] = [P]_T - [A - P]. \quad (2-15)$$

By assuming the binding between the analyte and protein-polymer conjugate reaches equilibrium, a dissociation constant  $K_d$  can be defined for the binding interaction:

$$K_d = \frac{[A][P]}{[A - P]}. \quad (2-16)$$

Equations (2-13) and (2-15) can be substituted into equation (2-16) and solved for  $[A-P]$  to give the following equation:

$$[A - P] = \frac{([A]_T + [P]_T + K_d) \pm \sqrt{([A]_T + [P]_T + K_d)^2 - 4[A]_T[P]_T}}{2}. \quad (2-17)$$

Since  $[A-P]$  must be less than both  $[A]_T$  and  $[P]_T$ , only the negative root in equation (2-17) gives a physically reasonable solution:

$$[A - P] = \frac{\beta - \sqrt{\beta^2 - 4\gamma}}{2}, \quad (2-18)$$

where  $\beta$  is defined as the sum of  $[A]_T$ ,  $[P]_T$ , and  $K_d$ , and  $\gamma$  is defined as the product of  $[A]_T$  and  $[P]_T$ .

By assuming that the observed mean fluorescent intensity (MFI) from a fluorescent binding assay is proportional to the total number of binding events by some proportionality constant  $\alpha$  such that  $\alpha$  represents the average MFI per binding event, the MFI can be related to  $[A-P]$  by

$\text{MFI} = \alpha[A-P]$ , which can be substituted into equation (2-18) to give:

$$\text{MFI} = \frac{\alpha}{2} \left( \beta - \sqrt{\beta^2 - 4\gamma} \right). \quad (2-19)$$

## 2.9 References

1. Mills, C. E., Elastin-Like Polypeptide (ELP) Tags for Self-Assembly and High-Throughput Processing of Functional Protein Materials. Ph.D. Dissertation, Massachusetts Institute of Technology, Cambridge, MA, 2019.
2. Miller, E. A.; Traxlmayr, M. W.; Shen, J.; Sikes, H. D., Activity-based assessment of an engineered hyperthermophilic protein as a capture agent in paper-based diagnostic tests. *Mol. Syst. Des. Eng.* **2016**, *1* (4), 377-381.
3. Zhang, K.; Diehl, M. R.; Tirrell, D. A., Artificial Polypeptide Scaffold for Protein Immobilization. *J. Am. Chem. Soc.* **2005**, *127* (29), 10136-10137.
4. Kapust, R. B.; Tözsér, J.; Fox, J. D.; Anderson, D. E.; Cherry, S.; Copeland, T. D.; Waugh, D. S., Tobacco etch virus protease: mechanism of autolysis and rational design of stable mutants with wild-type catalytic proficiency. *Protein Eng. Des. Sel.* **2001**, *14* (12), 993-1000.
5. Lam, C. N., Interactions Governing the Self-Assembly of Globular Protein-Polymer Block Copolymers. Ph.D. Dissertation, Massachusetts Institute of Technology, Cambridge, MA, 2019.
6. Thomas, C. S.; Glassman, M. J.; Olsen, B. D., Solid-State Nanostructured Materials from Self-Assembly of a Globular Protein-Polymer Diblock Copolymer. *ACS Nano* **2011**, *5* (7), 5697-5707.
7. Amine-Reactive Probes. Life Technologies Corporation (Thermo Fisher): 2013. <https://assets.thermofisher.com/TFS-Assets/LSG/manuals/mp00143.pdf>.
8. Chang, D.; Huang, A.; Olsen, B. D., Kinetic Effects on Self-Assembly and Function of Protein-Polymer Bioconjugates in Thin Films Prepared by Flow Coating. *Macromol. Rapid Commun.* **2017**, *38* (1), 1600449.
9. Balsara, N. P.; Perahia, D.; Safinya, C. R.; Tirrell, M.; Lodge, T. P., Birefringence detection of the order-to-disorder transition in block copolymer liquids. *Macromolecules* **1992**, *25* (15), 3896-3901.
10. Olsen, B. D.; Segalman, R. A., Phase Transitions in Asymmetric Rod-Coil Block Copolymers. *Macromolecules* **2006**, *39* (20), 7078-7083.
11. Boutris, C.; Chatzi, E. G.; Kiparissides, C., Characterization of the LCST behaviour of aqueous poly(N-isopropylacrylamide) solutions by thermal and cloud point techniques. *Polymer* **1997**, *38* (10), 2567-2570.
12. Greenfield, N. J., Using circular dichroism spectra to estimate protein secondary structure. *Nat. Prot.* **2007**, *1*, 2876.
13. Wei, Y.; Thyparambil, A. A.; Latour, R. A., Protein helical structure determination using CD spectroscopy for solutions with strong background absorbance from 190 to 230nm. *Biochim. Biophys. Acta* **2014**, *1844* (12), 2331-2337.
14. Jackson, D. Y.; King, D. S.; Chmielewski, J.; Singh, S.; Schultz, P. G., General approach to the synthesis of short .alpha.-helical peptides. *J. Am. Chem. Soc.* **1991**, *113* (24), 9391-9392.
15. Krylov, D.; Mikhailenko, I.; Vinson, C., A thermodynamic scale for leucine zipper stability and dimerization specificity: e and g interhelical interactions. *EMBO J.* **1994**, *13* (12), 2849-2861.
16. Schuck, P., Size-Distribution Analysis of Macromolecules by Sedimentation Velocity Ultracentrifugation and Lamm Equation Modeling. *Biophys. J.* **2000**, *78* (3), 1606-1619.
17. Dixit, C. K.; Vashist, S. K.; MacCraith, B. D.; O'Kennedy, R., Multisubstrate-compatible ELISA procedures for rapid and high-sensitivity immunoassays. *Nat. Prot.* **2011**, *6*, 439.

18. Schneider, C. A.; Rasband, W. S.; Eliceiri, K. W., NIH Image to ImageJ: 25 years of image analysis. *Nat. Methods* **2012**, *9*, 671.
19. Sprague, B. L.; Pego, R. L.; Stavreva, D. A.; McNally, J. G., Analysis of Binding Reactions by Fluorescence Recovery after Photobleaching. *Biophys. J.* **2004**, *86* (6), 3473-3495.
20. Abate, J.; Whitt, W., A Unified Framework for Numerically Inverting Laplace Transforms. *INFORMS J. Comput.* **2006**, *18* (4), 408-421.

## **Chapter 3. Improved Ordering in Low Molecular Weight Protein-Polymer Conjugates Through Oligomerization of the Protein Block**

*Reproduced (adapted) with permission from Paloni et al. Biomacromolecules, 19 (9), 3814-3824, (2018). Copyright 2018 American Chemical Society.*

### **3.1 Abstract**

The self-assembly of protein-polymer conjugates incorporating oligomers of a small, engineered high-affinity binding protein, rcSso7d.SA, is studied to determine the effect of protein oligomerization on nanoscale ordering. Oligomerization enables a systematic increase in the protein molar mass without changing its overall folded structure, leading to a higher driving force for self-assembly into well-ordered structures. Though conjugates of monomeric rcSso7d.SA are found to only exist in disordered states, oligomers of this protein linked to a poly(*N*-isopropylacrylamide) (PNIPAM) block self-assemble into lamellar nanostructures. Conjugates of trimeric and tetrameric rcSso7d.SA are observed to produce the strongest ordering in concentrated solution, displaying birefringent lamellae at concentrations as low as 40 wt. %. In highly concentrated solution, the oligomeric rcSso7d.SA-PNIPAM block copolymers exhibit ordering and domain spacing trends atypical from that of most block copolymers. Fluorescent binding assays indicate that oligomerized protein blocks retain binding functionality and exhibit limits of detection up to three times lower than that of surface-immobilized protein sensors. Therefore, oligomerization of the protein block in these block copolymers serves as an effective method to improve both nanoscale ordering and biosensing capabilities.

### **3.2 Introduction**

The highly-specific molecular recognition capabilities of proteins have enabled their widespread use in a variety of biosensor formats including lateral flow assays,<sup>1-4</sup> microfluidics,<sup>5-8</sup> and

microarrays.<sup>9-10</sup> In each of these biosensors, proteins are immobilized on a surface, where device sensitivity is enhanced by achieving densely-packed proteins that are well-oriented to allow free access to binding sites.<sup>11-13</sup> The simplest and most general methods for protein surface functionalization involve covalent anchoring via free amines on the surfaces of proteins. Because these amines are distributed at multiple points across the protein surface, however, the resulting orientation is random, reducing the active proportion of the surface-immobilized binding protein. As such, there is significant interest in developing techniques that enable site-specific immobilization. Current directed immobilization strategies include modifying functional groups that appear at only a single location on a protein,<sup>14-15</sup> adding ssDNA fragment linkers,<sup>16</sup> or fusing to proteins<sup>17-18</sup> and installing tags<sup>19-20</sup> that display high binding affinity to a specific surface. While all of these methods can be used to orient proteins and improve biosensor performance, these approaches can only be used for specific classes of proteins or require significant protein and/or surface pre-treatment.

One potentially straightforward and effective technique for creating a dense array of properly oriented proteins is through utilization of block copolymer-like self-assembly. By conjugating a protein to a polymer and dissolving the bioconjugate in concentrated aqueous solution, it has been demonstrated that these conjugates assemble into ordered nanostructures similar to coil-coil diblock copolymers.<sup>21-23</sup> While the individual ordered phases in both types of diblock copolymers are identical, the self-assembly of protein-polymer conjugates exhibits notable differences from that of traditional block copolymers. Protein-polymer conjugates display highly asymmetric phase behavior<sup>24</sup> and re-entrant order-disorder transition (ODT) behavior,<sup>24-25</sup> in contrast to the enhanced ordering in more concentrated block copolymer solutions predicted by the dilution approximation.<sup>26</sup> A complete explanation for these deviations from characteristic

block copolymer assembly has not yet been established, but it is known that coarse-grained features of the conjugates have significant effects on self-assembly: polymer topology,<sup>27</sup> polymer chemistry,<sup>25</sup> protein shape,<sup>28</sup> and electrostatics<sup>29</sup> have all been found to significantly affect phase behavior and ordering in protein-polymer block copolymers.

Initial studies have been performed on the activity and binding capabilities of enzymatic coatings and sensors developed from these conjugates. Thin films of myoglobin-*b*-poly(*N*-isopropylacrylamide) (PNIPAM) formed weakly-ordered lamellae in solution and exhibited up to a 10-fold improvement in catalytic activity compared to common surface-immobilization techniques.<sup>30</sup> Similar antibody-PNIPAM thin film biosensors displayed a two order of magnitude decrease in the limit of detection compared to an antibody monolayer and a linear relationship between the number of binding events and film thickness, which is related to the total amount of protein in the film.<sup>31</sup> These studies suggest that the increased number of proteins that can be immobilized on a surface in 3D arrays achieved through protein-polymer diblock copolymer self-assembly can greatly enhance protein catalytic and sensing capabilities.

While protein-polymer conjugates incorporating antibodies as the protein block have been shown to function as highly sensitive biosensors, there is a growing trend toward using small proteins as affinity elements in sensors due to their enhanced stability and the ease with which they can be recombinantly expressed. For example, nanobodies—the 12-15 kDa single binding domain of heavy chain-only antibodies—have been incorporated into biosensors to achieve improved sensitivities compared to antibody-based sensors due to the greater surface functionalization achievable with these smaller proteins.<sup>32</sup> This sensitivity improvement is more clearly seen in electrochemical sensors<sup>33-34</sup> where the decreased distance between binding events and the surface has resulted in increased signal strength. Small engineered affinity binding proteins have also

received more frequent use as sensors within the past decade. A class of 6 kDa proteins consisting of a three-helix bundle, affibodies, have been demonstrated to function effectively in microarray formats.<sup>35-36</sup> Similarly, 7 kDa DNA-binding proteins, particularly Sac7d and Sso7d, have been designed to bind with antibody-level affinities to a variety of targets.<sup>37-39</sup> Though their use in biosensors has only recently been explored,<sup>18, 39-40</sup> these engineered DNA-binding protein mutants display exceptional stability over a wide pH and temperature range,<sup>41</sup> making them attractive candidates for sensors that remain functional in conditions under which proteins typically unfold.

There are numerous potential benefits to using small proteins in biosensors fabricated from protein-polymer conjugates, but the weak ordering in these conjugates containing a small protein block remains a barrier to maximizing device sensitivity by self-assembly. In traditional coil-coil block copolymers, ordered phases are only observed when the overall degree of polymerization of the diblock copolymer is large enough to sufficiently reduce the entropic penalty due to chain stretching that occurs at the interfaces between domains. While the self-assembly of protein-polymer block copolymers is not fully understood, similar trends have been observed in these materials. Model studies using the fluorescent protein mCherry as the protein block in these conjugates have found that no ordered structures are observed at low coil fractions ( $0.2 \leq f \leq 0.3$ ),<sup>24</sup> and at intermediate coil fractions ( $0.3 \leq f \leq 0.5$ ), structures are significantly weaker ordered than the corresponding phases at high coil fractions ( $0.5 \leq f \leq 0.75$ ).<sup>24-25</sup> Thus, exploring approaches to increase the molecular weight of the protein block in protein-polymer conjugates may yield methods to create well-ordered structures of these conjugates incorporating a low molecular weight protein.

Herein, the effect of increasing molecular weight of low molecular weight protein blocks on ordering in protein-polymer conjugates is explored using protein blocks incorporating an Sso7d

mutant engineered to bind strongly to streptavidin, rcSso7d.SA.<sup>39</sup> Oligomers of rcSso7d.SA are created by linking the proteins with short, flexible peptide sequences, and the phase behavior of conjugates of these oligomers—monomer to tetramer—with PNIPAM is studied. While conjugates of monomeric rcSso7d.SA are disordered under all conditions studied, conjugates of oligomeric rcSso7d.SA are observed to self-assemble into well-ordered lamellar structures. The biosensing capabilities of these conjugates are also explored, and it is discovered that the trimer conjugates provide over a 3-fold reduction in limit of detection compared to monolayers of rcSso7d.SA.

### **3.3 Materials and Methods**

#### **3.3.1 Synthesis**

Poly(*N*-isopropylacrylamide) (PNIPAM) functionalized with a maleimide group was synthesized by reversible addition-fragmentation chain transfer (RAFT) polymerization, as described previously.<sup>21</sup> Polymer molecular weight and dispersity were characterized by gel permeation chromatography performed on an Agilent 1260 LC system equipped with two columns (ResiPore, 300 × 7.5 mm, up to 500k Da, Agilent Technologies, CA) in series, a Wyatt miniDAWN TREOS multi-angle light scattering detector, and a Wyatt Optilab T-rEX diffractometer (**Figure B-1**). DMF with 0.02 LiBr was used as the mobile phase with a flow rate of 1 mL/min at 70 °C.

Details for the construction of genes for monomeric, dimeric, trimeric, and tetrameric rcSso7d.SA each containing an N-terminal Cys residue are provided in **Chapter 2**. Each gene was inserted into a pET28b(+) vector, which encodes an N-terminal 6xHis tag, and transformed into BL21(de3) *E. coli* cells. Each protein was expressed in 1 L of Terrific Broth at 37 °C inoculated with 5 mL of overnight culture and induced with 1 mM isopropyl- $\beta$ -D-1-thiogalactopyranoside (IPTG) at an OD<sub>600</sub> of 0.8-1.0. After induction the cells were cultured at 20 °C for 18-20 hours and

harvested. The cells were resuspended in lysis buffer (50 mM NaH<sub>2</sub>PO<sub>4</sub>, 300 mM NaCl, 10 mM imidazole, 10 mM β-mercaptoethanol (BME), pH 8.0) and frozen at -80 °C overnight. After thawing, the cells were lysed by ultrasonication. The lysate was clarified by centrifugation, and the protein was purified using Ni-NTA metal affinity chromatography. Throughout the purification, 10 mM BME was used in all buffers. Elution fractions containing purified protein were immediately exchanged into resuspension buffer (50 mM Tris buffer, 100 mM NaCl, 0.25 mM tris(2-carboxyethyl)phosphine (TCEP), pH 7.4) by performing a 1000x buffer exchange in Millipore-Ultra 15 centrifugal filters (molecular weight cutoff of 3 kDa for monomeric rcSso7d.SA or 10 kDa for rcSso7d.SA oligomers). The purity of the protein was confirmed by denaturing gel electrophoresis (SDS-PAGE) (**Figure A-2a**). Protein concentration was determined by performing a reducing-agent compatible BCA assay, and proper secondary structure folding of the proteins was assessed using circular dichroism (CD) (**Figure A-3a**). The typical yields of purified protein for the monomeric, dimeric, trimeric, and tetrameric rcSso7d.SA species were 120, 160, 75, and 40 mg per liter of culture, respectively.

### **3.3.2 Bioconjugation and Preparation of Bulk Samples**

Bioconjugations between rcSso7d.SA oligomers and maleimide-functionalized PNIPAM were performed in resuspension buffer. Solutions of rcSso7d.SA oligomers were diluted to approximately 5 mg/mL, and a 5x molar excess of PNIPAM was added. After complete dissolution of PNIPAM, samples were incubated at 4 °C for 24 h. Ammonium sulfate was then added to a concentration of 1.0 M to remove unconjugated protein. Following centrifugation, the supernatant was discarded and the precipitates were resuspended in resuspension buffer to approximately 5 mg/mL. Two additional ammonium sulfate precipitations were performed, after which the resulting solution was purified by Ni-NTA chromatography to remove unconjugated PNIPAM.

Purified protein-PNIPAM conjugates were dialyzed against MilliQ water. Bioconjugate purity was confirmed using SDS-PAGE and Native PAGE (**Figure A-2b-c**), and retention of protein secondary structure was assessed using CD (**Figure A-3b**). Conjugate solution was concentrated to approximately 100 mg/mL using Millipore-Ultra 15 centrifugal filters (molecular weight cutoff of 10 kDa). Bulk solid samples were prepared by drop-casting aliquots of this concentrated solution onto Teflon sheets and drying under vacuum to a final pressure of 5 Torr (ramp rate 50 Torr/h) at room temperature. Samples were then collected and stored at 4 °C until future use. Typical yields after purification ranged from 50% with monomeric rcSso7d.SA to 25% with tetrameric rcSso7d.SA.

### **3.3.3 Solution-phase Sample Preparation and Characterization**

Dehydrated samples were rehydrated in MilliQ water at 4 °C to the desired concentration immediately prior to use. The concentrated solution phase behavior of rcSso7d.SA-PNIPAM conjugates was characterized using small-angle X-ray scattering (SAXS) (**Figures B-2 to B-5**), depolarized light scattering (DPLS) and turbidimetry (**Figures B-6 to B-9**), and differential scanning calorimetry (DSC) (**Figure B-10**). Details of the sample preparation and measurement conditions for these techniques are provided in **Chapter 2**.

### **3.3.4 Thin Film Preparation**

Silicon wafers (Wafer World, P-type Silicon with boron as dopant, (100) orientation, single-side polished) were cut into 0.9 cm-by-5 cm sections and sequentially and thoroughly rinsed with acetone, methanol, and water. Wafers were then dried under a filtered air flow and treated with oxygen plasma for 3 minutes. Immediately following plasma cleaning, conjugate samples rehydrated to 10 wt.% in MilliQ water were flow coated onto the silicon wafers in a chamber maintained at 60% relative humidity, as described previously.<sup>42</sup> To stabilize thin films against

dissolution in water, the cast films were preheated to 40 °C and immersed in a 1.4 wt.% aqueous solution of glutaraldehyde at 40 °C for 20 s to lightly crosslink the protein nanodomains. Immediately following immersion, thin films were thoroughly rinsed with water until the surfaces became hydrophilic, indicating complete removal of unlinked glutaraldehyde. Films were dried under filtered airflow and stored at ambient conditions until use. Film thickness was determined using a Woolam M-2000D spectroscopic ellipsometer using a single incidence angle of 70°. Curves were fit using a three-layer model consisting of a 0.4 mm bottom silicon substrate, a native silicon oxide layer of 18 Å, and a top conjugate layer fit using a Cauchy model. rcSso7d.SA monolayers were prepared by coupling protein activated by 1-Ethyl-3-(3-dimethylaminopropyl)carbodiimide/N-hydroxysuccinimide (EDC/NHS) with amine-functionalized silicon wafers using literature methods.<sup>43</sup>

### 3.3.5 Fluorescence Assays

The binding function of rcSso7d.SA oligomer-PNIPAM thin films was measured using fluorescently-labeled monomeric streptavidin (mSA2). Details for the expression, purification, and fluorescent labeling of mSA2 are provided in **Chapter 2**. 0.5 µL drops of solutions containing serially diluted fluorescent mSA2 samples in PBS (pH 7.4) were gently applied to the surface of each bioconjugate thin film. Films were incubated in a sealed chamber saturated with water vapor at room temperature to prevent to prevent drying of the applied fluorescent samples. After 1 hour, films were thoroughly rinsed with water, dried under filtered airflow, and immediately analyzed for fluorescent signal. Fluorescence microscopy images were acquired at 4x magnification using a Cy5 filter set and exposure time of 5000 ms on an Olympus IX-81 inverted fluorescence microscope with an AxioCam HRC CCD camera. Fluorescent intensity was calculated using ImageJ software<sup>44</sup> by determining the average fluorescent signal in a rectangular area of the

fluorescent image free of defects and occupying no less than half of the full sample application area.

### 3.4 Results and Discussion

#### 3.4.1 Phase Behavior

Oligomers of rcSso7d.SA, a modified DNA-binding protein designed to exhibit high-affinity streptavidin binding,<sup>39</sup> linked together by flexible (Gly<sub>4</sub>Ser)<sub>2</sub> peptides (**Figure 3-1a**),<sup>46</sup> were expressed and conjugated to poly(*N*-isopropylacrylamide) (PNIPAM) (**Figure 3-1b**). Each oligomer—hereafter referred to as *n*x rcSso7d.SA, where *n* is the number of rcSso7d.SA proteins in the oligomer—was conjugated to PNIPAM of comparable molar mass as the oligomer (**Table 3-1**). A PNIPAM volume fraction could not be calculated for these protein-polymer block copolymers since the molar volume of the protein is not known, so all conjugates were synthesized with symmetric weight fraction, as this is the approximate condition at which optimal ordering has previously been observed in protein-polymer conjugates.<sup>24</sup>

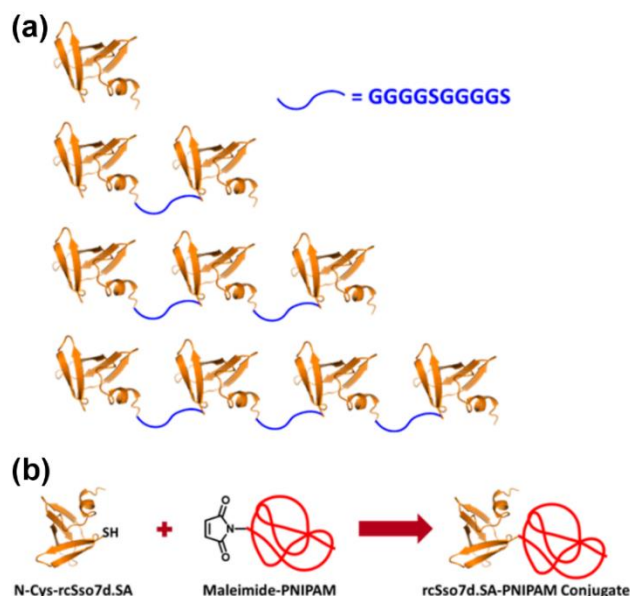


**Figure 3-1.** (a) Representation of rcSso7d.SA oligomers. From top to bottom: 1x rcSso7d.SA, 2x rcSso7d.SA, 3x rcSso7d.SA, 4x rcSso7d.SA. (b) General schematic of N-Cys-rcSso7d.SA oligomer conjugation to maleimide end-functionalized PNIPAM. Protein is a cartoon representation of the Sso7d crystal structure (PDB 1SSO).<sup>45</sup>

**Table 3-1.** Composition of rcSso7d.SA oligomer-PNIPAM Conjugates

Conjugate	Protein	Protein MW (kDa)	PNIPAM M <sub>n</sub> (kDa)	PNIPAM Đ	PNIPAM Weight Fraction
1xSP9.8k	1x rcSso7d.SA	9.4	9.8	1.09	0.51
2xSP17k	2x rcSso7d.SA	17.1	16.8	1.10	0.50
3xSP25k	3x rcSso7d.SA	24.9	24.9	1.10	0.50
4xSP30k	4x rcSso7d.SA	32.5	30.0	1.10	0.48

Analysis of the four studied conjugates in concentrated solution suggests a clear effect of oligomerization (molar mass) on morphology. Phase diagrams are constructed for each conjugate (**Figure 3-2**) using SAXS to determine nanostructure periodicity, DPLS to assess long-range ordering, turbidimetry to determine transitions to macrophase separated states, and DSC to estimate PNIPAM desolvation temperatures (**Table 3-2**). While the conjugates are assumed to exhibit equilibrium morphology under most of the studied conditions, 100 wt. % samples created by drying solutions under vacuum at a controlled pressure ramp rate of 50 Torr/h are known to be kinetically trapped in a weakly-ordered morphology.<sup>24</sup>

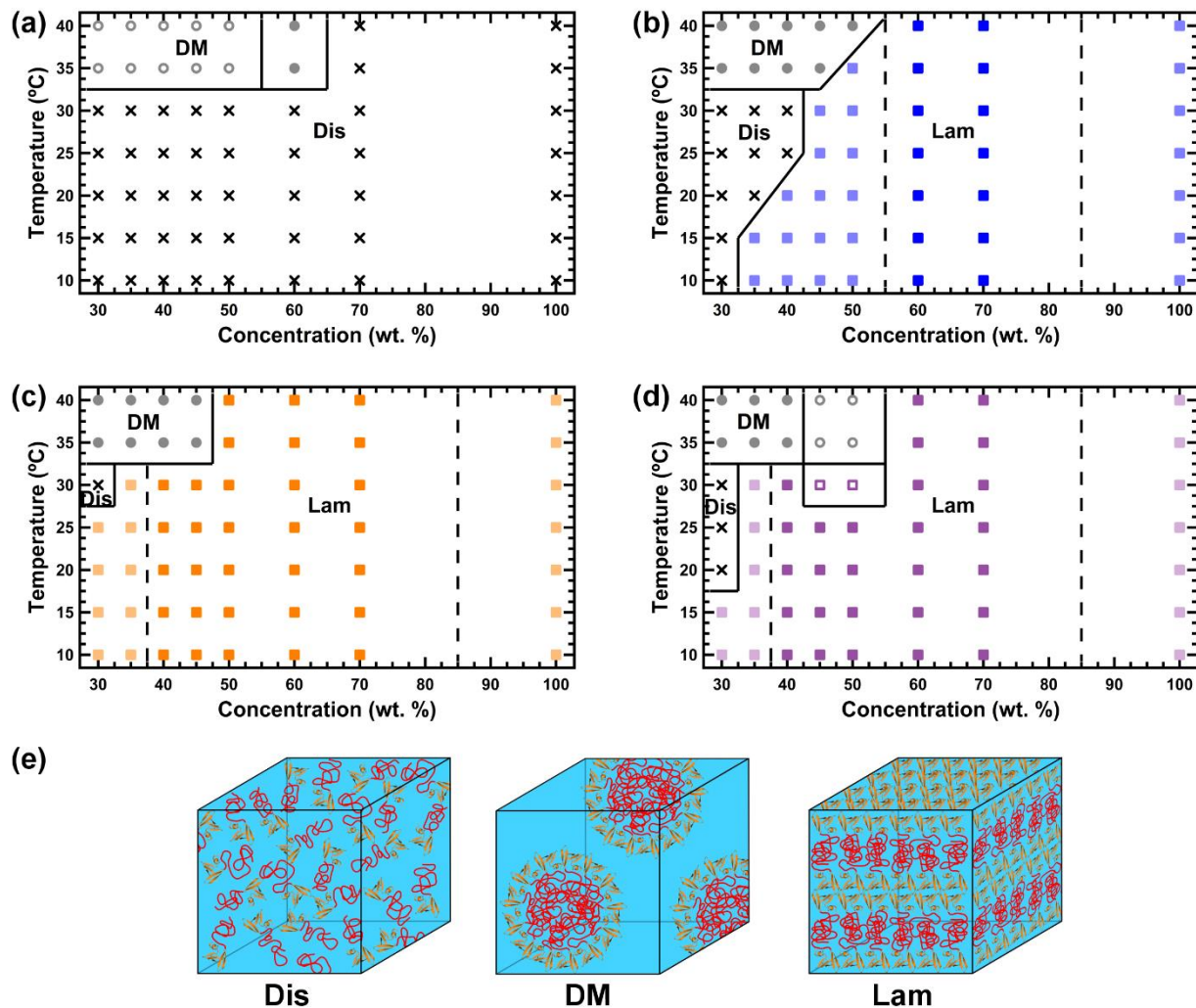


**Figure 3-2.** Phase diagrams of (a) 1xSP9.8k, (b) 2xSP17k, (c) 3xSP25k, and (d) 4xSP30k as a function of concentration and temperature. Phases are assigned in the diagrams as disordered (Dis), disordered micellar (DM), or lamellar (Lam) and are also (e) represented schematically. Light colored symbols represent non-birefringent lamellar phases, which are separated by dashed lines from shaded colored symbols representing birefringent lamellar phases. Solid symbols indicate a homogeneous phase, while open symbols indicate a macrophase-separated phase.

**Table 3-2.** Thermal Transitions for rcSso7d.SA Oligomer-PNIPAM Conjugates in Concentrated Solution

Conjugate	Conc. (wt. %)	$T_{DPLS}^a$ (°C)	$T_t^b$ (°C)	$T_{DSC}^b$ (°C)
1xSP9.8k	30	○	30.1	29.6
	35	○	30.3	29.0
	40	○	30.9	28.5
	45	○	34.2	27.2
	50	○	31.3	25.5
	60	●	--	24.8
	70	○	--	--
2xSP17k	30	○	--	28.7
	35	○	--	28.6
	40	○	--	27.3
	45	○	--	26.1
	50	○	--	25.4
	60	●	--	--
	70	●	--	--
3xSP25k	30	○	--	27.8
	35	○	--	28.4
	40	●	--	28.0
	45	●	--	26.6
	50	●	--	26.1
	60	●	--	23.0
	70	●	--	--
4xSP30k	30	○	--	29.4
	35	○	--	28.3
	40	●	--	27.5
	45	●	26.1	26.0
	50	●	26.7	25.4
	60	●	--	22.1
	70	●	--	--

<sup>a</sup>○ denotes samples that never display birefringent behavior within the studied temperature range. ● denotes samples that remain birefringent throughout the entire studied temperature range. <sup>b</sup>The symbol "--" signifies that no thermal transition is observed at the given concentration.

Conjugates containing oligomerized rcSso7d.SA protein blocks are observed to exhibit well-ordered structures. 1xSP9.8k remains disordered under all studied conditions (**Figure 3-2a**), but all oligomer conjugates display lamellar morphology over a wide concentration range (**Figures 3-2b-d**). The size of disordered regions in the phase diagrams also generally shrinks with increasing molecular weight of the protein block: 2xSP17k remains disordered up to concentrations of 40 wt. %, whereas 3xSP25k and 4xSP30k only display a disordered phase at 30

wt. %. Accordingly, the order-disorder transition concentration ( $C_{ODT}$ ) is decreased for higher-order oligomer conjugates, with values of 45, 35, and  $\leq 30$  wt. % (only concentrations as low as 30 wt. % were studied) for 2xSP17k, 3xSP25k, and 4xSP30k, respectively. Concentration ranges over which birefringent lamellae can be seen follow a similar trend, as the range expands from 60-70 wt. % for 2xSP17k to 40-70 wt. % for 3xSP25k and 4xSP30k.

Despite the significant differences in ordering between the four oligomer conjugates, their phase diagrams contain many similar attributes. At high temperatures where water is selective for the protein block, PNIPAM blocks collapse inward away from a water-rich phase, resulting in the formation of disordered micelles. As can be seen in the SAXS curves (**Figure 3-3a**), increasing temperature results in a gradual decrease in intensity of the scattering peaks corresponding to periodic nanostructures, but above the PNIPAM transition temperature, these peaks are almost entirely replaced by form factor scattering from the micelles. In 1xSP9.8k and 4xSP30k solutions, macrophase separated regions between conjugate-rich and conjugate-poor phases of disordered micelles exist, and these regions always exist above the PNIPAM thermal transition temperature (**Table 3-2**). As concentration increases, the temperature at which this transition to a macrophase separated state occurs also increases, which has been attributed to the ability of the protein domains to accommodate water.<sup>23</sup> Once PNIPAM chains begin to collapse and expel water above their thermal transition temperature, the excess water is initially accommodated through swelling of the protein domains. Above a certain temperature, the excess water can no longer be taken up by the proteins, resulting in the separation of micelles from a water-rich phase. As conjugate concentration increases, more protein is present to accommodate water from collapsed PNIPAM chains, so the macrophase separation transition temperature increases and—at high

concentrations—does not occur below 40 °C, indicating that the water is fully accepted into the protein domains.

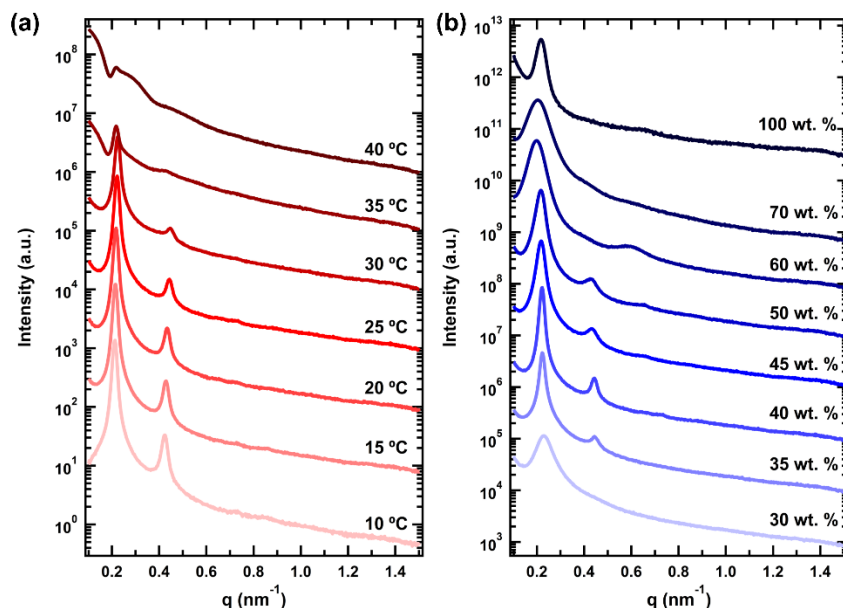


**Figure 3-3.** SAXS curve displaying changes in conjugate phase behavior with (a) temperature and (b) concentration. Both graphs contain data for 4xSP30k at either (a) 40 wt. % or (b) 25 °C and are representative of trends observed across all studied conjugates.

Many similarities also exist between the three conjugates that form ordered phases. Below the thermal transition temperature of PNIPAM where water acts as a good solvent for both blocks, lamellar phases are observed. This strong preference for lamellae is consistent with phase behavior in rod-coil diblock copolymers,<sup>47</sup> which, similar to protein-polymer block copolymers, contain one rigid and one flexible block. Unlike previous work analyzing the self-assembly of protein-PNIPAM conjugates of mCherry and GFP,<sup>28</sup> no hexagonally packed cylinder phase is observed in any of the rcSso7d.SA oligomer conjugates. However, this phase was only seen when PNIPAM represented the minority block in both volume and weight fraction. In this study where only symmetric diblocks were considered, it is likely that the volume fraction of the polymer block is not low enough to thermodynamically favor bending of the protein-polymer interface to form cylindrical nanodomains. Below 45 wt. %, increases in concentration promote the formation of

well-defined lamellar phases (**Figure 3-3b**) with increasing birefringence (**Figures B-6 to B-9**) for 2xSP17k, 3xSP25k, and 4xSP30k. In highly concentrated solutions, though, ordering worsens as peaks significantly broaden, which is suggestive of the re-entrant order-disorder transition (ODT) behavior that has been previously observed in protein-polymer conjugates.<sup>24-25</sup>

DSC measurements of PNIPAM desolvation temperatures reveal clear trends within and across the studied rcSso7d.SA oligomer-PNIPAM conjugates. All four conjugates display decreasing transition temperatures with increasing concentration, consistent with previous findings in protein-polymer conjugates.<sup>23, 28-29</sup> As the molecular weight of the PNIPAM block increases, the transition temperatures at a given concentration also generally decrease. This trend agrees with findings for homopolymer solutions of PNIPAM and other polymers with LCST behavior:<sup>48</sup> as polymer molecular weight increases, the exothermic contribution from polymer solvation decreases relative to the magnitude of the entropic penalty associated with the corresponding decrease in solvent free volume.<sup>49</sup> However, the PNIPAM desolvation temperature appears to be a weaker function of molar mass in the considered block copolymers, presumably a result of both the decreased free volume contribution from chain ends as well as differences in solvent partitioning in block copolymers compared to homopolymer solutions.

### **3.4.2 Ordering Quality**

#### **3.4.2.1 Concentrated Solution**

Increased degree of oligomerization in the protein block of rcSso7d.SA oligomer-PNIPAM conjugates produces a significantly enhanced ordering quality in concentrated solution. This improved ordering is apparent by mere visual inspection of the SAXS curves for each conjugate at the concentration where the strongest ordering is observed at 25 °C (**Figure 3-4a**). While 1xSP9.8k shows a single, broad scattering peak indicative of disordered structure, all three

conjugates containing oligomerized rcSso7d.SA protein blocks display long-range periodic structures, as signified by the presence of higher-order scattering peaks. As the degree of oligomerization of the protein block increases, scattering peaks narrow, and ordering quality improves.

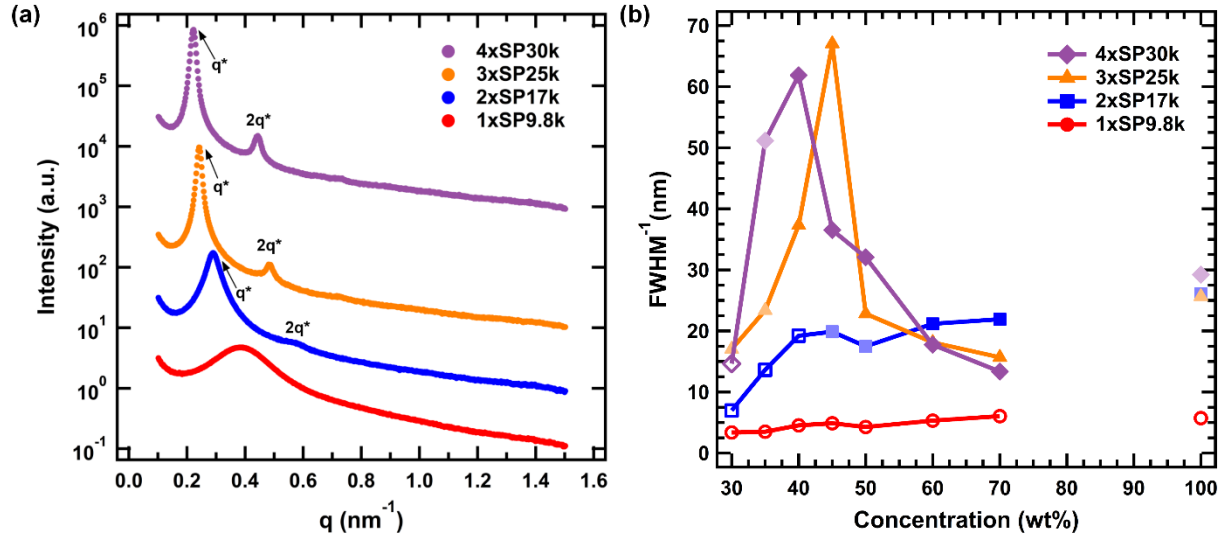


**Figure 3-4.** Ordering quality of rcSso7d.SA oligomer-PNIPAM conjugates indicated through (a) SAXS curves and (b)  $\text{FWHM}^{-1}$  of the primary scattering peak, where greater  $\text{FWHM}^{-1}$  values correspond to stronger ordering. SAXS curves in (a) are each collected at 25 °C, with the curves for 1xSP9.8k, 2xSP17k, and 3xSP25k collected at 45 wt. % and the curve for 4xSP30k collected at 40 wt. %. In graph (b), open symbols represent disordered phases, light symbols represent non-birefringent lamellar phases, and shaded symbols indicate a birefringent lamellar phase. Bulk data are disconnected from concentrated solution data to indicate that the 100 wt. % data are not at equilibrium.

A more quantitative measure of this enriched ordering can be obtained by calculating the full width at half maximum (FWHM) of the primary scattering peak. FWHM were calculated by simultaneously fitting a Lorentzian to the primary scattering peak and a background function to the scattering intensity as follows:

$$I(q) = \{Aq^{-4} + Bq^{-2} + C\} + \left\{ I_0 \left[ \frac{\gamma^2}{(q - q_0)^2 + \gamma^2} \right] \right\}, \quad (3-1)$$

where the first term in braces accounts for background scattering with individual parameters to capture the scattering in the Porod regime, in the Guinier regime, and from a constant background,

and the second term in braces represent the Lorentzian fit where  $I_0$  is the peak height,  $q_0$  is the peak position, and  $2\gamma$  is the FWHM. In **Figure 3-4b**, where  $\text{FWHM}^{-1}$  values are plotted so greater values correspond to stronger ordering, oligomerization of rcSso7d.SA can be seen to result in significantly larger  $\text{FWHM}^{-1}$  values. Again, ordering increases with degree of oligomerization of the protein block, with 3xSP25k and 4xSP30k conjugates displaying highly-ordered structures between 40 and 45 wt. %. At concentrations less than 60 wt. %, the  $\text{FWHM}^{-1}$  value also serves as a very good indicator of phase behavior in these four studied conjugates. For  $\text{FWHM}^{-1}$  less than 18 nm, conjugates almost exclusively form disordered phases, for  $\text{FWHM}^{-1}$  between 18 and 23 nm, primarily non-birefringent lamellae are observed, and for  $\text{FWHM}^{-1}$  greater than 23 nm, conjugates self-assemble into birefringent lamellae. At and above 60 wt. %, however, these phase predictions fail, as all lamellae not in the bulk state are birefringent. This is expected based on previous studies where the materials are shown to transition into a nematic phase as concentration increases out of the lamellar region.<sup>25</sup>

#### 3.4.2.2 Highly Concentrated Solution

Phase behavior in highly concentrated solutions (classified here as concentrations greater than or equal to 60 wt. %) deviates significantly from that at lower concentrations. At and above 60 wt. %, 3xSP25k and 4xSP30k conjugates experience a drop in  $\text{FWHM}^{-1}$  from lower concentrations, suggesting a disordering of lamellar nanophases (**Figure 3-4b**). This observation is in stark contrast to typical phase behavior in concentrated block copolymer solutions, where ordering is predicted<sup>26</sup> and observed<sup>50-51</sup> to strictly increase as a function of concentration, regardless of solvent selectivity. Though uncommon, this type of disordering has previously been observed in block copolymer solutions, typically as re-entrant ODT phase behavior. In polystyrene-*b*-polyisoprene (PS-PI) diblock copolymers in diethyl phthalate, a strongly selective solvent for PS,

a thermotropic re-entrant ODT has been observed at low polymer concentration ( $\phi = 0.2$ ), where heating causes phase changes from a disordered micellar phase to FCC-arranged micelles and finally to a disordered phase.<sup>52</sup> A lyotropic re-entrant ODT has also been documented in PS-PI solutions in decane (selective for PI) between 10 and 16 wt. % as a BCC phase composed of PS-PI micelles disorders then re-forms the BCC phase.<sup>53</sup> In this latter system, the odd phase behavior has been postulated to be a non-equilibrium effect that results from kinetic trapping of the micelles as the cores become glassy.<sup>51</sup> Re-entrant ODT behavior has been observed in previously-studied protein-polymer conjugates at high concentration as well,<sup>24-25</sup> for which it has been hypothesized that protein-polymer interactions become net attractive at high concentration.<sup>25</sup>

In this study, domain spacing analysis also reveals atypical behavior for block copolymers in highly concentrated solutions. For diblock copolymer solutions, domain spacing analysis can be performed to reveal the selectivity of a solvent towards each block through a power law relationship: domain spacing  $d$  scales with polymer volume fraction  $\phi$  according to  $d \sim \phi^{-\beta}$ , where the value of exponent  $\beta$  is indicative of solvent selectivity.<sup>54</sup> In general for nonselective and weakly selective solvents,  $\beta$  is negative, and domain spacing increases with polymer volume fraction as the solvent slightly preferentially migrates to the interfaces between phases to screen unfavorable interactions between the two blocks.<sup>54-55</sup> Conversely, for strongly selective solvents  $\beta$  becomes positive—as high as unity—as one phase swells with added solvent to minimize interfacial area and therefore unfavorable solvent interactions with the insoluble block. Previously, water has been found to be slightly selective for the PNIPAM block in protein-PNIPAM conjugates,<sup>23</sup> and—accordingly—lamellar domain spacing increases with concentration at relatively low concentrations in the rcSSo7d.SA oligomer conjugates considered here (**Figure 3-5a**). However, in highly concentrated solution, the domain spacing of all lamellae-forming conjugates decreases

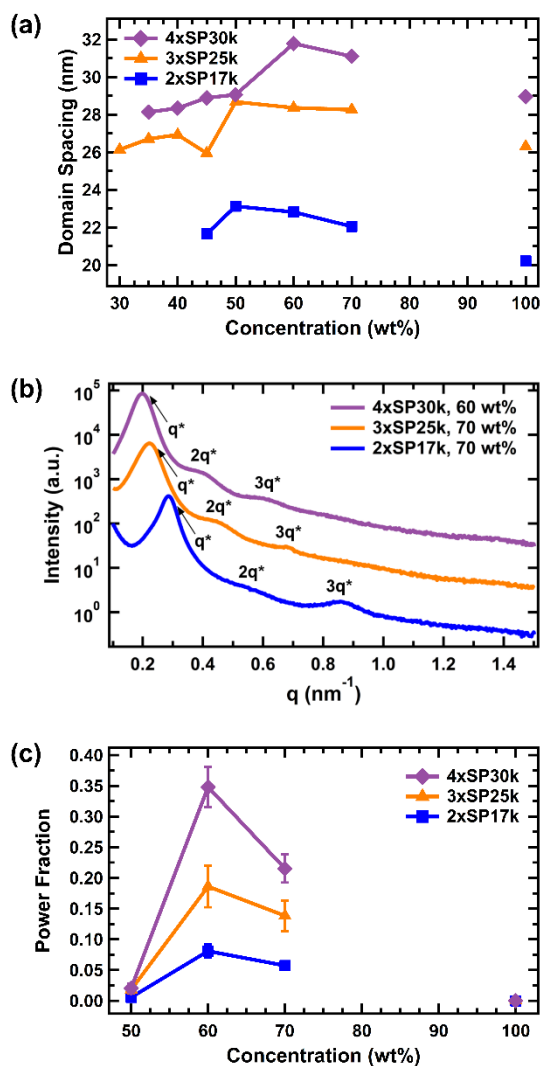


**Figure 3-5.** (a) Domain spacings in lamellar phases, (b) high concentration SAXS traces, and (c) average power fraction across heating and cooling cycles for 2xSP17k, 3xSP25k, and 4xSP30. Data in (a) and (b) are collected at 25 °C, and bulk data are disconnected from concentrated solution data to indicate that the 100 wt. % data are not at equilibrium. In (b) the low intensity of the  $2q^*$  peak in the 2xSP17k scattering pattern is likely a result of a coincidence with a minimum in the form factor. Error bars in (c) represent standard deviation of the data set.

with increasing concentration, seemingly suggesting that water becomes a selective solvent at high concentration.

Similar domain spacing behavior has previously been observed in highly concentrated PS-PI solutions in toluene (a nonselective solvent) near room temperature,<sup>56-57</sup> for which it was proposed that the decrease in domain spacing resulted primarily from chain swelling effects due to reduced mobility of the polymer chains under these conditions. When incubated at room temperature, the conjugates in this study do in fact show a slight improvement in ordering as incubation time is increased (**Figure B-11**). While the results here display qualitative agreement with this theory, the PS-PI systems exhibited a continuous change in domain spacing across all compositions whereas the rcSso7d.SA oligomer-PNIPAM conjugates all contain a discontinuity between the regions of increasing and decreasing domain spacing. Thus, even if similar kinetic control of domain spacing is occurring in the studied systems, additional features of the

conjugates beyond chain swelling appear to also have a significant effect on the self-assembly dynamics, such as the hydrophobic interaction between PNIPAM and protein.<sup>58-60</sup> At high concentrations, these hydrophobic interactions may become relevant, resulting in an attractive force between PNIPAM and protein blocks that decreases domain spacing and disorders lamellar phases.

The long-range ordering of highly concentrated solutions of the studied bioconjugates exhibits key differences from that at lower concentrations. All lamellae-forming conjugates display  $q^*$  reflections up to  $3q^*$  at concentrations at and above 60 wt. % (**Figure 3-5b**) while only reflections up to  $2q^*$  are observed at lower concentrations, indicating retention of lamellar ordering over longer length scales at higher concentration—at least within small grains. Birefringence signals also display substantial increases between 50 wt. % and 60 wt. % in these conjugates (**Figure 3-5c**). It is unlikely that these jumps in birefringence correspond to an improvement in long-range lamellar ordering, however, as 2xSP17k and 3xSP25k bulk samples also display lamellar reflections up to  $3q^*$  (**Figures B-3 to B-4**) but are not birefringent (**Figure 3-5c**). Indeed, even the 1xSP9.8k conjugates display a weak birefringent signal at 60 wt. % (**Table 3-2, Figure B-6f**) despite being highly disordered at this concentration. Instead, the increased birefringence signal is presumably a result of orientational ordering within the sample, similar to the nematic ordering previously observed at 70 and 80 wt. % in mCherry protein-polymer conjugates.<sup>25</sup>

### 3.4.3 Biosensing Capabilities

To confirm the sensing capabilities of rcSso7d.SA in oligomerized states, binding assays were performed. It has previously been demonstrated that protein-polymer block copolymers display size-exclusion properties in which molecular diffusion into the conjugates is controlled by diffusion through the polymer nanodomains, as only molecules of sufficiently lower molecular

weight than the polymer block can diffuse into the matrix.<sup>31</sup> Correspondingly, diffusion experiments using streptavidin—the biomolecule which rcSso7d.SA was genetically modified to bind—as the analyte displayed weak binding strength relative to an rcSso7d.SA monolayer (**Figure B-12**). It was reasoned that due to the large molar mass of streptavidin (53 kDa), very large (~100 kDa) PNIPAM molecules would need to be synthesized and conjugated to the rcSso7d.SA oligomers to permit free diffusion. With a much higher polymer weight fraction, conjugates of these high- $M_n$  PNIPAM molecules would represent a significant departure in ordering behavior from the symmetric weight fraction conjugates studied here. Because streptavidin is a tetrameric species, it was assumed that a smaller, monomeric streptavidin variant (14 kDa) would display only a slightly weaker binding strength to rcSso7d.SA due to the lack of multivalent binding effects<sup>61-62</sup> but experience little resistance to diffusion even in low molecular weight PNIPAM blocks. Thus, a monomeric form of streptavidin, mSA2,<sup>63</sup> was selected as the analyte for assays.

Binding assays were performed by adding serially diluted solutions of fluorescently-labeled mSA2 to thin films of each studied conjugate (**Figure 3-6a**). To maintain consistent transport properties between samples, each oligomer was conjugated to the same previously-synthesized 25 kDa PNIPAM sample. Analyte bound to thin films was quantified using fluorescence microscopy, and binding curves were fit to the collected mean fluorescent intensity (MFI) data using the following equation:

$$\text{MFI} = \frac{\alpha}{2} \left( \beta - \sqrt{\beta^2 - 4\gamma} \right), \quad (3-2)$$

where  $\alpha$  is the average MFI per binding event,  $\beta$  represents the sum of the total concentration of analyte molecules, total concentration of binding sites, and dissociation constant describing the

binding equilibrium, and  $\gamma$  is the product of two aforementioned concentrations. A derivation of this equation is provided in **Chapter 2**.

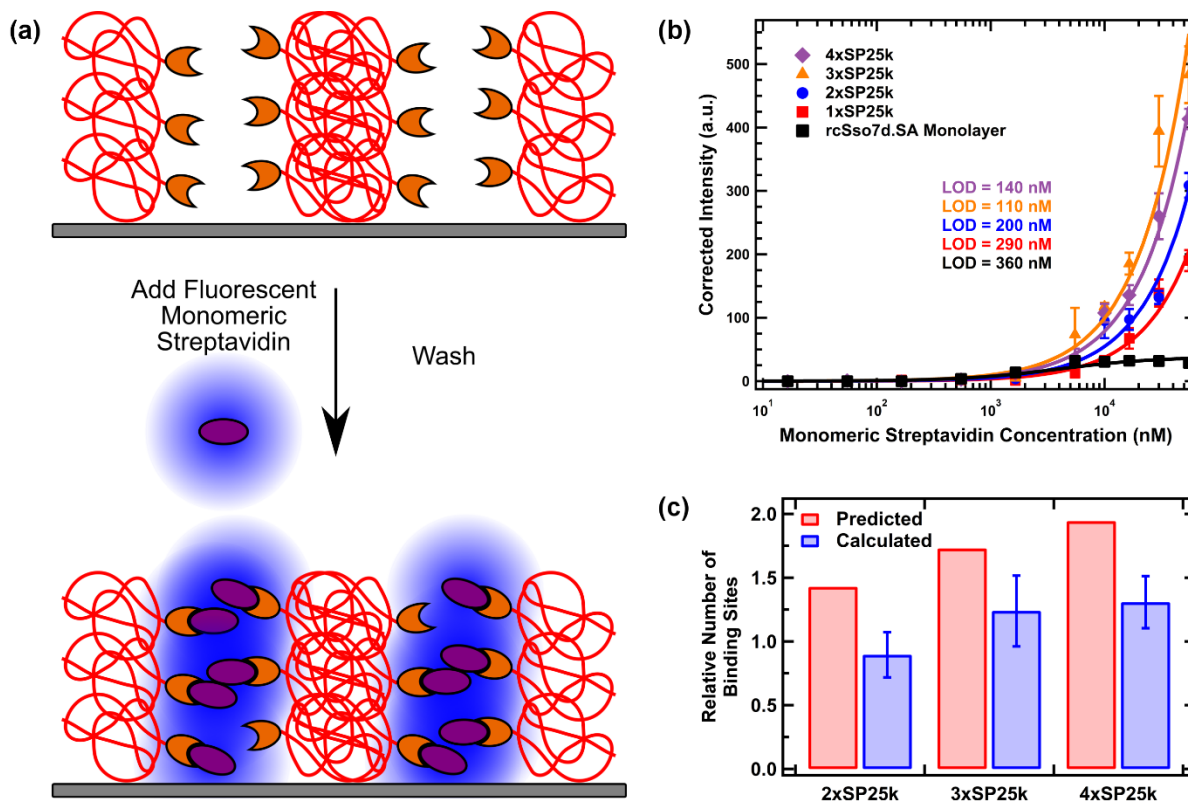


**Figure 3-6.** (a) Schematic representation of fluorescent binding assays performed within rcSso7d.SA oligomer-PNIPAM conjugate thin films. (b) Comparison of binding curves obtained for each considered conjugate and rcSso7d.SA monolayer. All curves are shifted to a background signal of 0 for clarity. Thicknesses for the 1xSP9.8k, 2xSP17k, 3xSP25k, and 4xSP30k films are 155, 130, 150, and 170 nm, respectively. Error bars represent the standard deviation of three replicates. (c) Predicted and calculated relative number of binding sites in each conjugate thin film. All values are relative to the number of binding sites in the 1xSP9.8k thin film. Error bars represent 95% confidence intervals for the calculated relative number of binding sites.

Curve fits performed on the binding assay data gave reasonable parameter values. Each fit yielded the same  $\alpha$  value—which should be independent of sensor type—within the parameter uncertainty, demonstrating good self-consistency of the model. All thin film sensors also gave values for the total concentration of accessible binding sites  $[P]_T$  significantly greater than that for the monolayer, as expected due to the greater thickness and thus total protein present in the thin films. Dissociation constant  $K_d$  values for the conjugate thin film biosensors, however, are

unreasonably large. These extremely high values likely result from the apparent rightward shift in fluorescent intensity values compared to the monolayer; since the  $K_d$  parameter is the only parameter in the used model that can significantly control left/right movement of the binding curve, this value presumably increased to accommodate the shift. As such, the  $K_d$  values reported for the thin film biosensors should be interpreted as fitting parameters only, as the values are not physically reasonable. Though it leads to inflated  $K_d$  values, the rightward shift of the binding curve in the thin film samples is consistent with behavior previously observed when increasing the concentration of binding sites within a protein biosensor.<sup>18</sup>

**Table 3-3.** Best-fit Parameter Values for Fits to Monomeric Streptavidin Binding Assays

Biosensor	$\alpha^a$ (MFI)	$[P]_{T^a}$ (nM)	$K_d^a$ (nM)
rcSso7d.SA Monolayer	100 ± 10	0.34 ± 0.05	2000 ± 1000
1xSP25k Thin Film	100 ± 10	3100 ± 400	$8 \times 10^7 \pm 1 \times 10^7$
2xSP25k Thin Film	100 ± 10	3300 ± 500	$6.0 \times 10^7 \pm 9 \times 10^6$
3xSP25k Thin Film	120 ± 20	3900 ± 700	$4.7 \times 10^7 \pm 9 \times 10^6$
4xSP25k Thin Film	112 ± 9	3700 ± 300	$5.2 \times 10^7 \pm 4 \times 10^6$

<sup>a</sup>Reported errors represent 95% confidence intervals for the parameter estimate.

Analysis of binding curves indicates that rcSso7d.SA oligomer conjugates not only retain binding capacity, but also significantly enhance rcSso7d.SA biosensing capabilities (**Figure 3-6b**). All conjugate samples show increased fluorescent signal at high concentration relative to a rcSso7d.SA monolayer, with the conjugate of the trimer displaying an improvement of over an order of magnitude at the highest measured concentration. Additionally, while the fluorescent intensity of the monolayer saturates for concentrations above 5  $\mu$ M, all thin film samples show continually increasing signal at high analyte concentrations. Unlike the monolayer, the thin film samples contain densely-packed proteins in three-dimensions, thereby providing substantially more binding sites within the sensor and allowing distinction between a greater range of analyte concentrations before saturating. All binding curves are also considerably right-shifted compared to previously-reported curves for rcSso7d.SA in yeast-display experiments ( $K_d \sim 500$  pM),<sup>39</sup>

though the presence of an equivalent shift in the monolayer binding curve indicates that the weaker binding is not a result of inherently worse binding kinetics within the conjugate thin films. The monolayer curve does, however, indicate similar binding strength compared to previous surface-immobilized rcSso7d.SA assays using streptavidin as the analyte,<sup>18, 39</sup> indicating that rcSso7d.SA has similar binding affinities for streptavidin and mSA2.

Oligomerization of rcSso7d.SA also brings about a decrease in biosensor limit of detection (LOD). By calculating LOD using the standard definition as the minimum concentration which gives a signal three standard deviations above that of the average blank, it is found that the LODs for the monolayer and 1xSP25k, 2xSP25k, 3xSP25k, and 4xSP25k thin films are 360, 290, 200, 110, and 140 nM, respectively. While all thin films display improvements up to threefold in LOD over the monolayer, the trend in LOD with respect to degree of oligomerization is non-monotonic. The primary factor that is expected to affect LOD in the studied biosensors is number of binding sites, as more binding sites enable a greater number of analyte molecules to be captured and shifts analyte-receptor equilibrium in favor of binding events. Since the number of binding sites is a function of both the density of accessible rcSso7d.SA proteins within a plane parallel to the underlying substrate and the number of these planes within a biosensor, both rcSso7d.SA volume fraction and film thickness are required to determine the number of these sites.

Calculation of the number of binding sites reveals a significant increase in both number and density of available sites in conjugate thin films relative to rcSso7d.SA monolayers. To determine the density of binding proteins within a single plane of each thin film, the concentration of accessible binding sites throughout the entire film—taken directly from the binding assay curve fits (**Table 3-3**)—was multiplied by the corresponding film thickness. When accounting for differences in film thickness, the density of oligomerized rcSso7d.SA proteins capable of binding

mSA2 is found to increase monotonically with degree of oligomerization (**Table B-1**). This calculated density decreases, though, between the 1xSP25k and 2xSP25k thin films, indicating a lower density of accessible binding sites in the protein domains of the oligomerized rcSso7d.SA conjugate film. The total number of predicted binding sites within each thin film assuming complete accessibility should be proportional to the volume fraction of rcSso7d.SA in the conjugate with PNIPAM. Reasonable estimates for relative values of the predicted number of sites can thus be obtained by normalizing the weight fraction of rcSso7d.SA in each conjugate by the corresponding weight fraction in 1xSP25k. Comparing these predicted relative number of binding sites to the calculated values (**Figure 3-6c**), all oligomeric rcSso7d.SA conjugates are found to contain fewer proteins capable of binding mSA2 than predicted. It is likely that this effect results from a combination of steric blocking of binding sites by bound mSA2 molecules as well as an absence of the free volume required to incorporate mSA2 molecules into the protein nanodomains at high degrees of binding. Despite the lower than expected binding capacity of the conjugate thin films, these biosensors contain approximately  $10^4$  times the quantity of accessible binding sites compared to rcSso7d.SA monolayers on a volumetric basis (**Table 3-3**). Recognizing that each plane (and a monolayer) of rcSso7d.SA proteins is roughly 1-2 nm thick,<sup>64</sup> the studied thin films can be determined to contain approximately 100 more planes of protein than a monolayer. Therefore, by accounting for differences in height between the thin films and monolayers, the thin films are found to contain around 2 orders of magnitude more moles of accessible protein per area, offering a significant improvement in protein density over traditional surface-immobilized protein biosensors.

### 3.5 Conclusions

The oligomerization of the low molecular weight protein rcSso7d.SA in protein-polymer conjugates is demonstrated to significantly improve the concentrated solution self-assembly in these materials. Block copolymers containing oligomerized rcSso7d.SA connected with flexible peptide sequences as a protein block display long-range lamellar ordering that is strongest in trimer and tetramer conjugates. In highly concentrated solution, the studied conjugates assemble into weakly-ordered lamellae and display domain spacings that vary non-monotonically across the studied concentration range.

Thin films of the rcSso7d.SA oligomer conjugates are also found to function as highly sensitive biosensors, retaining binding capabilities and providing up to threefold decreases in limit of detection compared to traditionally-used protein monolayers. In general, oligomerization is observed to lower the limit of detection by increasing density of binding sites, but some evidence suggests too high protein densities result in inaccessibility of some sites. Despite not containing fully-accessible binding sites, the protein-polymer conjugate thin film biosensors are estimated to contain a 100-fold greater density of accessible sites within a single plane of conjugates than an rcSso7d.SA monolayer. By identifying a strategy that both improves ordering in low molecular weight protein-polymer conjugates and enables the development of more sensitive biosensors, this work provides a substantial framework for future research in protein design for both fundamental understanding of protein-polymer conjugate self-assembly and biosensing applications.

### 3.6 References

1. Bahadır, E. B.; Sezgentürk, M. K., Lateral flow assays: Principles, designs and labels. *TrAC, Trends Anal. Chem.* **2016**, *82*, 286-306, DOI: 10.1016/j.trac.2016.06.006
2. Li, J.; Macdonald, J., Multiplexed lateral flow biosensors: Technological advances for radically improving point-of-care diagnoses. *Biosens. Bioelectron.* **2016**, *83*, 177-192, DOI: 10.1016/j.bios.2016.04.021

3. Quesada-González, D.; Merkoçi, A., Nanoparticle-based lateral flow biosensors. *Biosens. Bioelectron.* **2015**, *73*, 47-63, DOI: 10.1016/j.bios.2015.05.050
4. Sajid, M.; Kawde, A.-N.; Daud, M., Designs, formats and applications of lateral flow assay: A literature review. *J. Saudi Chem. Soc.* **2015**, *19* (6), 689-705, DOI: 10.1016/j.jscs.2014.09.001
5. Yetisen, A. K.; Akram, M. S.; Lowe, C. R., Paper-based microfluidic point-of-care diagnostic devices. *Lab Chip* **2013**, *13* (12), 2210-2251, DOI: 10.1039/C3LC50169H
6. Yang, H.; Gijs, M. A. M., Micro-optics for microfluidic analytical applications. *Chem. Soc. Rev.* **2018**, *47* (4), 1391-1458, DOI: 10.1039/C5CS00649J
7. Myers, F. B.; Lee, L. P., Innovations in optical microfluidic technologies for point-of-care diagnostics. *Lab Chip* **2008**, *8* (12), 2015-2031, DOI: 10.1039/B812343H
8. Kim, D.; Herr, A. E., Protein immobilization techniques for microfluidic assays. *Biomicrofluidics* **2013**, *7* (4), 041501, DOI: 10.1063/1.4816934
9. Ling, M. M.; Ricks, C.; Lea, P., Multiplexing molecular diagnostics and immunoassays using emerging microarray technologies. *Expert Rev. Mol. Diagn.* **2007**, *7* (1), 87-98, DOI: 10.1586/14737159.7.1.87
10. Chandra, P. E.; Sokolove, J.; Hipp, B. G.; Lindstrom, T. M.; Elder, J. T.; Reveille, J. D.; Eberl, H.; Klaus, U.; Robinson, W. H., Novel multiplex technology for diagnostic characterization of rheumatoid arthritis. *Arthrit. Res. Ther.* **2011**, *13* (3), R102, DOI: 10.1186/ar3383
11. Cracknell, J. A.; Vincent, K. A.; Armstrong, F. A., Enzymes as Working or Inspirational Electrocatalysts for Fuel Cells and Electrolysis. *Chem. Rev.* **2008**, *108* (7), 2439-2461, DOI: 10.1021/cr0680639
12. Makaraviciute, A.; Ramanaviciene, A., Site-directed antibody immobilization techniques for immunosensors. *Biosens. Bioelectron.* **2013**, *50* (Supplement C), 460-471, DOI: 10.1016/j.bios.2013.06.060
13. Squires, T. M.; Messinger, R. J.; Manalis, S. R., Making it stick: convection, reaction and diffusion in surface-based biosensors. *Nat. Biotechnol.* **2008**, *26* (4), 417-426, DOI: 10.1038/nbt1388
14. Ho, J.-a. A.; Hsu, W.-L.; Liao, W.-C.; Chiu, J.-K.; Chen, M.-L.; Chang, H.-C.; Li, C.-C., Ultrasensitive electrochemical detection of biotin using electrically addressable site-oriented antibody immobilization approach via aminophenyl boronic acid. *Biosens. Bioelectron.* **2010**, *26* (3), 1021-1027, DOI: 10.1016/j.bios.2010.08.048
15. Peluso, P.; Wilson, D. S.; Do, D.; Tran, H.; Venkatasubbaiah, M.; Quincy, D.; Heidecker, B.; Poindexter, K.; Tolani, N.; Phelan, M.; Witte, K.; Jung, L. S.; Wagner, P.; Nock, S., Optimizing antibody immobilization strategies for the construction of protein microarrays. *Anal. Biochem.* **2003**, *312* (2), 113-124, DOI: 10.1016/S0003-2697(02)00442-6
16. Boozer, C.; Ladd, J.; Chen, S.; Jiang, S., DNA-Directed Protein Immobilization for Simultaneous Detection of Multiple Analytes by Surface Plasmon Resonance Biosensor. *Anal. Chem.* **2006**, *78* (5), 1515-1519, DOI: 10.1021/ac051923l
17. Naal, Z.; Park, J. H.; Bernhard, S.; Shapleigh, J. P.; Batt, C. A.; Abruña, H. D., Amperometric TNT Biosensor Based on the Oriented Immobilization of a Nitroreductase Maltose Binding Protein Fusion. *Anal. Chem.* **2002**, *74* (1), 140-148, DOI: 10.1021/ac010596o
18. Miller, E. A.; Baniya, S.; Osorio, D.; Al Maalouf, Y. J.; Sikes, H. D., Paper-based diagnostics in the antigen-depletion regime: High-density immobilization of rcSso7d-cellulose-

- binding domain fusion proteins for efficient target capture. *Biosens. Bioelectron.* **2018**, *102*, 456-463, DOI: 10.1016/j.bios.2017.11.050
19. Sinem, E.; Dagmar, F.; Doris, W.; Ljiljana, F., SNAP-tag as a Tool for Surface Immobilization. *Curr. Pharm. Des.* **2013**, *19* (30), 5443-5448, DOI: 10.2174/1381612811319300015
20. Wasserberg, D.; Cabanas-Danés, J.; Prangmsma, J.; O'Mahony, S.; Cazade, P.-A.; Tromp, E.; Blum, C.; Thompson, D.; Huskens, J.; Subramaniam, V.; Jonkheijm, P., Controlling Protein Surface Orientation by Strategic Placement of Oligo-Histidine Tags. *ACS Nano* **2017**, *11* (9), 9068-9083, DOI: 10.1021/acsnano.7b03717
21. Thomas, C. S.; Glassman, M. J.; Olsen, B. D., Solid-State Nanostructured Materials from Self-Assembly of a Globular Protein–Polymer Diblock Copolymer. *ACS Nano* **2011**, *5* (7), 5697-5707, DOI: 10.1021/nn2013673
22. Thomas, C. S.; Xu, L.; Olsen, B. D., Kinetically Controlled Nanostructure Formation in Self-Assembled Globular Protein–Polymer Diblock Copolymers. *Biomacromolecules* **2012**, *13* (9), 2781-2792, DOI: 10.1021/bm300763x
23. Lam, C. N.; Olsen, B. D., Phase transitions in concentrated solution self-assembly of globular protein-polymer block copolymers. *Soft Matter* **2013**, *9* (8), 2393-2402, DOI: 10.1039/C2SM27459K
24. Thomas, C. S.; Olsen, B. D., Coil fraction-dependent phase behaviour of a model globular protein-polymer diblock copolymer. *Soft Matter* **2014**, *10* (17), 3093-3102, DOI: 10.1039/C3SM52531G
25. Chang, D.; Lam, C. N.; Tang, S.; Olsen, B. D., Effect of polymer chemistry on globular protein-polymer block copolymer self-assembly. *Polymer Chemistry* **2014**, *5* (17), 4884-4895, DOI: 10.1039/C4PY00448E
26. Huang, C.-I.; Lodge, T. P., Self-Consistent Calculations of Block Copolymer Solution Phase Behavior. *Macromolecules* **1998**, *31* (11), 3556-3565, DOI: 10.1021/ma980007p
27. Qin, G.; Glassman, M. J.; Lam, C. N.; Chang, D.; Schaible, E.; Hexemer, A.; Olsen, B. D., Topological Effects on Globular Protein-ELP Fusion Block Copolymer Self-Assembly. *Adv. Funct. Mater.* **2015**, *25* (5), 729-738, DOI: 10.1002/adfm.201403453
28. Lam, C. N.; Kim, M.; Thomas, C. S.; Chang, D.; Sanoja, G. E.; Okwara, C. U.; Olsen, B. D., The Nature of Protein Interactions Governing Globular Protein–Polymer Block Copolymer Self-Assembly. *Biomacromolecules* **2014**, *15* (4), 1248-1258, DOI: 10.1021/bm401817p
29. Lam, C. N.; Yao, H.; Olsen, B. D., The Effect of Protein Electrostatic Interactions on Globular Protein–Polymer Block Copolymer Self-Assembly. *Biomacromolecules* **2016**, *17* (9), 2820-2829, DOI: 10.1021/acs.biomac.6b00522
30. Huang, A.; Qin, G.; Olsen, B. D., Highly Active Biocatalytic Coatings from Protein–Polymer Diblock Copolymers. *ACS Appl. Mater. Interfaces* **2015**, *7* (27), 14660-14669, DOI: 10.1021/acsami.5b01884
31. Dong, X. H.; Obermeyer, A. C.; Olsen, B. D., Three-Dimensional Ordered Antibody Arrays Through Self-Assembly of Antibody–Polymer Conjugates. *Angew. Chem. Int. Ed.* **2017**, *56* (5), 1273-1277, DOI: 10.1002/anie.201607085
32. Hassanzadeh-Ghassabeh, G.; Devoogdt, N.; Pauw, P. D.; Vincke, C.; Muyldermans, S., Nanobodies and their potential applications. *Nanomedicine* **2013**, *8* (6), 1013-1026, DOI: 10.2217/nmm.13.86
33. Wang, H.; Li, G.; Zhang, Y.; Zhu, M.; Ma, H.; Du, B.; Wei, Q.; Wan, Y., Nanobody-Based Electrochemical Immunoassay for Ultrasensitive Determination of Apolipoprotein-A1

- Using Silver Nanoparticles Loaded Nanohydroxyapatite as Label. *Anal. Chem.* **2015**, *87* (22), 11209-11214, DOI: 10.1021/acs.analchem.5b04063
34. Li, H.; Sun, Y.; Elseviers, J.; Muyldermans, S.; Liu, S.; Wan, Y., A nanobody-based electrochemiluminescent immunosensor for sensitive detection of human procalcitonin. *Analyst* **2014**, *139* (15), 3718-3721, DOI: 10.1039/C4AN00626G
35. Renberg, B.; Nordin, J.; Merca, A.; Uhlén, M.; Feldwisch, J.; Nygren, P.-Å.; Eriksson Karlström, A., Affibody Molecules in Protein Capture Microarrays: Evaluation of Multidomain Ligands and Different Detection Formats. *J. Proteome Res.* **2007**, *6* (1), 171-179, DOI: 10.1021/pr060316r
36. Nygren, P. Å., Alternative binding proteins: Affibody binding proteins developed from a small three-helix bundle scaffold. *FEBS J.* **2008**, *275* (11), 2668-2676, DOI: 10.1111/j.1742-4658.2008.06438.x
37. Miranda, F. F.; Briant-Litzler, E.; Zidane, N.; Pecorari, F.; Bedouelle, H., Reagentless fluorescent biosensors from artificial families of antigen binding proteins. *Biosens. Bioelectron.* **2011**, *26* (10), 4184-4190, DOI: 10.1016/j.bios.2011.04.030
38. Traxlmayr, M. W.; Kiefer, J. D.; Srinivas, R. R.; Lobner, E.; Tisdale, A. W.; Mehta, N. K.; Yang, N. J.; Tidor, B.; Wittrup, K. D., Strong Enrichment of Aromatic Residues in Binding Sites from a Charge-neutralized Hyperthermostable Sso7d Scaffold Library. *J. Biol. Chem.* **2016**, *291* (43), 22496-22508, DOI: 10.1074/jbc.M116.741314
39. Miller, E. A.; Traxlmayr, M. W.; Shen, J.; Sikes, H. D., Activity-based assessment of an engineered hyperthermophilic protein as a capture agent in paper-based diagnostic tests. *Mol. Syst. Des. Eng.* **2016**, *1* (4), 377-381, DOI: 10.1039/C6ME00032K
40. Zhao, N.; Spencer, J.; Schmitt, M. A.; Fisk, J. D., Hyperthermostable binding molecules on phage: Assay components for point-of-care diagnostics for active tuberculosis infection. *Anal. Biochem.* **2017**, *521*, 59-71, DOI: 10.1016/j.ab.2016.12.021
41. Kalichuk, V.; Béhar, G.; Renodon-Cornière, A.; Danovski, G.; Obal, G.; Barbet, J.; Mouratou, B.; Pecorari, F., The archaeal “7 kDa DNA-binding” proteins: extended characterization of an old gifted family. *Sci. Rep.* **2016**, *6*, 37274, DOI: 10.1038/srep37274
42. Chang, D.; Huang, A.; Olsen, B. D., Kinetic Effects on Self-Assembly and Function of Protein–Polymer Bioconjugates in Thin Films Prepared by Flow Coating. *Macromol. Rapid Commun.* **2017**, *38* (1), 1600449, DOI: 10.1002/marc.201600449
43. Dixit, C. K.; Vashist, S. K.; MacCraith, B. D.; O’Kennedy, R., Multisubstrate-compatible ELISA procedures for rapid and high-sensitivity immunoassays. *Nat. Prot.* **2011**, *6*, 439, DOI: 10.1038/nprot.2011.304
44. Schneider, C. A.; Rasband, W. S.; Eliceiri, K. W., NIH Image to ImageJ: 25 years of image analysis. *Nat. Methods* **2012**, *9*, 671, DOI: 10.1038/nmeth.2089
45. Baumann, H.; Knapp, S.; Lundbäck, T.; Ladenstein, R.; Härd, T., Solution structure and DNA-binding properties of a thermostable protein from the archaeon *Sulfolobus solfataricus*. *Nat. Struct. Biol.* **1994**, *1*, 808, DOI: 10.1038/nsb1194-808
46. Chen, X.; Zaro, J. L.; Shen, W.-C., Fusion protein linkers: Property, design and functionality. *Adv. Drug Del. Rev.* **2013**, *65* (10), 1357-1369, DOI: 10.1016/j.addr.2012.09.039
47. Olsen, B. D.; Shah, M.; Ganesan, V.; Segalman, R. A., Universalization of the Phase Diagram for a Model Rod–Coil Diblock Copolymer. *Macromolecules* **2008**, *41* (18), 6809-6817, DOI: 10.1021/ma800978c

48. Xia, Y.; Yin, X.; Burke, N. A. D.; Stöver, H. D. H., Thermal Response of Narrow-Disperse Poly(N-isopropylacrylamide) Prepared by Atom Transfer Radical Polymerization. *Macromolecules* **2005**, *38* (14), 5937-5943, DOI: 10.1021/ma050261z
49. Lessard, D. G.; Ousalem, M.; Zhu, X. X., Effect of the molecular weight on the lower critical solution temperature of poly(N,N-diethylacrylamide) in aqueous solutions. *Can. J. Chem.* **2001**, *79* (12), 1870-1874, DOI: 10.1139/v01-180
50. Lodge, T. P.; Hanley, K. J.; Pudil, B.; Alahapperuma, V., Phase Behavior of Block Copolymers in a Neutral Solvent. *Macromolecules* **2003**, *36* (3), 816-822, DOI: 10.1021/ma0209601
51. Lodge, T. P.; Pudil, B.; Hanley, K. J., The Full Phase Behavior for Block Copolymers in Solvents of Varying Selectivity. *Macromolecules* **2002**, *35* (12), 4707-4717, DOI: 10.1021/ma0200975
52. Hanley, K. J.; Lodge, T. P.; Huang, C.-I., Phase Behavior of a Block Copolymer in Solvents of Varying Selectivity. *Macromolecules* **2000**, *33* (16), 5918-5931, DOI: 10.1021/ma000318b
53. McConnell, G. A.; Gast, A. P., Melting of Ordered Arrays and Shape Transitions in Highly Concentrated Diblock Copolymer Solutions. *Macromolecules* **1997**, *30* (3), 435-444, DOI: 10.1021/ma961241n
54. Lai, C.; Russel, W. B.; Register, R. A., Scaling of Domain Spacing in Concentrated Solutions of Block Copolymers in Selective Solvents. *Macromolecules* **2002**, *35* (10), 4044-4049, DOI: 10.1021/ma0122223
55. Lodge, T. P.; Hamersky, M. W.; Hanley, K. J.; Huang, C.-I., Solvent Distribution in Weakly-Ordered Block Copolymer Solutions. *Macromolecules* **1997**, *30* (20), 6139-6149, DOI: 10.1021/ma970720z
56. Shibayama, M.; Hashimoto, T.; Hasegawa, H.; Kawai, H., Ordered structure in block polymer solutions. 3. Concentration dependence of microdomains in nonselective solvents. *Macromolecules* **1983**, *16* (9), 1427-1433, DOI: 10.1021/ma00243a005
57. Hashimoto, T.; Shibayama, M.; Kawai, H., Ordered structure in block polymer solutions. 4. Scaling rules on size of fluctuations with block molecular weight, concentration, and temperature in segregation and homogeneous regimes. *Macromolecules* **1983**, *16* (7), 1093-1101, DOI: 10.1021/ma00241a010
58. Kawaguchi, H.; Fujimoto, K.; Mizuhara, Y., Hydrogel microspheres III. Temperature-dependent adsorption of proteins on poly-N-isopropylacrylamide hydrogel microspheres. *Colloid. Polym. Sci.* **1992**, *270* (1), 53-57, DOI: 10.1007/bf00656929
59. Gan, D.; Lyon, L. A., Synthesis and Protein Adsorption Resistance of PEG-Modified Poly(N-isopropylacrylamide) Core/Shell Microgels. *Macromolecules* **2002**, *35* (26), 9634-9639, DOI: 10.1021/ma021186k
60. Duracher, D.; Elaissari, A.; Mallet, F.; Pichot, C., Adsorption of Modified HIV-1 Capsid p24 Protein onto Thermosensitive and Cationic Core-Shell Poly(styrene)-Poly(N-isopropylacrylamide) Particles. *Langmuir* **2000**, *16* (23), 9002-9008, DOI: 10.1021/la0004045
61. Dubacheva, G. V.; Araya-Callis, C.; Geert Volbeda, A.; Fairhead, M.; Codée, J.; Howarth, M.; Richter, R. P., Controlling Multivalent Binding through Surface Chemistry: Model Study on Streptavidin. *J. Am. Chem. Soc.* **2017**, *139* (11), 4157-4167, DOI: 10.1021/jacs.7b00540
62. Pérez-Luna, V. H.; O'Brien, M. J.; Opperman, K. A.; Hampton, P. D.; López, G. P.; Klumb, L. A.; Stayton, P. S., Molecular Recognition between Genetically Engineered

Streptavidin and Surface-Bound Biotin. *J. Am. Chem. Soc.* **1999**, *121* (27), 6469-6478, DOI: 10.1021/ja983984p

63. DeMonte, D.; Drake, E. J.; Lim, K. H.; Gulick, A. M.; Park, S., Structure-based engineering of streptavidin monomer with a reduced biotin dissociation rate. *Proteins: Struct., Funct., Bioinf.* **2013**, *81* (9), 1621-1633, DOI: 10.1002/prot.24320

64. Merlino, A.; Graziano, G.; Mazzarella, L., Structural and dynamic effects of  $\alpha$ -Helix deletion in Sso7d: Implications for protein thermal stability. *Proteins: Struct., Funct., Bioinf.* **2004**, *57* (4), 692-701, DOI: 10.1002/prot.20270

## **Chapter 4. Coiled-Coil Domains for Self-Assembly and Sensitivity Enhancement of Protein-Polymer Conjugate Biosensors**

*Reproduced (adapted) with permission from Paloni et al. ACS Applied Polymer Materials, 2 (3), 1114-1123, (2020). Copyright 2020 American Chemical Society.*

### **4.1 Abstract**

While protein self-assembly has been used to improve the performance of biosensors and biocatalysts, few general techniques have been demonstrated to achieve well-ordered protein arrays under the highly concentrated conditions required to optimize device performance. The strong association strength of coiled-coils, supercoiled bundles of alpha helices wrapped around each other, makes these structures promising scaffolds from which proteins can be linked into ordered assemblies in concentrated solution. Herein, the two component alpha helices of a heterodimeric coiled-coil are fused to a weakly ordering protein, 2x rcSso7d.SA (2x), to improve its self-assembly as a protein-poly(N-isopropylacrylamide) (PNIPAM) conjugate. Three fusion protein conjugates are developed, from which two distinct heterodimeric coiled-coil conjugates are formed, but only one of these heterodimer conjugates significantly improves the ordering quality of 2x. Additionally, the alpha helical segment in one of the three synthesized fusion protein conjugates remains almost entirely unfolded, and this conjugate is found to achieve both the strongest ordering quality and over an order of magnitude enhancement in biosensor performance compared to unmodified 2x. These findings suggest that certain arrangements of coiled-coil fusions produce well-ordered protein-polymer conjugates, and unfolded coiled-coil sequences may also serve as effective order-inducing protein sequences.

## 4.2 Introduction

The ability of proteins to recognize, bind, and modify substrates with high specificity has motivated their use in applications such as biosensing,<sup>1-3</sup> biocatalysis,<sup>4-5</sup> and immunotherapy.<sup>6-7</sup> In biosensors, proteins are immobilized onto a surface, where proper orientation of the proteins is necessary for their active sites to be freely accessible.<sup>8-10</sup> Correspondingly, the performance of a surface-bound affinity protein or enzyme is critically dependent on the method used for immobilization.<sup>11-12</sup> Techniques incorporating self-assembly have therefore been explored in an effort to achieve properly-oriented protein surfaces, with approaches including attaching proteins to self-assembled monolayers<sup>13</sup> and direct fusion to self-assembling peptide structures.<sup>14-15</sup> Although these methods do yield ordered protein surfaces, all achieve a low degree of functionalization relative to the available surface area or do not produce assemblies with predictable architectures.

Protein-polymer conjugates offer a potentially robust platform for protein self-assembly. By conjugating a polymer to a protein, the resulting molecules can undergo block copolymer nanoscale assembly in both solution and bulk.<sup>16-19</sup> Due to the diverse set of side chain chemistries of both canonical and non-canonical amino acids, strategies have been developed to achieve site-specific conjugation to a wide range of proteins.<sup>20</sup> While there are several accessible routes to the synthesis of protein-polymer conjugates, only a small subset of these conjugates display strong self-assembly in bulk and highly concentrated solution. In fact, though poly(*N*-isopropylacrylamide) (PNIPAM) has been shown to yield the lowest order-disorder transition concentration among polymers when conjugated to a protein,<sup>21</sup> many proteins cannot form order structures even when conjugated to PNIPAM. Recently, the ordering quality of protein-PNIPAM block copolymers was found to be highly dependent on the molecular weight and secondary

structure of the protein block, revealing that only certain proteins will achieve strong ordering as protein-PNIPAM conjugates.<sup>22</sup> Additionally, unlike traditional block copolymers, protein-containing block copolymers cannot be thermally annealed due to the unfolding of proteins at elevated temperatures. While solvent vapor annealing has also been demonstrated to produce well-ordered block copolymers,<sup>23</sup> the instability of proteins in most organic solvents restricts the usable solvents to aqueous solutions. When protein-polymer conjugates were exposed to neutral and slightly acidic water vapor, however, only modest improvements in ordering were achieved.<sup>24</sup> As a result, not all proteins can be self-assembled into ordered nanostructures when conjugated to a polymer.

Due to this limitation, protein molecular engineering has been explored as a route to enhance ordering quality. Since it has been demonstrated that low molecular weight proteins order poorly when conjugated to a polymer,<sup>22</sup> protein oligomerization has been used to achieve a significant enhancement in conjugate ordering quality due to enhancement in molar mass.<sup>25</sup> This technique is principally applicable to very small proteins and requires different gene cloning strategies to be developed for each protein to be oligomerized. A more general approach to produce ordered protein structures involves utilizing peptide sequences that promote self-assembly. For example,  $\beta$ -sheet-forming sequences have been shown to retain the ability to assemble into  $\beta$ -sheets after attachment to a polymer block.<sup>26-27</sup> Pairs of complementary peptide sequences with high binding affinities have also been developed to enhance long-range and directional ordering within materials.<sup>28-31</sup> Because these peptide sequences can be fused to an existing protein, this approach affords the opportunity to self-assemble a protein while retaining protein functionality.

One well-understood motif that has been widely used to link and self-assemble materials is the coiled-coil, a supercoil composed of two or more alpha helices wrapped around each other.

This structure is stabilized in solution by a core of hydrophobic amino acids as well as electrostatic interactions between adjacent alpha helices.<sup>32-33</sup> Because coiled-coil stability can be easily modified by changing the amino acids in the constituent helices, such as by tuning electrostatic interactions to be attractive or repulsive,<sup>34-35</sup> stabilizing surface residues with salt bridges,<sup>36</sup> and modulating the positions of residues in the hydrophobic core,<sup>37</sup> design rules for creating stable and strongly-associating coiled-coils have been developed, resulting in a large library of coiled-coil designs.<sup>38</sup> As a result, coiled-coils have been used to direct the self-assembly of various soft materials, including both polymers<sup>39-41</sup> and proteins.<sup>42-45</sup> In addition, coiled-coil assembly has been controlled using a variety of techniques including pH,<sup>46</sup> metal coordination,<sup>47-49</sup> and electrochemical conditions.<sup>50</sup> Therefore, fusing coiled-coils to the protein block in a protein-polymer conjugate may provide a general route to create ordered protein arrays that preserve the functionality of the original protein.

In this paper, coiled-coil sequences are fused to a protein with a strong binding affinity for streptavidin, 2x rcSso7d.SA (2x), that has been shown to exhibit weak self-assembly<sup>25</sup> to determine if coiled-coils can significantly enhance ordering. Two previously developed complementary coiled-coil sequences, ZE and ZR,<sup>51</sup> are fused to either the C- or N-terminus of 2x, and the self-assembly of conjugates of these fusion proteins is studied. Two of the three coiled-coil fusions display no significant improvement in self-assembly in homogeneous solutions, but when mixed with a fusion protein containing the complementary coiled-coil sequence, an improvement in self-assembly is observed. The fusion proteins or protein mixtures that display the strongest ordering quality in concentrated aqueous solution are also found to achieve significantly enhanced streptavidin binding capabilities compared to unmodified 2x.

## **4.3 Materials and Methods**

### **4.3.1 Gene Cloning**

#### **4.3.1.1 Design of Gene with C-terminus Cysteine**

Fusion genes were constructed using the previously-designed 2x rcSso7d.SA (2x) gene,<sup>25</sup> which contains an rcSso7d.SA<sup>52</sup> dimer and an N-terminus cysteine. Removal of the N-terminus cysteine and insertion of a C-terminus cysteine was accomplished using an Agilent QuikChange multi site-directed mutagenesis kit. In brief, two primers were designed to remove/insert a cysteine at the desired positions (**Table C-1**). The desired gene was generated by running polymerase chain reaction (PCR) amplification of the two primers with the template sequence in a pET28b(+) vector. The template DNA was then digested using DpnI, and the resulting ssDNA was transformed into XL10 Gold ultracompetent cells. Proper deletion and insertion were verified using Sanger sequencing.

#### **4.3.1.2 Preparation of Genes for Insertion of Coiled-Coil Sequences**

For both the N-Cys and C-Cys variants of 2x in pET28b(+), a pair of primers was designed to extract the 2x gene with an N-terminus NdeI restriction site and a C-terminus XhoI restriction site (**Table C-1**). In addition, the primers added a BsaI restriction site and recognition sequence on the side of the gene opposite from the cysteine residue to allow scar-free insertion of coiled-coil gene sequences. Each template plasmid was PCR amplified with the appropriate primers, and the desired DNA fragments were purified by gel extraction. Sanger sequencing was used to confirm the sequences of the extracted fragments. The DNA fragments and pET28b(+) were then digested with NdeI/XhoI, purified by gel extraction, and ligated using a 3:1 insert to vector molar ratio. Ligated plasmids were transformed into chemically competent NEB5 $\alpha$  cells, a New England Biolabs (NEB) derivative of the DH5 $\alpha$  cell line. Sequences of the two 2x genes (one with an N-

terminus Cys and a C-terminus BsaI/XhoI cloning site and the other with an N-terminus NdeI/BsaI cloning site and a C-terminus Cys) were confirmed using Sanger sequencing.

#### **4.3.1.3 Cloning of Coiled-Coil Fusions**

Genes encoding coiled-coil sequences ZE and ZR<sup>51</sup> were synthesized and cloned into pUC57 by GenScript USA (**Table 2-2**). The plasmids containing ZE, ZR, and the variant of 2x with an N-terminus Cys were digested with BsaI/XhoI and purified by gel extraction. Each digested coiled-coil gene was separately ligated with the digested 2x plasmid using a 3:1 insert to vector molar ratio. Ligated plasmids were transformed into chemically competent NEB5 $\alpha$  cells. Gene sequences were confirmed using Sanger sequencing and then transformed into BL21(de3) cells. The same procedure was used for inserting the ZE coiled-coil sequence onto the N-terminus of the 2x gene with a C-terminus Cys, except the initial digest was performed with NdeI/BsaI. Verified DNA sequences and amino acid sequences for the fusion proteins can be found in **Appendix A**.

### **4.3.2 Synthesis**

#### **4.3.2.1 PNIPAM Synthesis**

Poly(N-isopropylacrylamide) (PNIPAM) functionalized with a maleimide endgroup was synthesized by reversible addition-fragmentation chain transfer (RAFT) polymerization, as described previously.<sup>19</sup> Polymer molecular weight and dispersity were characterized by gel permeation chromatography performed on an Agilent 1260 LC system equipped with two columns (ResiPore, 300  $\times$  7.5 mm, up to 500kDa, Agilent Technologies, CA) in series, a Wyatt miniDAWN TREOS multi-angle light scattering detector, and a Wyatt Optilab T-rEX diffractometer (**Figure C-1**). Dimethylformamide (DMF) with 0.02 LiBr was used as the mobile phase with a flow rate of 1 mL/min at 70 °C.

#### 4.3.2.2 Protein Expression

2x was expressed as described previously.<sup>25</sup> 2x with an N-terminus Cys and fused to ZE at the C-terminus (2xZEC) or ZR at the C-terminus (2xZRC) as well as 2x with a C-terminus Cys and fused to ZE at the N-terminus (2xZEN) were expressed in BL21(de3) Escherichia coli cells. Each protein was expressed in 1 L of Terrific Broth at 37 °C inoculated with 5 mL of overnight culture and induced with 1 mM isopropyl- $\beta$ -D-1-thiogalactopyranoside (IPTG) at an OD<sub>600</sub> of 0.8-1.0. After induction, the cells were cultured at 20 °C for 18-20 hours and harvested. The cells were resuspended in lysis buffer (50 mM NaH<sub>2</sub>PO<sub>4</sub>, 300 mM NaCl, 10 mM imidazole, 10 mM  $\beta$ -mercaptoethanol (BME), pH 8.0) and frozen at -80 °C overnight. The cells were then thawed and frozen/thawed two additional times, after which the cells were lysed by ultrasonication. The lysate was clarified by centrifugation, and the protein was purified using Ni-NTA metal affinity chromatography. Throughout the purification, 10 mM BME was used in all buffers. Elution fractions containing purified protein were immediately exchanged into either ZE resuspension buffer (50 mM Tris buffer, 500 mM NaCl, 0.25 mM tris(2-carboxyethyl)phosphine (TCEP), pH 8.0) for 2xZEC and 2xZEN or ZR resuspension buffer (50 mM Tris buffer, 500 mM NaCl, 0.25 mM TCEP, pH 7.0) for 2xZRC by performing a 1000x buffer exchange in Millipore-Ultra 15 centrifugal filters (molecular weight cut-off of 10 kDa). Buffer recipes were developed by increasing the salt concentration of the buffer used to resuspend 2x<sup>25</sup> and adjusting the pH to allow full solubility of the coiled-coil fusion. The purity of the protein was confirmed by denaturing gel electrophoresis (SDS-PAGE) (**Figure A-4a**). Protein concentration was determined by performing a reducing-agent compatible BCA assay, and proper secondary structure folding of the proteins was assessed using circular dichroism (CD) (**Figure A-5a**). The typical yields of purified protein for 2xZEC, 2xZRC, and 2xZEN were 100, 180, and 20 mg per liter of culture, respectively.

### 4.3.2.3 Bioconjugation

Bioconjugations between 2x coiled-coil fusions and maleimide-functionalized PNIPAM were performed in ZE resuspension buffer. Solutions of the proteins were diluted to approximately 1 mg/mL, and a 5x molar excess of PNIPAM was added. After complete dissolution of PNIPAM, samples were incubated at 4 °C for 24 h. Ammonium sulfate was then added to a concentration of 1.0 M to remove unconjugated protein. Following centrifugation, the supernatant was discarded, and the precipitates were resuspended in resuspension buffer to approximately 1 mg/mL. Two additional ammonium sulfate precipitations were performed, after which the resulting solution was purified by Ni-NTA chromatography to remove unconjugated PNIPAM. Purified protein-PNIPAM conjugates were dialyzed against Milli-Q water. Bioconjugate purity was confirmed using SDS-PAGE and native PAGE (**Figure A-4b-c**), and retention of protein secondary structure was assessed using CD (**Figure A-5b**). Conjugate solution was concentrated to approximately 100 mg/mL using Millipore-Ultra 15 centrifugal filters (molecular weight cutoff of 10 kDa). Bulk solid samples were prepared by drop-casting aliquots of this concentrated solution onto Teflon sheets and drying under vacuum to a final pressure of 5 Torr (ramp rate 50 Torr/h) at room temperature. Samples were then collected and stored at 4 °C until future use. Typical yield after purification for all conjugates was 30%.

To form heterodimer coiled-coil bioconjugates, dried bioconjugate samples were dissolved at a concentration of 0.1 mg/mL in Milli-Q water at 4 °C. Then, the solutions of either 2xZEC and 2xZRC (to form 2xZEC-ZRC) or 2xZEN and 2xZRC (to form 2xZEN-ZRC) were mixed in an equimolar ratio and incubated at 4 °C overnight. Bulk samples were prepared by concentrating and drying as described previously. Samples were stored at 4 °C until future use.

### 4.3.3 Characterization

#### 4.3.3.1 Circular Dichroism (CD) Single Temperature Measurements

CD spectroscopy was performed using a JASCO Model J-1500 CD spectrometer to measure far UV CD spectroscopy between 195 and 250 nm. Measurements were conducted at concentrations of 0.1, 1, and 10 mg/mL in 1, 0.1, and 0.01 mm path length quartz cuvettes, respectively. All unconjugated proteins were measured in both ZE buffer (50 mM Tris buffer, 500 mM NaCl, 0.25 mM TCEP, pH 8.0) and Milli-Q water. All conjugates were measured in Milli-Q water. Single-temperature measurements were collected at 25 °C. Raw CD signal was smoothed and converted to molar ellipticity using literature methods.<sup>53</sup>

The percentage of folding within coiled-coiled domains was estimated by first subtracting the molar ellipticity at 222 nm ( $[\theta]_{222}$ ) of 2x in Milli-Q water from that of a 2x coiled-coil fusion in Milli-Q water at the same concentration. This estimate of the  $[\theta]_{222}$  value corresponding to the coiled-coil region was then multiplied by the ratio of the molecular weights of the full fusion protein to that of the coiled-coil region to renormalize the signal by the appropriate molecular weight. The resulting  $[\theta]_{222}$  value was then used to estimate percent folding of the coiled-coil using the following equation:<sup>54</sup>

$$\% \textit{Folded} = \frac{[\theta]_{222} - [\theta]_{222,un\textit{folded}}}{[\theta]_{222,fo\textit{lded}} - [\theta]_{222,un\textit{folded}}} \times \frac{100}{\textit{Frac Coil Residues}}, \quad (4-1)$$

where a value of  $-3,000 \text{ deg cm}^2 \text{ dmol}^{-1}$  was assumed for  $[\theta]_{222,un\textit{folded}}$ ,<sup>54</sup>  $[\theta]_{222,fo\textit{lded}}$  was estimated to be  $-37,000 \text{ deg cm}^2 \text{ dmol}^{-1}$  using an approximation based on the number of residues in the helix,<sup>55</sup> and *Frac Coil Residues* was 0.81 for all samples, as each fusion protein had 53 residues in the non-2x region of the protein, 43 of which were part of the ZE or ZR coiled-coil.

#### 4.3.3.2 Analytical Ultracentrifugation

Sedimentation velocity experiments were run on a Beckman XL-I analytical ultracentrifuge equipped with an AN-50 Ti rotor. Each bioconjugate sample was centrifuged at concentrations of 1, 0.5, and 0.33 mg/mL in Milli-Q water. Samples were equilibrated at 10 °C for 1 hour, then spun at 42,000 rpm and 10 °C for 18 hours while constantly measuring absorbance at 280 nm. A temperature of 10 °C, well below the thermal transition temperature of PNIPAM, was selected to avoid forming aggregates due to PNIPAM precipitation that would interfere with data analysis. Data were fit with SEDFIT software<sup>56</sup> using a continuous size distribution.

#### 4.3.3.3 CD Melting Curve Measurements

Melting curves were collected by continuously measuring  $[\theta]_{222}$  while heating samples from 10 to 90 °C at a rate of 1 °C/min. Samples were equilibrated at 10 °C for 10 minutes prior to starting the temperature ramp. All samples were measured at a concentration of 0.1 mg/mL in Milli-Q water. Data were fit using a previously-derived thermodynamic model in which the equilibrium constant was assumed to exclusively describe the bimolecular reaction of coiled-coil monomers forming the intended homodimer or heterodimer.<sup>57</sup>

#### 4.3.3.4 Additional Characterization Methods

The concentrated solution phase behavior of the studied bioconjugates was characterized using small-angle X-ray scattering (SAXS) (**Figures C-2 to C-6**), depolarized light scattering (DPLS) and turbidimetry (**Figures C-7 to C-11**), and differential scanning calorimetry (DSC) (**Figure C-12**). Details of the sample preparation and measurement conditions for these techniques are provided in **Chapter 2**. Thin film sample preparation and fluorescence binding assay procedures are also provided in **Chapter 2**.

## 4.4 Results and Discussion

### 4.4.1 Conjugate Design

The two component leucine zipper alpha helices in a previously designed heterodimeric coiled-coil, ZE and ZR,<sup>51</sup> were fused to the streptavidin binding protein 2x<sup>25</sup> to create a set of coiled-coil fusions where interactions between coiled-coils could promote self-assembly. Each fusion contained its coiled-coil alpha helix either at the C-terminus (2xZEC and 2xZRC) or at the N-terminus (2xZEN) with a cysteine residue at the opposite terminus of the protein (**Figure 4-1a**, top row). A maleimide-functionalized poly(N-isopropylacrylamide) (PNIPAM) molecule was conjugated to this cysteine residue to form protein-polymer conjugates (**Figure 4-1b**, **Table 4-1**). With the three conjugates synthesized in this study, both unique coiled-coil heterodimer morphologies (containing either adjacent or opposite 2x regions) were formed from an equimolar mixture of two of these conjugates: 2xZEC-ZRC, a mixture of 2xZEC and 2xZRC, and 2xZEN-ZRC, a mixture of 2xZEN and 2xZRC (**Figure 4-1a**, bottom row).

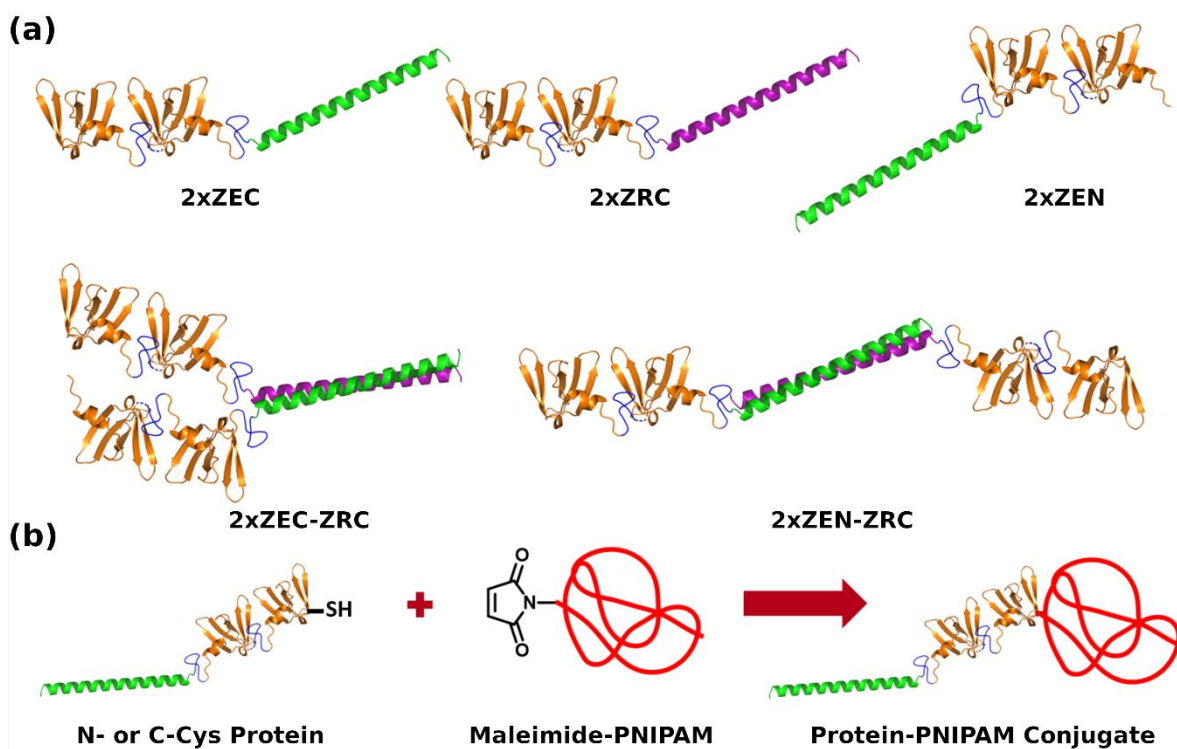


**Figure 4-1.** (a) Synthesized coiled-coil fusion monomers (top row) and heterodimers (bottom row). (b) General synthetic scheme for conjugation of 2x coiled-coil fusion to maleimide-functionalized PNIPAM. Green alpha helices represent ZE and purple helices represent ZR. Blue regions represent (Gly<sub>4</sub>Ser)<sub>2</sub> peptide linkers. Orange regions in the protein are cartoon representations of the Sso7d crystal structure (PDB 1SSO).<sup>58</sup>

**Table 4-1.** Composition of Coiled-coil Fusion-PNIPAM Conjugates

Conjugate	Protein MW (kDa)	PNIPAM M <sub>n</sub> (kDa) <sup>a</sup>	PNIPAM Đ <sup>a</sup>
2xZEC	22.6		
2xZRC	22.9	26.1	1.05
2xZEN	22.9		

<sup>a</sup>All conjugates were synthesized using the same PNIPAM molecule.

#### 4.4.2 Coiled-Coil Folding and Stability

Circular dichroism (CD) experiments indicate different degrees of alpha helical folding between the coiled-coil fusion proteins. Though all 5 of the protein solutions have very similar CD spectra in buffer, presumably due to shielding effects from salt ions, these spectra differ significantly in pure water (**Figure A-5a**). Using the value of molar ellipticity at 222 nm for each sample, which

corresponds to a maximum in the absolute value of molar ellipticity for alpha helices, the percent of folded residues within the ZE and ZR alpha helices can be estimated (**Table 4-2**). At low concentrations, 2xZEC is completely unfolded, 2xZEC-ZRC is mostly folded, and the remaining proteins are only partially folded. As concentration increases, these data show that alpha helices initially become more folded but eventually begin to unfold at higher concentrations. Although the protein concentration in the conjugate samples used for nanostructure determination is always greater than 100 mg/mL, a concentration higher than can be measured using commercially-available CD cuvettes, the concentration trends in **Table 4-2** can be used to estimate the helical folding in the high concentration samples. As such, the results suggest that in these samples 2xZEC is mostly or entirely unfolded, 2xZEC-ZRC is likely mostly folded, and the alpha helices in the 3 other proteins are partially folded.

**Table 4-2.** Percent Folding within Alpha Helical Region of Coiled-Coil Fusion Proteins

Conc. in Milli-Q Water (mg/mL)	2xZEC <sup>a</sup>	2xZRC <sup>a</sup>	2xZEN <sup>a</sup>	2xZEC-ZRC <sup>a</sup>	2xZEN-ZRC <sup>a</sup>
0.1	-2 ± 2	37 ± 4	43 ± 4	72 ± 7	35 ± 4
1	36 ± 4	NS <sup>b</sup>	72 ± 8	100 ± 10	43 ± 5
10	32 ± 4	NS <sup>b</sup>	50 ± 6	NS <sup>b</sup>	NS <sup>b</sup>

<sup>a</sup>Reported errors represent the standard deviation from three replicates. <sup>b</sup>Not soluble.

The degree of association between coiled-coils is largely dependent on the degree of folding of the component alpha helices. Even though most alpha helices appear to exhibit a slightly greater degree of folding when conjugated to PNIPAM, the fraction of folded alpha helices is still similar to that of the unconjugated proteins (**Figure A-5b**). Consistent with the finding that the alpha helices in 2xZEC are primarily or entirely unfolded up to concentrations of at least 10 mg/mL, this conjugate does not significantly form homodimerized coiled-coils at concentrations up to at least 1 mg/mL, as quantified by analytical ultracentrifugation (**Figure 4-2a**). Similarly,

2xZRC, which exhibited partial alpha helical folding, only forms coiled-coil homodimers to a small degree at all measured concentrations (**Figure 4-2b**). Despite having partially or primarily folded alpha helices (some of which have fractional folding comparable to that of 2xZRC), the three remaining conjugates all exist exclusively as coiled-coils, with minor fractions of coiled-coil trimers (**Figure 4-2c-e**).

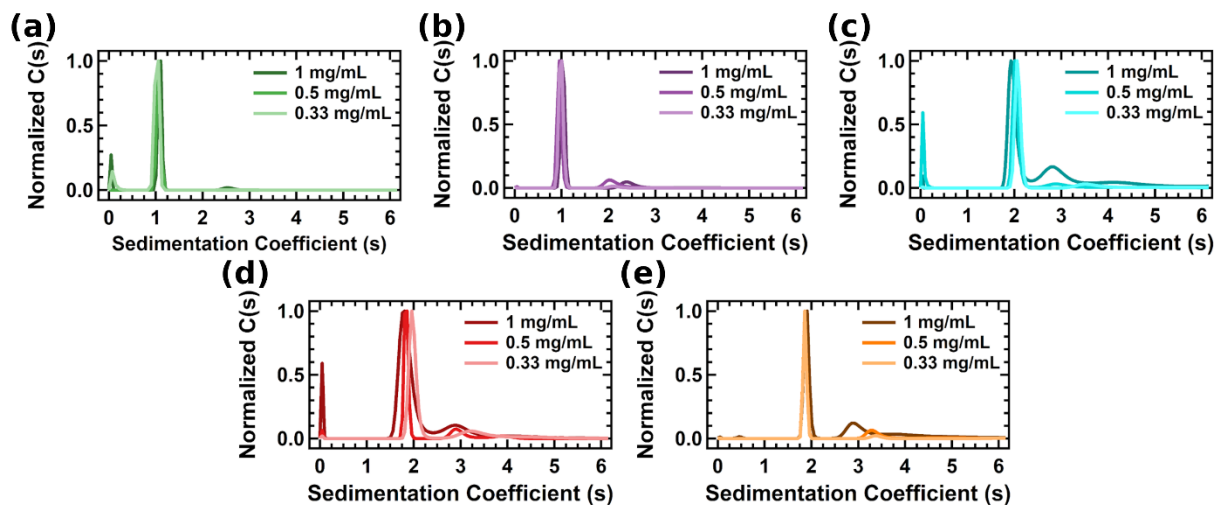


**Figure 4-2.** Analytical ultracentrifugation continuous size distributions for coiled-coil fusion conjugates (a) 2xZEC, (b) 2xZRC, (c) 2xZEN, (d) 2xZEC-ZRC, and (e) 2xZEN-ZRC in Milli-Q water at 10 °C. Due to the molecular weights of the conjugates, sedimentation coefficient closely corresponds to the oligomerization state of the component coiled-coils.

Coiled-coil fusion protein thermal stability data provides further evidence for the structure of the alpha helices. When compared to the melting curve for 2x, 2xZEC has a very similar thermal behavior, signifying that the alpha helices in 2xZEC do not significantly dimerize and are almost entirely unfolded (**Figure 4-3a**). 2xZRC is found to slightly homodimerize (consistent with analytical centrifugation data) with a relatively low melting temperature, and the coiled-coils in 2xZEC-ZRC are found to have a melting temperature higher than can be experimentally measured (**Figure 4-3a**), in agreement with the binding strengths of similar coiled-coils.<sup>57</sup> While 2xZEN-ZRC does form coiled-coils, these structures do not appear to be ZE-ZR heterodimers. Rather, the data are fit very well by a model assuming an equimolar mixture of 2xZRC and 2xZEN

homodimerized coiled-coils (**Figure 4-3b**). Although the data show slightly lower molar ellipticity than predicted by this model, indicating that some heterodimer coiled-coils are formed, 2xZEN-ZRC is predominantly unable to heterodimerize. Since the same ZE and ZR helices can form heterodimeric coiled-coils in 2xZEC-ZRC, it is possible that geometric constraints in 2xZEN-ZRC inhibit coiled-coil heterodimer formation.

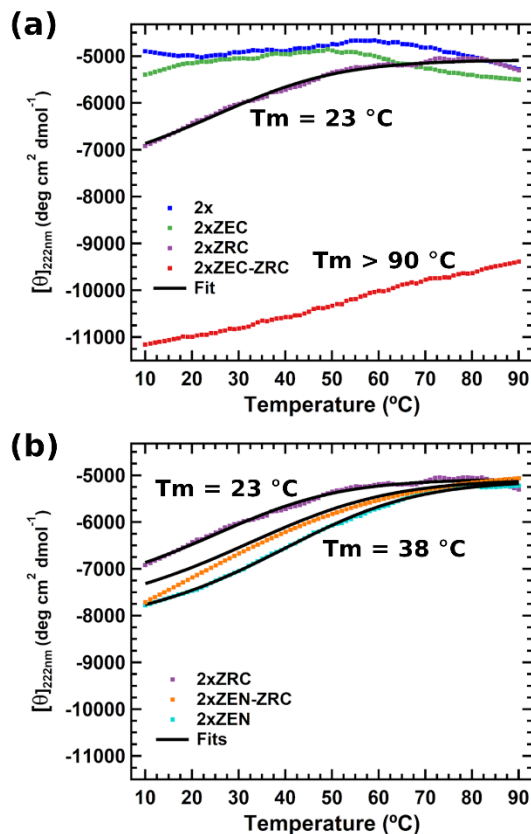


**Figure 4-3.** Melting curves for (a) 2x and 2xZEC-ZRC and component coiled-coil fusion proteins and (b) 2xZEN-ZRC and component coiled-coil fusion proteins. Black curves represent fits to melting curve data used to extract melting temperatures ( $T_m$ ), except for the curve fit to the 2xZEN-ZRC data, for which the curve represents a 1:1 mixture of 2xZRC and 2xZEN homodimerized coiled-coils.

### 4.4.3 Self-Assembly

#### 4.4.3.1 Phase Behavior

In concentrated aqueous solution, the synthesized coiled-coil fusion heterodimers display a wider range of well-ordered phases than unmodified 2x. Representative SAXS data are presented in

**Figure 4-4.** At low temperatures where water is a good solvent for both the protein and PNIPAM blocks, all conjugates display lamellar or hexagonal ordered phases (**Figure 4-5**). The predominance of lamellar phases is consistent with previous studies of protein-polymer conjugates.<sup>25, 59-60</sup> While the phase diagram for 2xZRC is almost identical to that for 2x,<sup>25</sup> all other conjugates produce lamellar phases at a broader range of temperature and concentration conditions, particularly at concentrations below 40 weight percent. The two conjugates with coiled-coil heterodimers also have the widest range of concentrations over which birefringent phases are observed (**Figure 4-5d, e**), suggesting that these coiled-coil fusions both expand the conditions under which ordered phases are observed and enhance the ordering quality of these phases compared to 2x.

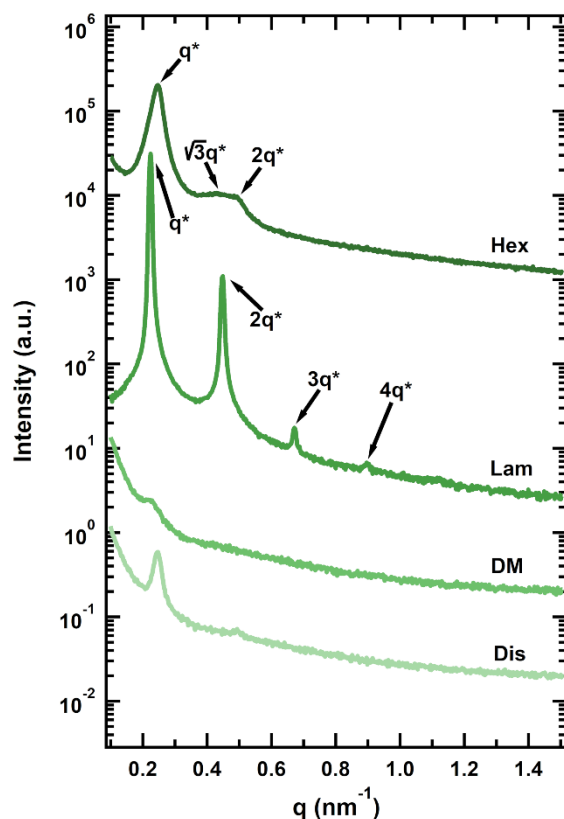


**Figure 4-4.** Representative SAXS traces for 2xZEC conjugates. Phase assignments represent hexagonally packed cylinders (Hex), lamellae (Lam), disordered micelles (DM), and disordered (Dis).

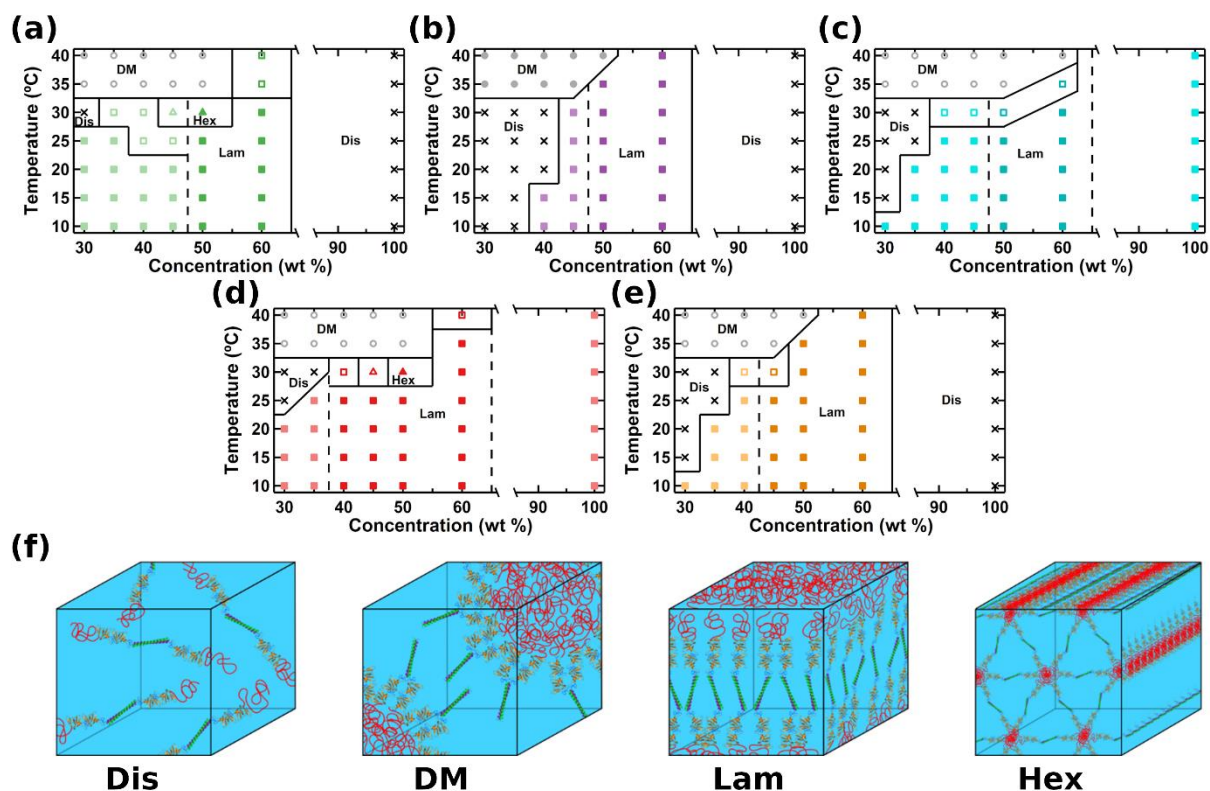


**Figure 4-5.** Phase diagrams of the protein-PNIPAM conjugates (a) 2xZEC, (b) 2xZRC, (c) 2xZEN, (d) 2xZEC-ZRC, and (e) 2xZEN-ZRC as a function of concentration and temperature. Phases assigned in the diagrams are disordered (Dis), disordered micelles (DM), lamellae (Lam), or hexagonally packed cylinders (Hex) and are also (f) represented schematically. Light colored symbols represent non-birefringent ordered phases, which are separated by dashed lines from shaded colored symbols representing birefringent ordered phases. Solid symbols represent a homogeneous phase, while open symbols indicate macrophase separation.

The LCST behavior of the PNIPAM block produces thermal phase transitions in the coiled-coil fusion conjugates. At temperatures above the thermal transition temperature of PNIPAM, water becomes a poor solvent for the polymer block, causing PNIPAM chains to collapse, thereby producing a disordered micellar phase with a water-poor PNIPAM core at low concentrations (**Figure 4-5**). At temperatures just below this transition to a disordered phase, a small window for hexagonally packed cylinder formation is observed in both 2xZEC and 2xZEC-ZRC (**Figure 4-5a, d**). This behavior has been seen in mCherry and EGFP conjugates and has been attributed to

the water loss in the polymer block resulting in a reduced polymer volume fraction, favoring phases with higher interfacial curvature.<sup>60-61</sup>

Though their phase behavior as a function of temperature is consistent with previous studies, most of the conjugates exhibit atypical trends in macrophase transition temperatures. In all previously studied protein-PNIPAM conjugates, the macrophase transition temperatures have been found to monotonically increase as a function of concentration due to the greater capacity for the protein block to accommodate water expelled from the PNIPAM block at higher conjugate concentrations.<sup>25, 61-62</sup> However, all of the coiled-coil fusions that display macrophase separation have separation temperatures that first decrease before increasing with concentration (**Figure C-13a**). This behavior suggests that at lower concentrations, less free energy is required to cause conjugate molecules to break apart from a conjugate-rich phase and form a conjugate-poor phase as temperature increases. Since decreasing macrophase transition temperatures were not observed in 2x conjugates, this trend likely results from a physical change in the coiled-coil domains. For example, increasing temperature was shown to cause coiled-coils to at least partially dissociate (**Figure 4-3**). Since coiled-coil dissociation exposes previously-buried hydrophobic residues on the helix surfaces, this dissociation destabilizes the conjugates in solution. As such, dissociation should reduce the free energy required to form conjugate rich (water poor) phases, reducing macrophase transition temperatures. At high concentrations, the capacity of the protein phase to accommodate excess water significantly increases, which disfavors macrophase separation and may explain the trend of all macrophase transition temperatures initially decreasing but eventually increasing with temperature. Furthermore, even though the PNIPAM desolvation temperatures show no significant differences across 2x conjugates with and without coiled-coils (**Figure C-13b**), macrophase separation is only observed in coiled-coil conjugates. The observed desolvation

temperatures for all conjugates approach that of PNIPAM homopolymer at low concentration (32 °C)<sup>63-64</sup> and decrease with increasing concentration, which is consistent with behavior of other conjugates<sup>25, 60</sup> and PNIPAM homopolymer.<sup>63-64</sup> Thus, differences in macrophase separation temperatures cannot be attributed to changes in PNIPAM desolvation, and the low transition temperatures of the coiled-coil conjugates is likely attributable to coiled-coil dissociation.

#### 4.4.3.2 Ordering Quality

With one exception, the coiled-coil fusion heterodimer conjugates display stronger ordering than the component coiled-coil fusion monomers. Ordering quality was quantified using inverse full width at half maximum ( $\text{FWHM}^{-1}$ ) of the primary SAXS scattering peak so that larger values corresponded to stronger ordering (**Figure 4-6**). Two of the coiled-coil fusion monomer conjugates, 2xZEN and 2xZRC, exhibit similar ordering quality to unmodified 2x across most concentrations. While the heterodimer 2xZEN-ZRC shows minor improvements in ordering across most concentrations compared to 2x, the other heterodimer, 2xZEC-ZRC, displays significantly improved ordering over these concentrations. However, 2xZEC displays nanostructures even more well-ordered than 2xZEC-ZRC under most conditions, with its strongest ordering, stronger than any previously-measured protein-PNIPAM conjugate,<sup>22</sup> observed at 35 weight percent in solution.

No clear relationship can be established between ordering quality and the assumed binding strength between coiled-coils. While the binding interaction between ZE and ZR is known to be extremely strong,<sup>51</sup> any coiled-coils formed by ZE or ZR homodimerization would be expected to be significantly less stable due to the repulsive interactions between glutamate (in ZE) or arginine (in ZR) residues within the structure.<sup>57</sup> Therefore, if coiled-coil stability (and therefore binding strength between conjugates) were the primary driving force for the formation of ordered nanophases, the conjugate monomers (2xZEC, 2xZRC, and 2xZEN) would be expected to have

significantly weaker ordered structures in solution than the conjugate heterodimers (2xZEC-ZRC and 2xZEN-ZRC). Clearly, this is not the case for 2xZEC. Additionally, 2xZEC-ZRC displays significantly stronger ordering than 2xZEN-ZRC at concentrations around 40 weight percent even though the same coiled-coil heterodimer is formed in these two systems. Of course, the arrangement of 2x regions in 2xZEC-ZRC and 2xZEN-ZRC is substantially different (**Figure 4-1a**), so it is possible that the formation of 2xZEN-ZRC introduces additional steric hindrance, reducing the fraction of heterodimer coiled-coils. Indeed, the domain spacings for 2xZEC-ZRC are larger than those for 2xZEN-ZRC at all measured concentrations, suggesting that the protein domains in 2xZEN-ZRC may not pack as efficiently (**Figure C-14**).

The structural and stability data for the coiled-coils suggest that unfolded coiled-coil sequences improve self-assembly. While the alpha helices in 2xZEC were shown to be predominantly unfolded up to concentrations of at least 10 mg/mL, conjugates of this protein displayed the strongest ordering quality at most conditions in concentrated solution (**Figure 4-6**). The temperature behavior of the measured 2xZRC SAXS curves also suggests that coiled-coil unfolding improves self-assembly. For all studied conjugates that form stable coiled-coils except for 2xZRC, ordered phases are observed only below the coiled-coil melting temperature (due to this temperature being above the PNIPAM desolvation temperature), and FWHM-1 decreases as temperature increases. Because the melting temperature of 2xZRC is low enough that ordered phases are observed even at temperatures above this point, though, it can be seen that ordering quality begins to increase just below this melting temperature (**Figure C-15**). Therefore, unfolded protein sequences may enhance conjugate ordering quality. We hypothesize that this is observed because unfolded coiled-coils have a relatively large number of uncovered hydrophobic residues, resulting in a relatively hydrophobic domain along the polymer chain that can help to drive self-

assembly. It is also possible that these unfolded coiled-coils refold into beta-sheets at high concentrations, as has been observed in some coiled-coil sequences when drying<sup>65</sup> or in sequences that contain a large number of charged residues.<sup>66</sup> Therefore, conjugates that can undergo an alpha helix to beta-sheet transition would be greatly stabilized at high concentration, and, if only 2xZEC is capable of undergoing this transition due to its low degree of alpha helix folding, this phenomenon could explain the enhanced self-assembly in conjugates containing this fusion protein.

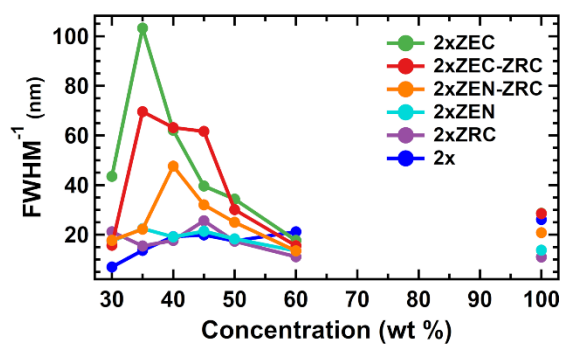


**Figure 4-6.** Ordering quality of coiled-coil fusion conjugates in aqueous solution at 25 °C. Bulk data are disconnected from solution-phase data to indicate that the bulk samples are not at equilibrium. Data for 2x are taken from the literature.<sup>25</sup>

#### 4.4.4 Thin Film Activity Assays

The activity of biosensors incorporating the coiled-coil fusion conjugates generally increases with stronger conjugate ordering. Conjugates of 2x and all the studied coiled-coil fusion proteins were cast into thin film biosensors and their ability to bind streptavidin was assayed (**Figure 4-7**). For all coiled-coil fusion conjugates except for 2xZEN-ZRC, an increase in activity and decrease in limit of detection is observed (**Table 4-3**). With the exception of 2xZEN-ZRC, the most well-ordered conjugates, 2xZEC and 2xZEC-ZRC, have the greatest biosensor activity, while 2xZRC and 2xZEN, which had similar ordering quality to 2x, both also have comparable activity to unmodified 2x. The reduced activity in biosensors constructed from 2xZEN-ZRC may result from

packing frustrations within the protein domains due to the geometry of this conjugate, thereby restricting streptavidin binding. Though the established trends between biosensor activity and ordering quality are merely qualitative, it is clear that both 2xZEC and 2xZEC-ZRC offer both significantly enhanced self-assembly and improved biosensor performance over unmodified 2x.

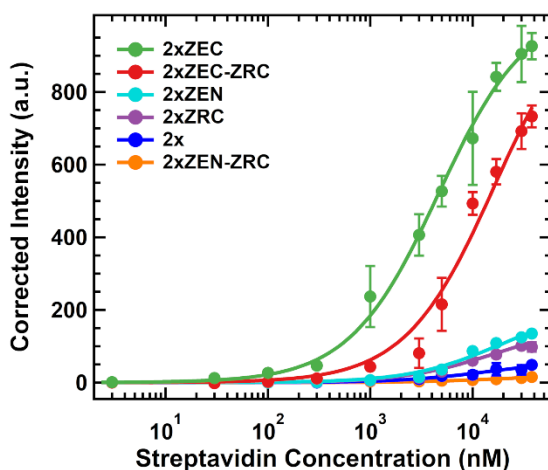


**Figure 4-7.** Streptavidin binding curves for 2x and coiled-coil fusion conjugate thin film assays. Error bars represent the standard deviation of three replicates.

**Table 4-3.** Relative Activity of Coiled-Coil Fusion Conjugate Thin Films

Conjugate	Relative Activity <sup>a</sup>	LOD <sup>b</sup> (nM)
2xZEC	21 ± 3	3.6 ± 0.5
2xZEC-ZRC	11 ± 2	12 ± 2
2xZEN	3.8 ± 0.7	70 ± 10
2xZRC	2.5 ± 0.5	100 ± 10
Control (2x)	1.0 ± 0.2	190 ± 30
2xZEN-ZRC	0.3 ± 0.1	800 ± 200

<sup>a</sup>Activity is relative to that of a 2x conjugate thin film and accounts for differences in film thickness. Reported errors represent the standard deviation across three replicates. <sup>b</sup>Limit of detection, calculated as the concentration at which intensity equalled the value three standard deviations above the signal of a blank sample.

## 4.5 Conclusions

The self-assembly of a series of 5 coiled-coil fusion proteins conjugated to PNIPAM was explored to determine if coiled-coil sequences could enhance conjugate nanostructuring and thereby improve biosensor performance. The physical state of the alpha helical segment in the conjugates

was found to dictate the quality of conjugate self-assembly in solution. The 2xZEN and 2xZRC conjugates formed weakly associating coiled-coils that provide no significant improvement in ordering over 2x. Almost entirely unable to produce heterodimerized coiled-coils as a possible result of geometric constraints, 2xZEN-ZRC offered only modest improvements in self-assembly over a small concentration range. Conversely, 2xZEC-ZRC was able to form mostly folded and extremely stable coiled-coils that produce well-defined nanostructures, presumably due to the increased molar mass of the complex. Though its alpha helical regions were almost entirely unfolded and this conjugate did not form coiled-coils, 2xZEC was observed to have the strongest ordering in solution. It is hypothesized that in this case the exposed hydrophobic regions can drive assembly, possibly due to formation of beta-sheets at high concentration.

These findings suggest that there may be limitations in the use of coiled-coils to direct protein-polymer conjugate self-assembly. Coiled-coil association was demonstrated to enhance conjugate ordering, but only one of the two protein systems designed to form stable heterodimerized coiled-coils was able to strongly associate. Because the systems differed only in the site at which one of the coiled-coil sequences was installed, association appears to be highly dependent on the location at which these sequences are fused to proteins.

Whereas folded coiled-coils only significantly enhanced conjugate self-assembly in one of two designed systems, unfolded coiled-coil sequences were found to improve conjugate ordering quality in both instances in which these unstructured sequences were observed. At temperatures near the melting point of its coiled-coil homodimers, 2xZRC displayed an ordering quality that significantly increased with temperature and degree of coiled-coil unfolding. Furthermore, 2xZEC was found to have the least structured coiled-coil fusion sequence, and conjugates of this protein assembled into the most well-ordered nanostructures that afforded over an order of magnitude

improvement in biosensor performance, greater than all other coiled-coil fusion conjugates. Though additional studies will need to be conducted to confirm their effectiveness as order-directing protein sequences, these findings suggest that unfolded coiled-coil sequences should be explored as general fusion partners that can be used to improve protein self-assembly and activity.

#### 4.6 References

1. Sharma, S.; Byrne, H.; O'Kennedy, Richard J., Antibodies and antibody-derived analytical biosensors. *Essays Biochem.* **2016**, *60* (1), 9-18, DOI: 10.1042/ebc20150002
2. Engvall, E.; Perlmann, P., Enzyme-Linked Immunosorbent Assay, Elisa. *J. Immunol.* **1972**, *109* (1), 129-135, DOI:
3. Ferrigno, Paul K., Non-antibody protein-based biosensors. *Essays Biochem.* **2016**, *60* (1), 19-25, DOI: 10.1042/ebc20150003
4. Bommarius, A. S., Biocatalysis: A Status Report. *Annu. Rev. Chem. Biomol. Eng.* **2015**, *6* (1), 319-345, DOI: 10.1146/annurev-chembioeng-061114-123415
5. Britton, J.; Majumdar, S.; Weiss, G. A., Continuous flow biocatalysis. *Chem. Soc. Rev.* **2018**, *47* (15), 5891-5918, DOI: 10.1039/C7CS00906B
6. Khazaeli, M. B.; Conry, R. M.; LoBuglio, A. F., Human Immune Response to Monoclonal Antibodies. *J. Immunother.* **1994**, *15* (1), 42-52, DOI:
7. Weiner, Louis M.; Murray, Joseph C.; Shuptrine, Casey W., Antibody-Based Immunotherapy of Cancer. *Cell* **2012**, *148* (6), 1081-1084, DOI: 10.1016/j.cell.2012.02.034
8. Cracknell, J. A.; Vincent, K. A.; Armstrong, F. A., Enzymes as Working or Inspirational Electrocatalysts for Fuel Cells and Electrolysis. *Chem. Rev.* **2008**, *108* (7), 2439-2461, DOI: 10.1021/cr0680639
9. Makaraviciute, A.; Ramanaviciene, A., Site-directed antibody immobilization techniques for immunosensors. *Biosens. Bioelectron.* **2013**, *50* (Supplement C), 460-471, DOI: 10.1016/j.bios.2013.06.060
10. Squires, T. M.; Messinger, R. J.; Manalis, S. R., Making it stick: convection, reaction and diffusion in surface-based biosensors. *Nat. Biotechnol.* **2008**, *26* (4), 417-426, DOI: 10.1038/nbt1388
11. Rusmini, F.; Zhong, Z.; Feijen, J., Protein Immobilization Strategies for Protein Biochips. *Biomacromolecules* **2007**, *8* (6), 1775-1789, DOI: 10.1021/bm061197b
12. Sheldon, R. A., Enzyme Immobilization: The Quest for Optimum Performance. *Adv. Synth. Catal.* **2007**, *349* (8-9), 1289-1307, DOI: 10.1002/adsc.200700082
13. Chaki, N. K.; Vijayamohan, K., Self-assembled monolayers as a tunable platform for biosensor applications. *Biosens. Bioelectron.* **2002**, *17* (1), 1-12, DOI: 10.1016/S0956-5663(01)00277-9
14. Zhang, G.; Schmidt-Dannert, S.; Quin, M. B.; Schmidt-Dannert, C., Chapter Thirteen - Protein-based scaffolds for enzyme immobilization. In *Methods Enzymol.*, Schmidt-Dannert, C.; Quin, M. B., Eds. Academic Press: 2019; Vol. 617, pp 323-362.
15. Al-Halifa, S.; Babych, M.; Zottig, X.; Archambault, D.; Bourgault, S., Amyloid self-assembling peptides: Potential applications in nanovaccine engineering and biosensing. *Peptide Science* **2019**, *111* (1), e24095, DOI: 10.1002/pep2.24095

16. Hamley, I. W., PEG–Peptide Conjugates. *Biomacromolecules* **2014**, *15* (5), 1543-1559, DOI: 10.1021/bm500246w
17. Rabotyagova, O. S.; Cebe, P.; Kaplan, D. L., Protein-Based Block Copolymers. *Biomacromolecules* **2011**, *12* (2), 269-289, DOI: 10.1021/bm100928x
18. Shu, J. Y.; Panganiban, B.; Xu, T., Peptide-Polymer Conjugates: From Fundamental Science to Application. *Annu. Rev. Phys. Chem.* **2013**, *64* (1), 631-657, DOI: 10.1146/annurev-physchem-040412-110108
19. Thomas, C. S.; Glassman, M. J.; Olsen, B. D., Solid-State Nanostructured Materials from Self-Assembly of a Globular Protein–Polymer Diblock Copolymer. *ACS Nano* **2011**, *5* (7), 5697-5707, DOI: 10.1021/nn2013673
20. Gauthier, M. A.; Klok, H.-A., Peptide/protein–polymer conjugates: synthetic strategies and design concepts. *Chem. Commun.* **2008**, (23), 2591-2611, DOI: 10.1039/B719689J
21. Chang, D.; Lam, C. N.; Tang, S.; Olsen, B. D., Effect of polymer chemistry on globular protein–polymer block copolymer self-assembly. *Polymer Chemistry* **2014**, *5* (17), 4884-4895, DOI: 10.1039/C4PY00448E
22. Huang, A.; Paloni, J. M.; Wang, A.; Obermeyer, A. C.; Sureka, H. V.; Yao, H.; Olsen, B. D., Predicting Protein–Polymer Block Copolymer Self-Assembly from Protein Properties. *Biomacromolecules* **2019**, DOI: 10.1021/acs.biomac.9b00768
23. Sinturel, C.; Vayer, M.; Morris, M.; Hillmyer, M. A., Solvent Vapor Annealing of Block Polymer Thin Films. *Macromolecules* **2013**, *46* (14), 5399-5415, DOI: 10.1021/ma400735a
24. Thomas, C. S.; Xu, L.; Olsen, B. D., Kinetically Controlled Nanostructure Formation in Self-Assembled Globular Protein–Polymer Diblock Copolymers. *Biomacromolecules* **2012**, *13* (9), 2781-2792, DOI: 10.1021/bm300763x
25. Paloni, J. M.; Miller, E. A.; Sikes, H. D.; Olsen, B. D., Improved Ordering in Low Molecular Weight Protein–Polymer Conjugates Through Oligomerization of the Protein Block. *Biomacromolecules* **2018**, *19* (9), 3814-3824, DOI: 10.1021/acs.biomac.8b00928
26. Hamley, I. W.; Ansari, I. A.; Castelletto, V.; Nuhn, H.; Rösler, A.; Klok, H. A., Solution Self-Assembly of Hybrid Block Copolymers Containing Poly(ethylene glycol) and Amphiphilic  $\beta$ -Strand Peptide Sequences. *Biomacromolecules* **2005**, *6* (3), 1310-1315, DOI: 10.1021/bm049286g
27. Rathore, O.; Sogah, D. Y., Self-Assembly of  $\beta$ -Sheets into Nanostructures by Poly(alanine) Segments Incorporated in Multiblock Copolymers Inspired by Spider Silk. *J. Am. Chem. Soc.* **2001**, *123* (22), 5231-5239, DOI: 10.1021/ja004030d
28. Gurunatha, K. L.; Fournier, A. C.; Urvoas, A.; Valerio-Lepiniec, M.; Marchi, V.; Minard, P.; Dujardin, E., Nanoparticles Self-Assembly Driven by High Affinity Repeat Protein Pairing. *ACS Nano* **2016**, *10* (3), 3176-3185, DOI: 10.1021/acsnano.5b04531
29. Speltz, E. B.; Nathan, A.; Regan, L., Design of Protein–Peptide Interaction Modules for Assembling Supramolecular Structures in Vivo and in Vitro. *ACS Chem. Biol.* **2015**, *10* (9), 2108-2115, DOI: 10.1021/acscchembio.5b00415
30. Watson, Randall P.; Christen, Martin T.; Ewald, C.; Bumbak, F.; Reichen, C.; Mihajlovic, M.; Schmidt, E.; Güntert, P.; Cafilisch, A.; Plückthun, A.; Zerbe, O., Spontaneous Self-Assembly of Engineered Armadillo Repeat Protein Fragments into a Folded Structure. *Structure* **2014**, *22* (7), 985-995, DOI: 10.1016/j.str.2014.05.002
31. Zakeri, B.; Fierer, J. O.; Celik, E.; Chittock, E. C.; Schwarz-Linek, U.; Moy, V. T.; Howarth, M., Peptide tag forming a rapid covalent bond to a protein, through engineering a

- bacterial adhesin. *Proc. Natl. Acad. Sci. U.S.A.* **2012**, *109* (12), E690-E697, DOI: 10.1073/pnas.1115485109
32. Apostolovic, B.; Danial, M.; Klok, H.-A., Coiled coils: attractive protein folding motifs for the fabrication of self-assembled, responsive and bioactive materials. *Chem. Soc. Rev.* **2010**, *39* (9), 3541-3575, DOI: 10.1039/B914339B
33. Mason, J. M.; Arndt, K. M., Coiled Coil Domains: Stability, Specificity, and Biological Implications. *ChemBioChem* **2004**, *5* (2), 170-176, DOI: doi:10.1002/cbic.200300781
34. Acharya, A.; Ruvinov, S. B.; Gal, J.; Moll, J. R.; Vinson, C., A Heterodimerizing Leucine Zipper Coiled Coil System for Examining the Specificity of a Position Interactions: Amino Acids I, V, L, N, A, and K. *Biochemistry* **2002**, *41* (48), 14122-14131, DOI: 10.1021/bi020486r
35. Moll, J. R.; Ruvinov, S. B.; Pastan, I.; Vinson, C., Designed heterodimerizing leucine zippers with a ranger of pIs and stabilities up to 10–15 M. *Protein Sci.* **2001**, *10* (3), 649-655, DOI: 10.1110/ps.39401
36. Drobnak, I.; Gradišar, H.; Ljubetič, A.; Merljak, E.; Jerala, R., Modulation of Coiled-Coil Dimer Stability through Surface Residues while Preserving Pairing Specificity. *J. Am. Chem. Soc.* **2017**, *139* (24), 8229-8236, DOI: 10.1021/jacs.7b01690
37. Fletcher, J. M.; Bartlett, G. J.; Boyle, A. L.; Danon, J. J.; Rush, L. E.; Lupas, A. N.; Woolfson, D. N., N@a and N@d: Oligomer and Partner Specification by Asparagine in Coiled-Coil Interfaces. *ACS Chem. Biol.* **2017**, *12* (2), 528-538, DOI: 10.1021/acscchembio.6b00935
38. Woolfson, D. N., The Design of Coiled-Coil Structures and Assemblies. In *Adv. Protein Chem.*, Academic Press: 2005; Vol. 70, pp 79-112.
39. Marsden, H. R.; Korobko, A. V.; van Leeuwen, E. N. M.; Pouget, E. M.; Veen, S. J.; Sommerdijk, N. A. J. M.; Kros, A., Noncovalent Triblock Copolymers Based on a Coiled-Coil Peptide Motif. *J. Am. Chem. Soc.* **2008**, *130* (29), 9386-9393, DOI: 10.1021/ja800254w
40. Pechar, M.; Kopečková, P.; Joss, L.; Kopeček, J., Associative diblock copolymers of poly(ethylene glycol) and coiled-coil peptides. *Macromol. Biosci.* **2002**, *2* (5), 199-206, DOI: 10.1002/1616-5195(200206)2:5<199::Aid-mabi199>3.0.Co;2-2
41. Vandermeulen, G. W. M.; Tziatzios, C.; Klok, H.-A., Reversible Self-Organization of Poly(ethylene glycol)-Based Hybrid Block Copolymers Mediated by a De Novo Four-Stranded  $\alpha$ -Helical Coiled Coil Motif. *Macromolecules* **2003**, *36* (11), 4107-4114, DOI: 10.1021/ma034124i
42. Jang, Y.; Champion, J. A., Self-Assembled Materials Made from Functional Recombinant Proteins. *Acc. Chem. Res.* **2016**, *49* (10), 2188-2198, DOI: 10.1021/acs.accounts.6b00337
43. Park, W. M.; Champion, J. A., Two-Step Protein Self-Assembly in the Extracellular Matrix. *Angew. Chem. Int. Ed.* **2013**, *52* (31), 8098-8101, DOI: 10.1002/anie.201302331
44. Park, W. M.; Champion, J. A., Thermally Triggered Self-Assembly of Folded Proteins into Vesicles. *J. Am. Chem. Soc.* **2014**, *136* (52), 17906-17909, DOI: 10.1021/ja5090157
45. Ross, J. F.; Wildsmith, G. C.; Johnson, M.; Hurdiss, D. L.; Hollingsworth, K.; Thompson, R. F.; Mosayebi, M.; Trinh, C. H.; Paci, E.; Pearson, A. R.; Webb, M. E.; Turnbull, W. B., Directed Assembly of Homopentameric Cholera Toxin B-Subunit Proteins into Higher-Order Structures Using Coiled-Coil Appendages. *J. Am. Chem. Soc.* **2019**, *141* (13), 5211-5219, DOI: 10.1021/jacs.8b11480

46. Tian, Y.; Zhang, H. V.; Kiick, K. L.; Saven, J. G.; Pochan, D. J., Transition from disordered aggregates to ordered lattices: kinetic control of the assembly of a computationally designed peptide. *Org. Biomol. Chem.* **2017**, *15* (29), 6109-6118, DOI: 10.1039/C7OB01197K
47. More, H. T.; Zhang, K. S.; Srivastava, N.; Frezzo, J. A.; Montclare, J. K., Influence of Fluorination on Protein-Engineered Coiled-Coil Fibers. *Biomacromolecules* **2015**, *16* (4), 1210-1217, DOI: 10.1021/bm5019062
48. Nepal, M.; Sheedlo, M. J.; Das, C.; Chmielewski, J., Accessing Three-Dimensional Crystals with Incorporated Guests through Metal-Directed Coiled-Coil Peptide Assembly. *J. Am. Chem. Soc.* **2016**, *138* (34), 11051-11057, DOI: 10.1021/jacs.6b06708
49. Tavenor, N. A.; Murnin, M. J.; Horne, W. S., Supramolecular Metal-Coordination Polymers, Nets, and Frameworks from Synthetic Coiled-Coil Peptides. *J. Am. Chem. Soc.* **2017**, *139* (6), 2212-2215, DOI: 10.1021/jacs.7b00651
50. Lin, Y.; An, B.; Bagheri, M.; Wang, Q.; Harden, J. L.; Kaplan, D. L., Electrochemically Directed Assembly of Designer Coiled-Coil Telechelic Proteins. *ACS Biomater. Sci. Eng.* **2017**, *3* (12), 3195-3206, DOI: 10.1021/acsbmaterials.7b00599
51. Zhang, K.; Diehl, M. R.; Tirrell, D. A., Artificial Polypeptide Scaffold for Protein Immobilization. *J. Am. Chem. Soc.* **2005**, *127* (29), 10136-10137, DOI: 10.1021/ja051457h
52. Miller, E. A.; Traxlmayr, M. W.; Shen, J.; Sikes, H. D., Activity-based assessment of an engineered hyperthermophilic protein as a capture agent in paper-based diagnostic tests. *Mol. Syst. Des. Eng.* **2016**, *1* (4), 377-381, DOI: 10.1039/C6ME00032K
53. Greenfield, N. J., Using circular dichroism spectra to estimate protein secondary structure. *Nat. Prot.* **2007**, *1*, 2876, DOI: 10.1038/nprot.2006.202
54. Wei, Y.; Thyparambil, A. A.; Latour, R. A., Protein helical structure determination using CD spectroscopy for solutions with strong background absorbance from 190 to 230nm. *Biochim. Biophys. Acta* **2014**, *1844* (12), 2331-2337, DOI: 10.1016/j.bbapap.2014.10.001
55. Jackson, D. Y.; King, D. S.; Chmielewski, J.; Singh, S.; Schultz, P. G., General approach to the synthesis of short .alpha.-helical peptides. *J. Am. Chem. Soc.* **1991**, *113* (24), 9391-9392, DOI: 10.1021/ja00024a067
56. Schuck, P., Size-Distribution Analysis of Macromolecules by Sedimentation Velocity Ultracentrifugation and Lamm Equation Modeling. *Biophys. J.* **2000**, *78* (3), 1606-1619, DOI: 10.1016/S0006-3495(00)76713-0
57. Krylov, D.; Mikhailenko, I.; Vinson, C., A thermodynamic scale for leucine zipper stability and dimerization specificity: e and g interhelical interactions. *EMBO J.* **1994**, *13* (12), 2849-2861, DOI:
58. Baumann, H.; Knapp, S.; Lundbäck, T.; Ladenstein, R.; Härd, T., Solution structure and DNA-binding properties of a thermostable protein from the archaeon *Sulfolobus solfataricus*. *Nat. Struct. Biol.* **1994**, *1*, 808, DOI: 10.1038/nsb1194-808
59. Huang, A.; Olsen, B. D., Self-Assembly of Differently Shaped Protein-Polymer Conjugates through Modification of the Bioconjugation Site. *Macromol. Rapid Commun.* **2016**, *37* (15), 1268-1274, DOI: 10.1002/marc.201500744
60. Lam, C. N.; Olsen, B. D., Phase transitions in concentrated solution self-assembly of globular protein-polymer block copolymers. *Soft Matter* **2013**, *9* (8), 2393-2402, DOI: 10.1039/C2SM27459K
61. Lam, C. N.; Kim, M.; Thomas, C. S.; Chang, D.; Sanoja, G. E.; Okwara, C. U.; Olsen, B. D., The Nature of Protein Interactions Governing Globular Protein-Polymer Block Copolymer Self-Assembly. *Biomacromolecules* **2014**, *15* (4), 1248-1258, DOI: 10.1021/bm401817p

62. Lam, C. N.; Yao, H.; Olsen, B. D., The Effect of Protein Electrostatic Interactions on Globular Protein–Polymer Block Copolymer Self-Assembly. *Biomacromolecules* **2016**, *17* (9), 2820-2829, DOI: 10.1021/acs.biomac.6b00522
63. Heskins, M.; Guillet, J. E., Solution Properties of Poly(N-isopropylacrylamide). *J. Macromol. Sci. A* **1968**, *2* (8), 1441-1455, DOI: 10.1080/10601326808051910
64. Schild, H. G.; Tirrell, D. A., Microcalorimetric detection of lower critical solution temperatures in aqueous polymer solutions. *J. Phys. Chem.* **1990**, *94* (10), 4352-4356, DOI: 10.1021/j100373a088
65. Dong, H.; Hartgerink, J. D., Role of Hydrophobic Clusters in the Stability of  $\alpha$ -Helical Coiled Coils and Their Conversion to Amyloid-like  $\beta$ -Sheets. *Biomacromolecules* **2007**, *8* (2), 617-623, DOI: 10.1021/bm060871m
66. Pagel, K.; Wagner, S. C.; Samedov, K.; von Berlepsch, H.; Böttcher, C.; Koks, B., Random Coils,  $\beta$ -Sheet Ribbons, and  $\alpha$ -Helical Fibers: One Peptide Adopting Three Different Secondary Structures at Will. *J. Am. Chem. Soc.* **2006**, *128* (7), 2196-2197, DOI: 10.1021/ja057450h

## **Chapter 5. Protein-Polymer Block Copolymer Thin Films for Highly Sensitive Detection of Small Proteins in Biological Fluids**

*Reproduced (adapted) with permission from Paloni et al. ACS Sensors, 4 (11), 2869-2878, (2019).*

*Copyright 2019 American Chemical Society.*

### **5.1 Abstract**

In nearly all biosensors, sensitivity is greatly reduced for measurements conducted in biological matrices due to nonspecific binding from off-target molecules. One method to overcome this issue is to design a sensor that enables selective size-based uptake of proteins. Herein, a protein-polymer conjugate thin film biosensor is fabricated that self-assembles into lamellae containing alternating domains of protein and polymer. Analyte is captured in protein regions while polymer domains restrict diffusion of large molecules. Device sensitivity and size-based exclusion properties are probed using two analytes: streptavidin (SA, 52.8 kDa) and monomeric streptavidin (mSA2, 15.6 kDa). Tuning domain spacing by adjusting polymer molecular weight allows design of films that relatively freely uptake mSA2 and largely restrict SA diffusion. Furthermore, when detecting the smaller mSA2, no reduction in limit of detection (LOD) is observed when transitioning from detection in buffer to detection in biological fluids. As a result, LOD measured in fluid samples is reduced by 2 orders of magnitude compared to a traditional surface-immobilized protein monolayer.

### **5.2 Introduction**

Proteins such as antibodies<sup>1</sup> and other high-affinity binders<sup>2-3</sup> have seen widespread use as molecular recognition elements in biosensors due to their ability to bind a specific analyte with high sensitivity and selectivity. After the analyte is captured in a biosensor, this binding event is converted to a detectable signal using one of a variety of mechanisms including colorimetric

signal,<sup>4</sup> electrical signal,<sup>5</sup> or optical measurements.<sup>6-8</sup> For each of these detection techniques, however, nonspecific binding from off-target molecules increases background signal, which can increase the limit of detection (LOD) by orders of magnitude.<sup>9-10</sup> This noise issue is particularly problematic in blood, urine, and other biological matrices commonly used for analysis, which can contain molecules present at concentrations billions of times greater than the target analyte.<sup>9</sup> While methods have been developed to at least partially overcome nonspecific binding problems such as by developing biosensor surface morphologies that significantly enhance specificity for an analyte,<sup>11-12</sup> coating the biosensor surface with a hydrogel layer or Nafion membrane,<sup>13</sup> or using magnetic beads for detection,<sup>14-15</sup> these methods either have long-term stability issues or increase biosensor complexity, thereby decreasing robustness.

One potentially simple method to reduce nonspecific binding in biosensors is through size-based exclusion. Though preventing molecules significantly larger than the target analyte from contacting the binding sites in a biosensor has been demonstrated to improve device sensitivity, current technologies have primarily focused on separating small molecules from proteins<sup>16-17</sup> or proteins from red blood cells.<sup>18-19</sup> Comparatively few methods have been investigated to selectively detect small proteins in biological matrices despite the presence of many relevant protein biomarkers that are smaller than 15 kDa including markers for sepsis,<sup>20</sup> heart failure,<sup>21</sup> and Alzheimer's disease.<sup>22</sup> These molecules are all significantly smaller than the majority of proteins in blood<sup>23</sup> and urine,<sup>24</sup> providing a potential route for selective matrix detection of these small proteins via size exclusion methods.

Entropic repulsion of large proteins has been demonstrated using a variety of polymeric materials. One of the most commonly used techniques to prevent nonspecific adsorption of large proteins onto a biosensor surface is through grafting polymer brushes onto the device.<sup>25-27</sup> Similar

protein exclusion properties have been observed in vesicles coated with a polymer brush exterior.<sup>28-29</sup> As polymer brush density increases, the maximum size of a protein that can diffuse into the brush decreases,<sup>30</sup> which is consistent with theoretical predictions.<sup>31</sup> Size-exclusion behavior has also been observed in hydrogels, in which smaller mesh sizes have been found to increase the frictional force experienced by molecules diffusing through the gel<sup>32-33</sup> and cause exclusion of particles sufficiently larger than this mesh size.<sup>34</sup> Although the various aforementioned methods of entropic protein repulsion are effective at excluding these molecules, the techniques have not been incorporated into a biosensor for the purpose of differentiating between differently-sized proteins.

One material that could simultaneously provide size-based exclusion of proteins and act as an effective biosensor is a protein-polymer conjugate thin film. The self-assembly of protein-polymer conjugates has been extensively studied,<sup>35-40</sup> revealing that these materials assemble analogously to traditional diblock copolymers with an enhanced range of conditions over which lamellae are formed.<sup>36</sup> Within these lamellar nanostructures, domains of densely packed protein and polymer serve as regions that can allow analyte binding and control diffusion into the material using size-based exclusion, respectively. When cast into thin films, protein-polymer conjugates contain binding sites throughout the entire three-dimensional structure of the film, allowing enhanced sensitivity compared to traditional biosensors utilizing surface-immobilized proteins due to the larger effective areal density of binding sites.<sup>35,41</sup> Additionally, antibody-polymer conjugate thin films were observed to permit diffusion of protein G (22 kDa) into the film but excluded a horseradish peroxidase-protein G fusion protein (66 kDa),<sup>41</sup> providing evidence for a size-based exclusion mechanism for diffusion.

In this work, the size-exclusion properties of protein-polymer conjugate thin films are studied by varying the molecular weight of the polymer block and the analyte. Shorter polymer blocks and larger analyte size are found to restrict diffusion into the films more. Furthermore, no decrease in limit of detection is observed when using a small analyte (15.6 kDa) and transitioning from detection in buffer to that in biological fluids (blood and urine). This excellent sensitivity in these fluids is attributed to the exclusion of larger molecules in the fluids as well as the relatively enhanced diffusion rate of the small analyte into the film. A model sandwich assay is also designed for the protein-polymer conjugate thin film, indicating the feasibility of performing an enzyme-linked immunosorbent assay (ELISA) using this biosensor architecture.

## **5.3 Materials and Methods**

### **5.3.1 Materials**

All solvents were purchased from VWR, and all other chemicals were purchased from MilliporeSigma and used without further purification. Streptavidin labeled with Alex Fluor 647, biotinylated horseradish peroxidase (biotin-HRP), and Alex Fluor 647 and 488 NHS esters were purchased from Thermo Fisher Scientific. Whole blood was purchased from Research Blood Components, LLC. Bovine serum albumin (BSA) was purchased from MilliporeSigma. Unlabeled streptavidin was purchased from New England Biolabs. Silicon wafers were purchased from Wafer World, and quartz slides were purchased from Ted Pella, Inc.

### **5.3.2 Polymer Synthesis and Protein Expression and Bioconjugation**

Details for polymer synthesis, protein expression, and bioconjugation reactions between polymer and protein are described in **Chapter 2**.

### 5.3.3 Thin Film Preparation

Silicon wafers (P-type Silicon with boron as dopant, (100) orientation, single-side polished) cut into rectangular sections or quartz slides (only used in experiments for which binding intensity was measured as a function of film thickness) were sequentially rinsed with acetone, methanol, and water. Substrates were then dried under a filtered air flow and treated with oxygen plasma for 3 minutes. Immediately following plasma cleaning, conjugate samples rehydrated to 10 wt.% in Milli-Q water were flow coated onto the substrates in a chamber maintained at 60% relative humidity, as described previously.<sup>42</sup> To stabilize thin films against dissolution in water, the cast films were preheated to 40 °C and immersed in a 1.4 wt.% aqueous solution of glutaraldehyde at 40 °C for 20 s to lightly crosslink the protein nanodomains. Immediately following immersion, thin films were thoroughly rinsed with water until the surfaces became hydrophilic, indicating complete removal of unlinked glutaraldehyde. Films were dried under filtered air and stored at ambient conditions until use. Film thickness was determined using a Woolam M-2000D spectroscopic ellipsometer using a single incidence angle of 70°. Curves were fit using a three-layer model consisting of a 0.4 mm bottom silicon substrate, a native silicon oxide layer of 1.8 nm, and a top conjugate layer fit using a Cauchy model. Thin films were characterized using grazing-incidence small-angle X-ray scattering (GISAXS) as described in **Chapter 2**. rcSso7d.SA (Sso) monolayers were prepared by coupling protein activated by 1-Ethyl-3-(3-dimethylaminopropyl)carbodiimide/N-hydroxysuccinimide (EDC/NHS) with amine-functionalized silicon wafers using literature methods.<sup>43</sup>

### 5.3.4 Fluorescence Assays

The binding capabilities of Sso monolayers and conjugate thin films were measured using fluorescently-labeled streptavidin (SA) and monomeric streptavidin (mSA2). Details for the

expression, purification, and fluorescent labeling of mSA2 are provided in **Chapter 2**. Samples were prepared by serial dilution of SA or mSA2 in PBS (pH 7.4), human urine (diluted to 50% v/v in PBS, pH 7.4), or blood serum (obtained as the supernatant by centrifuging whole blood at 1500 xg for 10 minutes, then diluted to 50% v/v in PBS, pH 7.4). These solutions were gently applied to the surface of a bioconjugate thin film or Sso monolayer as 0.5  $\mu$ L drops. Films were incubated for a specified period of time in a sealed chamber saturated with water vapor at room temperature to prevent drying of the applied fluorescent samples. The films were then rinsed with water for 10 seconds (a time determined to be sufficient to remove unbound molecules from the film, (**Figure A-12**), dried under filtered air, and immediately analyzed for fluorescent signal. Fluorescence microscopy images were acquired at 4x magnification using a Cy5 filter set and exposure time of 5000 ms on an Olympus IX-81 inverted fluorescence microscope with an AxioCam HRC CCD camera. Fluorescent intensity was calculated using ImageJ software<sup>44</sup> by determining the average fluorescent signal in a rectangular area of the fluorescent image free of defects and occupying no less than half of the full sample application area. Corrected intensity was determined by subtracting the fluorescent intensity of a sample from that of an area on the substrate far away from regions exposed to fluorescent samples.

### **5.3.5 Sandwich Assays**

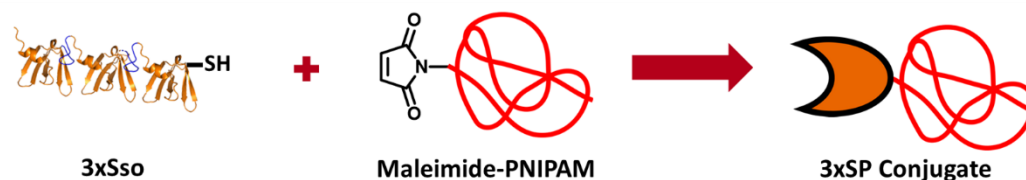
Bioconjugate thin films and Sso monolayers were cut into 0.25 cm-by-0.25 cm pieces and securely fastened to the bottom of Falcon polystyrene 12-well plates using double-sided carbon tape. Each well was submerged in 1 mL of 1% BSA in Milli-Q water, and the 12-well plate was incubated at 37 °C for 30 minutes. The wells were rinsed twice by adding 2 mL of Milli-Q water and gently shaking the well plate at 70 rpm for 5 minutes. 1 mL of streptavidin diluted in PBS, urine, or blood serum (prepared as described in the Fluorescent Assays section) containing 0.1% BSA was then

added to each well, and the well plate was shaken at 70 rpm for 4 hours at room temperature. Wells were rinsed twice with 2 mL of Milli-Q water then twice with 2 mL of 0.1% BSA in Milli-Q water by shaking at 70 rpm for 5 minutes. After rinsing, wells were submerged in 1 mL of 200 ng/mL biotin-HRP in Milli-Q water containing 0.1% BSA, and the well plate was shaken at 70 rpm for 1 hour at room temperature. Wells were then rinsed with water and 0.1% BSA as described previously. 1 mL of solution from a Pierce TMB substrate kit (Thermo Fisher Scientific) was added to each well, and the well plate was shaken vigorously at 125 rpm for 15 minutes at room temperature. 1 mL of 2M H<sub>2</sub>SO<sub>4</sub> was added to each well, and the absorbance at 450 nm was read using a Tecan Infinite M200 PRO plate reader.

## 5.4 Results and Discussion

### 5.4.1 Characterizing Diffusion into Biosensor Thin Films

Protein-polymer conjugate thin films were fabricated with a wide range of domain spacings to control diffusion into the films. Each conjugate was synthesized from a previously reported trimer of rcSso7d.SA (3xSso),<sup>35</sup> a modified DNA-binding protein with high binding affinities for streptavidin (SA)<sup>45</sup> and a monomeric variant of streptavidin (mSA2),<sup>35, 46</sup> conjugated to poly(N-isopropylacrylamide) (PNIPAM; **Scheme 5-1**). Thin films created using these conjugates all adopted a weak lamellar morphology (**Figure 5-1**) with domain spacings ranging from approximately 20 to 55 nm (**Table 5-1**) when swollen with water. Lamellar spacing was only observed in horizontal linecuts to GISAXS data (**Figure 5-1**), not in vertical linecuts (**Figure D-2**), suggesting that the lamellae adopted a predominantly perpendicular orientation. The film domain spacings were consistently larger than those measured in dry bulk conjugate samples (**Figure D-3, Table D-1**), presumably due to the swelling of PNIPAM causing an expansion of domains in the films.



**Scheme 5-1.** Bioconjugation of 3xSso containing an *N*-terminal cysteine residue to maleimide-functionalized PNIPAM. Orange regions in 3xSso are cartoon representations of the Sso7d crystal structure generated using Protein Data Bank ID: 1SSO.<sup>47</sup>

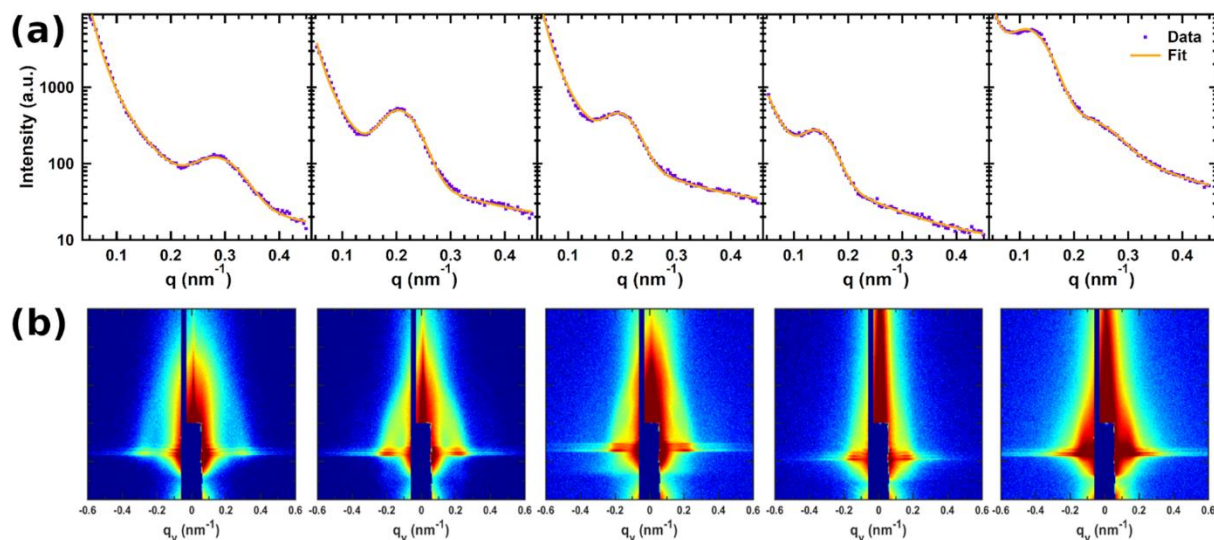


**Figure 5-1.** (a) Fit GISAXS horizontal linecuts used to calculate domain spacing in swollen thin films and (b) corresponding GISAXS patterns. In both (a) and (b), images represent data for 3xSP9.6k, 3xSP23.3k, 3xSP30.3k, 3xSP56.1k, 3xSP77.6k from left to right. GISAXS patterns were collected at an incident angle of  $0.140^\circ$ .

**Table 5-1.** Composition of 3xSso-PNIPAM Conjugates

Conjugate	PNIPAM $M_n$ (kDa)	PNIPAM $\bar{D}$	Protein Weight Fraction	Domain Spacing <sup>a</sup> (nm)
3xSP9.6k	9.6	1.05	0.72	21.9
3xSP23.3k	23.3	1.06	0.52	30.6
3xSP30.3k	30.3	1.08	0.45	32.0
3xSP56.1k	56.1	1.11	0.31	43.5
3xSP77.6k	77.6	1.13	0.24	53.9

<sup>a</sup>Calculated from GISAXS horizontal linecuts (Figure 5-1a)

Fluorescent assays performed on the thin films revealed gradual uptake of analyte. To assess effects of analyte size on diffusion into the films, the two aforementioned analytes that could be detected by the biosensor, SA (52.8 kDa) and mSA2 (15.6 kDa), were fluorescently-labeled,

exposed to the films for a prescribed time, rinsed, and measured for fluorescent intensity indicative of protein bound to the film. These experiments were also run using a monolayer of rcSso7d.SA (Sso) immobilized onto a surface, allowing a direct comparison between the thin films and traditional surfaced-immobilized protein biosensors. Both SA and mSA2 displayed a continuous uptake into the ~160 nm films over at least 8 hours, whereas the monolayers were observed to equilibrate with the protein solution after 30 minutes (**Figure 5-2**). Film structure and domain spacing were not found to change as a result of film swelling over an 8 hour time period (**Figure D-4**), suggesting that films remained stable throughout the experiment. It is worth noting that the film exposed to SA reached the same intensity observed in a monolayer after ~4.5 hours while the thin film exposed to mSA2 reached this intensity after only ~2.5 hours. These results are consistent with the idea that analyte size controls diffusion into these conjugate thin films. For a given domain spacing, a smaller molecule, such as mSA2, should experience less restricted diffusion into the films than a larger molecule, such as SA, due to the easier uptake of the smaller molecule into the polymer nanodomains (**Figure 5-3a**). Similarly, all molecules would be expected to diffuse into the films more quickly as domain spacing increases (**Figure 5-3b**). Because SA displayed slower uptake than mSA2 (relative to a monolayer) into films with the same domain spacing, it appears analyte size does indeed affect uptake rate. Thus, even this initial experiment provided evidence that the larger SA molecule experienced greater resistance to diffusion into the bioconjugate films than mSA2.

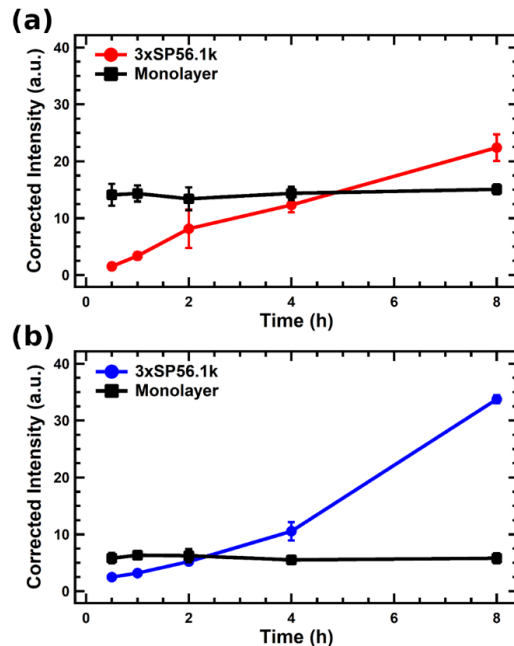


**Figure 5-2.** Fluorescent assays indicating the diffusion of (a) SA and (b) mSA2 into bioconjugate thin films over time. The film in (a) was 152 nm thick and exposed to an 800 nM solution of SA, and the film in (b) was 166 nm thick and exposed to an 800 nM solution of mSA2. Results are compared to those obtained using an Sso monolayer. Error bars represent the standard deviation of three replicates.

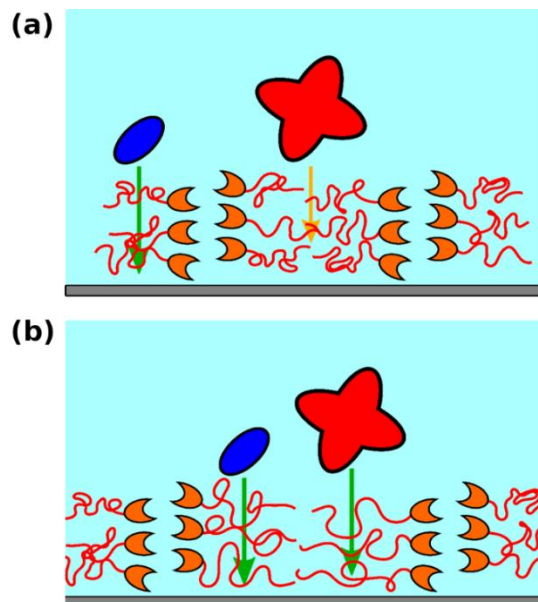


**Figure 5-3.** Diagram of SA (red) and mSA2 (blue) diffusion into 3xSP conjugate thin films with (a) a small domain spacing and (b) a larger domain spacing. Green arrows represent relatively quick diffusion into the film, while yellow arrows represent greatly restricted diffusion.

Larger domain spacings allowed faster diffusion into the thin films. Fluorescent assays were again run with both SA and mSA2, but films were exposed to protein solution for only 30 minutes to study diffusion into the thin films at early time points prior to saturation at equilibrium binding conditions. Fluorescent intensity remained constant with increasing film thickness for films with the smallest domain spacings when using SA as the analyte (**Figure 5-4a**). This behavior suggests that SA is only able to diffuse a small distance (less than the thickness of the shortest thin film) into the films within 30 minutes, resulting in SA only binding in a region at the surface of each film. Only in thin films constructed from 3xSP77.6k, which had the largest domain spacing, was an increase in signal with film thickness observed when using SA as the analyte (**Figure 5-4b**). In these films, SA is seemingly capable of diffusing through the entire thin film, causing this analyte to come into contact with and bind to more binding sites in thicker films. Because this less-restricted diffusion was only observed in the films with the largest domain spacing, these findings further support the idea that domain spacing controls diffusion into the films.

Film thickness measurements conducted using mSA2 as the analyte indicated that this smaller protein experienced less restricted diffusion into the thin films. In contrast to the constant intensity observed when using SA, films with the 4 smallest domain spacings all showed an increase in fluorescent intensity with film thickness (**Figure 5-4c**). As such, analyte could fully access the binding sites within thin films with a significantly smaller domain spacing when mSA2 was used as the analyte (21.9 nm) than when SA was used (53.9 nm). Furthermore, when using mSA2 no change in signal with film thickness was found for 3xSP77.6k thin films (**Figure 5-4d**). It is possible that, due to the significantly lower density of binding sites within the 3xSP77.6k films resulting from the low mass fraction of protein in this conjugate (**Table 5-1**), the greater intensity from increased mSA2 binding is difficult to detect. Indeed, only a very small increase in signal

was observed with increasing film thickness when SA was added to these same thin films (**Figure 5-4b**). On the whole, however, the different binding patterns when using mSA2 and SA strongly suggest that the smaller size of mSA2 permitted easier diffusion into the films.

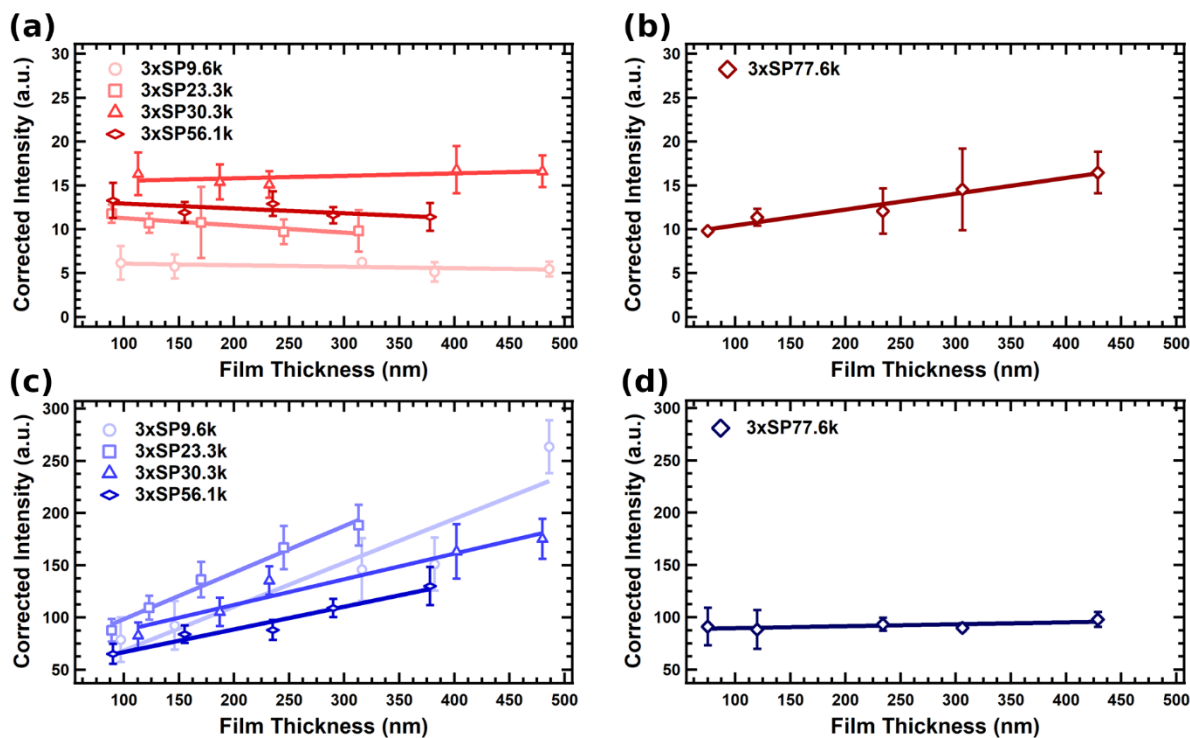


**Figure 5-4.** Results of 30 minute fluorescent binding assays performed in bioconjugate thin films using (a, b) SA or (c, d) mSA2 as the analyte. Films were cast on quartz slides to reduce background signal. Graphs are divided to differentiate between films with (a, c) low  $M_n$  PNIPAM and similar behavior and (b, d) high  $M_n$  PNIPAM and similar behavior. Lines in the figure are drawn to guide the eye. The films were exposed to a 4  $\mu$ M solution of (a, b) SA or (c, d) mSA2. Error bars represent the standard deviation of three replicates.

## 5.4.2 Biosensing Capabilities

### 5.4.2.1 Sensing in Buffer

To evaluate how the apparent size-based diffusion properties translated to biosensing capabilities, binding curves were measured using SA and mSA2 solutions in buffer. Binding curves were fit with a quadratic model described in **Chapter 2** that is a function of three parameters: the average MFI per binding event  $\alpha$ , the total concentration of binding sites  $[P]_T$ , and the apparent dissociation constant  $K_{d,app}$  describing the binding equilibrium between analyte and binding sites within the

thin film. Best-fit values for these parameters are provided in **Table D-2**. Nearly all independent fits gave 95% confidence intervals for  $\alpha$  that contained the value 100 MFI/nM, demonstrating good self-consistency of the model. Limit of detection (LOD) was calculated as the concentration along the binding curve at which the measured intensity was three times the standard deviation of a blank sample measured on the same film.

An Sso monolayer in general outperformed the 3xSso-PNIPAM biosensor thin films when exposed to SA solutions (**Figure 5-5a**). The sensitivity of films fabricated from conjugates with the smallest domain spacing (3xSP9.6k) was over an order of magnitude lower after 30 minutes of exposure and approximately 2-fold higher after 4 hours of exposure compared to a monolayer (**Figure 5-5b**). These results are consistent with findings that 3xSP9.6k films significantly restricted SA diffusion (**Figure 5-4a**). In contrast, 3xSP77.6k films that allowed much less restricted transport of SA (**Figure 5-4b**) were found to approach the sensitivity of a monolayer after 4 hours and displayed slightly enhanced sensitivity after 8 hours, demonstrating the positive effect of enhanced SA diffusivity on device performance. This improved diffusivity in 3xSP77.6k films is best demonstrated by comparing the 30 minute data for the two conjugate films. Because the 3xSP77.6k film has a significantly lower density of binding sites than the 3xSP9.6k film, it would be expected that at equilibrium the 3xSP9.6k film would display a significantly stronger fluorescent signal. Since instead the 3xSP77.6k thin film shows a greater fluorescent intensity after 30 minutes (prior to reaching equilibrium), it is likely that SA has a greater diffusivity in this film, enabling the protein to penetrate further into the film within this short time frame. In fact, the binding curve fits reveal that nearly four times as many binding sites are accessed in the 3xSP77.6k film after 30 minutes, despite the lower total concentration of binding sites in this film (**Table D-2**). Both films, though, demonstrate an increased number of accessible binding sites and  $K_{d,app}$

value (that approaches but does not reach the monolayer value) over time. These observations are reasonable, as SA would be expected to further diffuse into the film over time, gradually accessing more binding sites and approaching the equilibrium value for bound analyte concentration. This slow approach to equilibrium binding conditions is also consistent with the finding that the thin films require significantly more time to saturate than a simple protein monolayer (**Figure 5-2a**). Overall, these results indicate that compared to a monolayer, SA is largely excluded from the thin films due to reduced diffusivity, and the diffusion properties can be tuned by changing domain spacing.

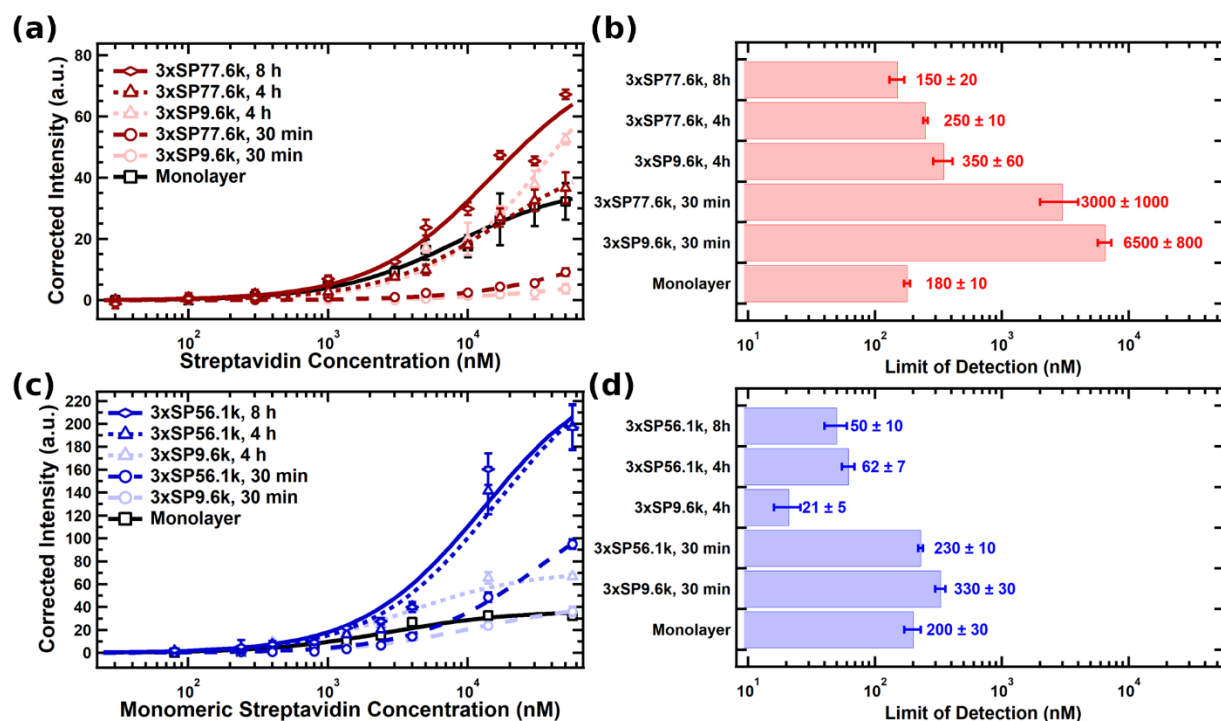


**Figure 5-5.** Binding curves for conjugate thin films exposed to (a) SA or (c) mSA2 in PBS for different periods of time. Results are compared to those obtained using an Sso monolayer with a 4 hour exposure time. The limit of detection determined for each binding curve is reported for films exposed to (b) SA or (d) mSA2. Film thicknesses are listed in **Table D-2**. Error bars represent the standard deviation of three replicates.

When using mSA2 as the analyte, the studied protein-polymer conjugate thin films displayed enhanced sensitivity compared to a protein monolayer. 3xSP9.6k films and 3xSP56.1k films were used to compare the biosensing capabilities of films that allowed complete mSA2

diffusion (**Figure 5-4c**) but have a large difference in density of binding sites. While both films achieved a lower LOD than the Sso monolayer after 4 hours (**Figure 5-5c-d**), using the film with a smaller domain spacing (3xSP9.6k, 10-fold reduction in LOD) reduced the LOD more than using the film with the larger domain spacing (3xSP56.1k, ~4-fold reduction in LOD). As the opposite trend was found when using SA, mSA2 is likely small enough relative to the domain spacing in 3xSP9.6k films such that the reduction in diffusivity compared to that in 3xSP56.1k films is not large enough to overcome the sensitivity-enhancing effect of the greater density of binding sites. This effect, however, is not a result of mSA2 accessing more binding sites in the 3xSP9.6k film, as over four times the number of binding sites are accessible in the 3xSP56.1k films (**Table D-2**). Instead, it appears that the enhanced sensitivity results from a lower  $K_{d,app}$  value within the 3xSP9.6k film (**Table D-2**), indicating that a greater fraction of mSA2 remains bound to these films. Thus, unlike when detecting SA, the thin film biosensors were able to effectively uptake and bind the smaller protein mSA2.

#### **5.4.2.2 Sensing in Biological Fluids**

Binding curve measurements in blood serum and urine (both 50% diluted) demonstrated that the size-based exclusion properties of the conjugate thin films could enable enhanced selectivity in biological fluids. 3xSP9.6k, 3xSP30.3k, and 3xSP77.6k films were used for these experiments, allowing comparison of device sensitivity using a range of domain spacings. When detecting SA, the thin films in general performed comparably to a monolayer (**Figure 5-6a-b**). In both blood serum and urine, the monolayers and most thin film samples experienced an approximate 4 to 5-fold increase in LOD compared to measurements in buffer as a result of nonspecific binding from other molecules in the fluid (**Figures 5-5b, 5-6e-f**). Correspondingly, the binding events in each film could be described by a  $K_{d,app}$  value ~4-5 times that of the monolayer value in buffer (**Table**

**D-3**). In fact, nearly all films were found to have the same concentration of accessible binding sites as a monolayer (**Table D-3**), suggesting inaccessibility of most binding sites likely resulting from restriction of diffusion into the film. Additionally, the relationship between sensitivity and domain spacing mirrors that found in buffer, as 3xSP9.6k and 3xSP30.3k films greatly restrict SA diffusion and perform worse than the monolayer, while the 3xSP77.6k urine sample performance is indistinguishable from that of the monolayer. The one outlier to this trend is the 3xSP77.6k blood sample, which displays a near 2-fold reduction in LOD compared to the Sso monolayer (**Figure 5-6f**). This enhanced performance may be attributable to the larger size of proteins in blood than in urine,<sup>23-24</sup> enabling SA to diffuse into the thin films faster than a greater fraction of proteins in blood.

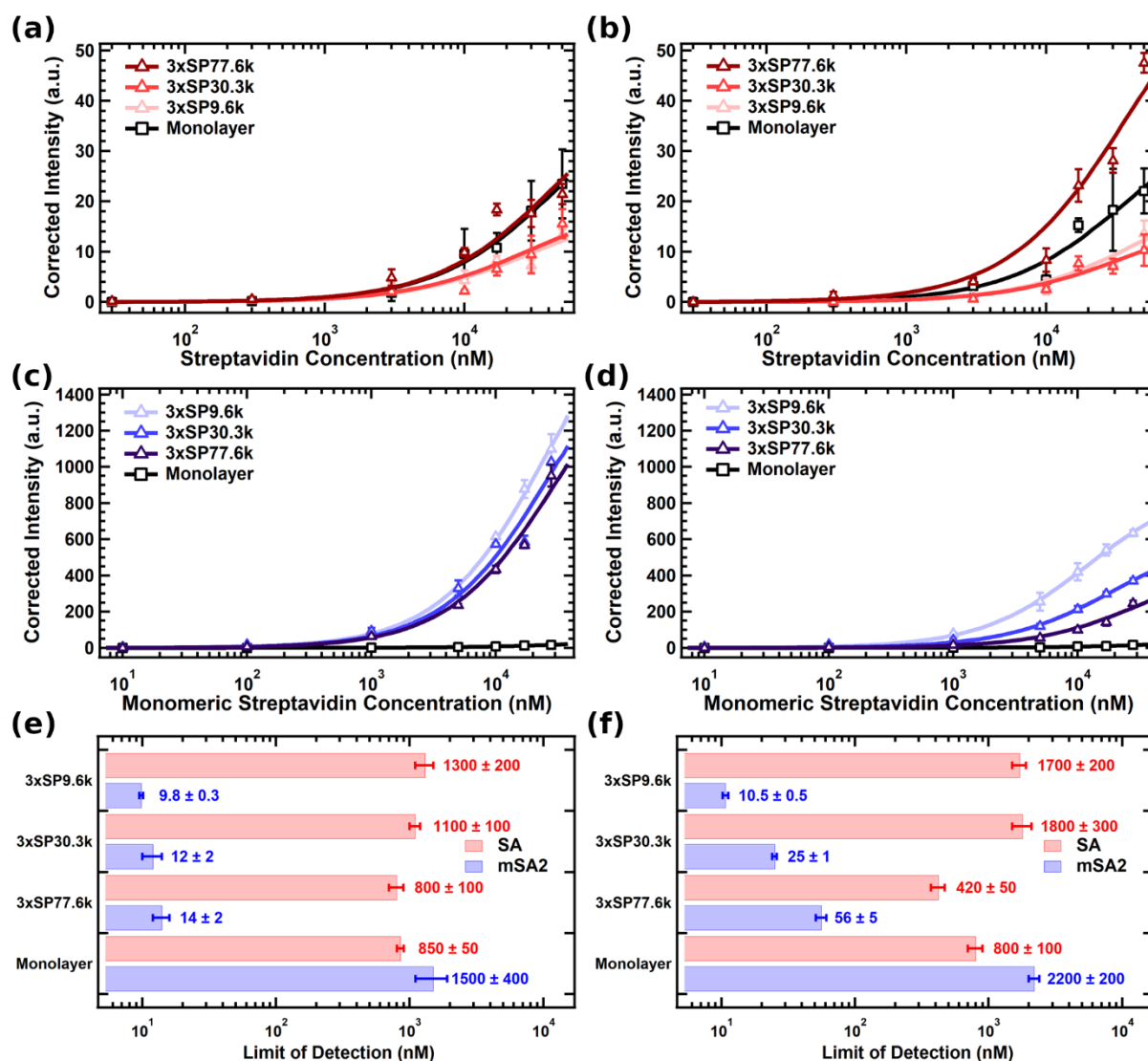


**Figure 5-6.** Binding curves for conjugate thin films exposed to (a, b) SA or (c, d) mSA2 in (a, c) 50% urine or (b, d) 50% blood serum solutions for 4 hours. Results are compared to those obtained using a Sso monolayer with a 4 hour exposure time. The limit of detection determined for each binding curve is reported for (e) urine samples and (f) blood samples. Film thicknesses are listed in **Table D-3**. Error bars represent the standard deviation of three replicates.

In the tested biological fluids, the small protein mSA2 could be detected with LOD values 2 orders of magnitude lower than those obtained when using a simple monolayer as the biosensor (**Figure 5-6c-f**). Whereas the sensitivity of the monolayer in the fluids was up to an order of magnitude worse than in buffer, the thin films showed no change or slight improvement in sensitivity. Though the linear ranges for these sensors cannot be fully calculated from the data set,

estimates of these ranges also suggest that the conjugate thin films have significantly wider linear ranges than the monolayer (**Table D-4**). The apparent improvement in thin film performance is likely a consequence of using slightly thicker films for the experiments performed in biological fluids (**Table D-3**). Indeed, more binding sites were accessible in these samples than in those used for buffer experiments (**Tables D-2, D-3**).  $K_{d,app}$  values were also consistently lower in the thin films than in the monolayers, implying that less nonspecific binding occurred in the thin films due to the greater exclusion of proteins larger than mSA2 (**Table D-3**). As expected, the  $K_{d,app}$  values increased with increasing domain spacing, corresponding to more proteins being able to penetrate films with larger domain spacings. These findings further demonstrate that domain spacing can be tuned to allow selective uptake of small proteins.

The sensing capabilities of the designed protein-polymer conjugate thin film biosensors provide substantial improvements to sensing in biological fluids compared to existing technologies. While previous studies have demonstrated that precisely designing the surface morphology of biosensors can allow sensitive analyte detection in the presence of other proteins,<sup>11-12</sup> these works either do not test their devices in mixtures of more than a few proteins<sup>12</sup> or show signal reduction when measurements are conducted in biological fluids.<sup>11</sup> In contrast, protein-polymer conjugate thin films exhibit no substantial reduction in signal or sensitivity when detecting a small protein in either serum or urine. As a more direct comparison to the biosensors developed in this study, porous silicon biosensors have been reported that act as both a filter and a substrate for biomolecule detection in whole blood.<sup>48</sup> Although the size of the silicon pores can be tuned to only permit molecules below a certain size to enter the pores (analogous to the domain spacing of polymer domains in protein-polymer conjugate thin films), nonspecific binding is still a potential issue. Blocking agents and wash buffers are required to prevent off-target molecules

that are small enough to diffuse into the pores from blocking surface binding sites. Because protein-polymer conjugate thin films contain binding sites not only on the surface of the device but also throughout the entire volume of the films, however, no blocking agents or rinsing steps are required to prevent nonspecific binding.

#### **5.4.2.3 Sensor Stability**

The developed biosensors displayed excellent stability for a protein-based sensor. When exposed to ambient conditions, films showed no significant decrease in binding capabilities over 4 weeks (**Figure D-5a**). Furthermore, when stored at 60 °C and 60% relative humidity, the films were still able to bind analyte to 50% of their original capacity after 2 weeks, only becoming completely inactive after 4 weeks. The exceptional temperature stability is unsurprising given that the Sso protein used as the molecular recognition element in these biosensors was engineered from a protein native to a hyperthermophilic microbe and was previously demonstrated to be resistant to extreme temperatures.<sup>45</sup> GISAXS linecuts indicated that no structural change had occurred in the films after 2 weeks (**Figure D-5b**), suggesting that the decrease in binding capability was the result of 3xSso denaturing without causing microstructural rearrangement.

#### **5.4.3 Sandwich Assay Demonstration**

To demonstrate that the thin film biosensors could be used in detection formats beyond simple imaging of fluorescently-labeled analytes, model sandwich assays were performed in the films. Specifically, these tests were designed to demonstrate the feasibility of using the films for multi-step detection assays such as a sandwich ELISA. The general procedure for this proof-of-concept experiment is diagramed in **Figure 5-7**. Films were first exposed to SA solutions and rinsed to remove unbound analyte. Taking advantage of the strong interaction between SA and biotin, thin films were then submerged in a solution of biotinylated horseradish peroxidase (biotin-HRP).

Bound SA was detected colorimetrically through the HRP-mediated oxidation of 3,3',5,5'-tetramethylbenzidine (TMB). Attempts to perform this assay using mSA2 as the analyte were unsuccessful, even when run on an Sso monolayer. Binding experiments with fluorescently-labeled biotin-HRP revealed extremely weak binding between biotin and mSA2 (**Figure D-6**), which is consistent with previous reports of the biotin-mSA2 dissociation constant being multiple orders of magnitude greater than that for biotin and streptavidin.<sup>46, 49</sup>

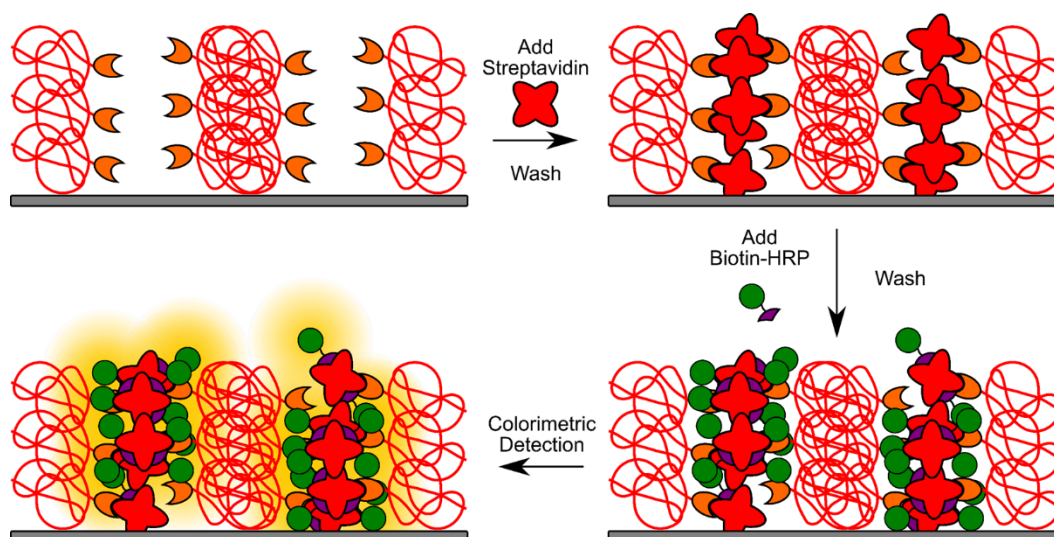


**Figure 5-7.** Schematic of model sandwich assay performed in conjugate thin film biosensors.

When SA was applied to the bioconjugate films in buffer, the films generally performed as well as a monolayer (**Figure 5-8**). In contrast to the findings using fluorescent assays, 3xSP9.6k films achieved essentially the same LOD as an Sso monolayer, while the LOD attained with 3xSP77.6k films was nearly twice as large. LOD was also found to be effectively independent of film thickness, giving a sensitivity that only varied based on the conjugate used to fabricate the film. Together, these results suggest that detection only occurred within a thin layer at the film surface. If diffusion limitations were significant enough to restrict analyte access to the majority of the film volume, the absorbance in 3xSP77.6k films would be predicted to consistently be less than that in 3xSP9.6k films due to the lower fraction of binding sites in the former films (**Table 5-**

1). This expectation is consistent with experimental observations and is reasonable when considering that in these experiments, HRP was also required to diffuse into the films to observe a signal. The relatively large size of HRP (44 kDa) combined with likely steric hindrance from SA molecules bound to the film may have resulted in restrictions to diffusion greater than in one-step fluorescent binding assays.

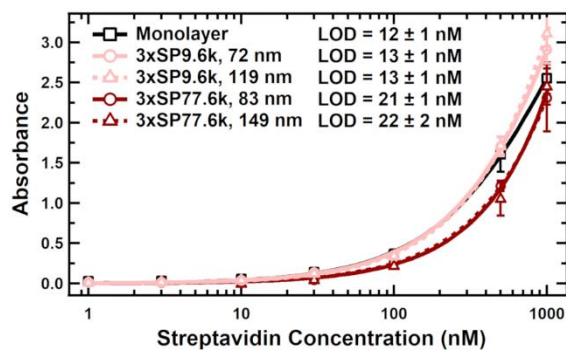


**Figure 5-8.** Binding curves for sandwich assays performed with SA in PBS. Error bars represent the standard deviation of three replicates.

Sandwich assays exposed to SA in urine and blood serum gave similar results to those found using fluorescent assays. As was observed in the fluorescent assays (**Figure 5-6a**), LODs for all tested thin films were similar to that of a monolayer when SA was dissolved in 50% urine (**Figure D-7a**). For SA samples in 50% blood serum, the LOD values for 3xSP9.6k and 3xSP30.3k films were 2-fold greater than that for an Sso monolayer (**Figure D-7b**), again mirroring results for the fluorescent assays (**Figure 5-6b**). Unlike the fluorescent assays, however, for which 3xSP77.6k films were found to give a slight improvement in LOD, these same films resulted in a 2-fold greater LOD than a monolayer in the sandwich assays, possibly due to additional diffusion limitations for HRP. Though sandwich assay experiments could not be performed using mSA2 as the analyte, the general similarities between findings for fluorescent and sandwich assays suggest that sandwich assays with a smaller analyte would yield improved LOD values relative to a

monolayer. Regardless, model sandwich assays using SA still demonstrate that these assays are feasible in the fabricated conjugate thin films.

## **5.5 Conclusions**

3xSso-PNIPAM thin films display an apparent size-based diffusional resistance for proteins entering the film. Experiments performed with both mSA2 and the larger protein SA reveal that SA experiences greater resistance to diffusion into the films. In all cases, SA either demonstrates a longer timescale for diffusion into the thin films or requires films with larger domain spacings to allow appreciable uptake. By varying the molecular weight of the polymer block in the protein-polymer conjugates used to create the thin films, domain spacing can be adjusted to tune the size of proteins that the films could uptake. This simple tuning method should allow facile design of biosensors optimized for uptake of a target analyte.

The size-based uptake properties of the bioconjugate thin films are also found to enable greatly enhanced biosensor performance in biological fluids. Not only do these films achieve an LOD an order of magnitude lower than that of a traditional surface-immobilized protein biosensor in buffer, but the LOD is also found to be up to 2 orders of magnitude lower for detection in biological fluids due to minimization of nonspecific binding events. Model sandwich assays performed in the thin films generally match results in fluorescent binding assays, demonstrating potential for application in a variety of detection formats. With their easily tunable structure and highly sensitive detection capabilities, the designed protein-polymer conjugate thin films represent an extremely promising technology for detection of small proteins and peptides (molecular weight < ca. 15 kDa) in biological matrices.

## 5.6 References

1. Byrne, B.; Stack, E.; Gilmartin, N.; O’Kennedy, R., Antibody-Based Sensors: Principles, Problems and Potential for Detection of Pathogens and Associated Toxins. *Sensors* **2009**, *9* (6), 4407, DOI: 10.3390/s90604407
2. Gebauer, M.; Skerra, A., Engineered protein scaffolds as next-generation antibody therapeutics. *Curr. Opin. Chem. Biol.* **2009**, *13* (3), 245-255, DOI: 10.1016/j.cbpa.2009.04.627
3. Binz, H. K.; Amstutz, P.; Plückthun, A., Engineering novel binding proteins from nonimmunoglobulin domains. *Nat. Biotechnol.* **2005**, *23*, 1257, DOI: 10.1038/nbt1127
4. Zhao, W.; Brook, M. A.; Li, Y., Design of Gold Nanoparticle-Based Colorimetric Biosensing Assays. *ChemBioChem* **2008**, *9* (15), 2363-2371, DOI: 10.1002/cbic.200800282
5. Grieshaber, D.; MacKenzie, R.; Vörös, J.; Reimhult, E., Electrochemical Biosensors - Sensor Principles and Architectures. *Sensors* **2008**, *8* (3), 1400, DOI: 10.3390/s80314000
6. Fan, X.; White, I. M.; Shopova, S. I.; Zhu, H.; Suter, J. D.; Sun, Y., Sensitive optical biosensors for unlabeled targets: A review. *Anal. Chim. Acta* **2008**, *620* (1), 8-26, DOI: 10.1016/j.aca.2008.05.022
7. Hoa, X. D.; Kirk, A. G.; Tabrizian, M., Towards integrated and sensitive surface plasmon resonance biosensors: A review of recent progress. *Biosens. Bioelectron.* **2007**, *23* (2), 151-160, DOI: 10.1016/j.bios.2007.07.001
8. Nguyen, H. H.; Park, J.; Kang, S.; Kim, M., Surface Plasmon Resonance: A Versatile Technique for Biosensor Applications. *Sensors* **2015**, *15* (5), 10481-10510, DOI: 10.3390/s150510481
9. Arlett, J. L.; Myers, E. B.; Roukes, M. L., Comparative advantages of mechanical biosensors. *Nat. Nano.* **2011**, *6* (4), 203-215, DOI: 10.1038/nnano.2011.44
10. Masson, J.-F., Surface Plasmon Resonance Clinical Biosensors for Medical Diagnostics. *ACS Sensors* **2017**, *2* (1), 16-30, DOI: 10.1021/acssensors.6b00763
11. Jo, J.; Yoon, J.; Lee, T.; Cho, H.-Y.; Lee, J.-Y.; Choi, J.-W., H<sub>2</sub>O<sub>2</sub> biosensor consisted of hemoglobin-DNA conjugate on nanoporous gold thin film electrode with electrochemical signal enhancement. *Nano Convergence* **2019**, *6* (1), 1, DOI: 10.1186/s40580-018-0172-z
12. Lee, J.-H.; Park, B.-S.; Ghang, H.-G.; Song, H.; Yang, S. Y., Nano-Protrusive Gold Nanoparticle-Hybridized Polymer Thin Film as a Sensitive, Multipatternable, and Antifouling Biosensor Platform. *ACS Appl. Mater. Interfaces* **2018**, *10* (16), 13397-13405, DOI: 10.1021/acami.8b03681
13. Wisniewski, N.; Reichert, M., Methods for reducing biosensor membrane biofouling. *Colloids Surf. B. Biointerfaces* **2000**, *18* (3), 197-219, DOI: 10.1016/S0927-7765(99)00148-4
14. Haun, J. B.; Yoon, T.-J.; Lee, H.; Weissleder, R., Magnetic nanoparticle biosensors. *Wiley Interdiscip. Rev. Nanomed. Nanobiotechnol.* **2010**, *2* (3), 291-304, DOI: 10.1002/wnan.84
15. Tekin, H. C.; Gijs, M. A. M., Ultrasensitive protein detection: a case for microfluidic magnetic bead-based assays. *Lab Chip* **2013**, *13* (24), 4711-4739, DOI: 10.1039/C3LC50477H
16. Desai, T. A.; Hansford, D. J.; Leoni, L.; Essenpreis, M.; Ferrari, M., Nanoporous anti-fouling silicon membranes for biosensor applications. *Biosens. Bioelectron.* **2000**, *15* (9), 453-462, DOI: 10.1016/S0956-5663(00)00088-9
17. Yuan, C.-J.; Hsu, C.-L.; Wang, S.-C.; Chang, K.-S., Eliminating the Interference of Ascorbic Acid and Uric Acid to the Amperometric Glucose Biosensor by Cation Exchangers Membrane and Size Exclusion Membrane. *Electroanalysis* **2005**, *17* (24), 2239-2245, DOI: 10.1002/elan.200503359

18. Wang, S.; Sarenac, D.; Chen, M. H.; Huang, S.-H.; Giguel, F. F.; Kuritzkes, D. R.; Demirci, U., Simple filter microchip for rapid separation of plasma and viruses from whole blood. *Int. J. Nanomed* **2012**, *7*, 5019-5028, DOI: 10.2147/IJN.S32579
19. Thorslund, S.; Klett, O.; Nikolajeff, F.; Markides, K.; Bergquist, J., A hybrid poly(dimethylsiloxane) microsystem for on-chip whole blood filtration optimized for steroid screening. *Biomed. Microdevices* **2006**, *8* (1), 73-79, DOI: 10.1007/s10544-006-6385-7
20. Pfäfflin, A.; Schleicher, E., Inflammation markers in point-of-care testing (POCT). *Anal. Bioanal. Chem.* **2008**, *393* (5), 1473, DOI: 10.1007/s00216-008-2561-3
21. Saito, Y.; Nakao, K.; Itoh, H.; Yamada, T.; Mukoyama, M.; Arai, H.; Hosoda, K.; Shirakami, G.; Suga, S.-i.; Minamino, N.; Kangawa, K.; Matsuo, H.; Imura, H., Brain natriuretic peptide is a novel cardiac hormone. *Biochem. Biophys. Res. Commun.* **1989**, *158* (2), 360-368, DOI: 10.1016/S0006-291X(89)80056-7
22. Murphy, M. P.; LeVine, H., Alzheimer's Disease and the  $\beta$ -Amyloid Peptide. *J. Alzheimers Dis.* **2010**, *19* (1), 311, DOI: 10.3233/JAD-2010-1221
23. Schenk, S.; Schoenhals, G. J.; de Souza, G.; Mann, M., A high confidence, manually validated human blood plasma protein reference set. *BMC Medical Genomics* **2008**, *1* (1), 41, DOI: 10.1186/1755-8794-1-41
24. Adachi, J.; Kumar, C.; Zhang, Y.; Olsen, J. V.; Mann, M., The human urinary proteome contains more than 1500 proteins, including a large proportion of membrane proteins. *Genome Biol.* **2006**, *7* (9), R80, DOI: 10.1186/gb-2006-7-9-r80
25. Burkert, S.; Bittrich, E.; Kuntzsch, M.; Müller, M.; Eichhorn, K.-J.; Bellmann, C.; Uhlmann, P.; Stamm, M., Protein Resistance of PNIPAAm Brushes: Application to Switchable Protein Adsorption. *Langmuir* **2010**, *26* (3), 1786-1795, DOI: 10.1021/la902505q
26. Rodriguez-Emmenegger, C.; Brynda, E.; Riedel, T.; Houska, M.; Šubr, V.; Alles, A. B.; Hasan, E.; Gautrot, J. E.; Huck, W. T. S., Polymer Brushes Showing Non-Fouling in Blood Plasma Challenge the Currently Accepted Design of Protein Resistant Surfaces. *Macromol. Rapid Commun.* **2011**, *32* (13), 952-957, DOI: 10.1002/marc.201100189
27. Chen, W.-L.; Cordero, R.; Tran, H.; Ober, C. K., 50th Anniversary Perspective: Polymer Brushes: Novel Surfaces for Future Materials. *Macromolecules* **2017**, *50* (11), 4089-4113, DOI: 10.1021/acs.macromol.7b00450
28. Blackman, L. D.; Varlas, S.; Arno, M. C.; Houston, Z. H.; Fletcher, N. L.; Thurecht, K. J.; Hasan, M.; Gibson, M. I.; O'Reilly, R. K., Confinement of Therapeutic Enzymes in Selectively Permeable Polymer Vesicles by Polymerization-Induced Self-Assembly (PISA) Reduces Antibody Binding and Proteolytic Susceptibility. *ACS Cent. Sci.* **2018**, *4* (6), 718-723, DOI: 10.1021/acscentsci.8b00168
29. Blackman, L. D.; Varlas, S.; Arno, M. C.; Fayter, A.; Gibson, M. I.; O'Reilly, R. K., Permeable Protein-Loaded Polymersome Cascade Nanoreactors by Polymerization-Induced Self-Assembly. *ACS Macro Lett.* **2017**, *6* (11), 1263-1267, DOI: 10.1021/acsmacrolett.7b00725
30. Yoshikawa, C.; Goto, A.; Tsujii, Y.; Fukuda, T.; Kimura, T.; Yamamoto, K.; Kishida, A., Protein Repellency of Well-Defined, Concentrated Poly(2-hydroxyethyl methacrylate) Brushes by the Size-Exclusion Effect. *Macromolecules* **2006**, *39* (6), 2284-2290, DOI: 10.1021/ma0520242
31. Halperin, A., Polymer Brushes that Resist Adsorption of Model Proteins: Design Parameters. *Langmuir* **1999**, *15* (7), 2525-2533, DOI: 10.1021/la981356f
32. Chrambach, A.; Rodbard, D., Polyacrylamide Gel Electrophoresis. *Science* **1971**, *172* (3982), 440-451, DOI: 10.1126/science.172.3982.440

33. Urueña, J. M.; Pitenis, A. A.; Nixon, R. M.; Schulze, K. D.; Angelini, T. E.; Gregory Sawyer, W., Mesh Size Control of Polymer Fluctuation Lubrication in Gemini Hydrogels. *Biotribology* **2015**, *1-2*, 24-29, DOI: 10.1016/j.biotri.2015.03.001
34. Lieleg, O.; Ribbeck, K., Biological hydrogels as selective diffusion barriers. *Trends Cell Biol.* **2011**, *21* (9), 543-551, DOI: 10.1016/j.tcb.2011.06.002
35. Paloni, J. M.; Miller, E. A.; Sikes, H. D.; Olsen, B. D., Improved Ordering in Low Molecular Weight Protein–Polymer Conjugates Through Oligomerization of the Protein Block. *Biomacromolecules* **2018**, *19* (9), 3814-3824, DOI: 10.1021/acs.biomac.8b00928
36. Thomas, C. S.; Olsen, B. D., Coil fraction-dependent phase behaviour of a model globular protein–polymer diblock copolymer. *Soft Matter* **2014**, *10* (17), 3093-3102, DOI: 10.1039/C3SM52531G
37. Lam, C. N.; Kim, M.; Thomas, C. S.; Chang, D.; Sanoja, G. E.; Okwara, C. U.; Olsen, B. D., The Nature of Protein Interactions Governing Globular Protein–Polymer Block Copolymer Self-Assembly. *Biomacromolecules* **2014**, *15* (4), 1248-1258, DOI: 10.1021/bm401817p
38. Thomas, C. S.; Glassman, M. J.; Olsen, B. D., Solid-State Nanostructured Materials from Self-Assembly of a Globular Protein–Polymer Diblock Copolymer. *ACS Nano* **2011**, *5* (7), 5697-5707, DOI: 10.1021/nn2013673
39. Thomas, C. S.; Xu, L.; Olsen, B. D., Kinetically Controlled Nanostructure Formation in Self-Assembled Globular Protein–Polymer Diblock Copolymers. *Biomacromolecules* **2012**, *13* (9), 2781-2792, DOI: 10.1021/bm300763x
40. Lam, C. N.; Olsen, B. D., Phase transitions in concentrated solution self-assembly of globular protein–polymer block copolymers. *Soft Matter* **2013**, *9* (8), 2393-2402, DOI: 10.1039/C2SM27459K
41. Dong, X. H.; Obermeyer, A. C.; Olsen, B. D., Three-Dimensional Ordered Antibody Arrays Through Self-Assembly of Antibody–Polymer Conjugates. *Angew. Chem. Int. Ed.* **2017**, *56* (5), 1273-1277, DOI: 10.1002/anie.201607085
42. Chang, D.; Huang, A.; Olsen, B. D., Kinetic Effects on Self-Assembly and Function of Protein–Polymer Bioconjugates in Thin Films Prepared by Flow Coating. *Macromol. Rapid Commun.* **2017**, *38* (1), 1600449, DOI: 10.1002/marc.201600449
43. Dixit, C. K.; Vashist, S. K.; MacCraith, B. D.; O’Kennedy, R., Multisubstrate-compatible ELISA procedures for rapid and high-sensitivity immunoassays. *Nat. Prot.* **2011**, *6*, 439, DOI: 10.1038/nprot.2011.304
44. Schneider, C. A.; Rasband, W. S.; Eliceiri, K. W., NIH Image to ImageJ: 25 years of image analysis. *Nat. Methods* **2012**, *9*, 671, DOI: 10.1038/nmeth.2089
45. Miller, E. A.; Traxlmayr, M. W.; Shen, J.; Sikes, H. D., Activity-based assessment of an engineered hyperthermophilic protein as a capture agent in paper-based diagnostic tests. *Mol. Syst. Des. Eng.* **2016**, *1* (4), 377-381, DOI: 10.1039/C6ME00032K
46. DeMonte, D.; Drake, E. J.; Lim, K. H.; Gulick, A. M.; Park, S., Structure-based engineering of streptavidin monomer with a reduced biotin dissociation rate. *Proteins: Struct., Funct., Bioinf.* **2013**, *81* (9), 1621-1633, DOI: 10.1002/prot.24320
47. Baumann, H.; Knapp, S.; Lundbäck, T.; Ladenstein, R.; Härd, T., Solution structure and DNA-binding properties of a thermostable protein from the archaeon *Sulfolobus solfataricus*. *Nat. Struct. Biol.* **1994**, *1*, 808, DOI: 10.1038/nsb1194-808
48. Bonanno, L. M.; DeLouise, L. A., Whole blood optical biosensor. *Biosens. Bioelectron.* **2007**, *23* (3), 444-448, DOI: 10.1016/j.bios.2007.05.008

49. Lim, K. H.; Huang, H.; Pralle, A.; Park, S., Stable, high-affinity streptavidin monomer for protein labeling and monovalent biotin detection. *Biotechnol. Bioeng.* **2013**, *110* (1), 57-67, DOI: 10.1002/bit.24605

## **Chapter 6. Polymer Domains Control Diffusion in Protein-Polymer Conjugate Biosensors**

### **6.1 Abstract**

While surface-based biosensors have been widely used in diagnostic applications, these sensors experience reduced sensitivity in the most common detection fluids due to nonspecific binding effects from non-analyte molecules. Protein-polymer conjugate thin films have been demonstrated to overcome many of these nonspecific binding issues due to their ability to restrict transport of impurity molecules into the film, but the transport mechanism within these films is not understood. Herein, the diffusion coefficients of 15 different proteins and dextran molecules are measured within protein gels and polymer solutions that mimic the phase-separated protein and polymer domains of the conjugate thin films using fluorescence recovery after photobleaching (FRAP). While most molecules have diffusivities that are consistent with size-based diffusion models, several protein diffusivities deviate significantly from these model predictions in polymer solutions. Mixtures of monomeric streptavidin (mSA2), an analyte for the thin film biosensors, with proteins that diffuse faster than mSA2 in the polymer solutions give greater biosensor sensitivity for mSA2 than solutions of mSA2 alone. Furthermore, a mixture containing several of the proteins in this work is also found to also result in greater sensitivity for mSA2 than a pure mSA2 solution. These findings suggest that the polymer domains are primarily responsible for transport in the thin films and, unlike other surface-based biosensors, protein-polymer conjugate biosensors can exhibit enhanced sensitivity in complex sensing mixtures.

### **6.2 Introduction**

Biosensors, devices that selectively detect one or more biomolecules and relay this detection in the form of a measurable signal, have seen widespread use in the diagnostics field.<sup>1-3</sup> The analyte recognition element, usually a protein, is often incorporated onto a surface using one of a wide

range of immobilization strategies.<sup>4-6</sup> As a result, a variety of device formats have been developed, including surface plasmon resonance,<sup>4, 7-9</sup> electrochemical sensing,<sup>10-11</sup> and microfluidic biosensors.<sup>12-13</sup> Despite decades of research on surface-based biosensors, many fundamental design challenges remain, such as ensuring accurate surface characterization<sup>14</sup> and experimental conditions that allow for consistent device performance.<sup>15</sup>

One of the most pervasive issues with surface-based biosensors, however, is reduction in performance due to nonspecific binding. Most detection fluids (e.g., blood, urine) primarily contain off-target molecules that block binding sites and bind to unfunctionalized surfaces of the sensors, even in diluted samples.<sup>16-17</sup> As such, the background signal is enhanced and/or the binding signal is reduced, resulting in decreases of limit of detection up to several orders of magnitude.<sup>18-19</sup> To minimize the effects of nonspecific binding, some techniques have been developed that make use of the weaker interactions of nonspecifically bound proteins to better select for the desired analyte, including molecular imprinting<sup>20</sup> and hypersonic resonance.<sup>21</sup> Other methods restrict diffusion of undesired molecules to the sensor surface using membranes that can filter molecules based on charge,<sup>22-23</sup> pores that enable size-based diffusion into the device,<sup>24</sup> or crosslinked gel coatings that greatly restrict diffusion to the sensor surface.<sup>25</sup> Since these latter approaches require differential diffusivities between the analyte and other species, controlling transport within surface-based biosensors is critical to their performance.

The drive to develop highly sensitive biosensors has motivated the study of numerous methods to measure and optimize transport in these devices. If a biosensor is simply composed of a functionalized surface, mass transport limitations can be assumed to occur within a region close to the surface, often referred to as the depletion region.<sup>26</sup> Full convection-reaction-diffusion models are able to replicate this depletion region, but these models can overpredict analyte binding

times by several orders of magnitude.<sup>27</sup> Analyte transport in biosensors with more complex surface geometries designed to enhance sensitivity has also been considered, such as in sensors with nanoscale sensing regions. However, this miniaturization enhances the signal-to-noise ratio at the expense of reduced mass transport.<sup>28</sup> Therefore, this requires shuttling or other forms of active transport of analyte to the sensing regions to avoid long binding times.<sup>29</sup> In addition, simply adding nanohole arrays between the bulk fluid and a nanochannel containing the sensing surface has been demonstrated to improve detection times by an order of magnitude.<sup>30</sup> Increasing the sensor surface area also facilitates more rapid mass transport,<sup>31-32</sup> though some geometries require slow reaction kinetics to realize this enhanced transport rate.<sup>31</sup> While these biosensor architectures do optimize transport for enhanced sensitivity or response time, few incorporate methods to combat nonspecific binding effects.

Concentrated polymer systems offer a mechanism for controlling transport of particles based on their physical properties. For nanoparticles in polymer solutions, the diffusivity of the particle is dependent upon the size of the particle relative to the radius of gyration ( $R_g$ ) of the polymer.<sup>33</sup> While diffusion follows the Stokes-Einstein relation if the nanoparticle is larger than the polymer  $R_g$ , the particle diffuses much faster than is predicted by this equation if the particle is smaller than the polymer  $R_g$ .<sup>34-36</sup> Theories have been developed to rationalize this phenomenon, which have assumed diffusion mechanisms including nanoparticle hopping between entanglements<sup>37</sup> and fast diffusion within a confined depletion region at small length scales.<sup>38-39</sup> Though protein diffusion in polymers should generally follow these principles, proteins can also interact with polymers, leading to more complex transport phenomena. Polymers such as dextran that interact with proteins increase the effective hydrodynamic diameter of the protein, causing negative deviations in translational diffusivity from Stokes-Einstein predictions.<sup>40-43</sup> Even

polymers that do not interact with proteins, however, can still affect diffusion by indirectly controlling protein-protein association. When these non-interacting polymers are in the dilute regime, the polymers induce preferential hydration of the proteins, reducing the likelihood of aggregation.<sup>42, 44</sup> In the semidilute regime, association rates are enhanced, while in the concentrated regime, protein-protein association is again diminished, which has been attributed to depletion effects.<sup>44</sup> Thus, diffusion of proteins in polymer solutions is incredibly complex, depending upon the identity and concentration of both the protein and polymer.

Because polymers can offer great control over protein diffusion, these molecules have been incorporated into biosensors to restrict diffusion of certain proteins near the surface of the sensor. For example, polymer brushes have commonly been installed to reduce nonspecific binding in both surface-based<sup>45-46</sup> and hydrogel biosensors.<sup>47</sup> Polymer matrices and films have similarly been installed on biosensor surfaces to control diffusion rates to the sensor surface<sup>48-50</sup> and have shown potential for hindering diffusion of large molecules.<sup>51</sup> Recently, our group reported the development of protein-polymer conjugate thin film biosensors, which exhibited self-assembly into phase-separated regions of polymer and binding proteins.<sup>52</sup> These sensors achieved a two order of magnitude improvement in limit of detection in plasma and urine compared to biosensors composed of the binding proteins directly immobilized onto a surface, and this enhanced sensitivity was attributed to size-based exclusion of off-target molecules. Despite the clear benefits that this biosensor architecture provides for sensing in biological fluids, relatively little is known about the transport mechanisms within these conjugate thin films.

In this work, the major factors controlling diffusion within protein-polymer conjugate thin film biosensors are determined. Diffusion coefficients of a library of 11 proteins and 4 dextran molecules are measured within analogues of the protein and polymer domains of these films using

fluorescence recovery after photobleaching (FRAP). These results are compared to binding experiments within the films, suggesting that diffusion within the thin films is primarily controlled by the polymer domains. It is also found that, in contrast to other surface-based biosensors, sensitivity of protein-polymer conjugate sensors can be increased during measurements in complex mixtures.

## **6.3 Materials and Methods**

### **6.3.1 Materials**

All solvents were purchased from VWR, and all other chemicals were purchased from Millipore Sigma and used without further purification. Cytochrome C (CytC) and Transferrin (TrFe) were purchased from Lee Biosolutions. Streptavidin (SA) was purchased from New England Biolabs. All dextran molecules and Alexa Fluor 647 NHS ester were purchased from Thermo Fisher Scientific. Lysozyme (Lys), bovine serum albumin (BSA), glucose oxidase (GOx), catalase (Cat), and fluorescein isothiocyanate (FITC) were purchased from Millipore Sigma. Silicon wafers were purchased from Wafer World.

### **6.3.2 PNIPAM Synthesis**

Poly(N-isopropylacrylamide) (PNIPAM) functionalized with a maleimide endgroup was synthesized by reversible addition-fragmentation chain transfer (RAFT) polymerization, as described previously.<sup>53</sup> Polymer molecular weight and dispersity were characterized by gel permeation chromatography performed on an Agilent 1260 LC system equipped with two columns (ResiPore, 300 × 7.5 mm, up to 500kDa, Agilent Technologies, CA) in series, a Wyatt miniDAWN TREOS multi-angle light scattering detector, and a Wyatt Optilab T-rEX diffractometer (**Figure E-1**). Dimethylformamide (DMF) with 0.02 LiBr was used as the mobile phase with a flow rate of 1 mL/min at 70 °C.

### **6.3.3 Protein Expression and Bioconjugation**

3x rcSso7d.SA (3xSso), monomeric streptavidin (mSA2), and GFP variants GFP(0), GFP(-8), and GFP(-21) were expressed as described previously.<sup>54-55</sup> Bioconjugations between 3xSso and maleimide-functionalized PNIPAM were performed in resuspension buffer (50 mM Tris buffer, 100 mM NaCl, 0.25 mM tris(2-carboxyethyl)phosphine (TCEP), pH 7.4). Solutions of 3xSso were diluted to approximately 1 mg/mL, and a 5x molar excess of PNIPAM was added. After complete dissolution of PNIPAM, samples were incubated at 4 °C for 24 h. Ammonium sulfate was then added to a concentration of 1.0 M to remove unconjugated protein. Following centrifugation, the supernatant was discarded, and the precipitates were resuspended in resuspension buffer to approximately 1 mg/mL. Two additional ammonium sulfate precipitations were performed, after which the resulting solution was purified by Ni-NTA chromatography to remove unconjugated PNIPAM. Purified protein-PNIPAM conjugates were dialyzed against Milli-Q water. Bioconjugate purity was confirmed using SDS-PAGE and native PAGE (**Figure A-8**), and retention of protein secondary structure was assessed using CD (**Figure A-7**). Conjugate solution was concentrated to approximately 100 mg/mL using Millipore-Ultra 15 centrifugal filters (molecular weight cutoff of 10 kDa). Bulk solid samples were prepared by drop-casting aliquots of this concentrated solution onto Teflon sheets and drying under vacuum to a final pressure of 5 Torr (ramp rate 50 Torr/h) at room temperature. Samples were then collected and stored at 4 °C until future use. Typical yield after purification for all conjugates was 30%.

### **6.3.4 Fluorescence Recovery After Photobleaching (FRAP) Sample Preparation**

The diffusion of a large library of molecular probes with a variety of physical properties was measured in FRAP experiments. Eight proteins with a wide range of hydrodynamic diameters, two of which displayed strong, selective binding for 3xSso (SA and mSA2), were selected for

measuring size-based diffusion within each solution. Three variants of superfolder GFP with formal charges ranging from 0 to -21 were used to measure the effect of molecular charge on diffusion. Dextran molecules, which contained a much more flexible structure than proteins, allowed determination of conformational effects on transport. Each of these molecules was labeled with FITC, as described in **Chapter 2**.

Crosslinked protein gels were prepared by concentrating a solution of 3xSso in sodium phosphate buffer (50 mM sodium phosphate, 150 mM NaCl, pH 7.2) to 20 wt.%. The concentrated protein solution was then heated to 40 °C, and a 10x glutaraldehyde solution (final concentration of 1.4 wt.% in MilliQ water) was added to the protein solution by quickly pipetting up and down. The mixture was crosslinked at 40 °C for 30 seconds, resulting in gelation. Residual glutaraldehyde was removed by rinsing the gel with Milli-Q water. The gel was then stored at 4 °C for future use.

To prepare samples for microscopy, a small section from the gel (volume of < ca. 1 mm<sup>3</sup>, thickness of at least 10 μm) was excised, and 200 μL of a 1 μM solution of FITC-labeled protein or dextran sample was added to the gel. The gel was allowed to equilibrate in the solution for 16 hours in the dark at 4 °C. Immediately before FRAP measurements were conducted, the fluorescent solution was pipetted off, and the gel was rinsed with 100 μL of Milli-Q water to remove protein on the gel surface. The gel was then placed between a glass slide and a coverslip containing double-sided tape edges to seal the gel in place. Milli-Q water was then pipetted into the channel formed between the glass slide and coverslip, and the two open edges of the channel were sealed using Sally Hansen Hard as Nails hardener.

Samples for diffusion measurements in PNIPAM solutions were prepared by first dissolving PNIPAM samples of the desired molecular weight in Milli-Q water to a final concentration of 20 wt.%. FITC-labeled protein and dextran samples in PBS were then

concentrated to  $\sim 10 \mu\text{M}$ , and  $5 \mu\text{L}$  of these solutions were added to PCR tubes containing  $55 \mu\text{L}$  of PNIPAM solution.

Microscope slides for diffusion measurements in PNIPAM solutions were prepared by adhering a Teflon spacer (No. 12 screw size, 0.25 in. ID, 0.5 in. OD, 0.06 in. thickness, McMaster-Carr) to the center of a glass microscope slide using Sally Hansen Hard as Nails hardener. The top of the spacer was then coated with a thin, even layer of nail hardener, the PNIPAM solution containing fluorescently-labeled protein was pipetted into the spacer, and a microscope slide was placed on top of the spacer to seal the PNIPAM solution. The hardener was allowed to dry for 1 hour at room temperature in the dark and then stored at  $4 \text{ }^\circ\text{C}$  in the dark for at least 16 hours.

### **6.3.5 FRAP Experiments**

Imaging was performed on a confocal laser scanning microscope (Zeiss LSM 710, W.M. Keck Microscopy Facility) equipped with an oil-immersion 40x objective lens. A circular region of interest was photobleached for 1 second using a 488 nm laser at full power, and fluorescence recovery was monitored by scanning the region of interest at low laser power (24%) every second for 1 min after bleaching. Images were also collected every second for 5 seconds prior to the bleaching event to obtain a pre-bleach intensity value within the bleached region.

FRAP curves were generated by using ImageJ software to process the full sequence of fluorescence images collected. For each image, fluorescence intensity values were adjusted to account for fluctuations in laser intensity by dividing the average fluorescence intensity within the circular bleach region by the average intensity within a rectangular area far from the bleach region. These fluctuation-adjusted fluorescence values were then normalized between values of 0 (the fluctuation-adjusted fluorescence value immediately after bleaching) and 1 (the average of the

fluctuation-adjusted fluorescence values in the 5 images collected prior to bleaching) to obtain a normalized FRAP curve as a function of time  $f(t)$ .

### **6.3.6 Thin Film Preparation**

Silicon wafers (P-type Silicon with boron as dopant, (100) orientation, single-side polished) cut into rectangular sections were sequentially rinsed with acetone, methanol, and water. Substrates were then dried under a filtered air flow and treated with oxygen plasma for 3 minutes. Immediately following plasma cleaning, conjugate samples rehydrated to 10 wt.% in Milli-Q water were flow coated onto the substrates in a chamber maintained at 60% relative humidity, as described previously.<sup>56</sup> To stabilize thin films against dissolution in water, the cast films were preheated to 40 °C and immersed in a 1.4 wt.% aqueous solution of glutaraldehyde at 40 °C for 20 s to lightly crosslink the protein nanodomains. Immediately following immersion, thin films were thoroughly rinsed with water until the surfaces became hydrophilic, indicating complete removal of unlinked glutaraldehyde. Films were dried under filtered air and stored at ambient conditions until use. Film thickness was determined using a Woolam M-2000D spectroscopic ellipsometer using a single incidence angle of 70°. Curves were fit using a three-layer model consisting of a 0.4 mm bottom silicon substrate, a native silicon oxide layer of 1.8 nm, and a top conjugate layer fit using a Cauchy model.

### **6.3.7 Fluorescence Assays**

The binding capabilities of conjugate thin films were measured using mSA2 labeled with Alexa Fluor 647. Samples were prepared by dissolving unlabeled proteins in PBS (pH 7.4) at a concentration of either 10 or 100 μM. A 100x solution of fluorescently-labeled mSA2 (final concentration of 1 μM) was added to each protein solution. These solutions containing mSA2 were gently applied to the surface of a bioconjugate thin film as 0.5 μL drops. Films were incubated for

4 hours in a sealed chamber saturated with water vapor at room temperature to prevent drying of the applied fluorescent samples. The films were then rinsed with Milli-Q water, dried under filtered air, and immediately analyzed for fluorescence signal. Fluorescence microscopy images were acquired at 4x magnification using a Cy5 filter set and exposure time of 5000 ms on an Olympus IX-81 inverted fluorescence microscope with an AxioCam HRC CCD camera. Fluorescence intensity was calculated using ImageJ software by determining the average fluorescence signal in a rectangular area of the fluorescent image free of defects and occupying no less than half of the full sample application area. Background-corrected intensity was determined by subtracting the fluorescence intensity of a sample from that of an area on the substrate far away from regions exposed to fluorescent samples.

### **6.3.8 Additional Characterization Methods**

The concentrated solution phase behavior of the studied bioconjugates was characterized using small-angle X-ray scattering (SAXS). Thin film morphology in both the swollen and dry states was characterized using grazing-incidence SAXS (GISAXS). Details of the sample preparation and measurement conditions for these techniques are provided in **Chapter 2**. Circular dichroism (CD) spectroscopy, dynamic light scattering (DLS), and small-angle neutron scattering (SANS) procedures are also provided in **Chapter 2**.

## **6.4 Results and Discussion**

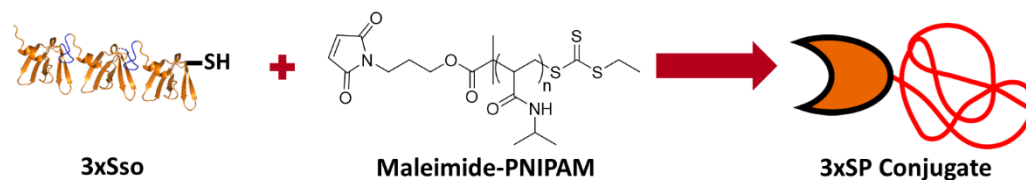
### **6.4.1 Overview of Diffusion Experiments**

Previous work has suggested that size-based diffusion in protein-polymer conjugate films that are phase-separated into alternating domains of protein and polymer is controlled by the molecular weight of the polymer block.<sup>52</sup> Thus, to determine if transport in one domain is more strongly correlated with transport in the entire thin film, diffusion measurements were performed in

crosslinked protein gels (an approximation of protein domains in the films) and polymer solutions (an approximation of the polymer domains). Appropriate concentrations for these two solutions were estimated by measuring the conjugate concentration within fully-swollen thin films, which is representative of the thin film state when exposed to an analyte in solution.

#### **6.4.2 Thin Film Characterization**

Protein-polymer conjugate thin films were fabricated with domain spacings that varied as a function of polymer molecular weight and degree of film swelling. By conjugating an rcSso7d.SA trimer (3xSso)<sup>55</sup> to poly(N-isopropylacrylamide) (PNIPAM), 3xSP conjugates were synthesized (**Scheme 6-1**). Six unique conjugates were created by varying the molecular weight of the PNIPAM molecule conjugated to 3xSso (**Table 6-1**). Thin films fabricated from these 3xSP conjugates all adopt a weakly phase-separated morphology with no strong directional orientation at 0% relative humidity (RH) (**Figures 6-1a, E-2**). The domain spacings within these dry films show good agreement with bulk SAXS data (**Figure 6-1b**), suggesting that the morphology within the thin films is similar to that of the bulk conjugates (**Figure E-3**). Crosslinking the 3xSso domains with glutaraldehyde results in a slight increase in domain spacing across all conjugate samples (**Figure 6-1b**), as has been observed in other protein-PNIPAM conjugate thin films.<sup>57</sup> Swelling these crosslinked films by exposure to an atmosphere at 95% RH causes a further increase in domain spacing due to water uptake within the domains (**Figure 6-1b**). Uncrosslinked thin films are also able to absorb water, but the lack of crosslinks in these films to stabilize the structure results in complete film dissolution at high RH.



**Scheme 6-1.** Bioconjugation of 3xSso containing an N-terminal cysteine residue to maleimide-functionalized PNIPAM to form a 3xSP conjugate. Orange regions in 3xSso are cartoon representations of the Sso7d crystal structure generated using Protein Data Bank ID: 1SSO.<sup>58</sup>

**Table 6-1.** Composition of 3xSP Conjugates

Conjugate	PNIPAM $M_n$ (kDa)	PNIPAM $\bar{D}$	Protein Weight Fraction
3xSP9.6k	9.6	1.05	0.72
3xSP23k	23.3	1.06	0.52
3xSP46k	46.6	1.13	0.35
3xSP56k	56.1	1.11	0.31
3xSP77k	77.6	1.13	0.24
3xSP117k	117	1.26	0.18

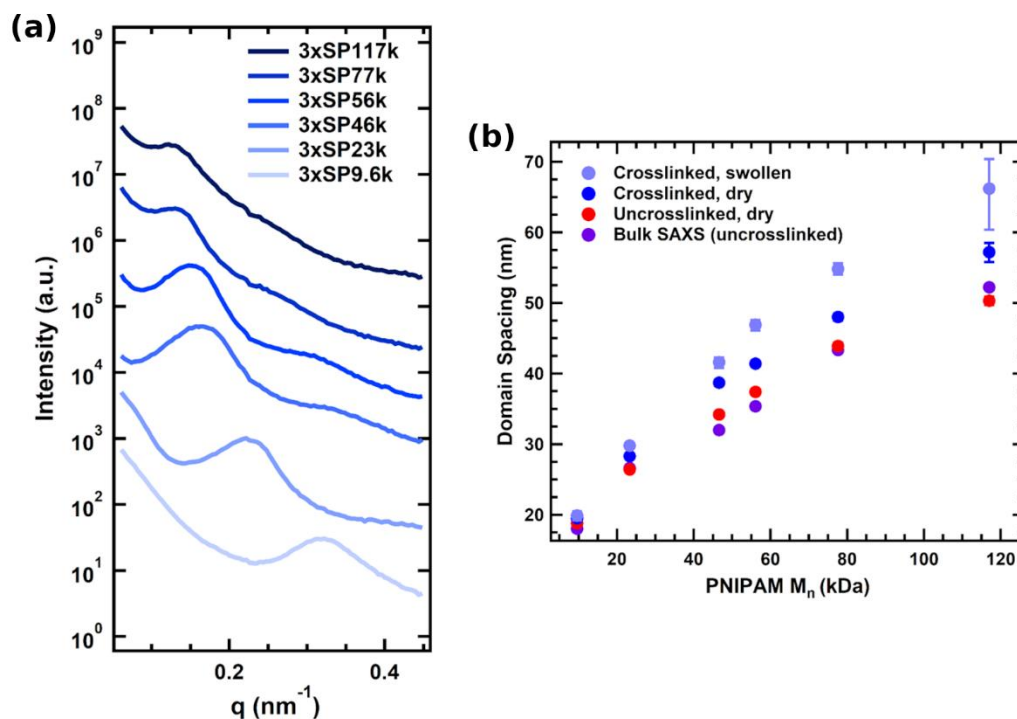


**Figure 6-1.** (a) Linecuts of GISAXS patterns for thin films crosslinked with glutaraldehyde at 0% RH, and (b) domain spacings of bulk conjugate samples and thin films at either 0% RH (dry) or 95% RH (swollen) and with 3xSso domains that were either uncrosslinked or crosslinked. Full GISAXS patterns from which linecuts in (a) were obtained are presented in **Figure E-2**. Error bars in (b) represent 95% confidence intervals for the fit parameter values, as described in **Chapter 2**.

The 3xSP thin films generally swell to the same degree in a humid environment regardless of the molar mass of the PNIPAM block. The average swelling ratio across all films is approximately 5, and most films have a swelling ratio close to this value (**Table 6-2**). It is unlikely that swelling effects resulting from possibly different PNIPAM topologies between the 3xSP films are relevant, as swelling ratio has a much stronger dependence on initial film thickness (similar across all samples) than PNIPAM topology.<sup>59</sup> Because each thin film has a different composition of protein and polymer (**Table 6-1**), the similar swelling ratios imply that water is close to a nonselective solvent, swelling the 3xSso and PNIPAM domains to an approximately equal degree. Indeed, previous studies of protein-PNIPAM conjugates have found that water is only slightly selective for the PNIPAM domains.<sup>60</sup> As such, the conjugate volume fraction in the swollen thin films, about 0.2, should be approximately equal to the volume fractions of 3xSso and PNIPAM within their respective domains in the films. Correspondingly, diffusion measurements within samples of each individual block were performed at a volume fraction of 0.2 in both 3xSso gels and PNIPAM solutions.

**Table 6-2.** Thicknesses of Dry and Swollen 3xSP Conjugate Thin Films

Conjugate	Dry Thickness <sup>a</sup> (nm)	Swollen Thickness <sup>b</sup> (nm)	Swelling Ratio <sup>c</sup>
3xSP9.6k	110 ± 10	400 ± 50	3.7 ± 0.6
3xSP23k	98 ± 8	490 ± 50	5.0 ± 0.7
3xSP46k	92 ± 9	400 ± 40	4.3 ± 0.6
3xSP56k	103 ± 5	590 ± 70	5.7 ± 0.7
3xSP77k	90 ± 10	410 ± 40	4.7 ± 0.8
3xSP117k	106 ± 8	560 ± 50	5.3 ± 0.6

<sup>a</sup>Film thickness at 0% RH. <sup>b</sup>Film thickness at 95% RH. <sup>c</sup>Ratio of swollen thickness to dry thickness. Errors for film thicknesses represent 95% confidence intervals for fits to reflectance curves. Errors for swelling ratios were calculated using standard error propagation techniques.

### 6.4.3 Diffusion Measurements

#### 6.4.3.1 FRAP Data Fitting

Fluorescence recovery after photobleaching (FRAP) was used to measure the diffusion of probe molecules in 3xSso gels and PNIPAM solutions. A large library of molecules was selected for measuring diffusion within each of these solutions (**Table 6-3**). Transport of these probes in the protein gels and polymer solutions is affected by both molecular diffusion and binding to the matrix (the 3xSso gel or PNIPAM chains). Accordingly, FRAP curves were fit using a model that assumed molecules could exist in either a single bound state (in which the molecules could not diffuse) or an unbound state (in which the molecules could freely diffuse through the matrix). This model is represented in Laplace space as follows:<sup>61</sup>

$$\begin{aligned}\bar{f}(s) &= F_{\infty} \left\{ \frac{1}{s} - \frac{F_{eq}}{s} [1 - 2K_1(qw)I_1(qw)] \left( 1 + \frac{k_{on}}{s + k_{off}} \right) - \frac{C_{eq}}{s + k_{off}} \right\}, \\ F_{eq} &= \frac{k_{off}}{k_{on} + k_{off}} \quad C_{eq} = \frac{k_{on}}{k_{on} + k_{off}}, \\ q^2 &= \left( \frac{s}{D_f} \right) \left( 1 + \frac{k_{on}}{s + k_{off}} \right),\end{aligned}\tag{6-1}$$

where  $\bar{f}$  is the mean relative fluorescence intensity within the bleach region (normalized by the mean fluorescence intensity in an area far from the bleach region),  $F_{\infty}$  is the equilibrium relative fluorescence intensity within the bleach region,  $s$  is the Laplace variable,  $I_1$  and  $K_1$  are the first-order modified Bessel functions of the first and second kind, respectively,  $w$  is the radius of the bleach spot,  $k_{on}$  and  $k_{off}$  are the rate constants describing the rate of fluorophore binding to and release from the matrix, respectively, and  $D_f$  is the diffusion coefficient of the fluorophore in the absence of binding. The effective diffusion coefficient  $D_{eff}$ , which accounts for reductions in diffusivity due to matrix binding, was calculated as follows:

$$D_{eff} = \frac{D_f}{1 + \frac{k_{on}}{k_{off}}}. \quad (6-2)$$

To convert equation (6-1) from Laplace space to real space as function of time, a numerical Laplace inversion was performed using the Talbot algorithm.<sup>62</sup> After performing this inversion, FRAP data collected as a function of time could be fit to the real space equation. When fitting data to this transformed equation, a reduced data set was used to avoid over-fitting data at longer time points. Reduced data sets of roughly equally-spaced points were generated by selecting all data points from the first 10 seconds after bleaching and every third data point after this time interval.

A representative fit to a FRAP curve is presented in **Figure 6-2**.

**Table 6-3.** Probe Molecules Used in FRAP Experiments

Molecule	Abbreviation	Charge at pH 7.4, Unfolded	Molar Mass (kDa)	Hydrodynamic Diameter (nm) <sup>a</sup>
Cytochrome C <sup>b</sup>	CytC	8.9	12.4	2.9 ± 0.3
Lysozyme <sup>b</sup>	Lys	7.3	14.3	4.3 ± 0.1
Bovine Serum Albumin <sup>b</sup>	BSA	-32.7	66.5	8.8 ± 0.4
Transferrin <sup>b</sup>	TrFe	-2.4	77.0	12.7 ± 0.1
Glucose Oxidase <sup>b</sup>	GOx	-29	160	9.2 ± 0.2
Catalase <sup>b</sup>	Cat	-16.2	232	11.0 ± 0.4
Monomeric Streptavidin <sup>c</sup>	mSA2	-5.5	15.6	3.2 ± 0.9
Streptavidin <sup>c</sup>	SA	-3.4	52.8	6.2 ± 0.3
Superfolder GFP(0) <sup>d</sup>	GFP(0)	0.3	28.4	8.6 ± 0.5
Superfolder GFP(-8) <sup>d</sup>	GFP(-8)	-6.7	28.4	8.3 ± 0.8
Superfolder GFP(-21) <sup>d</sup>	GFP(-21)	-19.7	28.5	8.4 ± 0.3
Dextran 10k <sup>e</sup>	Dex10k	negligible	~10	14 ± 2
Dextran 40k <sup>e</sup>	Dex40k	negligible	~40	26 ± 1

Dextran 70k <sup>e</sup>	Dex70k	negligible	~70	80 ± 6
Dextran 500k <sup>e</sup>	Dex500k	negligible	~500	420 ± 70

<sup>a</sup>Determined using SANS curve fitting for CytC and mSA2 (**Figure E-4**) and DLS for all other molecules. <sup>b</sup>Proteins that do not bind to 3xSso. <sup>c</sup>Proteins that bind to 3xSso. <sup>d</sup>Charge variants of superfolder GFP. <sup>e</sup>Dextran molecules. Molecular weights represent number-average molecular weights reported by the supplier.

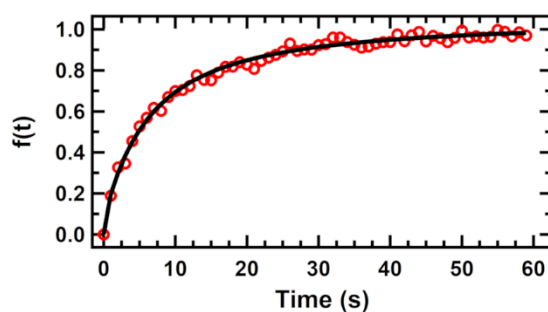


**Figure 6-2.** Representative fit to a normalized FRAP curve  $f(t)$ . The curve is normalized between 0 and 1 such that 0 corresponds to the fluorescence intensity within the bleach spot immediately after the bleach, and 1 corresponds to the average fluorescence intensity prior to bleaching.

Size-based diffusion models were fit to the diffusion coefficients collected for all molecular probes in each solution to ascertain the mechanism for diffusion within the solutions. If the effect of the matrix on molecular diffusion were simply to provide an effective viscosity, diffusion coefficients would be expected to follow the Stokes-Einstein relation:

$$D_{eff} = \frac{a_1}{d}, \quad (6-3)$$

where  $a_i$  is a fitting parameter and  $d$  is the hydrodynamic diameter of the probe molecule. Alternatively, the matrix can act as an entrapment for particles, restricting diffusion of large molecules due to physical constraints provided by a network structure. Under these conditions, Cai et al. have proposed that nanoparticles larger than the mesh size of the network must undergo a hopping mechanism to pass between regions of entrapment in the matrix.<sup>37</sup> The diffusion coefficients of these large particles at long time scales are primarily determined by the rate at which hopping events occur. For diffusion in a crosslinked gel, Cai et al. predict the following size-dependent relationship for the effective diffusion coefficient:<sup>37</sup>

$$D_{eff} = \frac{a_1}{d} e^{-a_2 d}. \quad (6-4)$$

In solutions of entangled polymer chains, the effective diffusion coefficient is predicted to follow the equation:<sup>37</sup>

$$D_{eff} = a_1 e^{-a_2 d}. \quad (6-5)$$

Thus, diffusion coefficients were fit to equations (6-3) and (6-4) for measurements in crosslinked 3xSso gels and equations (6-3) and (6-5) for measurements in PNIPAM solutions.

#### 6.4.3.2 Crosslinked 3xSso Gels

Protein diffusion within crosslinked 3xSso gels is qualitatively well-described by a hopping diffusion mechanism. As shown in **Figure 6-3a**, the diffusion coefficients of proteins that do not bind to 3xSso, including GFP variants, generally lie along the best-fit curve representing hopping diffusion in a crosslinked gel. Even though the hopping model developed by Cai assumes diffusion through crosslinked polymer gels in which long chains act as the crosslinks whereas the 3xSso gels have short glutaraldehyde crosslinks between bulky 3xSso junctions, the Cai model still is able to fit the data quite well. The Stokes-Einstein relationship, however, provides a poor fit to these data. Both models generally overpredict the diffusivities of mSA2 and SA, proteins that bind strongly to 3xSso, as these proteins likely are primarily bound to the gel, giving these molecules much lower effective diffusivities relative to their size than the other studied proteins. Additionally, despite the crosslinked gel and the protein probes being charged under the experimental conditions (**Table 6-3**), there is no significant difference between the effective diffusion coefficients of the three charged superfolder GFP variants. Since these diffusion coefficients also show no monotonic trend when considering the charge of the molecules (from smallest to largest, the proteins have formal charges of -8, -21, and 0), charge appears to only play a minor role in the transport of proteins in 3xSso gels.

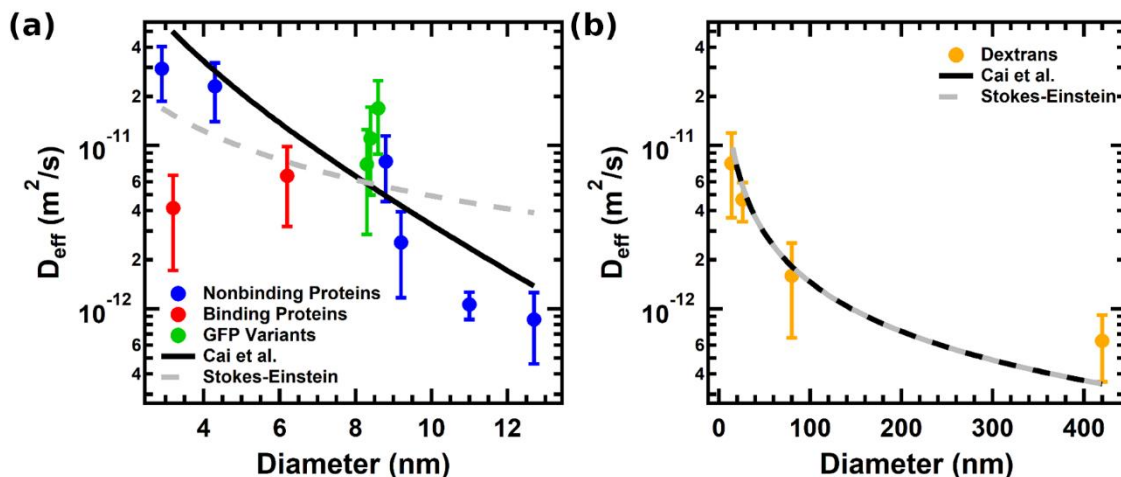


**Figure 6-3.** Effective diffusion coefficients of (a) proteins and (b) dextran molecules in 0.2 volume fraction solutions of crosslinked 3xSso gels measured using FRAP. Data are fit to both the Stokes-Einstein equation and a model developed by Cai et al. that describes hopping diffusion of large particles in crosslinked gels.<sup>37</sup> In (a), data points corresponding to proteins that bind strongly to 3xSso (mSA2 and SA) were excluded from the fits. Error bars represent the standard deviation across at least 5 replicates.

FRAP measurements of dextran molecules suggest that chain conformation and flexibility determine diffusion mechanisms in crosslinked 3xSso gels. In contrast to protein diffusion in these gels (**Figure 6-3a**), dextran diffusion is well-modeled by the Stokes-Einstein equation (**Figure 6-3b**). In fact, the Cai model for hopping diffusion reduces to the Stokes-Einstein equation when describing this diffusion of dextran molecules, indicating that even large dextran molecules do not become entrapped within the 3xSso gel. Indeed, even though the dextran molecules are up to two orders of magnitude larger than the measured proteins, the dextran molecules have diffusion coefficients of the same order of magnitude of the proteins. Unlike folded proteins, which have a well-defined, rigid structure, dextran molecules can adopt a much wider range of conformations due to greater chain flexibility, allowing these molecules to much more easily diffuse between topological constraints. As even fully-folded proteins can display varying levels of chain flexibility,<sup>63-64</sup> it is likely that this factor also results in varied diffusivities between proteins,

accounting for some of the spread of diffusion coefficients about the Cai model prediction in **Figure 6-3a**.

### 6.4.3.3 PNIPAM Solutions

Some proteins display very large deviations from Stokes-Einstein predictions of diffusivities in high- $M_n$  PNIPAM solutions. In low- $M_n$  PNIPAM solutions, most proteins have diffusion coefficients that coincide with a fit to the Stokes-Einstein equation (**Figure 6-4a-b**). In fact, in all measured PNIPAM solutions, the Cai model for hopping diffusion generally does not fit the data significantly better than the Stokes-Einstein equation (**Figure 6-4**), especially given that the Cai model uses an additional fitting parameter. This observation is reasonable, as the estimated entanglement molar mass of PNIPAM, somewhere in the range of 120-230 kDa (see **Appendix E** for estimation of entanglement molar mass), is greater than the molecular weight of even the largest PNIPAM molecule used in this study (117 kDa). As a result, PNIPAM chains are not expected to be entangled in any of the six solutions, and the Cai model for diffusion in entangled polymer solutions should not apply. In higher- $M_n$  PNIPAM solutions, four proteins consistently show large deviations from the Stokes-Einstein fit: BSA (diameter = 8.8 nm) and GOx (diameter = 9.2 nm) diffuse much faster than predicted, while extremely slow diffusion is observed in solutions with SA (diameter = 6.2 nm) and TrFe (diameter = 12.7 nm) (**Figure 6-4c-f**). The diffusivities of the other proteins, however, are still well-described by the Stokes-Einstein equation in these solutions. Also, in all six PNIPAM solutions, the three GFP variants show no significant differences in diffusivities, indicating that molecular charge has little influence on transport in PNIPAM solutions.

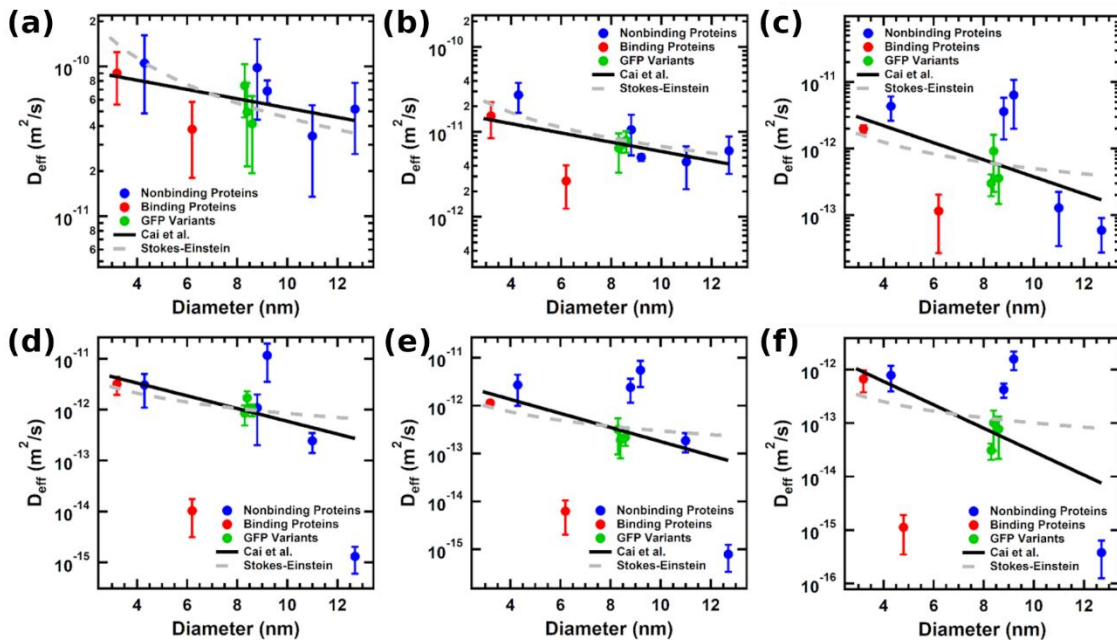


**Figure 6-4.** Effective diffusion coefficients of proteins in 0.2 volume fraction solutions of PNIPAM with  $M_n$  values of (a) 9.6, (b) 23, (c) 46, (d) 56, (e) 77, or (f) 117 kDa measured using FRAP. Data are fit to both the Stokes-Einstein equation and a model developed by Cai et al. that describes hopping diffusion of large particles in entangled polymer solutions.<sup>37</sup> CytC diffused too quickly in all solutions to obtain an accurate estimate of the diffusion coefficient. In (f), Cat showed essentially no fluorescence recovery, so a diffusion coefficient could not be estimated. Error bars represent the standard deviation across at least 5 replicates.

The large deviations in predicted diffusion coefficients are consistent with previous literature findings that polymers can interact with proteins on surfaces<sup>65-66</sup> and in solution,<sup>41, 67-68</sup> with larger polymers interacting more strongly.<sup>67-68</sup> The strength of these interactions can vary greatly depending on the identity of both the protein and the polymer involved,<sup>65-67</sup> and the interactions can become strong enough to overcome expected size-based transport effects.<sup>69</sup> Most experimental studies on the effects of protein-polymer interactions on diffusion have found that proteins diffuse faster than predicted by the Stokes-Einstein equation in the presence of polymers. For example, several groups have reported this enhanced diffusion in polymer solutions containing BSA, as is observed in the present study, which is often attributed to secondary structural changes in BSA caused by interaction with the polymer.<sup>67, 70-71</sup> CD studies of protein secondary structure reveal that the proteins in this study show very little, if any, change in secondary structure in the

presence of PNIPAM (**Figure E-5**). Because this change in structure has been reported to be as small as a difference of a few percentage between the compositions of certain secondary structure elements,<sup>67</sup> however, it is possible that the small differences in CD spectra after mixing with PNIPAM are the result of protein-PNIPAM interactions. While very few studies report proteins that diffuse significantly slower than predicted by the Stokes-Einstein equation, most of these studies also measure diffusion either with polymer molecules that are significantly smaller than the PNIPAM molecules used in this experiment or using much lower polymer concentrations. Indeed, in semidilute polymer solutions such as the ones used for FRAP experiments in this study, protein association rates are enhanced due to the formation of polymer cages around protein molecules.<sup>44, 72</sup> It is possible that SA and TrFe have high propensities for self-association while BSA and GOx are unlikely to self-associate, even when in close contact with other proteins. Regardless, DLS studies of the protein-PNIPAM mixtures are consistent with FRAP experiments, showing the appearance of slow relaxation times in PNIPAM mixtures containing SA or TrFe and relaxation times in mixture with BSA or GOx that are faster than those observed in solutions of either of these proteins without PNIPAM (**Figure E-6**). Therefore, a combination of protein-polymer interactions and protein-protein interactions enhanced in a semidilute polymer solution likely contribute to the deviations from Stokes-Einstein behavior.

No dextran molecules display repeated, significant differences from the Stokes-Einstein equation. As seen for diffusion of proteins in PNIPAM solutions, the diffusion coefficients of dextran molecules in PNIPAM solutions are generally no better fit by the hopping diffusion model than by the Stokes-Einstein equation (**Figure 6-5**). However, there is evidence that the greater flexibility of the dextran molecules permits less restricted diffusion. While the diffusivities of the dextran molecules all decrease by approximately one order of magnitude from the PNIPAM9.6k

solution to the PNIPAM117k solution (**Figure 6-5a, f**), most proteins experience a two order of magnitude decrease in diffusivity across these solutions (**Figure 6-4a, f**). In addition, similar to their diffusion in 3xSso gels, dextran molecules have diffusion coefficients of the same order of magnitude of the proteins (that follow the Stokes-Einstein model) in the same PNIPAM solutions despite being significantly larger than the proteins.

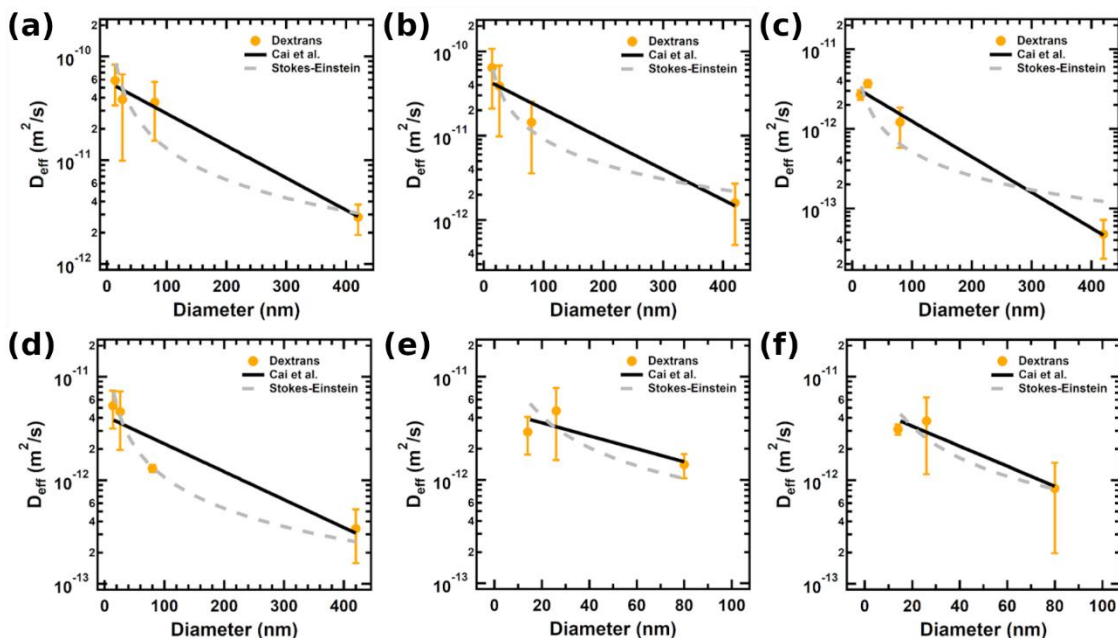


**Figure 6-5.** Effective diffusion coefficients of dextran molecules in 0.2 volume fraction solutions of PNIPAM with  $M_n$  values of (a) 9.6, (b) 23, (c) 46, (d) 56, (e) 77, or (f) 117 kDa measured using FRAP. Data are fit to both the Stokes-Einstein equation and a model developed by Cai et al. that describes hopping diffusion of large particles in entangled polymer solutions.<sup>37</sup> In (e) and (f), Dex500k showed essentially no fluorescence recovery, so a diffusion coefficient could not be estimated. Error bars represent the standard deviation across at least 5 replicates.

#### 6.4.4 Thin Film Binding Experiments

Comparison of FRAP results to thin film biosensing experiments suggests that the PNIPAM domains in 3xSP films have a much greater effect on protein transport than the 3xSso domains. While factors such as diffusion between domains and thin film morphology certainly affect diffusion in the films, the FRAP diffusion measurements in solutions analogous to the two domains within 3xSP conjugate thin films were compared against biosensing measurements to estimate the

relative impact of diffusion within these domains on overall transport. Because mSA2 mixtures were applied to the films for a period of time (4 hours) approximately half of that required for the films to saturate (8 hours),<sup>52</sup> transport within the thin films during the experiments was under dynamic control. Most of the nonbinding proteins considered in this study produce either no statistically significant change or a slight decrease in biosensor signal when applied to 3xSP thin film biosensors along with fluorescently-labeled mSA2, but mixtures of GOx or Lys with mSA2 both significantly enhance the fluorescence signal (**Figure 6-6**). While the fluorescence intensities of the nonbinding protein-mSA2 mixtures are slightly different (**Figure E-7**), the differences do not correlate with the observed fluorescence intensities in biosensing experiments. These different fluorescence values of the mixtures also cannot explain why the signal enhancement in Lys and GOx mixtures applied to 3xSP23k thin film biosensors is vastly altered from that when the mixtures are applied to 3xSP46k and 3xSP77k thin films (**Figure 6-6**). When considering all protein mixtures, there is no clear trend between biosensor signal enhancement and diffusion coefficient of the nonbinding protein in the mixture in crosslinked 3xSso domains (**Figure 6-6b-d**), as these graphs in **Figure 6-6** display a random distribution of points across all four quadrants. However, when comparing the signal enhancement to diffusion coefficients in PNIPAM solutions, it is clear that only proteins that diffuse faster than mSA2 in the PNIPAM solutions achieve an improvement in biosensor signal (**Figure 6-6e-g**). In fact, almost all points in these graphs are located in either the top right quadrant (the nonbinding protein diffuses faster than mSA2 and the binding signal is stronger than in the absence of the nonbinding protein) or the bottom left quadrant (the added protein diffuses slower than mSA2, causing reduced signal). Although not every protein that diffuses faster than mSA2 produces a signal enhancement, as both BSA and CytC mixtures give signals similar to that of solutions containing only mSA2, there is still a much clearer relation

between biosensor signal and diffusion relative to mSA2 in PNIPAM solutions than relative to that in 3xSso gels.

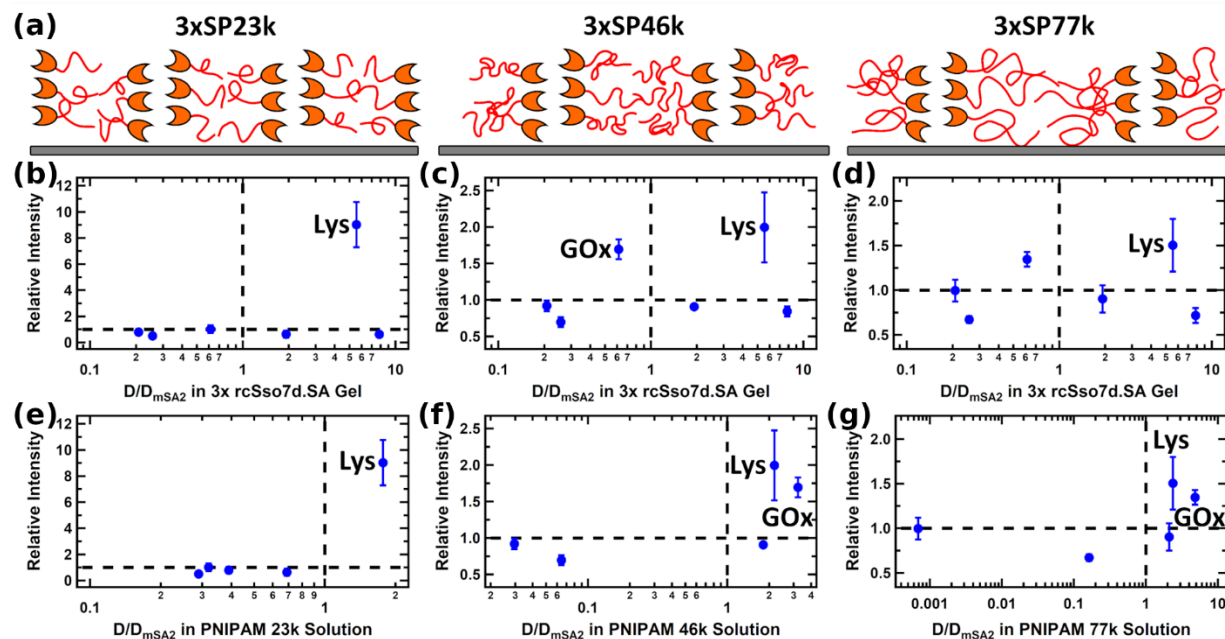


**Figure 6-6.** Fluorescence intensities of 1  $\mu\text{M}$  mixtures of fluorescently-labeled mSA2 with 100  $\mu\text{M}$  of one of the nonbinding proteins relative to that of a 1  $\mu\text{M}$  solution of only fluorescently-labeled mSA2 applied to (a) thin films of (b, e) 3xSP23k (thickness = 120 nm), (c, f) 3xSP46k (thickness = 110 nm), or (d, g) 3xSP77k (thickness = 160 nm) for 4 hours. Relative intensities are plotted against the ratio of the effective diffusion coefficient of the added protein to that of mSA2 in (b-d) crosslinked 3xSso gels or (e-g) PNIPAM solutions with PNIPAM of the same  $M_n$  value as the PNIPAM block in the thin film to which the solutions were applied. Points corresponding to mixtures containing CytC are absent from (e-g), as the diffusion coefficients of CytC were too fast to be measured in PNIPAM solutions. Labeled points represent mixtures with the named protein that gave a relative intensity significantly greater than that of solely mSA2. Error bars represent the standard deviations across 3 replicates on the same film that were calculated using standard error propagation techniques.

Biosensing experiments in protein mixtures suggest that 3xSP thin film biosensors can display enhanced sensitivity in complex mixtures. When exposed to a mixture containing mSA2 and all of the nonbinding proteins in this study (at concentrations 10 times lower than the experiments in **Figure 6-6**, due to solubility issues), the signal was over double that when sensing a solution containing only mSA2 (**Figure 6-7**). This signal enhancement is consistent with a previous study of 3xSP biosensors in which sensitivity for mSA2 was enhanced in blood serum

and urine relative to measurements in buffer.<sup>52</sup> In contrast, simply averaging the relative intensities produced from sensing in the six mixtures of each individual protein with mSA2 gave a value ( $1.2 \pm 0.2$ ) that was not significantly different from that of a solution with only mSA2 ( $2.16 \pm 0.08$ ). As such, the proteins that diffuse faster than mSA2 in PNIPAM solutions (which also enhance biosensing signal when mixed with mSA2) have a greater effect on mSA2 diffusion than those that diffuse slower than mSA2.

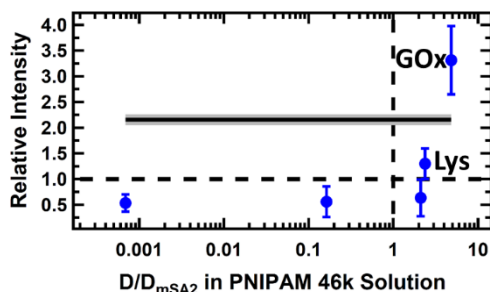


**Figure 6-7.** Fluorescence intensities of 1  $\mu\text{M}$  mixtures of fluorescently-labeled mSA2 with 10  $\mu\text{M}$  of one of the nonbinding proteins relative to that of a 1  $\mu\text{M}$  solution of only fluorescently-labeled mSA2 applied to a 3xSP46k thin film (thickness = 150 nm) for 4 hours. Relative intensities are plotted against the ratio of the effective diffusion coefficient of the added protein to that of mSA2 in a 0.2 volume percent solution of PNIPAM 46k. The point corresponding to a mixture containing CytC is absent, as the diffusion coefficient of CytC was too fast to be measured in PNIPAM 46k solutions. Labeled points represent mixtures with the named protein that gave a relative intensity significantly greater than that of solely mSA2. The solid line represents the relative intensity of a mixture containing 1  $\mu\text{M}$  mixtures of fluorescently-labeled mSA2 with 10  $\mu\text{M}$  of all of the nonbinding proteins (including CytC). Error bars and the bounds of the shaded region around the dashed line represent the standard deviations across 3 replicates on the same film that were calculated using standard error propagation techniques.

Given that the expected semidilute conditions within the PNIPAM domains of the swollen thin films promote protein-protein interactions,<sup>44, 72</sup> interactions between mSA2 and other proteins in the PNIPAM domains likely result in faster mSA2 diffusion in the presence of these faster diffusing proteins. In crowded molecular environments similar to the PNIPAM domains of the thin films in this study, weak, transient interactions between proteins are prevalent,<sup>73-74</sup> effectively reducing the diffusivities of all proteins.<sup>75</sup> When accounting for the greater viscosities of these crowded solutions, though, these protein-protein interactions have been found to produce diffusion

coefficients faster than would be expected from the Stokes-Einstein equation.<sup>41</sup> Because the thin films allow faster diffusing species to penetrate deeper into the film in a given period of time under dynamic control, mSA2 is more likely to encounter and interact with these faster proteins within the films. As a result, the transient clusters containing mSA2 that form deeper within the films would be expected to have greater diffusivities than those that would form in the original mixture of proteins. The strong dependence of transient interaction strength on the shapes of the interacting proteins<sup>76-77</sup> may explain why not all proteins that diffuse faster than mSA2 result in enhanced biosensing capabilities when mixed with mSA2. Despite the non-universal nature of sensitivity enhancement in the presence of proteins diffusing faster than the analyte, the results in this study imply that this improvement can be achieved if only a small number of proteins in a mixture diffuse faster than and can interact with the analyte. Therefore, unlike other surface-based sensors that experience reduced sensitivity in complex mixtures, protein diffusion within the PNIPAM domains of 3xSP conjugate thin films can facilitate improved biosensor sensitivity in protein mixtures.

## **6.5 Conclusions**

The diffusion in crosslinked 3xSso gels and PNIPAM solutions was studied to understand the major factors affecting diffusion within the two domains of phase-separated 3xSP thin films. In both solutions, charge was shown to have no significant impact on diffusion, and molecules with greater molecular flexibility were found to experience reduced diffusional resistance. In the crosslinked protein gels, the relationship between the diffusion coefficients and the sizes of proteins displayed qualitative agreement with a mechanism of hopping diffusion in a crosslinked gel. In the PNIPAM solutions, the diffusion coefficients of most proteins followed a Stokes-Einstein model. However, BSA and GOx were found to diffuse significantly faster in PNIPAM

solutions than predicted by the Stokes-Einstein equation, while SA and TrFe consistently had diffusion coefficients up to several orders of magnitude less than predicted by Stokes-Einstein. These deviations were attributed to a combination of protein-PNIPAM and PNIPAM-induced protein-protein interactions.

These diffusion measurements were compared against biosensing measurements of protein mixtures in 3xSP thin films in the diffusion-limited regime, indicating that PNIPAM domains have a much larger effect on protein transport than the 3xSso domains. When the analyte mSA2 was mixed with several proteins individually, the measured device sensitivities were uncorrelated with the diffusion coefficients of the added proteins in crosslinked 3xSso gels. In contrast, sensitivity enhancements relative to measurements in pure mSA2 solutions were only observed when the protein mixed with mSA2 diffused faster than mSA2 in PNIPAM solutions. A mixture of mSA2 with many proteins also gave enhanced sensitivity towards mSA2. It was hypothesized that enhanced sensitivity was achieved in the presence of off-target proteins due to faster diffusion of mSA2 in the PNIPAM domains of the thin films by transiently interacting with faster diffusing proteins. Regardless of the underlying transport mechanism, protein-PNIPAM conjugate thin films displayed improved biosensing capabilities in protein mixtures.

## 6.6 References

1. Asal, M.; Özen, Ö.; Şahinler, M.; Polatoğlu, İ., Recent Developments in Enzyme, DNA and Immuno-Based Biosensors. *Sensors* **2018**, *18* (6), DOI: 10.3390/s18061924
2. Grieshaber, D.; MacKenzie, R.; Vörös, J.; Reimhult, E., Electrochemical Biosensors - Sensor Principles and Architectures. *Sensors* **2008**, *8* (3), DOI: 10.3390/s80314000
3. Vigneshvar, S.; Sudhakumari, C. C.; Senthikumar, B.; Prakash, H., Recent Advances in Biosensor Technology for Potential Applications – An Overview. *Front. Bioeng. Biotechnol.* **2016**, *4* (11), DOI: 10.3389/fbioe.2016.00011
4. Oliverio, M.; Perotto, S.; Messina, G. C.; Lovato, L.; De Angelis, F., Chemical Functionalization of Plasmonic Surface Biosensors: A Tutorial Review on Issues, Strategies, and Costs. *ACS Appl. Mater. Interfaces* **2017**, *9* (35), 29394-29411, DOI: 10.1021/acsami.7b01583

5. Scouten, W. H.; Luong, J. H. T.; Stephen Brown, R., Enzyme or protein immobilization techniques for applications in biosensor design. *Trends Biotechnol.* **1995**, *13* (5), 178-185, DOI: 10.1016/S0167-7799(00)88935-0
6. Trilling, A. K.; Beekwilder, J.; Zuilhof, H., Antibody orientation on biosensor surfaces: a minireview. *Analyst* **2013**, *138* (6), 1619-1627, DOI: 10.1039/C2AN36787D
7. Guo, X., Surface plasmon resonance based biosensor technique: A review. *J. Biophotonics* **2012**, *5* (7), 483-501, DOI: 10.1002/jbio.201200015
8. Cao, J.; Sun, T.; Grattan, K. T. V., Gold nanorod-based localized surface plasmon resonance biosensors: A review. *Sensors Actuators B: Chem.* **2014**, *195*, 332-351, DOI: 10.1016/j.snb.2014.01.056
9. Zhao, Y.; Tong, R.-j.; Xia, F.; Peng, Y., Current status of optical fiber biosensor based on surface plasmon resonance. *Biosens. Bioelectron.* **2019**, *142*, 111505, DOI: 10.1016/j.bios.2019.111505
10. Ates, M., A review study of (bio)sensor systems based on conducting polymers. *Mater. Sci. Eng. C* **2013**, *33* (4), 1853-1859, DOI: 10.1016/j.msec.2013.01.035
11. Grieshaber, D.; MacKenzie, R.; Vörös, J.; Reimhult, E., Electrochemical Biosensors - Sensor Principles and Architectures. *Sensors* **2008**, *8* (3), 1400-1458, DOI: 10.3390/s151229783
12. Luka, G.; Ahmadi, A.; Najjaran, H.; Alocilja, E.; DeRosa, M.; Wolthers, K.; Malki, A.; Aziz, H.; Althani, A.; Hoorfar, M., Microfluidics Integrated Biosensors: A Leading Technology towards Lab-on-a-Chip and Sensing Applications. *Sensors* **2015**, *15* (12), DOI: 10.3390/s151229783
13. Pandey, C. M.; Augustine, S.; Kumar, S.; Kumar, S.; Nara, S.; Srivastava, S.; Malhotra, B. D., Microfluidics Based Point-of-Care Diagnostics. *Biotechnol. J.* **2018**, *13* (1), 1700047, DOI: 10.1002/biot.201700047
14. Bizzotto, D.; Burgess, I. J.; Doneux, T.; Sagara, T.; Yu, H.-Z., Beyond Simple Cartoons: Challenges in Characterizing Electrochemical Biosensor Interfaces. *ACS Sensors* **2018**, *3* (1), 5-12, DOI: 10.1021/acssensors.7b00840
15. Esteban Fernández de Ávila, B.; Watkins, H. M.; Pingarrón, J. M.; Plaxco, K. W.; Palleschi, G.; Ricci, F., Determinants of the Detection Limit and Specificity of Surface-Based Biosensors. *Anal. Chem.* **2013**, *85* (14), 6593-6597, DOI: 10.1021/ac4012123
16. Blawas, A. S.; Reichert, W. M., Protein patterning. *Biomaterials* **1998**, *19* (7), 595-609, DOI: 10.1016/S0142-9612(97)00218-4
17. Nedelkov, D.; Nelson, R. W., Analysis of native proteins from biological fluids by biomolecular interaction analysis mass spectrometry (BIA/MS): exploring the limit of detection, identification of non-specific binding and detection of multi-protein complexes. *Biosens. Bioelectron.* **2001**, *16* (9), 1071-1078, DOI: 10.1016/S0956-5663(01)00229-9
18. Masson, J.-F., Surface Plasmon Resonance Clinical Biosensors for Medical Diagnostics. *ACS Sensors* **2017**, *2* (1), 16-30, DOI: 10.1021/acssensors.6b00763
19. Arlett, J. L.; Myers, E. B.; Roukes, M. L., Comparative advantages of mechanical biosensors. *Nat. Nano.* **2011**, *6* (4), 203-215, DOI: 10.1038/nnano.2011.44
20. Shi, H.; Tsai, W.-B.; Garrison, M. D.; Ferrari, S.; Ratner, B. D., Template-imprinted nanostructured surfaces for protein recognition. *Nature* **1999**, *398* (6728), 593-597, DOI: 10.1038/19267
21. Pan, S.; Zhang, H.; Liu, W.; Wang, Y.; Pang, W.; Duan, X., Biofouling Removal and Protein Detection Using a Hypersonic Resonator. *ACS Sensors* **2017**, *2* (8), 1175-1183, DOI: 10.1021/acssensors.7b00298

22. Schlenoff, J. B., Zwitteration: Coating Surfaces with Zwitterionic Functionality to Reduce Nonspecific Adsorption. *Langmuir* **2014**, *30* (32), 9625-9636, DOI: 10.1021/la500057j
23. Soldatkin, A. P.; El'skaya, A. V.; Shul'ga, A. A.; Jdanova, A. S.; Dzyadevich, S. V.; Jaffrezic-Renault, N.; Martelet, C.; Clechet, P., Glucose sensitive conductometric biosensor with additional Nafion membrane: reduction of influence of buffer capacity on the sensor response and extension of its dynamic range. *Anal. Chim. Acta* **1994**, *288* (3), 197-203, DOI: 10.1016/0003-2670(93)E0627-J
24. Bonanno, L. M.; DeLouise, L. A., Whole blood optical biosensor. *Biosens. Bioelectron.* **2007**, *23* (3), 444-448, DOI: 10.1016/j.bios.2007.05.008
25. Sabaté del Río, J.; Henry, O. Y. F.; Jolly, P.; Ingber, D. E., An antifouling coating that enables affinity-based electrochemical biosensing in complex biological fluids. *Nat. Nano.* **2019**, *14* (12), 1143-1149, DOI: 10.1038/s41565-019-0566-z
26. Schuck, P.; Minton, A. P., Analysis of Mass Transport-Limited Binding Kinetics in Evanescent Wave Biosensors. *Anal. Biochem.* **1996**, *240* (2), 262-272, DOI: 10.1006/abio.1996.0356
27. Squires, T. M.; Messinger, R. J.; Manalis, S. R., Making it stick: convection, reaction and diffusion in surface-based biosensors. *Nat. Biotechnol.* **2008**, *26* (4), 417-426, DOI: 10.1038/nbt1388
28. Soleymani, L.; Li, F., Mechanistic Challenges and Advantages of Biosensor Miniaturization into the Nanoscale. *ACS Sensors* **2017**, *2* (4), 458-467, DOI: 10.1021/acssensors.7b00069
29. Katira, P.; Hess, H., Two-Stage Capture Employing Active Transport Enables Sensitive and Fast Biosensors. *Nano Lett.* **2010**, *10* (2), 567-572, DOI: 10.1021/nl903468p
30. Escobedo, C.; Brolo, A. G.; Gordon, R.; Sinton, D., Flow-Through vs Flow-Over: Analysis of Transport and Binding in Nanohole Array Plasmonic Biosensors. *Anal. Chem.* **2010**, *82* (24), 10015-10020, DOI: 10.1021/ac101654f
31. Anandan, V.; Yang, X.; Kim, E.; Rao, Y. L.; Zhang, G., Role of reaction kinetics and mass transport in glucose sensing with nanopillar array electrodes. *J. Biol. Eng.* **2007**, *1* (1), 5, DOI: 10.1186/1754-1611-1-5
32. Lang, X.-Y.; Fu, H.-Y.; Hou, C.; Han, G.-F.; Yang, P.; Liu, Y.-B.; Jiang, Q., Nanoporous gold supported cobalt oxide microelectrodes as high-performance electrochemical biosensors. *Nat. Commun.* **2013**, *4* (1), 2169, DOI: 10.1038/ncomms3169
33. Kohli, I.; Mukhopadhyay, A., Diffusion of Nanoparticles in Semidilute Polymer Solutions: Effect of Different Length Scales. *Macromolecules* **2012**, *45* (15), 6143-6149, DOI: 10.1021/ma301237r
34. Chen, T.; Qian, H.-J.; Lu, Z.-Y., Note: Chain length dependent nanoparticle diffusion in polymer melt: Effect of nanoparticle softness. *J. Chem. Phys.* **2016**, *145* (10), 106101, DOI: 10.1063/1.4962370
35. Pryamitsyn, V.; Ganesan, V., Noncontinuum effects on the mobility of nanoparticles in unentangled polymer solutions. *J. Polym. Sci., Part B: Polym. Phys.* **2016**, *54* (21), 2145-2150, DOI: 10.1002/polb.24138
36. Poling-Skutvik, R.; Krishnamoorti, R.; Conrad, J. C., Size-Dependent Dynamics of Nanoparticles in Unentangled Polyelectrolyte Solutions. *ACS Macro Lett.* **2015**, *4* (10), 1169-1173, DOI: 10.1021/acsmacrolett.5b00616
37. Cai, L.-H.; Panyukov, S.; Rubinstein, M., Hopping Diffusion of Nanoparticles in Polymer Matrices. *Macromolecules* **2015**, *48* (3), 847-862, DOI: 10.1021/ma501608x

38. Ochab-Marcinek, A.; Hołyst, R., Scale-dependent diffusion of spheres in solutions of flexible and rigid polymers: mean square displacement and autocorrelation function for FCS and DLS measurements. *Soft Matter* **2011**, *7* (16), 7366-7374, DOI: 10.1039/C1SM05217A
39. Tuinier, R.; Fan, T.-H., Scaling of nanoparticle retardation in semi-dilute polymer solutions. *Soft Matter* **2008**, *4* (2), 254-257, DOI: 10.1039/B711902J
40. Banks, D. S.; Fradin, C., Anomalous Diffusion of Proteins Due to Molecular Crowding. *Biophys. J.* **2005**, *89* (5), 2960-2971, DOI: 10.1529/biophysj.104.051078
41. Wang, Y.; Li, C.; Pielak, G. J., Effects of Proteins on Protein Diffusion. *J. Am. Chem. Soc.* **2010**, *132* (27), 9392-9397, DOI: 10.1021/ja102296k
42. Feng, X.; Chen, A.; Wang, J.; Zhao, N.; Hou, Z., Understanding Protein Diffusion in Polymer Solutions: A Hydration with Depletion Model. *J. Phys. Chem. B* **2016**, *120* (38), 10114-10123, DOI: 10.1021/acs.jpcc.6b06248
43. Li, C.; Wang, Y.; Pielak, G. J., Translational and Rotational Diffusion of a Small Globular Protein under Crowded Conditions. *J. Phys. Chem. B* **2009**, *113* (40), 13390-13392, DOI: 10.1021/jp907744m
44. Kozer, N.; Kuttner, Y. Y.; Haran, G.; Schreiber, G., Protein-Protein Association in Polymer Solutions: From Dilute to Semidilute to Concentrated. *Biophys. J.* **2007**, *92* (6), 2139-2149, DOI: 10.1529/biophysj.106.097717
45. Rodriguez-Emmenegger, C.; Brynda, E.; Riedel, T.; Houska, M.; Šubr, V.; Alles, A. B.; Hasan, E.; Gautrot, J. E.; Huck, W. T. S., Polymer Brushes Showing Non-Fouling in Blood Plasma Challenge the Currently Accepted Design of Protein Resistant Surfaces. *Macromol. Rapid Commun.* **2011**, *32* (13), 952-957, DOI: 10.1002/marc.201100189
46. Welch, M.; Rastogi, A.; Ober, C., Polymer brushes for electrochemical biosensors. *Soft Matter* **2011**, *7* (2), 297-302, DOI: 10.1039/C0SM00035C
47. Charles, T. P.; Stubbs, R. V.; Soto, M. C.; Martin, D. B.; White, J. B.; Taitt, R. C., Reduction of Non-Specific Protein Adsorption Using Poly(ethylene) Glycol (PEG) Modified Polyacrylate Hydrogels In Immunoassays for Staphylococcal Enterotoxin B Detection. *Sensors* **2009**, *9* (1), DOI: 10.3390/s90100645
48. Schuck, P., Kinetics of ligand binding to receptor immobilized in a polymer matrix, as detected with an evanescent wave biosensor. I. A computer simulation of the influence of mass transport. *Biophys. J.* **1996**, *70* (3), 1230-1249, DOI: 10.1016/S0006-3495(96)79681-9
49. Stein, E. W.; Singh, S.; McShane, M. J., Microscale Enzymatic Optical Biosensors Using Mass Transport Limiting Nanofilms. 2. Response Modulation by Varying Analyte Transport Properties. *Anal. Chem.* **2008**, *80* (5), 1408-1417, DOI: 10.1021/ac701738e
50. Wang, N.; Burugapalli, K.; Song, W.; Halls, J.; Moussy, F.; Ray, A.; Zheng, Y., Electrospun fibro-porous polyurethane coatings for implantable glucose biosensors. *Biomaterials* **2013**, *34* (4), 888-901, DOI: 10.1016/j.biomaterials.2012.10.049
51. Yarmush, M. L.; Patankar, D. B.; Yarmush, D. M., An analysis of transport resistances in the operation of BIAcore™; implications for kinetic studies of biospecific interactions. *Mol. Immunol.* **1996**, *33* (15), 1203-1214, DOI: 10.1016/S0161-5890(96)00075-2
52. Paloni, J. M.; Dong, X.-H.; Olsen, B. D., Protein-Polymer Block Copolymer Thin Films for Highly Sensitive Detection of Small Proteins in Biological Fluids. *ACS Sensors* **2019**, *4* (11), 2869-2878, DOI: 10.1021/acssensors.9b01020
53. Thomas, C. S.; Glassman, M. J.; Olsen, B. D., Solid-State Nanostructured Materials from Self-Assembly of a Globular Protein-Polymer Diblock Copolymer. *ACS Nano* **2011**, *5* (7), 5697-5707, DOI: 10.1021/nn2013673

54. Lam, C. N.; Yao, H.; Olsen, B. D., The Effect of Protein Electrostatic Interactions on Globular Protein–Polymer Block Copolymer Self-Assembly. *Biomacromolecules* **2016**, *17* (9), 2820-2829, DOI: 10.1021/acs.biomac.6b00522
55. Paloni, J. M.; Miller, E. A.; Sikes, H. D.; Olsen, B. D., Improved Ordering in Low Molecular Weight Protein–Polymer Conjugates Through Oligomerization of the Protein Block. *Biomacromolecules* **2018**, *19* (9), 3814-3824, DOI: 10.1021/acs.biomac.8b00928
56. Chang, D.; Huang, A.; Olsen, B. D., Kinetic Effects on Self-Assembly and Function of Protein–Polymer Bioconjugates in Thin Films Prepared by Flow Coating. *Macromol. Rapid Commun.* **2017**, *38* (1), 1600449, DOI: 10.1002/marc.201600449
57. Huang, A.; Qin, G.; Olsen, B. D., Highly Active Biocatalytic Coatings from Protein–Polymer Diblock Copolymers. *ACS Appl. Mater. Interfaces* **2015**, *7* (27), 14660-14669, DOI: 10.1021/acsami.5b01884
58. Baumann, H.; Knapp, S.; Lundbäck, T.; Ladenstein, R.; Härd, T., Solution structure and DNA-binding properties of a thermostable protein from the archaeon *Sulfolobus solfataricus*. *Nat. Struct. Biol.* **1994**, *1*, 808, DOI: 10.1038/nsb1194-808
59. Magerl, D.; Philipp, M.; Qiu, X.-P.; Winnik, F. M.; Müller-Buschbaum, P., Swelling and Thermoresponsive Behavior of Linear versus Cyclic Poly(N-isopropylacrylamide) Thin Films. *Macromolecules* **2015**, *48* (9), 3104-3111, DOI: 10.1021/acs.macromol.5b00436
60. Lam, C. N.; Olsen, B. D., Phase transitions in concentrated solution self-assembly of globular protein–polymer block copolymers. *Soft Matter* **2013**, *9* (8), 2393-2402, DOI: 10.1039/C2SM27459K
61. Sprague, B. L.; Pego, R. L.; Stavreva, D. A.; McNally, J. G., Analysis of Binding Reactions by Fluorescence Recovery after Photobleaching. *Biophys. J.* **2004**, *86* (6), 3473-3495, DOI: 10.1529/biophysj.103.026765
62. Abate, J.; Whitt, W., A Unified Framework for Numerically Inverting Laplace Transforms. *INFORMS J. Comput.* **2006**, *18* (4), 408-421, DOI: 10.1287/ijoc.1050.0137
63. Karplus, P. A.; Schulz, G. E., Prediction of chain flexibility in proteins. *Naturwissenschaften* **1985**, *72* (4), 212-213, DOI: 10.1007/BF01195768
64. Smith, D. K.; Radivojac, P.; Obradovic, Z.; Dunker, A. K.; Zhu, G., Improved amino acid flexibility parameters. *Protein Sci.* **2003**, *12* (5), 1060-1072, DOI: 10.1110/ps.0236203
65. Lee, R. G.; Kim, S. W., Adsorption of proteins onto hydrophobic polymer surfaces: Adsorption isotherms and kinetics. *J. Biomed. Mater. Res.* **1974**, *8* (5), 251-259, DOI: 10.1002/jbm.820080507
66. Young, B. R.; Pitt, W. G.; Cooper, S. L., Protein adsorption on polymeric biomaterials I. Adsorption isotherms. *J. Colloid Interface Sci.* **1988**, *124* (1), 28-43, DOI: 10.1016/0021-9797(88)90321-9
67. Bekale, L.; Agudelo, D.; Tajmir-Riahi, H. A., The role of polymer size and hydrophobic end-group in PEG–protein interaction. *Colloids Surf. B. Biointerfaces* **2015**, *130*, 141-148, DOI: 10.1016/j.colsurfb.2015.03.045
68. Wu, J.; Zhao, C.; Lin, W.; Hu, R.; Wang, Q.; Chen, H.; Li, L.; Chen, S.; Zheng, J., Binding characteristics between polyethylene glycol (PEG) and proteins in aqueous solution. *J. Mater. Chem. B* **2014**, *2* (20), 2983-2992, DOI: 10.1039/C4TB00253A
69. Dech, S.; Cramer, T.; Ladisch, R.; Bruns, N.; Tiller, J. C., Solid–Solid Interface Adsorption of Proteins and Enzymes in Nanophase-Separated Amphiphilic Conetworks. *Biomacromolecules* **2011**, *12* (5), 1594-1601, DOI: 10.1021/bm1015877

70. Hsieh, S.-R.; Reddy, P. M.; Chang, C.-J.; Kumar, A.; Wu, W.-C.; Lin, H.-Y., Exploring the Behavior of Bovine Serum Albumin in Response to Changes in the Chemical Composition of Responsive Polymers: Experimental and Simulation Studies. *Polymers* **2016**, *8* (6), 238, DOI: 10.1021/acs.jpcc.6b02402
71. Phillies, G. D. J., Diffusion of bovine serum albumin in a neutral polymer solution. *Biopolymers* **1985**, *24* (2), 379-386, DOI: 10.1002/bip.360240206
72. Odijk, T., Depletion Theory of Protein Transport in Semi-Dilute Polymer Solutions. *Biophys. J.* **2000**, *79* (5), 2314-2321, DOI: 10.1016/S0006-3495(00)76477-0
73. Rickard, M. M.; Zhang, Y.; Gruebele, M.; Pogorelov, T. V., In-Cell Protein-Protein Contacts: Transient Interactions in the Crowd. *J. Phys. Chem. Lett.* **2019**, *10* (18), 5667-5673, DOI: 10.1021/acs.jpclett.9b01556
74. Wang, Q.; Zhuravleva, A.; Gierasch, L. M., Exploring Weak, Transient Protein-Protein Interactions in Crowded In Vivo Environments by In-Cell Nuclear Magnetic Resonance Spectroscopy. *Biochemistry* **2011**, *50* (43), 9225-9236, DOI: 10.1021/bi201287e
75. Nawrocki, G.; Wang, P.-h.; Yu, I.; Sugita, Y.; Feig, M., Slow-Down in Diffusion in Crowded Protein Solutions Correlates with Transient Cluster Formation. *J. Phys. Chem. B* **2017**, *121* (49), 11072-11084, DOI: 10.1021/acs.jpcc.7b08785
76. Balbo, J.; Mereghetti, P.; Herten, D.-P.; Wade, Rebecca C., The Shape of Protein Crowders is a Major Determinant of Protein Diffusion. *Biophys. J.* **2013**, *104* (7), 1576-1584, DOI: 10.1016/j.bpj.2013.02.041
77. Kusova, A. M.; Sitnitsky, A. E.; Idiyatullin, B. Z.; Bakirova, D. R.; Zuev, Y. F., The Effect of Shape and Concentration on Translational Diffusion of Proteins Measured by PFG NMR. *Appl. Magn. Reson.* **2018**, *49* (1), 35-51, DOI: 10.1007/s00723-017-0957-y

## Chapter 7. Conclusions

### 7.1 Summary

This thesis has investigated the use of protein-poly(N-isopropylacrylamide) (PNIPAM) conjugate thin films as biosensors. Based on numerous literature reports of the self-assembly of these conjugates,<sup>1-4</sup> it was believed that the periodic structure of protein-PNIPAM thin films would be beneficial for biosensor performance. These films contain regions of densely packed analyte-binding proteins that could enhance device sensitivity in addition to polymer domains that were hypothesized to be capable of tailoring transport such that improved selectivity towards analyte diffusion into the thin films could be achieved. In this regard, there were two primary focuses in this thesis. First, techniques were developed for the self-assembly of protein-PNIPAM conjugates with a small protein block, representing a class of analyte-binding proteins used in biosensors that have superior stability and sensing capabilities compared to the more traditional antibodies.<sup>5-7</sup> Second, it was demonstrated that the conjugate biosensors were able to minimize the effects of nonspecific binding in complex sensing mixtures and even achieve enhanced sensitivity in these solutions.

The first method used to improve the self-assembly of protein-PNIPAM conjugates with a low molecular weight protein block was protein oligomerization. Using rcSso7d.SA (Sso) as a model small binding protein,<sup>7</sup> oligomers of this protein ranging from monomer to tetramer were created by attaching a short, flexible peptide sequence between repeats. While conjugates of the monomeric Sso variant were disordered under all studied conditions, conjugates of the other oligomers were able to self-assemble into ordered lamellar structures. As the Sso degree of oligomerization increased, the quality of self-assembly improved, and the concentration range over which ordered structures were observed widened. Analyte binding capabilities were retained upon

oligomerization, and conjugate thin films composed of higher order oligomer conjugates were found to have greater sensitivity towards analyte molecules.

Protein fusion to strongly-associating coiled-coil domains was also explored to achieve well-ordered protein-PNIPAM conjugates. The protein block in this study consisted of an Sso dimer fused at either the N- or C-terminus to one of the two component alpha helices of a coiled-coil. The alpha helices in these fusion proteins generally remained folded under the studied conditions and were able to weakly homodimerize, but one fusion protein had an almost completely unfolded alpha helical segment. When two fusion proteins each containing one of the two coiled-coil helices were mixed in an equimolar ratio, stable heterodimeric coiled-coils generally formed. However, in one of these equimolar mixtures, coiled-coils were almost exclusively homodimeric, which was attributed to geometric constraints preventing heterodimeric coiled-coil association. In solution, conjugates of the fusion proteins that could homodimerize displayed no significant difference in ordering quality from that of the Sso dimer, whereas equimolar mixtures of these conjugates showed enhanced ordering. The conjugate containing the fusion protein with an unfolded alpha helical segment, though, had the most improved ordering in solution over the Sso dimer. Biosensor thin films fabricated from the fusion protein-PNIPAM conjugates revealed that all of the conjugates were able to bind analyte, and most offered significantly enhanced sensing over biosensors made from Sso dimer conjugates.

The fifth chapter of this thesis studied the ability of protein-PNIPAM biosensors to control diffusion of protein analytes based on size. In this study, two proteins with the same binding affinity for the biosensor thin films that only differed in size, streptavidin (SA) and monomeric streptavidin (mSA2), were used as analytes. When buffer solutions containing one of these two analytes were applied to the thin films, limits of detection (LODs) over an order of magnitude

lower were reported in films exposed to solutions with the smaller protein mSA2 than in those exposed to solutions of the larger protein SA. Furthermore, it was demonstrated that by increasing the molecular weight of PNIPAM conjugated to the protein in these thin films, SA experienced less-restricted diffusion into the films, possibly as result of the increasing PNIPAM domain size. In contrast, in these same experiments mSA2 was able to relatively freely diffuse into all of the thin films. When SA and mSA2 were spiked into solutions of blood serum and urine and applied to the thin films, conjugate sensors detecting SA performed no better than those composed of the analyte binding protein directly functionalized to a surface. Thin film biosensors detecting mSA2, on the other hand, achieved a two order of magnitude improvement in LOD compared to the surface-functionalized sensors. In aggregate, these experiments suggested that diffusion into the thin films was dependent upon protein size and this principle allowed deleterious nonspecific binding effects to be minimized when detecting small proteins.

In the final research chapter, the main factors affecting diffusion in protein-PNIPAM thin films were studied. By performing diffusion measurements in solutions analogous to the phase-separated protein and PNIPAM domains within the films, it was found that most proteins diffuse according to a hopping diffusion model<sup>8</sup> within the protein solutions and follow Stokes-Einstein behavior in PNIPAM solutions. The diffusivities of some proteins in the PNIPAM solutions were measured to differ by up to several orders of magnitude from the Stokes-Einstein predictions, though, and these discrepancies were attributed to a combination of protein-protein and protein-PNIPAM interactions. Biosensing measurements performed in the thin films in which mSA2 was individually mixed with each of the proteins considered in the study indicated that proteins that diffused faster than mSA2 in PNIPAM solutions could also allow greater sensing of mSA2 when mixed with this analyte protein. Similar results were obtained during biosensing measurements of

mSA2 in a mixture of many proteins. Therefore, unlike other surface-based biosensors, protein-polymer conjugate thin films were found to achieve improved sensitivity in complex protein mixtures.

## **7.2 Outlook**

The self-assembly methods presented in this thesis provide a framework for creating ordered structures of functionally-relevant proteins. Since most proteins do not inherently assemble into well-ordered structures when conjugated to PNIPAM,<sup>9</sup> oligomerization of the protein or fusion to complementary coiled-coil sequences can be used to develop oriented arrays of these proteins necessary for optimizing protein activity.<sup>10-12</sup> Both of these modifications, however, have limitations that may need to be resolved before they can be generalized for use with any protein. For oligomerization, the cloning method is tedious and does not guarantee production of the desired gene. Additionally, it is possible that ordering improvements were only observed in the Sso oligomers because the proteins fell within the molecular weight range in which protein-PNIPAM conjugate self-assembly is optimized.<sup>9</sup> Potentially, nanoscale ordering in the oligomer conjugates also improved due to the greater molecular flexibility imparted by the peptide linkers, but further studies on the relationship between protein flexibility and self-assembly would be required to verify this hypothesis. While coiled-coil association was demonstrated in this thesis to improve conjugate self-assembly, improvements were inconsistent as a result of varied coiled-coil folding states and potential geometric constraints deriving from the region on the original protein to which the coiled-coil sequence was fused. As such, research into the relationship between the location at which order-directing sequences are fused to a protein and the resulting ordering quality would need to be performed before this ordering technique could be generalized.

One potential commercial application of the protein-polymer conjugate thin films is in the development of practical biosensors from these materials. First of all, thin films were cast on silicon wafers throughout the thesis for convenience, but development of procedures for casting on more useful surfaces such as paper and flexible polymers are necessary for use of this technology in point-of-care applications.<sup>13-14</sup> Also, this thesis was primarily focused on improving the analyte capture step in biosensors, and a method of detecting analyte that does not rely on fluorescently-labeled analyte molecules other would likely need to developed. One important consideration here is that the molecule or particle that produces the detectable signal would need to be relatively small, as the enzyme-linked immunosorbent assays (ELISAs) performed in the thesis suggested that the sensitivity of these assays was reduced due to the restricted diffusion of the relatively large protein horseradish peroxidase into the films. For this reason, quantum dots may be an ideal particle to be used for detection, as these materials are inherently colored and can be as small as 2 nm.<sup>15</sup> Beyond these considerations, manufacturing issues including designing a method for large-scale fabrication of thin films with consistent thicknesses and morphologies would need to be considered.

The final research chapter in this thesis indicates that there is a great need for fundamental studies of protein diffusion in polymer solution and materials. While it is understood that protein-protein interactions can be enhanced in polymer solutions,<sup>16</sup> how these interactions modify the directed transport of the involved proteins is relatively unknown. The effects of these transient interactions can be understood by performing fluorescence recovery after photobleaching (FRAP) experiments similar to those in chapter 6 of the thesis. By using FRAP to measure the diffusion coefficients of fluorescently-labeled proteins in protein solutions both with and without other non-labeled proteins added, it can be determined whether the presence of and transient interactions

with specific proteins and protein mixtures speed or slow the diffusion of a given protein. The strength of these interactions can be estimated using Förster resonance energy transfer (FRET), which has been used to measure transient protein-protein interactions in similar crowded environments in cells.<sup>17-19</sup> If protein-protein dynamics in polymer solutions becomes sufficiently well understood, then protein transport within protein-polymer conjugate thin films could be simulated. Of course, these simulations would require further information about other effects on transport within the films, such as accurate measurements of thin film morphology,<sup>20</sup> quantification of selective biomolecular transport effects within the protein domains,<sup>21</sup> and understanding of confinement effects within protein and polymer domains.<sup>22</sup> Accordingly, it will almost certainly be several years or even decades before the simulations of protein transport can be performed with high accuracy. In summary, this thesis demonstrates that there is a wealth of both fundamental and applied research that can be performed in the fields of self-assembly, biosensing, and biomolecular transport.

### 7.3 References

1. Thomas, C. S.; Glassman, M. J.; Olsen, B. D., Solid-State Nanostructured Materials from Self-Assembly of a Globular Protein–Polymer Diblock Copolymer. *ACS Nano* **2011**, *5* (7), 5697-5707, DOI: 10.1021/nn2013673
2. Lam, C. N.; Olsen, B. D., Phase transitions in concentrated solution self-assembly of globular protein-polymer block copolymers. *Soft Matter* **2013**, *9* (8), 2393-2402, DOI: 10.1039/C2SM27459K
3. Thomas, C. S.; Olsen, B. D., Coil fraction-dependent phase behaviour of a model globular protein-polymer diblock copolymer. *Soft Matter* **2014**, *10* (17), 3093-3102, DOI: 10.1039/C3SM52531G
4. Chang, D.; Lam, C. N.; Tang, S.; Olsen, B. D., Effect of polymer chemistry on globular protein-polymer block copolymer self-assembly. *Polymer Chemistry* **2014**, *5* (17), 4884-4895, DOI: 10.1039/C4PY00448E
5. Wang, H.; Li, G.; Zhang, Y.; Zhu, M.; Ma, H.; Du, B.; Wei, Q.; Wan, Y., Nanobody-Based Electrochemical Immunoassay for Ultrasensitive Determination of Apolipoprotein-A1 Using Silver Nanoparticles Loaded Nanohydroxyapatite as Label. *Anal. Chem.* **2015**, *87* (22), 11209-11214, DOI: 10.1021/acs.analchem.5b04063
6. Renberg, B.; Nordin, J.; Merca, A.; Uhlén, M.; Feldwisch, J.; Nygren, P.-Å.; Eriksson Karlström, A., Affibody Molecules in Protein Capture Microarrays: Evaluation of Multidomain

- Ligands and Different Detection Formats. *J. Proteome Res.* **2007**, *6* (1), 171-179, DOI: 10.1021/pr060316r
7. Miller, E. A.; Traxlmayr, M. W.; Shen, J.; Sikes, H. D., Activity-based assessment of an engineered hyperthermophilic protein as a capture agent in paper-based diagnostic tests. *Mol. Syst. Des. Eng.* **2016**, *1* (4), 377-381, DOI: 10.1039/C6ME00032K
  8. Cai, L.-H.; Panyukov, S.; Rubinstein, M., Hopping Diffusion of Nanoparticles in Polymer Matrices. *Macromolecules* **2015**, *48* (3), 847-862, DOI: 10.1021/ma501608x
  9. Huang, A.; Paloni, J. M.; Wang, A.; Obermeyer, A. C.; Sureka, H. V.; Yao, H.; Olsen, B. D., Predicting Protein–Polymer Block Copolymer Self-Assembly from Protein Properties. *Biomacromolecules* **2019**, *20* (10), 3713-3723, DOI: 10.1021/acs.biomac.9b00768
  10. Cracknell, J. A.; Vincent, K. A.; Armstrong, F. A., Enzymes as Working or Inspirational Electrocatalysts for Fuel Cells and Electrolysis. *Chem. Rev.* **2008**, *108* (7), 2439-2461, DOI: 10.1021/cr0680639
  11. Makaraviciute, A.; Ramanaviciene, A., Site-directed antibody immobilization techniques for immunosensors. *Biosens. Bioelectron.* **2013**, *50* (Supplement C), 460-471, DOI: 10.1016/j.bios.2013.06.060
  12. Squires, T. M.; Messinger, R. J.; Manalis, S. R., Making it stick: convection, reaction and diffusion in surface-based biosensors. *Nat. Biotechnol.* **2008**, *26* (4), 417-426, DOI: 10.1038/nbt1388
  13. Hu, J.; Wang, S.; Wang, L.; Li, F.; Pingguan-Murphy, B.; Lu, T. J.; Xu, F., Advances in paper-based point-of-care diagnostics. *Biosens. Bioelectron.* **2014**, *54*, 585-597, DOI: 10.1016/j.bios.2013.10.075
  14. Wang, S.; Chinnasamy, T.; Lifson, M. A.; Inci, F.; Demirci, U., Flexible Substrate-Based Devices for Point-of-Care Diagnostics. *Trends Biotechnol.* **2016**, *34* (11), 909-921, DOI: 10.1016/j.tibtech.2016.05.009
  15. Frasco, M. F.; Chaniotakis, N., Semiconductor Quantum Dots in Chemical Sensors and Biosensors. *Sensors* **2009**, *9* (9), 7266-7286, DOI: 10.3390/s9097266
  16. Kozer, N.; Kuttner, Y. Y.; Haran, G.; Schreiber, G., Protein-Protein Association in Polymer Solutions: From Dilute to Semidilute to Concentrated. *Biophys. J.* **2007**, *92* (6), 2139-2149, DOI: 10.1529/biophysj.106.097717
  17. Brzostowski, J. A.; Meckel, T.; Hong, J.; Chen, A.; Jin, T., Imaging Protein-Protein Interactions by Förster Resonance Energy Transfer (FRET) Microscopy in Live Cells. *Curr. Protoc. Protein Sci.* **2009**, *56* (1), 19.5.1-19.5.12, DOI: 10.1002/0471140864.ps1905s56
  18. Llères, D.; Swift, S.; Lamond, A. I., Detecting Protein-Protein Interactions In Vivo with FRET using Multiphoton Fluorescence Lifetime Imaging Microscopy (FLIM). *Curr. Protoc. Cytometry* **2007**, *42* (1), 12.10.1-12.10.19, DOI: 10.1002/0471142956.cy1210s42
  19. Sukenik, S.; Ren, P.; Grubele, M., Weak protein–protein interactions in live cells are quantified by cell-volume modulation. *Proc. Natl. Acad. Sci. U.S.A.* **2017**, *114* (26), 6776, DOI: 10.1073/pnas.1700818114
  20. Gu, K. L.; Zhou, Y.; Morrison, W. A.; Park, K.; Park, S.; Bao, Z., Nanoscale Domain Imaging of All-Polymer Organic Solar Cells by Photo-Induced Force Microscopy. *ACS Nano* **2018**, *12* (2), 1473-1481, DOI: 10.1021/acs.nano.7b07865
  21. Yang, Y. J.; Mai, D. J.; Dursch, T. J.; Olsen, B. D., Nucleopore-Inspired Polymer Hydrogels for Selective Biomolecular Transport. *Biomacromolecules* **2018**, *19* (10), 3905-3916, DOI: 10.1021/acs.biomac.8b00556

22. Burada, P. S.; Hänggi, P.; Marchesoni, F.; Schmid, G.; Talkner, P., Diffusion in Confined Geometries. *ChemPhysChem* **2009**, *10* (1), 45-54, DOI: 10.1002/cphc.200800526

## Appendix A. Supporting Information for Chapter 2

### A.1 DNA and Amino Acid Sequences for Proteins Recombinantly Expressed in Thesis

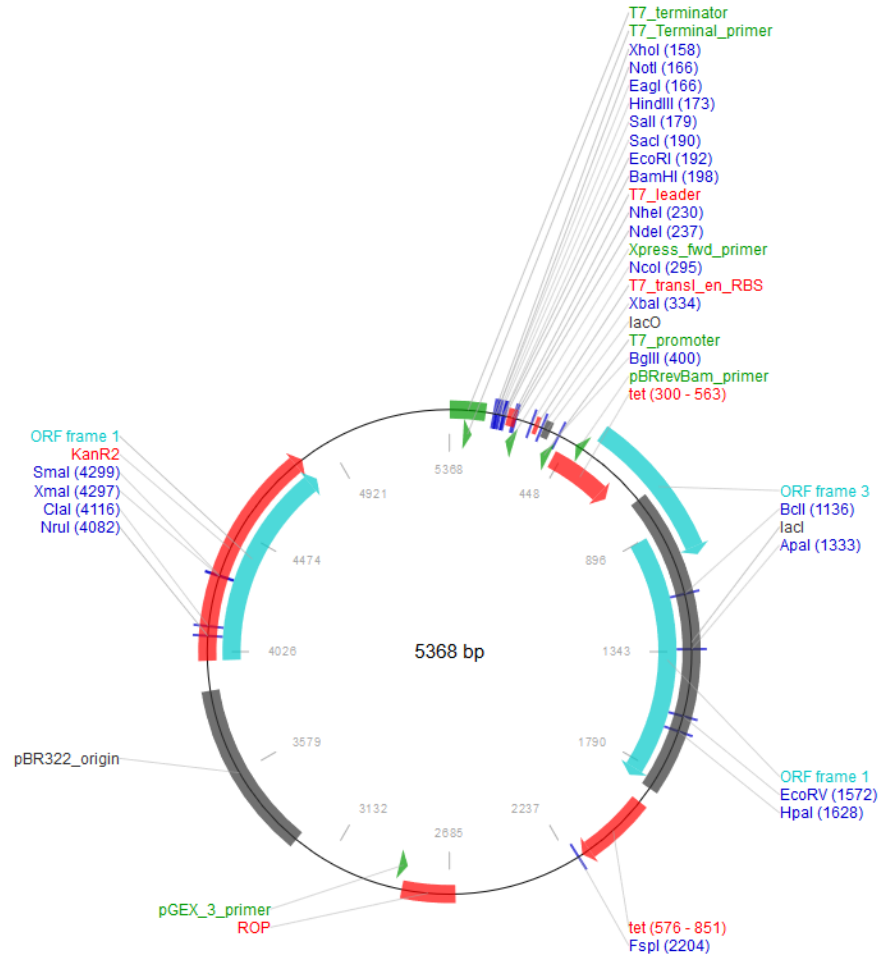


**Figure A-1.** Plasmid map for pET28b(+) vector used for all cloning experiment in this thesis.

In all cloning experiments, genes were inserted into pET28b(+) using XhoI/NdeI restriction sites.

Thus, the complete vector DNA sequence for each cloned vector can be obtained by replacing the

DNA between the underlined bases in the following sequence with that between the underlined

bases in the genes listed in sections **A1.1** to **A1.3**.

#### DNA Sequence of pET28b(+) Vector (XhoI/NdeI restriction sites are underlined)

```
ATCCGGATATAGTTCCTCCTTTTCAGCAAAAAACCCCTCAAGACCCGTTTATAGAGGCCCAAGGGGT
TATGCTAGTTATTGCTCAGCGGTGGCAGCAGCCAACCTCAGCTTCCTTTCGGGCTTTGTTAGCAGC
CGGATCTCAGTGGTGGTGGTGGTGGTGCCTCGAGTGCGGCCGCAAGCTTGTTCGACGGAGCTCGAAT
TCGGATCCCGACCCATTTGCTGTCCACCAGTCATGCTAGCCATATGGCTGCCGCGCGGCACCAGG
CCGCTGCTGTGATGATGATGATGATGGCTGCTGCCCATGGTATATCTCCTTCTTAAAGTTAAACA
```

AAATTATTTCTAGAGGGGAATTGTTATCCGCTCACAATTCCCCTATAGTGAGTCGTATTAATTTTC  
GCGGGATCGAGATCTCGATCCTCTACGCCGGACGCATCGTGGCCGGCATCACCGGCGCCACAGGT  
GCGGTTGCTGGCGCCTATATCGCCGACATCACCGATGGGGAAGATCGGGCTCGCCACTTCGGGCT  
CATGAGCGCTTGTTCGCGGTGGGTATGGTGGCAGGCCCGTGGCCGGGGGACTGTTGGGCGCCA  
TCTCCTTGCATGCACCATTCCTTGGCGGGCGGTGCTCAACGGCCTCAACCTACTACTGGGCTGC  
TTCCTAATGCAGGAGTCGCATAAGGGAGAGCGTCGAGATCCCGGACACCATCGAATGGCGCAAAA  
CCTTTCGCGGTATGGCATGATAGCGCCCGGAAGAGAGTCAATTCAGGGTGGTGAATGTGAAACCA  
GTAACGTTATACGATGTCGCAGAGTATGCCGGTGTCTCTTATCAGACCGTTTCCCGCGTGGTGAA  
CCAGGCCAGCCACGTTTCTGCGAAAACGCGGGAAAAAGTGGAAAGCGGGCGATGGCGGAGCTGAATT  
ACATTCCCAACCGCGTGGCACAACAACCTGGCGGGCAAAACAGTCGTTGCTGATTGGCGTTGCCACC  
TCCAGTCTGGCCCTGCACGCGCCGTTCGCAAATTTGTCGCGGGCGATTAATCTCGCGCCGATCAACT  
GGGTGCCAGCGTGGTGGTGTTCGATGGTAGAACGAAGCGGGCGTCAAGCCTGTAAAGCGGGCGGTGC  
ACAATCTTCTCGCGCAACGCGTCACTGGGCTGATCATTAACTATCCGCTGGATGACCAGGATGCC  
ATTGCTGTGGAAGCTGCCTGCACCTAATGTTCCGGCGTTATTTCTTGATGTCTCTGACCAGACACC  
CATCAACAGTATTATTTCTCCCATGAAGACGGTACGCGACTGGGCGTGGAGCATCTGGTTCGCAT  
TGGGTCAACAGCAAATCGCGCTGTTAGCGGGCCCAATTAAGTTCTGTCTCGGCGCGTTCGCGTCTG  
GCTGGCATAAAATATCTCACTCGCAATCAAATTCAGCCGATAGCGGAACGGGAAGCGGACTG  
GATGCCATGTCCGGTTTCAACAACAACCATGCAAAATGCTGAATGAGGGCATCGTTCCCACTGCGA  
TGCTGGTTGCCAACGATCAGATGGCGCTGGGCGCAATGCGCGCCATTACCGAGTCCGGGCTGCGC  
GTTGGTGCAGATATCTCGGTAGTGGGATACGACGATACCGAAGACAGCTCATGTTATATCCCGCC  
GTTAACACCACATCAAACAGGATTTTCGCCTGCTGGGGCAAACCAGCGTGGACCGCTTGCTGCAAC  
TCTCTCAGGGCCAGGCGGTGAAGGGCAATCAGCTGTTGCCCGTCTCACTGGTGA AAAAGAAAAACC  
ACCCTGGCGCCCAATACGCAAACCGCCTCTCCCCGCGGTTGGCCGATTCATTAATGCAGCTGGC  
ACGACAGGTTTCCCGACTGGAAAGCGGGCAGTGAGCGCAACGCAATTAATGTAAGTTAGCTCACT  
CATTAGGCACCGGGATCTCGACCGATGCCCTTGAGAGCCTTCAACCCAGTCAGCTCCTTCCGGTG  
GGCGCGGGGCATGACTATCGTCGCCGCACTTATGACTGTCTTCTTTATCATGCAACTCGTAGGAC  
AGGTGCCCGCAGCGCTCTGGGTCATTTTCGGCGAGGACCGCTTTCGCTGGAGCGCGACGATGATC  
GGCCTGTGCTTTCGGTATTCGGAATCTTGCACGCCCTCGCTCAAGCCTTCGTCACTGGTCCCGC  
CACC AAACGTTTTCGGCGAGAAGCAGGCCATTATCGCCGGCATGGCGGGCCACGGGTGCGCATGA  
TCGTGCTCCTGTGCTTGGAGACCCGGCTAGGCTGGCGGGGTTGCCTTACTGGTTAGCAGAATGAA  
TCACCGATACGCGAGCGAACGTGAAGCGACTGCTGCTGCAAAAACGTCTGCGACCTGAGCAACAAC  
ATGAATGGTCTTTCGGTTTCCGTGTTTCGTAAAGTCTGAAAACGCGGAAGTCAGCGCCCTGCACCA  
TTATGTTCCGGATCTGCATCGCAGGATGCTGCTGGCTACCCTGTGGAACACCTACATCTGTATTA  
ACGAAGCGCTGGCATTGACCCTGAGTGATTTTTCTCTGGTCCCGCCGCATCCATACCGCCAGTTG  
TTTACCCTCACAACGTTCCAGTAACCGGGCATGTTTCATCATCAGTAACCCGTATCGTGAGCATCC  
TCTCTCGTTTCATCGGTATCATTACCCCATGAACAGAAATCCCCCTTACACGGAGGCATCAGTG  
ACCAAACAGGAAAAAACCGCCCTTAACATGGCCCGCTTTATCAGAAGCCAGACATTAACGCTTCT  
GGAGAACTCAACGAGCTGGACGCGGATGAACAGGCAGACATCTGTGAATCGCTTACAGACCACG  
CTGATGAGCTTTACCGCAGCTGCCTCGCGCGTTCGGTGATGACGGTGA AAAACCTCTGACACATG  
CAGTCCCGGAGACGGTCACAGCTTGTCTGTAAGCGGATGCCGGGAGCAGACAAGCCCGTCAGGG  
CGGTCAGCGGGTGTGGCGGGTGTGGGGCGCAGCCATGACCCAGTCACGTAGCGATAGCGGAG  
TGTATACTGGCTTAACTATGCGGCATCAGAGCAGATTGTACTGAGAGTGCACCATATATGCGGTG  
TGAAATACCGCACAGATGCGTAAGGAGAAAATACCGCATCAGGCGCTCTTCCGCTTCCCTCGCTCA  
CTGACTCGTGCCTCGGTCGTTCCGCTGCGGCGAGCGGTATCAGCTCACTCAAAGCGGGTAATA  
CGGTTATCCACAGAATCAGGGGATAACGCAAGAAACAATGTGAGCAAAAAGCCAGCAAAAAGGC  
CAGGAACCGTAAAAAGGCCGCTTGCTGGCGTTTTTCCATAGGCTCCGCCCCCTGACGAGCATC  
ACAAAAATCGACGCTCAAGTCAGAGGTGGCGAAAACCCGACAGGACTATAAAGATACCAGGCGTTT  
CCCCCTGGAAGCTCCCTCGTGCCTCTCCTGTTCCGACCCTGCCGCTTACCGGATACCTGTCCGC  
CTTTCTCCCTTCGGGAAGCGTGGCGCTTTCTCATAGCTCACGCTGTAGGTATCTCAGTTCCGGTGT  
AGGTGCTTCGCTCCAAGCTGGGCTGTGTGCACGAACCCCCGTTTACGCCCGACCGCTGCGCCTTA  
TCCGGTAACTATCGTCTTGGTCCAACCCGGTAAGACACGACTTATCGCCACTGGCAGCAGCCAC  
TGGTAACAGGATTAGCAGAGCGAGGTATGTAGGCGGTGCTACAGAGTTCTTGAAGTGGTGGCCTA  
ACTACGGCTACACTAGAAGGACAGTATTTGGTATCTGCGCTCTGCTGAAGCCAGTTACCTTCGGA  
AAAAGAGTTGGTAGCTCTTGATCCGGCAAACAACACCAGCTGGTAGCGGTGGTTTTTTTTGTTT  
CAAGCAGCAGATTACGCGCAGAAAAAAGGATCTCAAGAAGATCCTTTGATCTTTTTCTACGGGGT  
CTGACGCTCAGTGAACGAAAACCTCACGTTAAGGGATTTTGGTCATGAACAATAAAACTGTCTGC

TTACATAAACAGTAATACAAGGGGTGTTATGAGCCATATTTCAACGGGAAACGTCTTGCTCTAGGC  
CGCGATTAAATTCCAACATGGATGCTGATTTATATGGGTATAAATGGGCTCGCGATAATGTCCGG  
CAATCAGGTGCGACAATCTATCGATTGTATGGGAAGCCCGATGCGCCAGAGTTGTTTCTGAAACA  
TGGCAAAGGTAGCGTTGCCAATGATGTTACAGATGAGATGGTCAGACTAAACTGGCTGACGGAAT  
TTATGCCTCTTCCGACCATCAAGCATTTTATCCGTACTCCTGATGATGCATGGTTACTCACCCT  
GCGATCCCCGGGAAAACAGCATTCCAGGTATTAGAAGAATATCCTGATTCAGGTGAAAATATTGT  
TGATGCGCTGGCAGTGTTCCTGCGCCGGTTGCATTCGATTCCTGTTTGTAAATTGTCTTTTAAACA  
GCGATCGCGTATTTTCGTCTCGCTCAGGCGCAATCACGAATGAATAACGGTTTGGTTGATGCGAGT  
GATTTTGGATGACGAGCGTAATGGCTGGCCTGTTGAACAAGTCTGGAAAAGAAAATGCATAAACTTTT  
GCCATTCTCACCCGATTTCAGTCGTCACCTCATGGTGATTTCTCACTTGATAACCTTATTTTGGACG  
AGGGGAAAATTAATAGGTTGTATTGATGTTGGACGAGTCGGAATCGCAGACCGATAACCAGGATCTT  
GCCATCCTATGGAACCTGCCTCGGTGAGTTTTCTCCTTCATTACAGAAACGGCTTTTTCAAAAATA  
TGGTATTGATAATCCTGATATGAATAAATTGCAGTTTCATTTGATGCTCGATGAGTTTTTCTAAG  
AATTAATTCATGAGCGGATACATATTTGAATGTATTTAGAAAAATAAACAAATAGGGGTTCCGCG  
CACATTTCCCCGAAAAGTGCCACCTGAAATTTGTAACGTTAATATTTTGTAAAATTCGCGTTAA  
AATTAATGACCCGAGATAGGGTTGAGTGTGTTCCAGTTTGGAAACAAGAGTCCACTATTAAGAA  
CGTGGACTCCAACGTCAAAGGGCGAAAACCGTCTATCAGGGCGATGGCCACTACGTGAACCAT  
CACCTAATCAAGTTTTTTGGGGTCGAGGTCGCGTAAAGCACTAAATCGGAACCTTAAAGGGAGC  
CCCCGATTTAGAGCTTGACGGGGAAAGCCGGCAACGTGGCGAGAAAGGAAGGAAAGGCGAA  
AGGAGCGGGCGCTAGGGCGCTGGCAAGTGTAGCGGTCACGCTGCGCGTAACCACCACACCCGCCG  
CGCTTAATGCGCCGCTACAGGGCGCGTCCCATTCCGCCA

### A.1.1 Oligomers of rcSso7d.SA

#### A.1.1.1 1x rcSso7d.SA

Vector: pET28b(+); Cloning Site: XhoI/NdeI

DNA Sequence (XhoI/NdeI restriction sites are underlined)

CATATGGGCAGCATCCATCATCATCATCACAGCAGCGGCCTGGTGCCGCGCGGCAGCCATAT  
GTGTGCAACCGTGAAATTCACATACCAAGGCGAAGAAAAACAGGTGGATATTAGCAAAAATCAAGA  
TCGTGGCTCGTGACGGCCAGTACATTGACTTTAAATATGATGAAGGTGGTGGTGCCTATGGTTAT  
GGTTGGGTGAGCGAAAAAGATGCACCGAAAGAAGTCTGCAGATGCTGAAAAGCAATAACTCGA  
G

Amino Acid Sequence

MGS IHHHHHHSSGLVPRGSHMCATVKFTYQGEEKQVDISKIKIVARDGQYIDFKYDEGGGAYGYG  
WVSEKDAPKELLQMLEKQ

#### A.1.1.2 2x rcSso7d.SA

Vector: pET28b(+); Cloning Site: XhoI/NdeI

DNA Sequence (XhoI/NdeI restriction sites are underlined)

CATATGGGCAGCAGCCATCATCATCATCACAGCAGCGGCCTGGTGCCGCGCGGCAGCCATAT  
GTGTGCAACCGTGAAATTCACATACCAAGGCGAAGAAAAACAGGTGGATATTAGCAAAAATCAAGA  
TCGTGGCTCGTGACGGCCAGTACATTGACTTTAAATATGATGAAGGTGGTGGTGCCTATGGTTAT  
GGTTGGGTGAGCGAAAAAGATGCACCGAAAGAAGTCTGCAGATGCTGAAAAGCAAGGTGGTGG  
TGGTAGCGGTGGTGGCGGTTCAATGGCAACCGTGAAATTCACATACCAAGGCGAAGAAAAACAGG  
TGGATATTAGCAAAAATCAAGATCGTGGCTCGTGACGGCCAGTACATTGACTTTAAATATGATGAA  
GGTGGTGGTGCCTATGGTTATGGTTGGGTGAGCGAAAAAGATGCACCGAAAGAAGTCTGCAGAT  
GCTGAAAAGCAAGGTGGATAACTCGAG

### Amino Acid Sequence

MGSSHHHHHHSSGLVPRGSHMCATVKFTYQGEEKQVDISKIKIVARDGQYIDFKYDEGGGAYGYG  
WVSEKDAPKELLQMLEKQGGGGSGGGGSMATVKFTYQGEEKQVDISKIKIVARDGQYIDFKYDEG  
GGAYGYGWVSEKDAPKELLQMLEKQGG

### **A.1.1.3 3x rcSso7d.SA**

Vector: pET28b(+); Cloning Site: XhoI/NdeI

### DNA Sequence (XhoI/NdeI restriction sites are underlined)

CATATGGGCAGCAGCCATCATCATCATCACAGCAGCGGCCTGGTGCCGCGCGGCAGCCATAT  
GTGTGCAACCGTGAAATTCACATACCAAGGCGAAGAAAAACAGGTGGATATTAGCAAAATCAAGA  
TCGTGGCTCGTGACGGCCAGTACATTGACTTTAAATATGATGAAGGTGGTGGTGCCTATGGTTAT  
GGTTGGGTGAGCGAAAAAGATGCACCGAAAGAACTGCTGCAGATGCTGGAAAAGCAAGGTGGTGG  
TGGTAGCGGTGGTGGCGGTTCAATGGCAACCGTGAAATTCACATACCAAGGCGAAGAAAAACAGG  
TGGATATTAGCAAAATCAAGATCGTGGCTCGTGACGGCCAGTACATTGACTTTAAATATGATGAA  
GGTGGTGGTGCCTATGGTTATGGTTGGGTGAGCGAAAAAGATGCACCGAAAGAACTGCTGCAGAT  
GCTGGAAAAGCAAGGTGGTGGTGGTAGCGGTGGTGGCGGTTCAATGGCAACCGTGAAATTCACAT  
ACCAAGGCGAAGAAAAACAGGTGGATATTAGCAAAATCAAGATCGTGGCTCGTGACGGCCAGTAC  
ATTGACTTTAAATATGATGAAGGTGGTGGTGCCTATGGATATGGTTGGGTGAGCGAAAAAGATGC  
ACCGAAAGAACTGCTGCAGATGCTGGAAAAGCAAGGTGGATAACTCGAG

### Amino Acid Sequence

MGSSHHHHHHSSGLVPRGSHMCATVKFTYQGEEKQVDISKIKIVARDGQYIDFKYDEGGGAYGYG  
WVSEKDAPKELLQMLEKQGGGGSGGGGSMATVKFTYQGEEKQVDISKIKIVARDGQYIDFKYDEG  
GGAYGYGWVSEKDAPKELLQMLEKQGGGGSGGGGSMATVKFTYQGEEKQVDISKIKIVARDGQYI  
DFKYDEGGGAYGYGWVSEKDAPKELLQMLEKQGG

### **A.1.1.4 4x rcSso7d.SA**

Vector: pET28b(+); Cloning Site: XhoI/NdeI

### DNA Sequence (XhoI/NdeI restriction sites are underlined)

CATATGGGCAGCAGCCATCATCATCATCACAGCAGCGGCCTGGTGCCGCGCGGCAGCCATAT  
GTGTGCAACCGTGAAATTCACATACCAAGGCGAAGAAAAACAGGTGGATATTAGCAAAATCAAGA  
TCGTGGCTCGTGACGGCCAGTACATTGACTTTAAATATGATGAAGGTGGTGGTGCCTATGGTTAT  
GGTTGGGTGAGCGAAAAAGATGCACCGAAAGAACTGCTGCAGATGCTGGAAAAGCAAGGTGGTGG  
TGGTAGCGGTGGTGGCGGTTCAATGGCAACCGTGAAATTCACATACCAAGGCGAAGAAAAACAGG  
TGGATATTAGCAAAATCAAGATCGTGGCTCGTGACGGCCAGTACATTGACTTTAAATATGATGAA  
GGTGGTGGTGCCTATGGTTATGGTTGGGTGAGCGAAAAAGATGCACCGAAAGAACTGCTGCAGAT  
GCTGGAAAAGCAAGGTGGTGGTGGTAGCGGTGGTGGCGGTTCAATGGCAACCGTGAAATTCACAT  
ACCAAGGCGAAGAAAAACAGGTGGATATTAGCAAAATCAAGATCGTGGCTCGTGACGGCCAGTAC  
ATTGACTTTAAATATGATGAAGGTGGTGGTGCCTATGGTTATGGTTGGGTGAGCGAAAAAGATGC  
ACCGAAAGAACTGCTGCAGATGCTGGAAAAGCAAGGTGGTGGTGGTAGCGGTGGTGGCGGTTCAA  
TGGCAACCGTGAAATTCACATACCAAGGCGAAGAAAAACAGGTGGATATTAGCAAAATCAAGATC  
GTGGCTCGTGACGGCCAGTACATTGACTTTAAATATGATGAAAGTGGTGGTGCCTATGGTTATGG  
TTGGGTGAGCGAAAAAGATGCACCGAAAGAACTGCTGCAGATGCTGGAAAAGCAATAACTCGAG

### Amino Acid Sequence

MGSSHHHHHHSSGLVPRGSHMCATVKFTYQGEEKQVDISKIKIVARDGQYIDFKYDEGGGAYGYG  
WVSEKDAPKELLQMLEKQGGGGSGGGGSMATVKFTYQGEEKQVDISKIKIVARDGQYIDFKYDEG  
GGAYGYGWVSEKDAPKELLQMLEKQGGGGSGGGGSMATVKFTYQGEEKQVDISKIKIVARDGQYI

DFKYDEGGGAYGYGWVSEKDAPKELLQMLEKQGGGGSGGGSMATVKFTYQGEEKQVDISKIKIV  
ARDGQYIDFKYDESGGAYGYGWVSEKDAPKELLQMLEKQ

## **A.1.2 Intermediate Genes Designed for Coiled-Coil Fusions of 2x rcSso7d.SA**

### **A.1.2.1 2x C-Cys**

Vector: pET28b(+); Cloning Site: XhoI/NdeI

DNA Sequence (XhoI/NdeI restriction sites are underlined)

CATATGGGCAGCAGCCATCATCATCATCACAGCAGCGGCCTGGTGCCGCGCGGCAGCCATAT  
GGCAACCGTGAAATTCACATACCAAGGCGAAGAAAAACAGGTGGATATTAGCAAAATCAAGATCG  
TGGCTCGTGACGGCCAGTACATTGACTTTAAATATGATGAAGGTGGTGGTGCCTATGGTTATGGT  
TGGGTGAGCGAAAAAGATGCACCGAAAGAAGCTGCTGCAGATGCTGGAAAAGCAAGGTGGTGGTGG  
TAGCGGTGGTGGCGGTTCAATGGCAACCGTGAAATTCACATACCAAGGCGAAGAAAAACAGGTGG  
ATATTAGCAAAATCAAGATCGTGGCTCGTGACGGCCAGTACATTGACTTTAAATATGATGAAGGT  
GGTGGTGCCTATGGTTATGGTTGGGTGAGCGAAAAAGATGCACCGAAAGAAGCTGCTGCAGATGCT  
GGAAAAGCAATGTGGTGGATAACTCGAG

### **A.1.2.2 2x N-Cys\_C-BsaI**

Vector: pET28b(+); Cloning Site: XhoI/NdeI

DNA Sequence (XhoI/NdeI restriction sites are underlined)

GGCAGCCCATATGGGCAGCAGCCATCATCATCATCACAGCAGCGGCCTGGTGCCGCGCGGCAG  
CCATATGTGTGCAACCGTGAAATTCACATACCAAGGCGAAGAAAAACAGGTGGATATTAGCAAAA  
TCAAGATCGTGGCTCGTGACGGCCAGTACATTGACTTTAAATATGATGAAGGTGGTGGTGCCTAT  
GGTTATGGTTGGGTGAGCGAAAAAGATGCACCGAAAGAAGCTGCTGCAGATGCTGGAAAAGCAAGG  
TGGTGGTGGTAGCGGTGGTGGCGGTTCAATGGCAACCGTGAAATTCACATACCAAGGCGAAGAAA  
AACAGGTGGATATTAGCAAAATCAAGATCGTGGCTCGTGACGGCCAGTACATTGACTTTAAATAT  
GATGAAGGTGGTGGTGCCTATGGTTATGGTTGGGTGAGCGAAAAAGATGCACCGAAAGAAGCTGCT  
GCAGATGCTGGAAAAGCAAGGTGGATAAGGTGAGGTCTCCTCGAGTGACAC

### **A.1.2.3 2x C-Cys\_N-BsaI**

Vector: pET28b(+); Cloning Site: XhoI/NdeI

DNA Sequence (XhoI/NdeI restriction sites are underlined)

TGTCAGCCATATGGGTCTCCAATGGGCAGCAGCCATCATCATCATCACAGCAGCGGCCTGGTG  
CCGCGCGGCAGCCATATGGCAACCGTGAAATTCACATACCAAGGCGAAGAAAAACAGGTGGATAT  
TAGCAAAATCAAGATCGTGGCTCGTGACGGCCAGTACATTGACTTTAAATATGATGAAGGTGGTG  
GTGCCTATGGTTATGGTTGGGTGAGCGAAAAAGATGCACCGAAAGAAGCTGCTGCAGATGCTGGAA  
AAGCAAGGTGGTGGTGGTAGCGGTGGTGGCGGTTCAATGGCAACCGTGAAATTCACATACCAAGG  
CGAAGAAAAACAGGTGGATATTAGCAAAATCAAGATCGTGGCTCGTGACGGCCAGTACATTGACT  
TTAAATATGATGAAGGTGGTGGTGCCTATGGTTATGGTTGGGTGAGCGAAAAAGATGCACCGAAA  
GAAGTCTGCAGATGCTGGAAAAGCAATGTGGTGGATAACTCGAGCACCAC

## **A1.3 Coiled-Coil Fusions of 2x rcSso7d.SA**

### **A.1.3.1 2xZEC**

Vector: pET28b(+); Cloning Site: XhoI/NdeI

**DNA Sequence** (XhoI/NdeI restriction sites are underlined)

CATATGGGCAGCAGCCATCATCATCATCATCACAGCAGCGGCCTGGTGCCGCGCGGCAGCCATAT  
GTGCGCGACCGTTAAGTTCACCTACCAGGGCGAGGAAAAACAAGTTGACATCAGCAAGATCAAAA  
TTGTGGCGCGTGATGGCCAGTACATTGACTTTAAGTATGATGAAGGTGGCGGTGCGTACGGTTAT  
GGCTGGGTTAGCGAAAAGGACGCGCCGAAAGAGCTGCTGCAGATGCTGGAAAAACAAGCGGTGG  
CGGTAGCGGCGGTGGCGGTAGCATGGCGACCGTGAAGTTCACCTATCAAGGCGAAGAGAAGCAGG  
TGGATATTAGCAAAATTAAGATCGTGGCGCGTGATGGTCAATATATCGATTTCAAGTATGATGAA  
GGCGGTGGCGCGTACGGTTACGGTTGGGTGAGCGAGAAGGATGCGCCGAAAGAACTGCTGCAGAT  
GCTGGAGAAACAAGGTGGCGGTGGCAGCGGTGGCGGTGGCAGCCTGGAGATTGAAGCGGCGGCGC  
TGGAGCAGGAAAACACCGCGCTGGAAACCGAGGTGGCGGAGCTGGAACAGGAAGTGAACCGTCTG  
GAGAACATTTGTGAGCCAATACCGTACCGTTATGGTCCGCTGTAACTCGAG

**Amino Acid Sequence**

MGSSHHHHHHSSGLVPRGSHMCATVKF'ITYQGEEKQVDISKIKIVARDGQYIDFKYDEGGGAYGYG  
WVSEKDAPKELLQMLEKQGGGSGGGGSMATVKF'ITYQGEEKQVDISKIKIVARDGQYIDFKYDEG  
GGAYGYGWVSEKDAPKELLQMLEKQGGGSGGGGSLEIEAAALEQENTALETEVAELEQEVQRLE  
NIVSQYRTRYGPL

**A.1.3.2 2xZRC**

Vector: pET28b(+); Cloning Site: XhoI/NdeI

**DNA Sequence** (XhoI/NdeI restriction sites are underlined)

CATATGGGCAGCAGCCATCATCATCATCATCACAGCAGCGGCCTGGTGCCGCGCGGCAGCCATAT  
GTGCGCGACCGTTAAGTTCACCTACCAGGGCGAGGAAAAACAAGTTGACATCAGCAAGATCAAAA  
TTGTGGCGCGTGATGGCCAGTACATTGACTTTAAGTATGATGAGGGTGGCGGTGCGTACGGTTAT  
GGCTGGGTTAGCGAGAAGGACGCGCCGAAAGAACTGCTGCAGATGCTGGAGAAACAAGCGGTGG  
CGGTAGCGGCGGTGGCGGTAGCATGGCGACCGTGAAGTTCACCTATCAAGGCGAAGAGAAGCAGG  
TGGATATTAGCAAAATTAAGATCGTGGCGCGTGATGGTCAATATATCGACTTTAAGTATGATGAA  
GGCGGTGGCGCGTACGGTTACGGTTGGGTGAGCGAAAAGGATGCGCCGAAAGAGCTGCTGCAGAT  
GCTGGAAAAACAAGGTGGCGGTGGCAGCGGTGGCGGTGGCAGCCTGGAGATCCGTGCGGCGGCGC  
TGCCTCGTAAACACCGCGCTGCGTACCGGTGTGGCGGAACTGCGTCAGCGTGTCAACGTCTG  
CGTAACGAGGTGAGCCAGTACGAAACCGTTATGGTCCGCTGTAACTCGAG

**Amino Acid Sequence**

MGSSHHHHHHSSGLVPRGSHMCATVKF'ITYQGEEKQVDISKIKIVARDGQYIDFKYDEGGGAYGYG  
WVSEKDAPKELLQMLEKQGGGSGGGGSMATVKF'ITYQGEEKQVDISKIKIVARDGQYIDFKYDEG  
GGAYGYGWVSEKDAPKELLQMLEKQGGGSGGGGSLEIRAAALRRRNTALRTRVAELRQRVQRLR  
NEVSQYETRYGPL

**A.1.3.3 2xZEN**

Vector: pET28b(+); Cloning Site: XhoI/NdeI

**DNA Sequence** (XhoI/NdeI restriction sites are underlined)

CATATGGGCAGCAGCCATCATCATCATCATCACAGCAGCGGCCTGGTGCCGCGCGGCAGCCATAT  
GCTGGAGATCGAAGCGGCGCGCTGGAGCAGGAAAACACCGCGCTGGAAACCGAGGTGGCGGAGC  
TGAACAGGAAGTGAACCGTCTGAAAACATTGTGAGCCAATACCGTACCGTTATGGTCCGCTG  
GGTGGTGGTGGTAGCGGTGGTGGCGGTTCAATGGCAACCGTGAAATTCACATACCAAGGCGAAGA  
AAAACAGGTGGATATTAGCAAAATCAAGATCGTGGCTCGTGACGGCCAGTACATTGACTTTAAAT

ATGATGAAGGTGGTGGTGCCTATGGTTATGGTTGGGTGAGCGAAAAAGATGCACCGAAAGAACTG  
CTGCAGATGCTGGAAAAGCAAGGTGGTGGTGGTAGCGGTGGTGGCGGTTCAATGGCAACCGTGAA  
ATTCACATACCAAGGCGAAGAAAAACAGGTGGATATTAGCAAAATCAAGATCGTGGCTCGTGACG  
GCCAGTACATTGACTTTAAATATGATGAAGGTGGTGGTGCCTATGGTTATGGTTGGGTGAGCGAA  
AAAGATGCACCGAAAGAACTGCTGCAGATGCTGGAAAAGCAATGTGGTGGATAACTCGAG

**Amino Acid Sequence**

MGSSHHHHHSSGLVPRGSHMLEIEAAALEQENTALETEVAELEQEVQRLLENIVSQYRTRYGPLG  
GGSGGGGSMATVKFTYQGEEKQVDISKIKIVARDGQYIDFKYDEGGGAYGYGWSEKDAPKELL  
QMLEKQGGGSGGGGSMATVKFTYQGEEKQVDISKIKIVARDGQYIDFKYDEGGGAYGYGWSEK  
DAPKELLQMLEKQCGG

## A.2 PAGE Gels and CD Spectra for Proteins Recombinantly Expressed in Thesis

### A.2.1 Oligomers of rcSso7d.SA

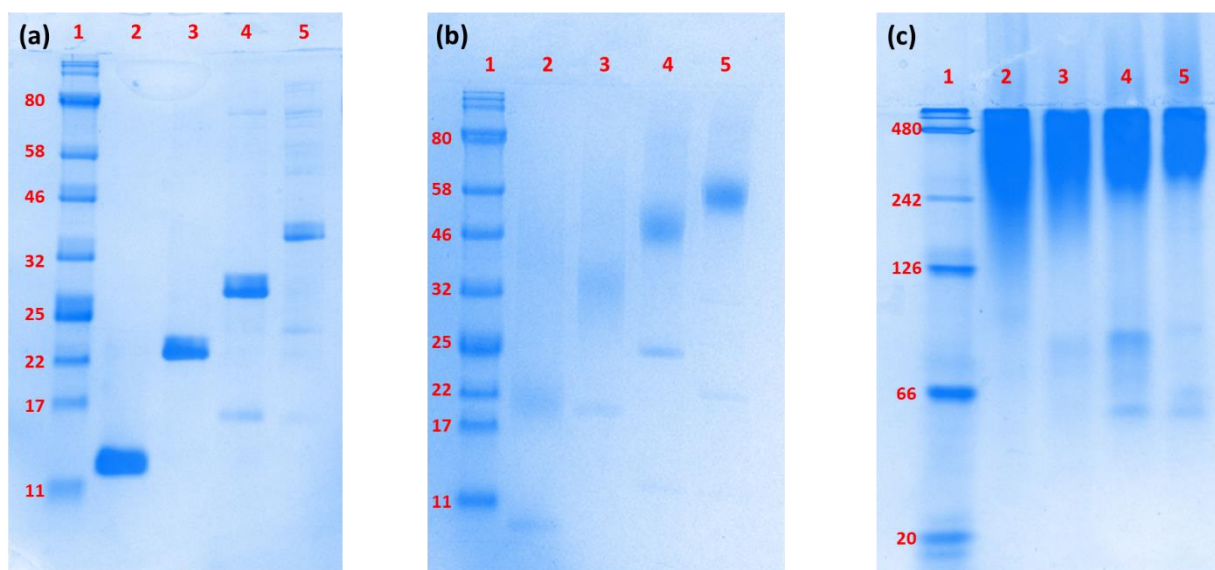


**Figure A-2.** Denaturing protein gels (12% acrylamide) of (a) Sso7d.SA oligomers and (b) bioconjugates, and (c) native protein gel (8% acrylamide) of bioconjugates. Lanes 1-5 in (a) represent ladder, 1x rcSso7d.SA, 2x rcSso7d.SA, 3x rcSso7d.SA, and 4x rcSso7d.SA, respectively. Lanes 1-5 in (b) and (c) represent ladder, 1xSP9.8k, 2xSP17k, 3xSP25k, and 4xSP30k, respectively. All ladders represent molecular weight in kDa. Minor impurities in denaturing gel (b) are primarily the result of hydrolysis of an ester linkage between protein and PNIPAM during heating of samples; integration of the bands in native gel (c) reveals that all conjugate samples are > 98% pure.

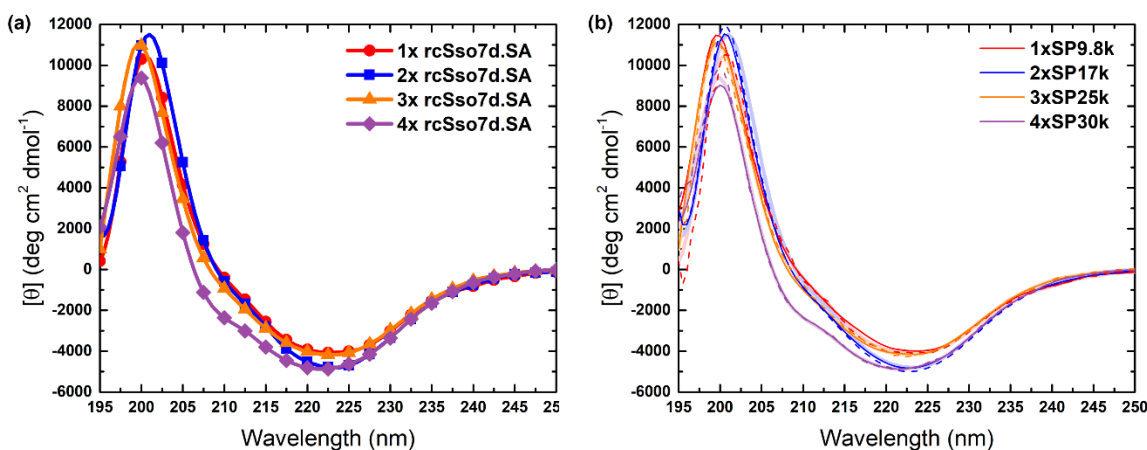


**Figure A-3.** Circular dichroism spectroscopy of (a) rcSso7d.SA oligomers and (b) rcSso7d.SA-PNIPAM conjugates before dehydration and after rehydration of solid conjugate pellets confirm minimal change in secondary structure. In (b) light colored lines represent the corresponding unconjugated rcSso7d.SA oligomer, dashed lines represent conjugates before dehydration, and

dark colored lines represent conjugates after rehydration. All rcSso7d.SA oligomers were measured in 50 mM Tris buffer, 100 mM NaCl, 0.25 mM TCEP, pH 7.4. Conjugates were measured in MilliQ water. Measurements were performed at 25 °C. Slight differences between CD spectra of conjugates in (b) below 205 nm are primarily due to high noise in the CD spectrometer at these wavelengths.

### A.2.2 Coiled-Coil Fusions of 2x rcSso7d.SA

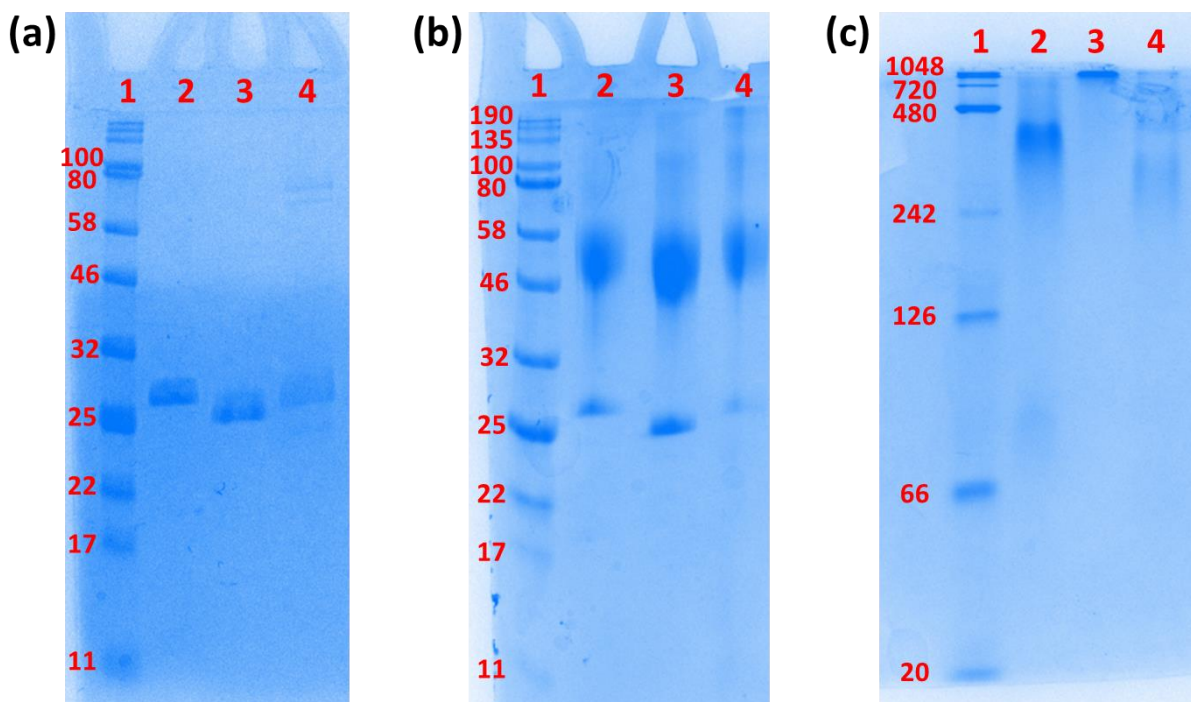


**Figure A-4.** Denaturing protein gels (12% acrylamide) of (a) 2x rcSso7d.SA coiled-coil fusion proteins and (b) bioconjugates, and (c) native protein gel (8% acrylamide) of bioconjugates. Lanes 1-4 in (a) represent ladder, 2xZEC, 2xZRC, and 2xZEN, respectively. Lanes 1-4 in (b) and (c) represent ladder and 2xZEC, 2xZRC, and 2xZEN conjugated to PNIPAM ( $M_n = 26.1$  kDa), respectively. All ladders represent molecular weight in kDa. Minor impurities in denaturing gel (b) are primarily the result of hydrolysis of an ester linkage between protein and PNIPAM during heating of samples; integration of the bands in native gel (c) reveals that all conjugate samples are > 98% pure. Native gel (c) was performed in a running buffer with a pH of 10.0. Relatively little movement of the 2xZRC conjugate band is likely a result of the running buffer pH being close to the isoelectric point of 2xZRC ( $pI = 9.0$ ). Higher running buffer pH was avoided to prevent denaturation of the protein block.

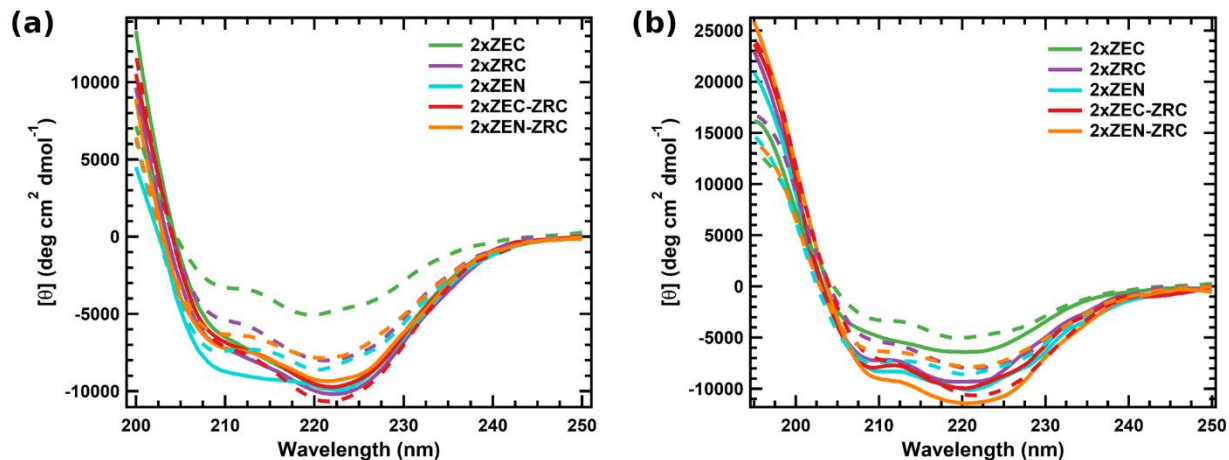


**Figure A-5.** Circular dichroism spectroscopy of (a) 2x coiled-coil fusion proteins and (b) conjugates in MilliQ water at concentrations of 0.1 mg/mL. In (a) dashed lines represent spectra in MilliQ water and solid lines represent spectra in ZE buffer. In (b) dashed lines represent spectra for the unconjugated fusion protein in MilliQ water and solid lines represent spectra for the corresponding conjugates. CD Spectra in (a) were only collected down to wavelengths of 200 nm due to interference from high salt concentrations in ZE buffer at lower wavelengths.

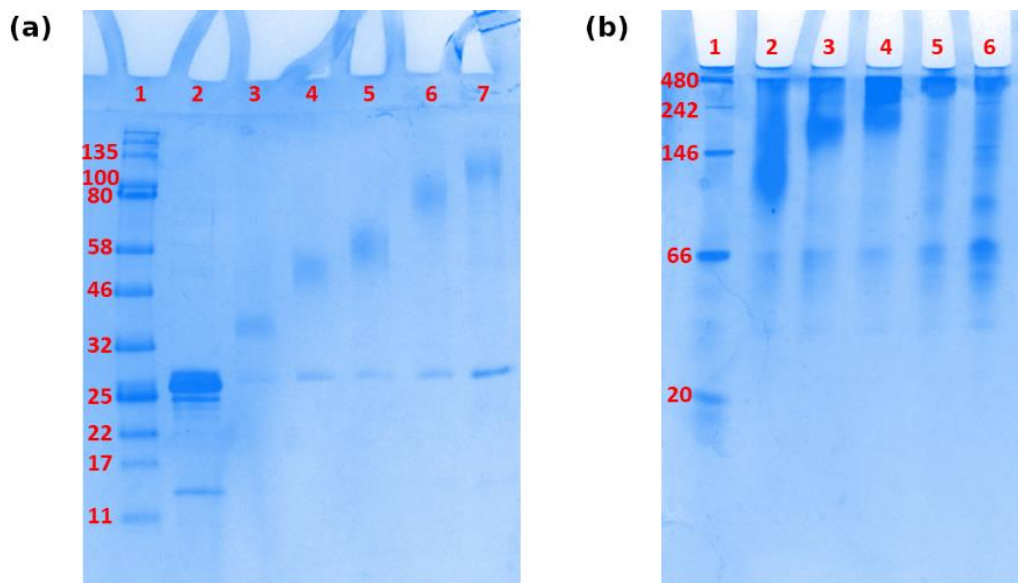


**Figure A-6.** Denaturing protein gel (12% acrylamide) of (a) 3x rcSso7d.SA and bioconjugates, and (b) native protein gel (8% acrylamide) of bioconjugates. Lanes 1-7 in (a) represent ladder, 3x rcSso7d.SA, 3xSP9.6k, 3xSP23.3k, 3xSP30.3k, 3xSP56.1k, 3xSP77.6k, respectively. Lanes 1-6 in (b) represent ladder, 3xSP9.6k, 3xSP23.3k, 3xSP30.3k, 3xSP56.1k, 3xSP77.6k, respectively. All ladders are labeled with molar mass in kDa. Minor impurities in denaturing gel (a) are primarily the result of hydrolysis of an ester linkage between protein and PNIPAM during heating of samples; integration of the bands in native gel (b) reveals that all conjugate samples are > 90% pure.

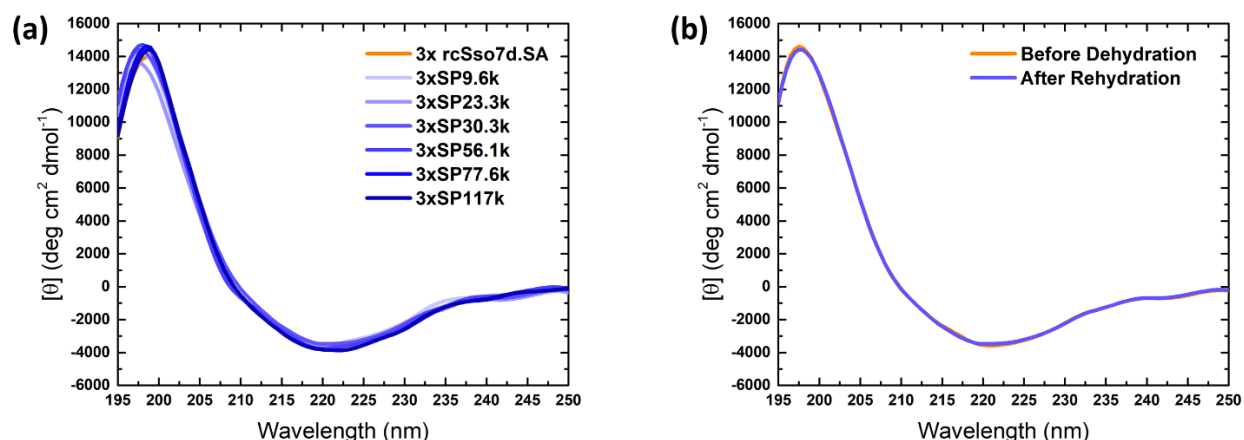


**Figure A-7.** Circular dichroism spectroscopy of (a) 3x rcSso7d.SA and all plotted bioconjugates and (b) 3xSP30.3k before dehydration and after rehydration of solid conjugate pellets confirm minimal change in protein secondary structure. Results in (b) are representative of all conjugates. Slight differences between CD spectra of conjugates in (a) below 205 nm are primarily due to high noise in the CD spectrometer at these wavelengths.

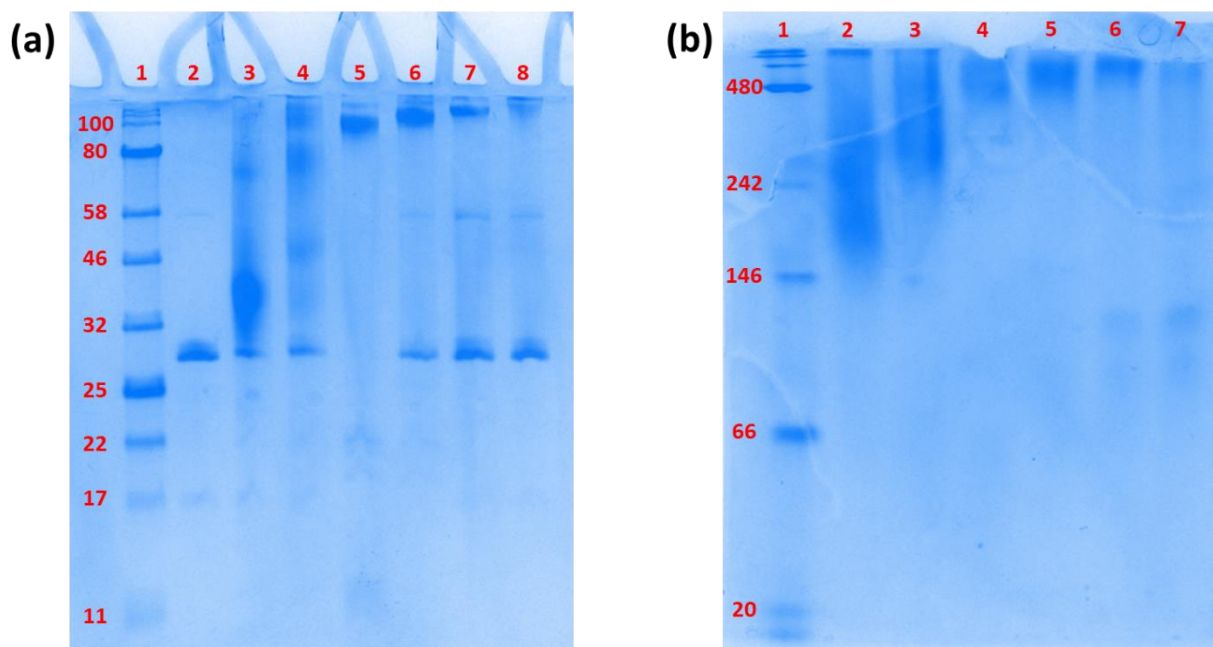


**Figure A-8.** Denaturing protein gel (12% acrylamide) of (a) 3x rcSso7d.SA and bioconjugates, and (b) native protein gel (8% acrylamide) of bioconjugates. Lanes 1-8 in (a) represent ladder, 3x rcSso7d.SA, 3xSP9.6k, 3xSP23.3k, 3xSP46.6k, 3xSP56.1k, 3xSP77.6k, and 3xSP117k, respectively. Lanes 1-7 in (b) represent ladder, 3xSP9.6k, 3xSP23.3k, 3xSP46.6k, 3xSP56.1k, 3xSP77.6k, and 3xSP117k, respectively. All ladders are labeled with molar mass in kDa. Minor impurities in denaturing gel (a) are primarily the result of hydrolysis of an ester linkage between protein and PNIPAM during heating of samples; integration of the bands in native gel (b) reveals that all conjugate samples are > 98% pure.

### A.3. $^1\text{H-NMR}$ Spectra

#### A.3.1 EMP

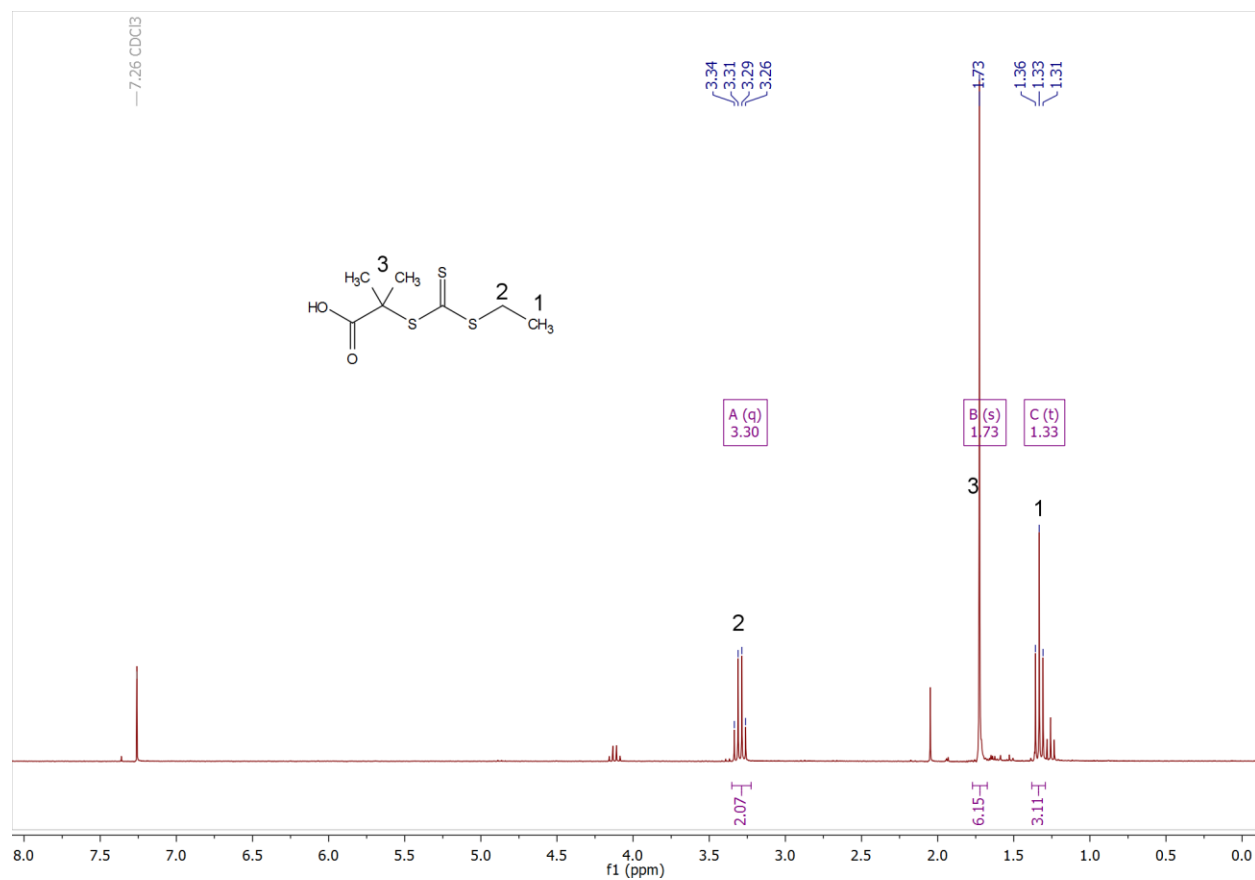


**Figure A-9.**  $^1\text{H-NMR}$  spectra for EMP. A TLC of this compound can be found in **Figure 2-6**.

**A.3.2 exo-3a,4,7,7a-Tetrahydro-2-(3-hydroxypropyl)-4,7-epoxy-14-isoindole-1,3(2H)-dione (1)**

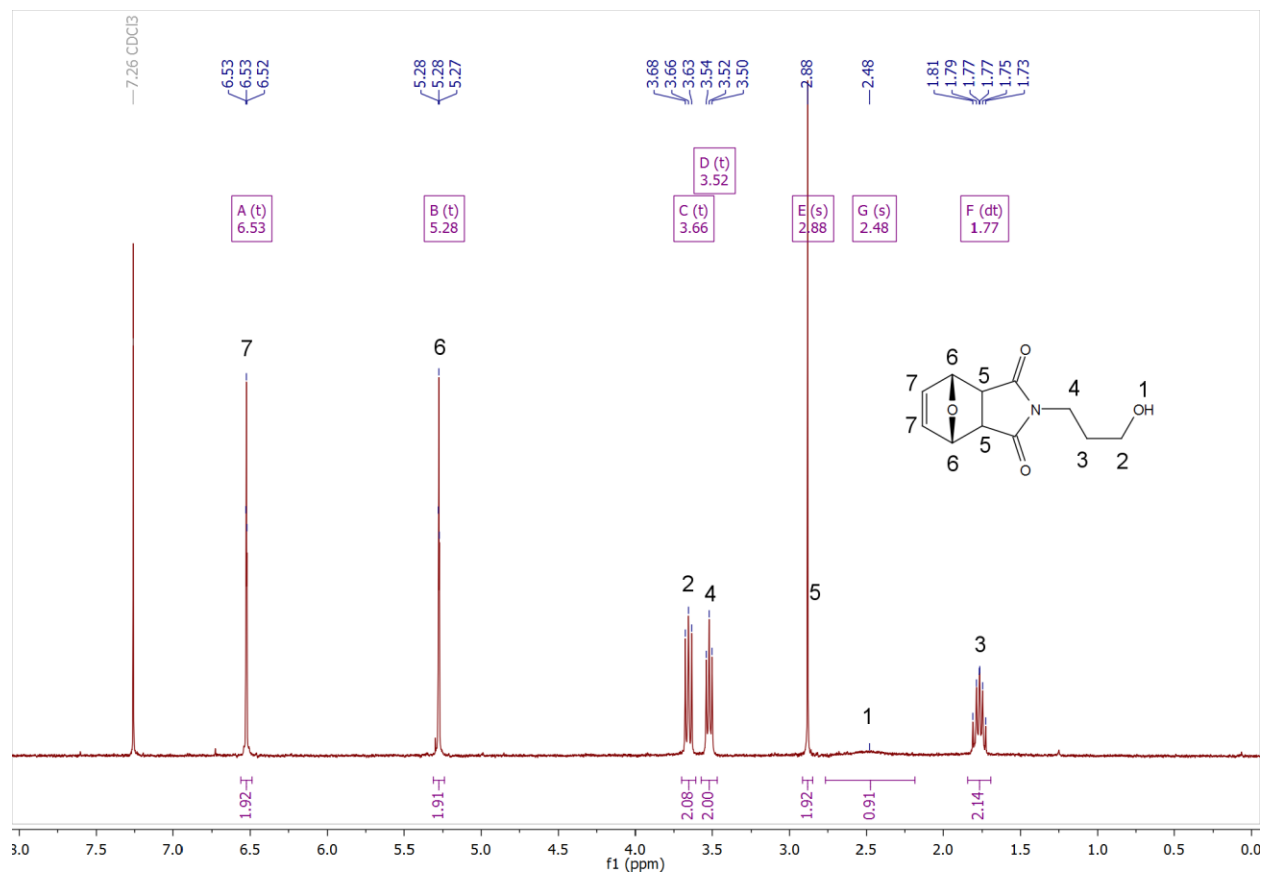


**Figure A-10.**  $^1\text{H-NMR}$  spectra for *exo*-3a,4,7,7a-Tetrahydro-2-(3-hydroxypropyl)-4,7-epoxy-14-isoindole-1,3(2H)-dione (1).

### A.3.3 CTA

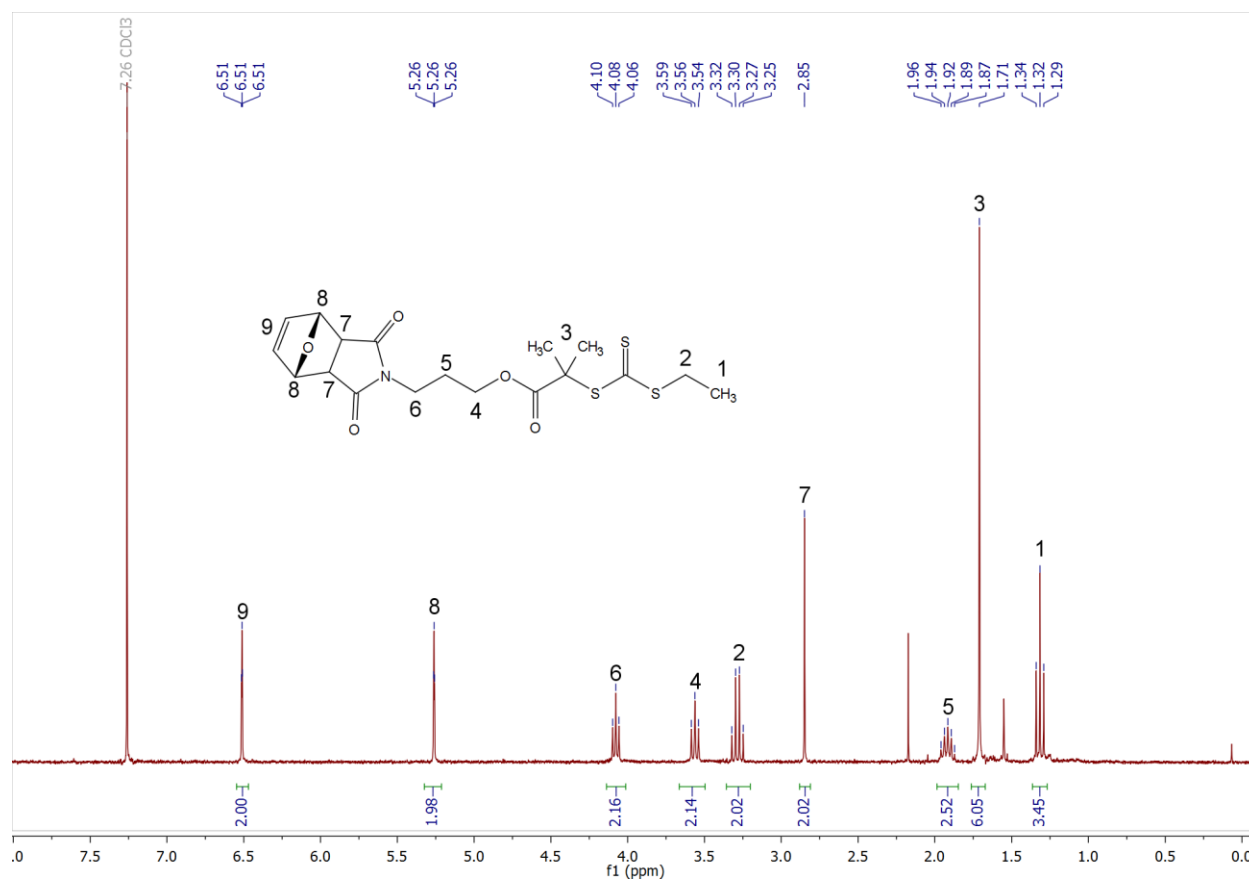


**Figure A-11.** <sup>1</sup>H-NMR spectra for CTA. A TLC of this compound can be found in **Figure 2-7**.

#### A.4 Supporting Figures for Biosensor Measurements

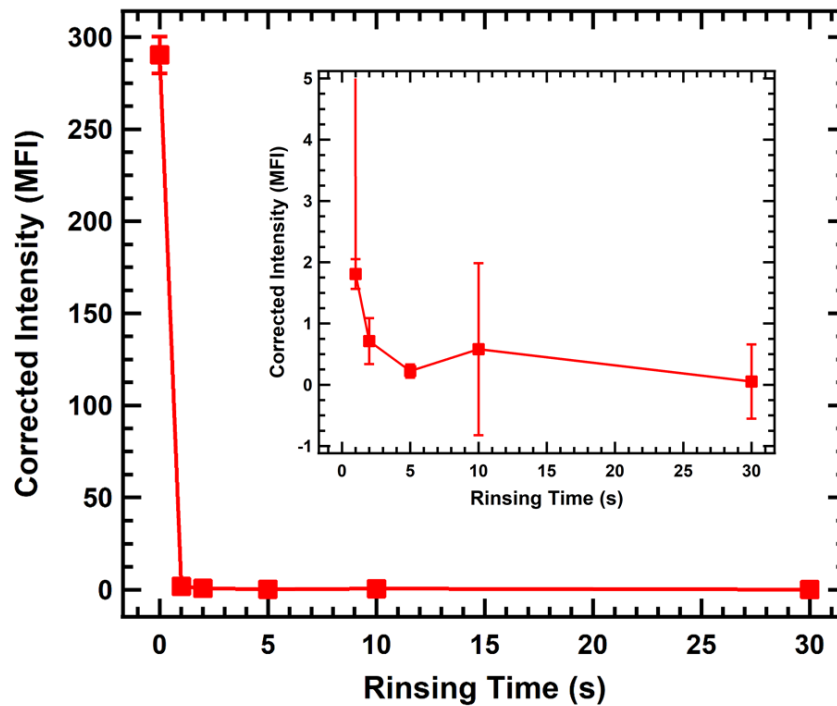


**Figure A-12.** Fluorescent intensity of BSA labeled with Alexa Fluor 488 retained in 3xSP77.6k thin film after various rinsing times. Inset shows enlarged view of low intensity data. The film was 144 nm thick and exposed to a 10  $\mu$ M solution of BSA. Error bars represent the standard deviation of three replicates.

## A.5. Data Processing Code

### A.5.1 SAXS Data Processing Code

```
function process11_BM_SAXS(directIn,directExp,headData,headBlank,T,numWP)
%This function imports processed SAXS data obtained from beamline 11-BM
%at NSLS-II using the txt2mat function (obtained from MathWorks file
%exchange) and groups/exports the data in a format that is optimal for
%plotting
%
%Inputs
% directIn: String containing the directory from which data will be
% imported
% directExp: String containing the directory to which data will be
% exported. Must include desired filename and end with
% ".xlsx"
% headData: Cell array of strings at beginning of each filename to be
% plotted together (e.g., if ABC1.dat and ABC2.dat should be
% plotted in same graph, headData should contain 'ABC').
% Strings should be organized such that data corresponding
% to the same conjugate are adjacent and in order of
% increasing weight percent. Weight percents should be
% denoted as Pxx at the end of each string, where "xx" is the
% weight percent, in percent (e.g., 50)
% headBlank: String at beginning of each filename for blank samples
% T: Cell array of strings containing temperatures at which
% data was collected (e.g., {'10C','20C','30C'})
% numWP: Vector of number of weight percent data collected for each
% conjugate, as listed in headData (e.g., if headData were
% {'A30P','A40P','B30P','C30P','C40P'}, numWT should be
% [2,1,2])
%Outputs
% Data exported to Excel file in directory determined by directExp
%
%Written by Justin Paloni on 10/10/2017

%% Input Parameters for 11-BM SAXS Data
qCol = 1; %Column in which q values are stored
I_Col = 3; %Column in which intensity values are stored
datStart = 30; %Row in which non-noisy data begins
datEnd = 289; %Row in which non-noisy data ends

%% Extract Blank Data
dirListing = dir(strcat(directIn,'\*.dat'));
numFiles = length(dirListing);

%Create vector of filenames
datNames = string(zeros(size(dirListing)));

for i = 1:numFiles
    datNames(i) = string(dirListing(i).name);
end

%Import q values
filename = char(strcat(directIn,'\ ',datNames(1)));
dat = txt2mat(filename); %Download txt2mat from MathWorks file exchange
```

```

q = dat(datStart:end-datEnd,qCol)*10; %nm-1

%Import blank data
datBlank = zeros(length(q),length(T));

for i = 1:length(T)
    indBlank = find(startsWith(datNames,...
        strcat(headBlank,'_T',string(T(i)))));
    filename = char(strcat(directIn,'\ ',datNames(indBlank)));
    dat = txt2mat(filename);
    datBlank(:,i) = dat(datStart:end-datEnd,I_Col);
end

%Check blank data exists for all temperatures
if size(datBlank,2) ~= length(T)
    error('Blank data not collected at each temperature.')
end

%% Extract Data, Subtract Background, and Group Together
Data = cell(length(headData),length(T));

for i = 1:length(headData)
    for j = 1:length(T)
        indData = find(startsWith(datNames,...
            strcat(headData(i),'_T',string(T(j)))));
        %If replicates taken at lower exposure times, average replicates
        rep = length(indData);

        I_dat = zeros(length(q),rep);

        for k = 1:rep
            filename = char(strcat(directIn,'\ ',datNames(indData(k))));
            dat = txt2mat(filename);
            I_dat(:,k) = dat(datStart:end-datEnd,I_Col)*(10^(j-1));
        end
        %Subtract background from average
        Data{i,j} = mean(I_dat,2) - datBlank(:,j);
    end
end

%% Export Grouped Data
%Suppress warning
warning('off','MATLAB:xlswrite:AddSheet');

%Export data at constant weight percent
header = cell(3,length(T) + 1);
header(1,1) = {'q'};
header(2,1) = {'nm\+(-1)'};
header(3,1) = {' '};

for i = 1:length(T)
    header(1,i+1) = {'Intensity'};
    header(2,i+1) = {'a.u.'};
    tSam = char(T(i));
    header(3,i+1) = {[tSam(1:2), sprintf('%cC', char(176))]};
end

```

```

for i = 1:length(headData)
    constWP = [q cell2mat(Data(i,:))];
    xlswrite(directExp,header,char(headData(i)), 'A1');
    xlswrite(directExp,constWP,char(headData(i)), 'A4');

    %Display progress
    fprintf('\n%d of %d weight percent files processed',i,length(headData))
end

%Export all weight percent data for each conjugate at 25C
DataT = Data';
datExp = 0;

for i = 1:length(numWP)
    start = datExp + 1;
    stop = datExp + numWP(i);

    %Offset data for clarity
    mult = zeros(1,numWP(i));
    for j = 1:numWP(i)
        mult(j) = 10^(j-1);
    end

    multM = diag(mult);

    DataTM = cell2mat(DataT(4,start:stop))*multM;

    constT = [q DataTM];

    sheetStart = char(headData(start));
    sheetName = strcat(string(sheetStart(1:end-3)), 'T', string(T(4)));

    xlswrite(directExp,constT,char(sheetName), 'A4');

    %Create header
    header = cell(3,numWP(i) + 1);

    header(1,1) = {'q'};
    header(2,1) = {'nm\+(-1)'};
    header(3,1) = {' '};

    for j = 1:numWP(i)
        header(1,j+1) = {'Intensity'};
        header(2,j+1) = {'a.u.'};
        wpSam = char(headData(datExp + j));
        header(3,j+1) = {[wpSam(end-1:end), sprintf(' wt%c', char(37))]}];
    end

    xlswrite(directExp,header,char(sheetName), 'A1');

    datExp = datExp + numWP(i);

    %Display progress
    fprintf('\n%d of %d constant T files processed',i,length(numWP))

end

```

## A.5.2 FRAP Image Processing Code

```
currPos = newArray(235,229,41,41); /* Initial bleach position */
prevPos = newArray(4); /* Previous bleach position */
rect1 = newArray(87,196,56,105); /* Area 1 far from bleach region */
rect2 = newArray(373,196,56,105); /* Area 2 far from bleach region */
maxMove = 5; /* Maximum movement of bleach spot in x- and y-directions */
moves = 2*maxMove + 1;
movePos = newArray(moves); /* Movements around current position to track */
for (i=0; i<moves; i++){
    movePos[i] = i - maxMove;
}
moveLen = movePos.length;
prevInt = newArray(moveLen*moveLen); /* Previous intensities around bleach region */
currInt = newArray(moveLen*moveLen); /* Current intensities around bleach region */
normInt = newArray(moveLen*moveLen); /* Ratio of current to previous intensities around
bleach region */
critDelta = 1; /* Minimum decrease in intensity corresponding to move in bleach spot */

for (i=1; i<=nSlices; i++) {
    origBetter = 0;

    /* Track bleach spot in [moves]-by-[moves] region to account for drifting */
    if (i>4) {
        for (j=0; j<movePos.length; j++) {
            for (k=0; k<movePos.length; k++) {
                arrayPos = k + (movePos.length*j);

                makeOval(prevPos[0]+movePos[k],prevPos[1]+movePos[j],prevPos[2],prevPos[3]);
                run("Measure");
                currInt[arrayPos] = getResult("Mean",arrayPos);
            }
        }
        run("Clear Results");

        /* Determine new bleach spot position */
        if (i>5) {

            /* Determine if spot has moved */
            Array.getStatistics(currInt, minInt, maxInt, meanInt, stdInt);
            delta = minInt/meanInt;

            for (j=0; j<currPos.length; j++) {
                currPos[j] = prevPos[j];
            }
        }
    }
}
```

```

if (delta<critDelta) {

    /* Determine position of largest intensity decrease */
    minArr = currInt[0];
    minIndex = 0;

    for (j=1; j<currInt.length; j++) {
        if (currInt[j] < minArr) {
            /* Only consider move if new circle has slightly
lower intensity than original position */
            if (1.001*currInt[j]<currInt[(currInt.length-1)/2]) {
                minArr = currInt[j];
                minIndex = j;
            }
        }
    }

    /* Prevent too large steps */
    makeOval(235,229,41,41); /* Initial bleach region */
    run("Measure");
    origInt = getResult("Mean",0);
    run("Clear Results");
    if (minArr < origInt) {
        col = minIndex%movePos.length;
        row = (minIndex-col)/movePos.length;

        currPos[0] = currPos[0] + movePos[col];
        currPos[1] = currPos[1] + movePos[row];
    }
    else {
        origBetter = 1;
    }
}

}

/* Measure intensities inside and outside of bleach region */
makeOval(currPos[0],currPos[1],currPos[2],currPos[3]); /* Bleach region */
run("Measure");
makeRectangle(rect1[0],rect1[1],rect1[2],rect1[3]); /* Area 1 far from bleach region */
run("Measure");
makeRectangle(rect2[0],rect2[1],rect2[2],rect2[3]); /* Area 2 far from bleach region */
run("Measure");
M1 = getResult("Mean",0);
if (origBetter==1) {

```

```

        makeOval(235,229,41,41); /* Original bleach region */
        run("Measure");
        M1 = getResult("Mean",3);
    }
    M2 = (getResult("Mean",1) + getResult("Mean",2))/2;

    /* Calculate ratio of intensity inside to outside bleach region */
    relInt = M1/M2;

    /* Determine mean relInt pre-bleach */
    if (i<6) {
        if (i==1) {
            total = 0;
        }

        total = total + relInt;

        if (i==5) {
            max = total/5;
        }
    }

    /* Determine relInt immediately after bleach */
    else if (i==6) {
        min = relInt;
    }

    /* Calculate relInt over time, noramlized between 0 and 1 */
    else {
        num = relInt - min;
        den = max - min;
        frac = num/den;
        write(frac);
    }

    /* Advance to next image */
    for (j=0; j<currInt.length; j++) {
        prevInt[j] = currInt[j];
    }
    for (j=0; j<currPos.length; j++) {
        prevPos[j] = currPos[j];
    }
    run("Clear Results");
    run("Next Slice [>]");
}

```

### A.5.3 FRAP Curve Fitting Code

```
function [D_eff,k_on,k_off,F_inf,D_f,I_fit] = FRAP_fit_77k

close all
clear
clc

load('FRAP_Data_77k.mat') %Change to have correct filename

points = size(FRAP_Curves_77k, 2) - 1;

%Initialize Vectors
F_inf = zeros(1,points);
D_eff = zeros(1,points);
k_on = zeros(1,points);
k_off = zeros(1,points);
D_f = zeros(1,points);

%Define constants
w = 7.45E-6; %m
fname = 'C:\Users\User1\Documents\Research\FRAP Data\Final Fits\77k';

%Set range of k values to test
k_on_test = logspace(-4,4,30);
k_off_test = logspace(-4,4,30);

%Parse data
time = FRAP_Curves_77k(:,1);
time_no0 = FRAP_Curves_77k(2:end,1);
time3 = [FRAP_Curves_77k(2:10,1); FRAP_Curves_77k(11:3:end,1)];
I_fit = zeros(points,length(time));

%Define simplified function to be fit for determination of initial values
%for D and F_inf
curveFitIn = @(D,t) D(1).*exp(-w.^2./(2.*t.*D(2))).*...
    (besseli(0,w.^2./(2.*t.*D(2))) + besseli(1,w.^2./(2.*t.*D(2))));

options = optimset('Display','off','TolFun',1e-20,'TolX',1e-20,...
    'FunValCheck','on');

%Fit each curve to function
for i = 1:points

    maxFrac = max(FRAP_Curves_77k(:,i+1));
    F_inf0 = maxFrac;

    D0 = 1E-12;

    fit3 = [FRAP_Curves_77k(2:10,i+1); FRAP_Curves_77k(11:3:end,i+1)];

    %Implement error-handling strategy to obtain initial values for D and
    %F_inf, using the largest D value that does not result in an error
    try
        D_out = nlinfit(time3,fit3,curveFitIn,[F_inf0,D0],options);
    catch
```

```

try
    D_out = nlinfit(time3,fit3,curveFitIn,[F_inf0,1E-13],options);
catch
    try
        D_out = nlinfit(time3,fit3,curveFitIn,[F_inf0,1E-14],...
            options);
    catch
        try
            D_out = nlinfit(time3,fit3,curveFitIn,...
                [F_inf0,1E-15],options);
        catch
            D_out = [F_inf0,1E-16];
        end
    end
end
end
end

%Determine good initial values for k_on and k_off
resid = zeros(length(k_on_test),length(k_off_test));
D_fit = zeros(length(k_on_test)*length(k_off_test),2);
n = 1;

for j = 1:length(k_on_test)
    for k = 1:length(k_off_test)

        k_fixed = [k_on_test(j),k_off_test(k)];

        try
            [beta_out,R] = nlinfit(time3,fit3,...
                @(params,t) curveFit2(params,t,k_fixed),...
                D_out',options);

            D_fit(n,:) = beta_out';

            resid_test = sum(R.^2);

            if isnan(resid_test) == 1
                resid(k,j) = 1E6; %Ignore k_on, k_off values that yield
                    %imaginary values for part of curve
            else
                resid(k,j) = resid_test;
            end

        catch
            resid(k,j) = 1E6; %Ignore k_on, k_off values that give
                %errors
        end

        n = n + 1; %Keep track of which k_on-k_off combination is used
    end
end

%Select k_on, k_off pair that gave the lowest residuals
[min_col,row] = min(resid);
[~,col] = min(min_col);

row = row(col);

```

```

min_pos = row + (length(k_off_test)*(col - 1));

F_inf0 = D_fit(min_pos,1);
D0 = D_fit(min_pos,2);
k_on0 = k_on_test(col);
k_off0 = k_off_test(row);

beta0 = [F_inf0,D0,k_on0,k_off0];

%Attempt to optimize parameter values around this course-grain minimum
try
    beta_out = nlinfit(time3,fit3,@curveFit,beta0,options);
catch
    beta_out = beta0;
end

sprintf('Fit %d of %d completed.',i,points)

%Store optimized parameter values
F_inf(i) = beta_out(1);
D_f(i) = beta_out(2);
k_on(i) = beta_out(3);
k_off(i) = beta_out(4);

%Caluclate D_eff
D_eff(i) = D_f(i)./(1 + (k_on(i)./k_off(i)));

I_fit(i,2:end) = curveFit(beta_out,time_no0);

figure
hold on
plot(time,FRAP_Curves_77k(:,i+1),'ro')
plot(time,I_fit(i,:),'k--')
title(num2str(i))
xlabel('Time (s)')
ylabel('f(t)')
hold off

saveas(gca,fullfile(fname,num2str(i)),'png');
close all

end

end

%Full function to be fit
function f_t = curveFit(params,t)

w = 7.45E-6; %m^-6

F_inf = params(1);
D = params(2);
k_on = params(3);
k_off = params(4);

F_eq = k_off./(k_on + k_off);
C_eq = k_on./(k_on + k_off);

```

```

frap = @(s) F_inf.*((1./s) - ((F_eq./s).*(1 - 2.*...
    besselk(1,sqrt((s./D).*(1 + (k_on./(s + k_off))))).*w).*...
    besseli(1,sqrt((s./D).*(1 + (k_on./(s + k_off))))).*w)).*...
    (1 + (k_on./(s + k_off)))) - (C_eq./(s + k_off)));

f_t = talbot_inversion(frap, t');

end

%Full function to be fit, given fixed values for k_on and k_off
function f_t = curveFit2(params,t,k_fixed)

w = 7.45E-6; %m^-6

F_inf = params(1);
D = params(2);
k_on = k_fixed(1);
k_off = k_fixed(2);

F_eq = k_off./(k_on + k_off);
C_eq = k_on./(k_on + k_off);

frap = @(s) F_inf.*((1./s) - ((F_eq./s).*(1 - 2.*...
    besselk(1,sqrt((s./D).*(1 + (k_on./(s + k_off))))).*w).*...
    besseli(1,sqrt((s./D).*(1 + (k_on./(s + k_off))))).*w)).*...
    (1 + (k_on./(s + k_off)))) - (C_eq./(s + k_off)));

f_t = talbot_inversion(frap, t');

end

```

Appendix B. Supporting Information for Chapter 3

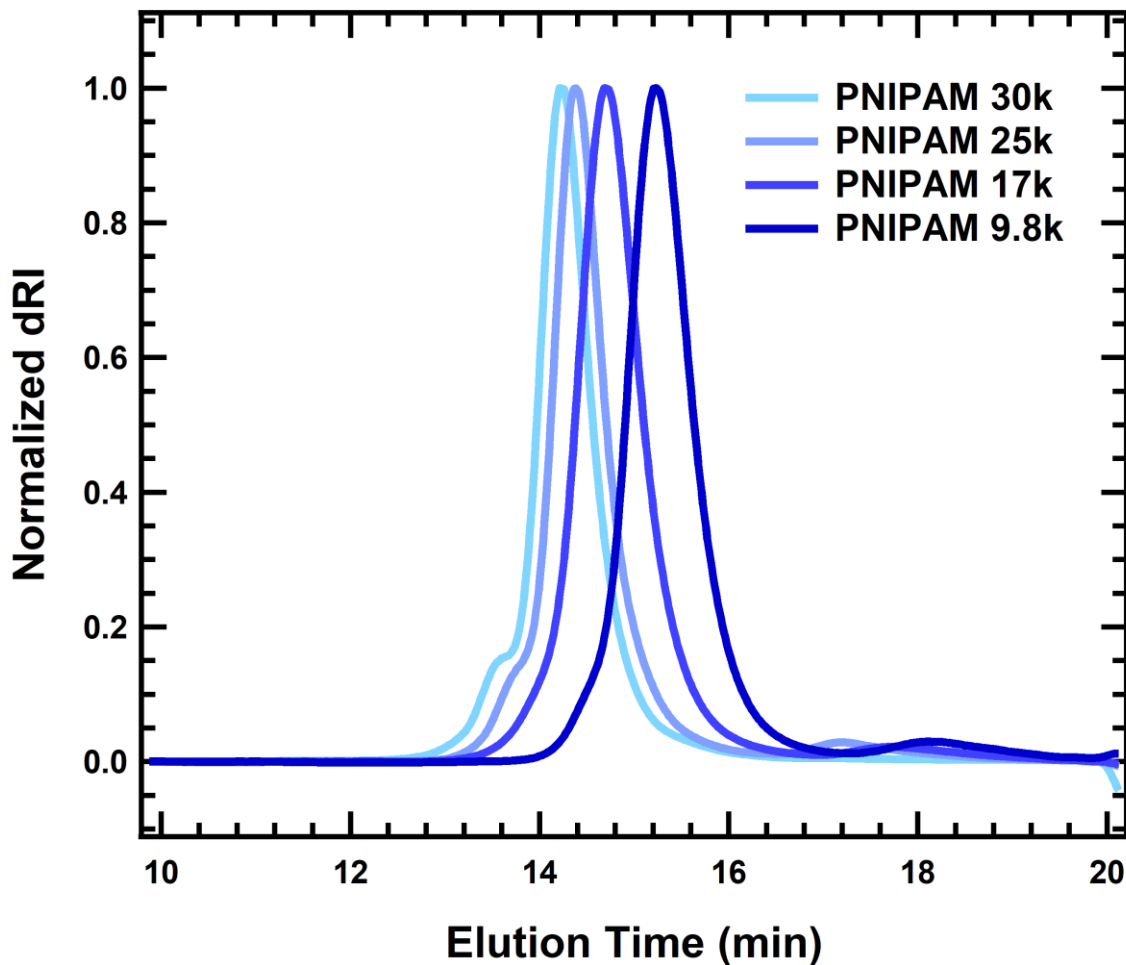


**Figure B-1.** Normalized differential refractive index signals from gel permeation chromatography of PNIPAM samples. The small shoulder at earlier elution times corresponding to twice the peak molecular weight in some samples results from slight reactivity of the double bond in the furan-protected maleimide of the CTA, as reported previously.<sup>1</sup>

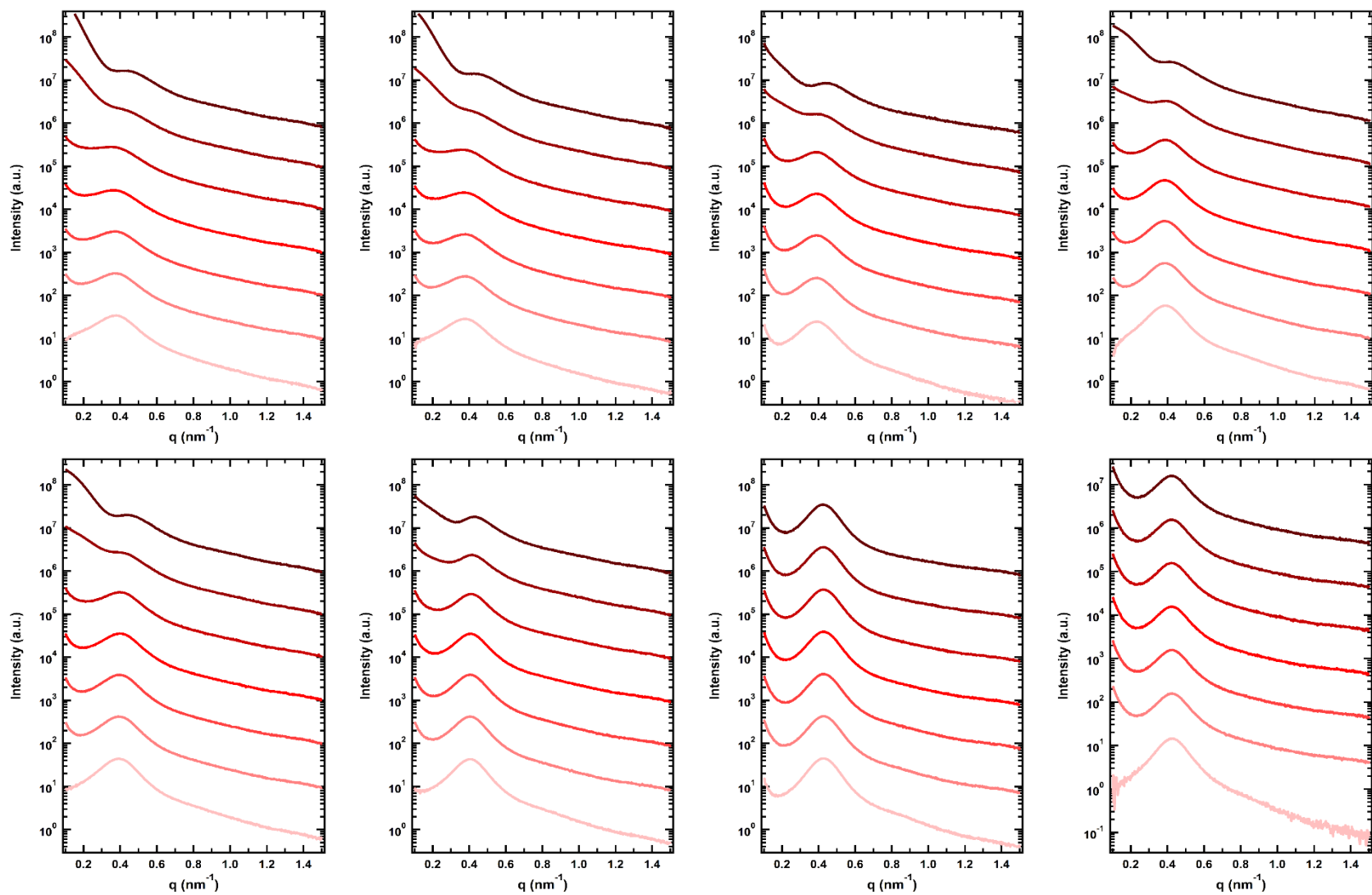


**Figure B-2.** Radially averaged SAXS patterns for 1xSP9.8k. Top row (left to right): 30 wt.%, 35 wt.%, 40 wt.%, 45 wt.%. Bottom row (left to right): 50 wt.%, 60 wt.%, 70 wt.%, 100 wt.%. Curves are offset vertically for clarity. The seven curves in each plot correspond to temperatures of 10 °C to 40 °C in 5 °C intervals, from bottom to top.

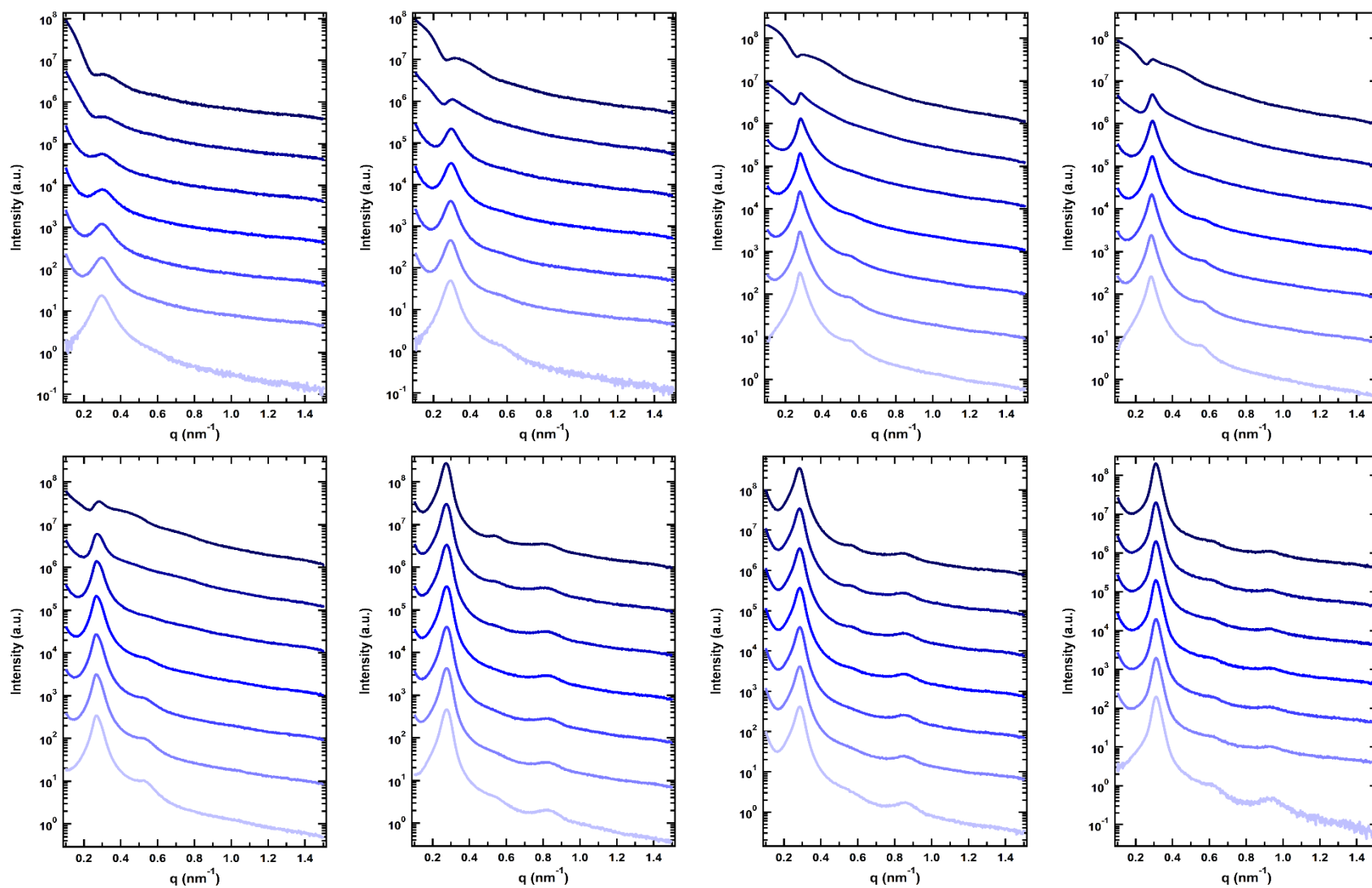


**Figure B-3.** Radially averaged SAXS patterns for 2xSP17k. Top row (left to right): 30 wt.%, 35 wt.%, 40 wt.%, 45 wt.%. Bottom row (left to right): 50 wt.%, 60 wt.%, 70 wt.%, 100 wt.%. Curves are offset vertically for clarity. The seven curves in each plot correspond to temperatures of 10 °C to 40 °C in 5 °C intervals, from bottom to top.

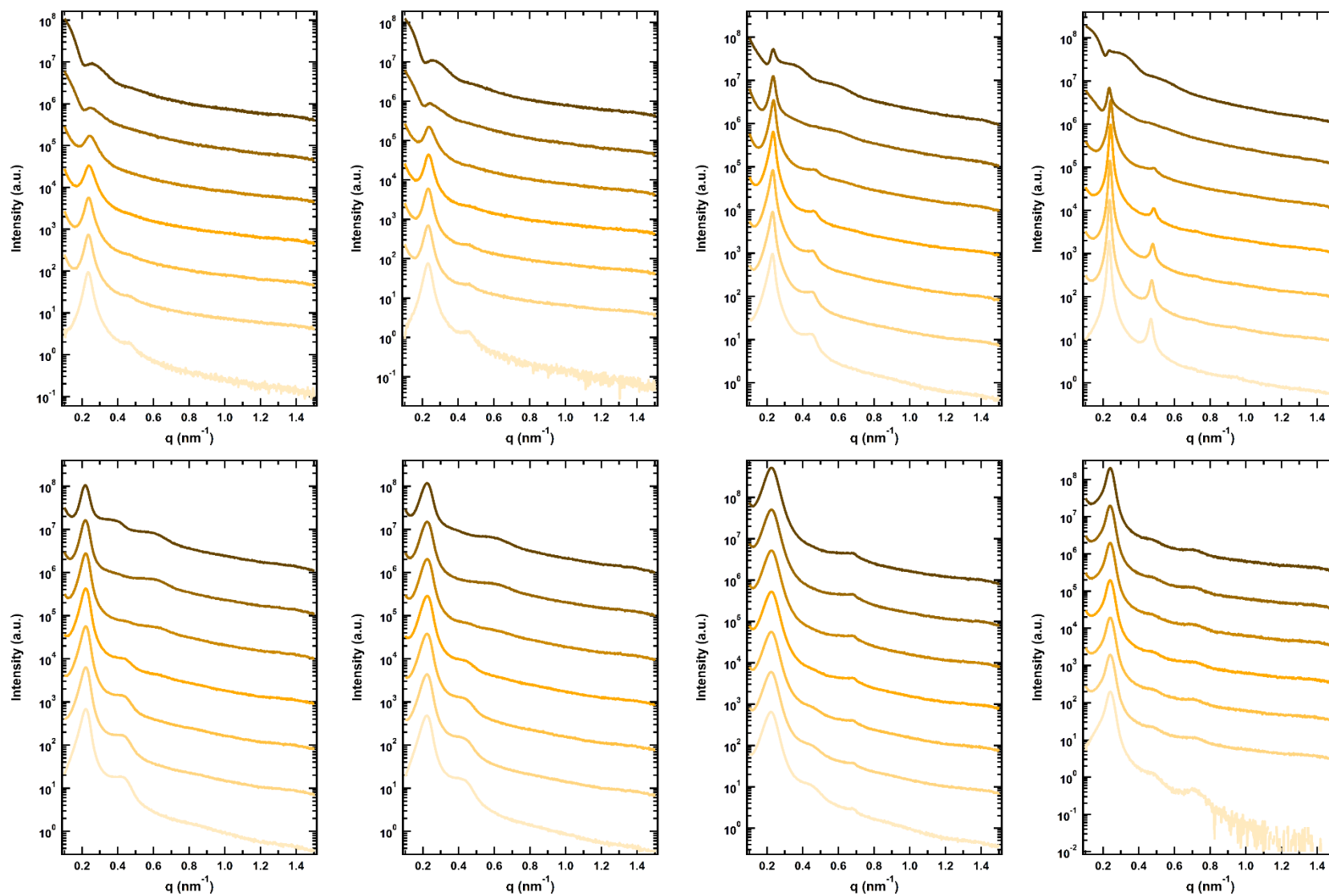


**Figure B-4.** Radially averaged SAXS patterns for 3xSP25k. Top row (left to right): 30 wt.%, 35 wt.%, 40 wt.%, 45 wt.%. Bottom row (left to right): 50 wt.%, 60 wt.%, 70 wt.%, 100 wt.%. Curves are offset vertically for clarity. The seven curves in each plot correspond to temperatures of 10 °C to 40 °C in 5 °C intervals, from bottom to top.

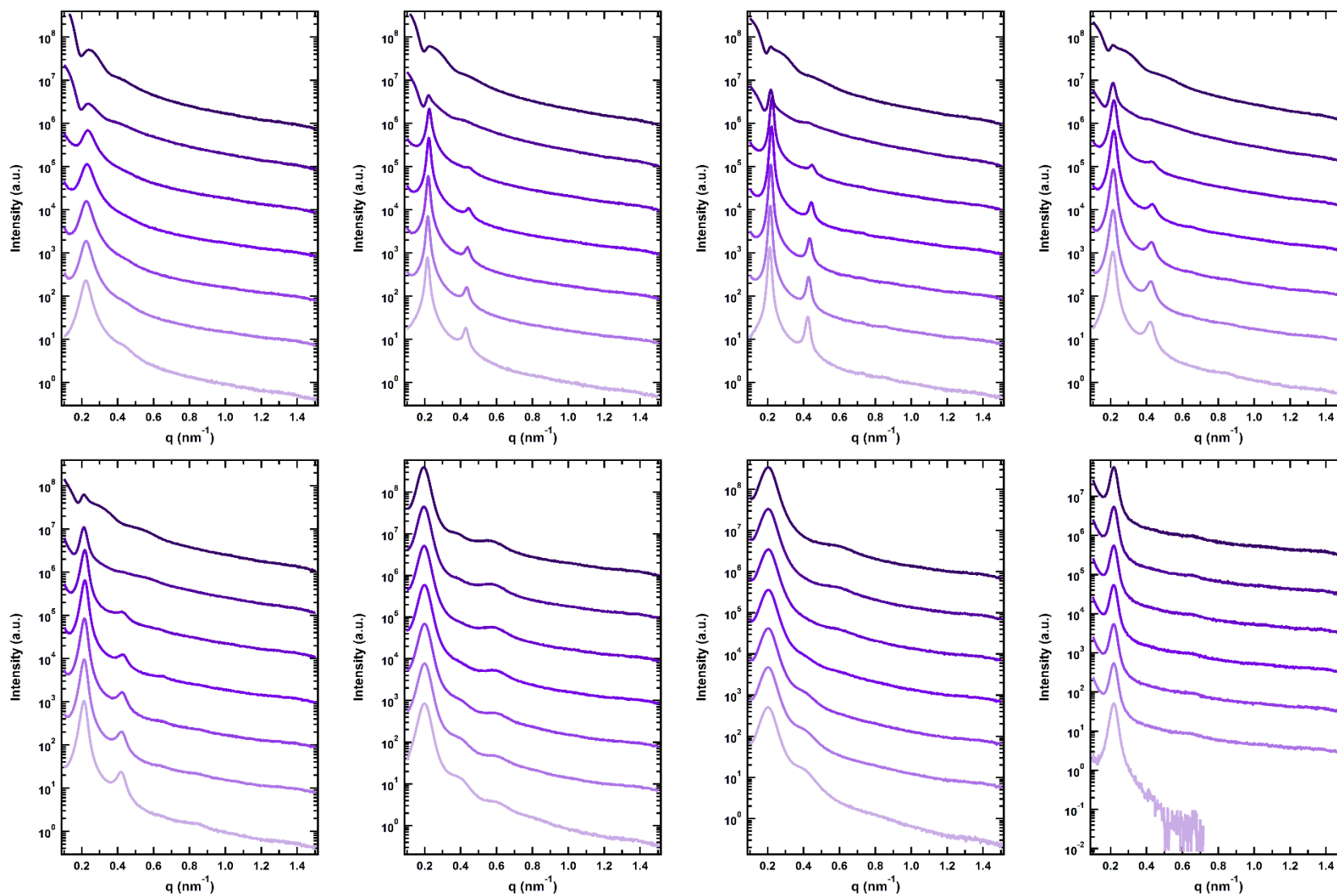


**Figure B-5.** Radially averaged SAXS patterns for 4xSP30k. Top row (left to right): 30 wt.%, 35 wt.%, 40 wt.%, 45 wt.%. Bottom row (left to right): 50 wt.%, 60 wt.%, 70 wt.%, 100 wt.%. Curves are offset vertically for clarity. The seven curves in each plot correspond to temperatures of 10 °C to 40 °C in 5 °C intervals, from bottom to top.

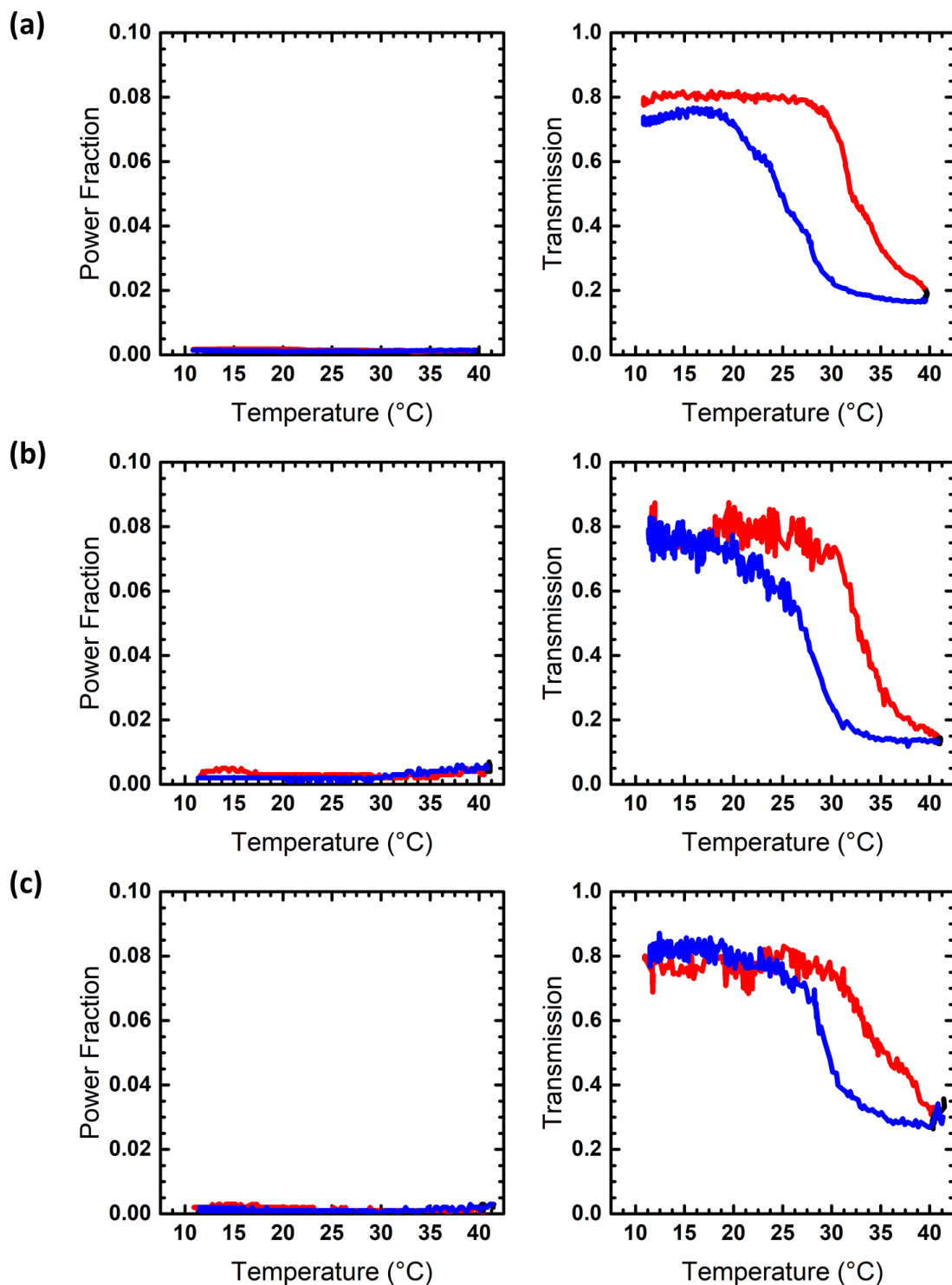


**Figure B-6 a-c.** DPLS and turbidimetry heating/cooling cycles for 1xSP9.8k at (a) 30 wt.%, (b) 35 wt.%, and (c) 40 wt.%. The red curve represents the heating cycle, and the blue curve represents the cooling cycle. The black curve represents the 10-minute equilibration at the end of the heating cycle before cooling.

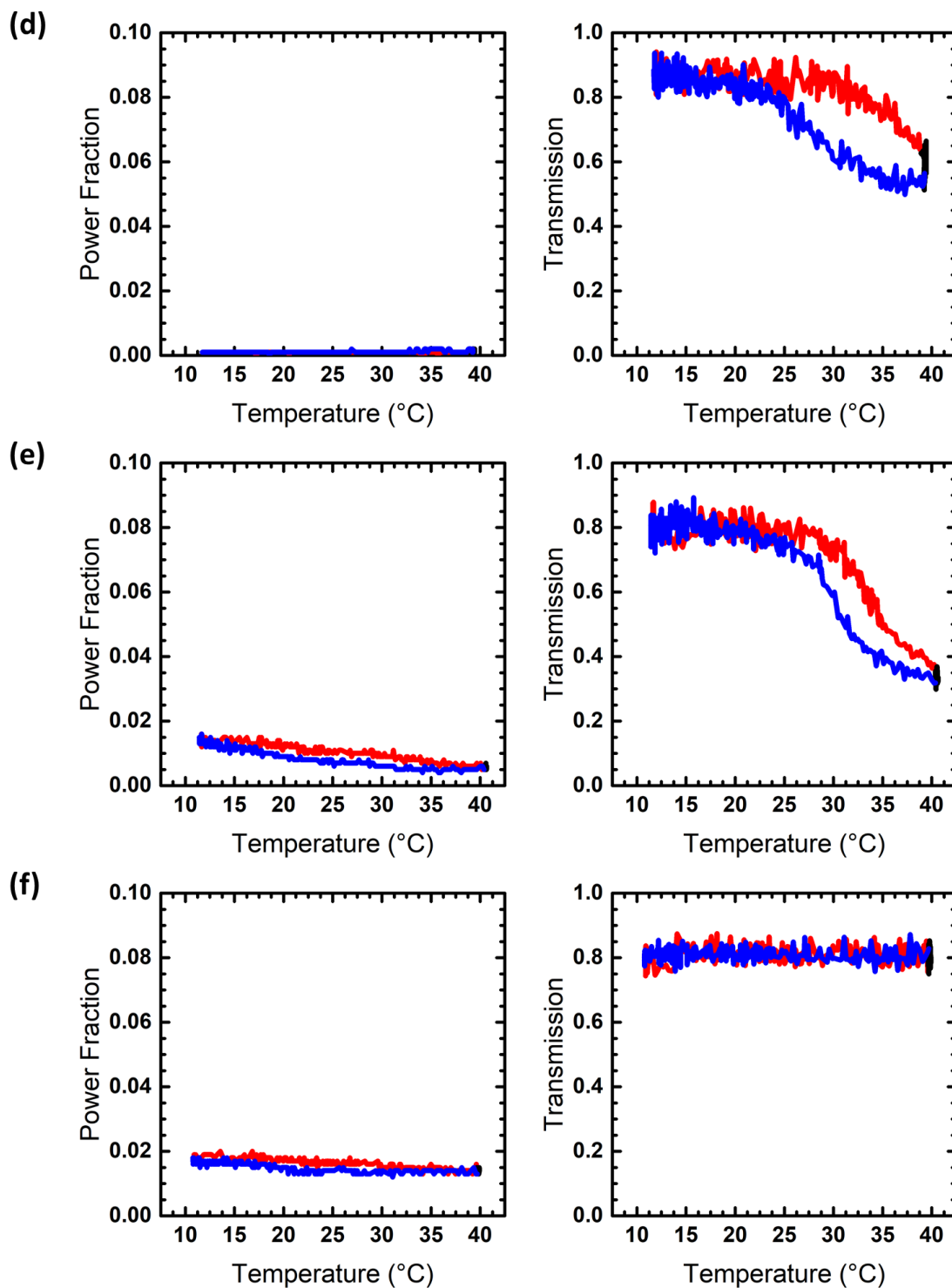


**Figure B-6 d-f.** DPLS and turbidimetry heating/cooling cycles for 1xSP9.8k at (d) 45 wt.%, (e) 50 wt.%, and (f) 60 wt.%. The red curve represents the heating cycle, and the blue curve represents the cooling cycle. The black curve represents the 10-minute equilibration at the end of the heating cycle before cooling.

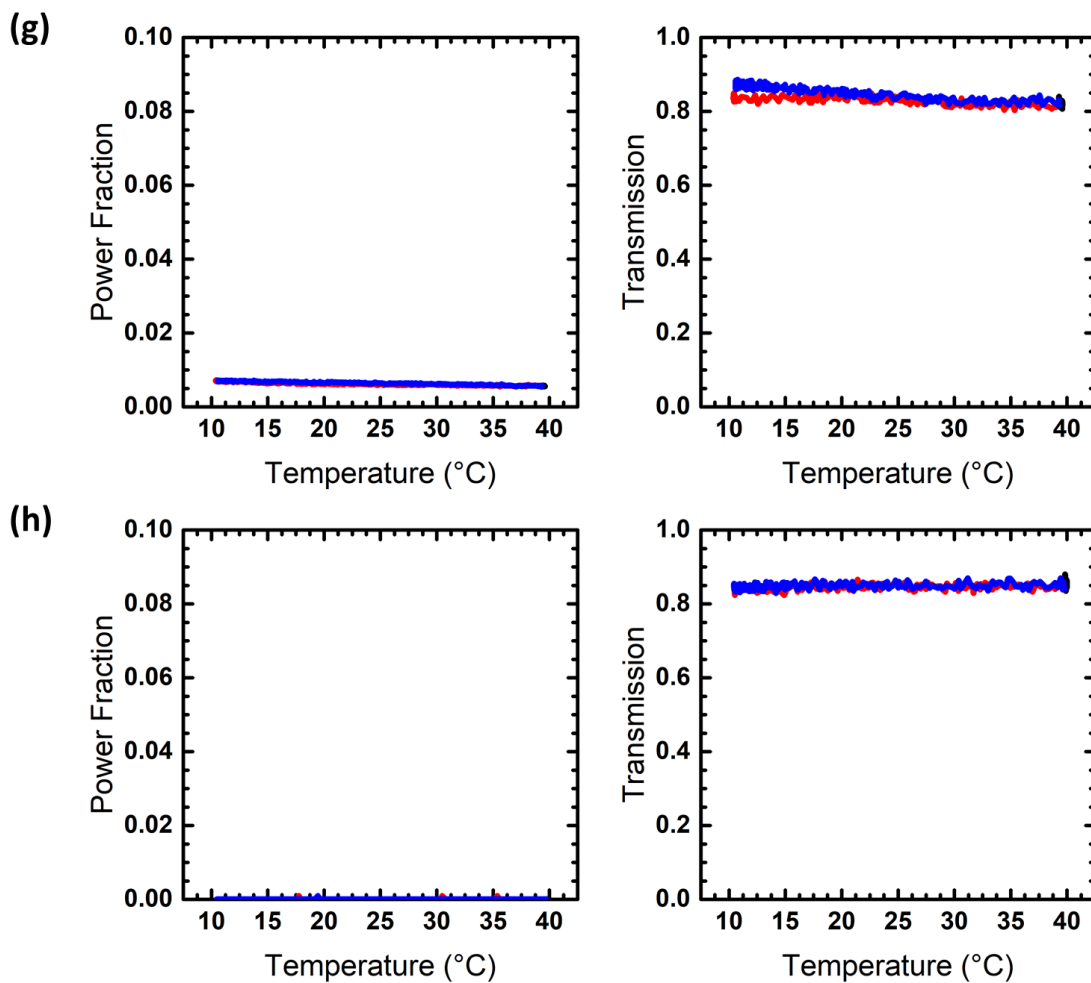


**Figure B-6 g-h.** DPLS and turbidimetry heating/cooling cycles for 1xSP9.8k at (g) 70 wt.% and (h) 100 wt.%. The red curve represents the heating cycle, and the blue curve represents the cooling cycle. The black curve represents the 10-minute equilibration at the end of the heating cycle before cooling. For the 100 wt.% sample, power fraction is zero under all measured conditions.

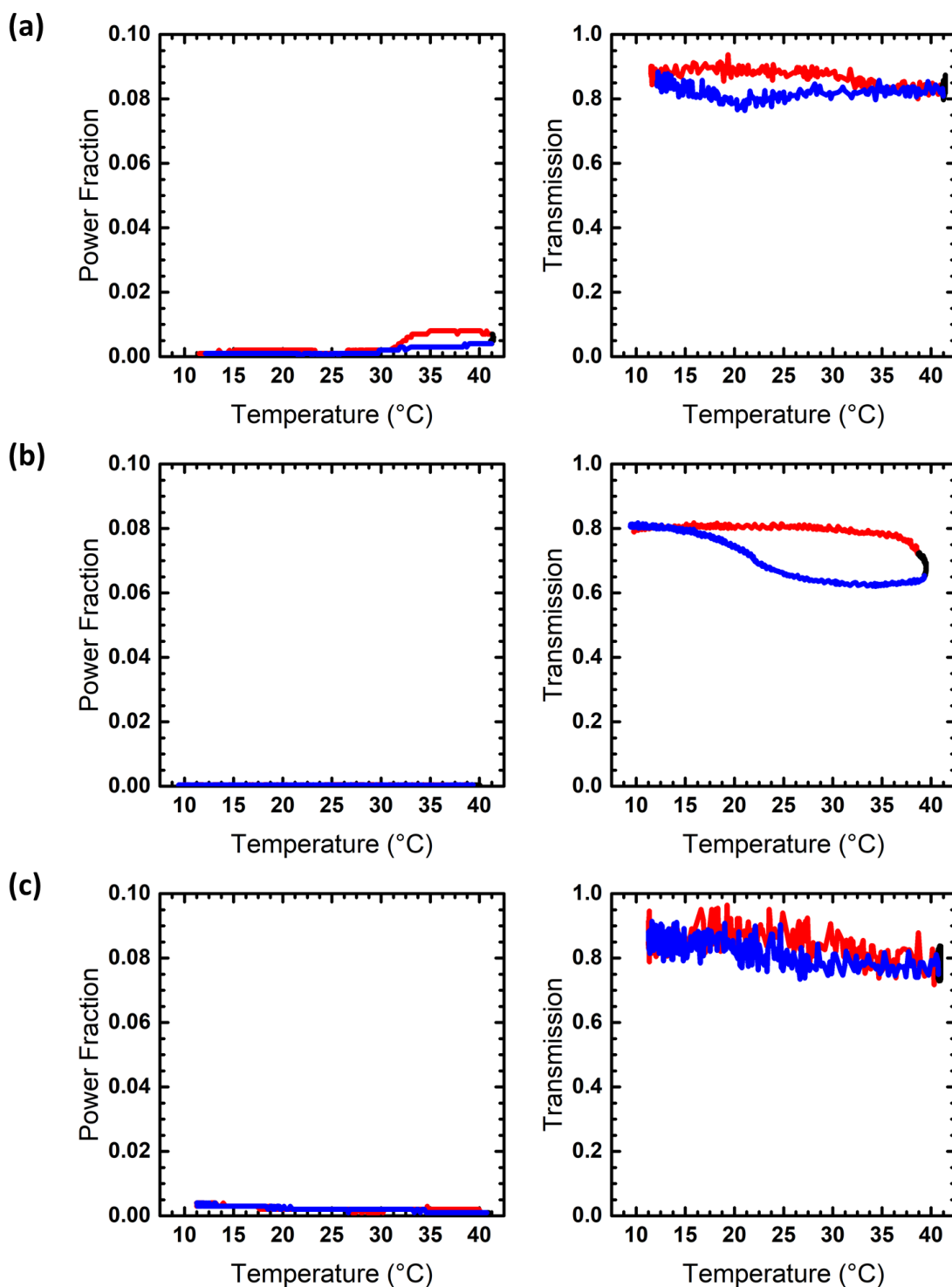


**Figure B-7 a-c.** DPLS and turbidimetry heating/cooling cycles for 2xSP17k at (a) 30 wt.%, (b) 35 wt.%, and (c) 40 wt.%. The red curve represents the heating cycle, and the blue curve represents the cooling cycle. The black curve represents the 10-minute equilibration at the end of the heating cycle before cooling. For the 35 wt.% sample, power fraction is zero under all measured conditions.

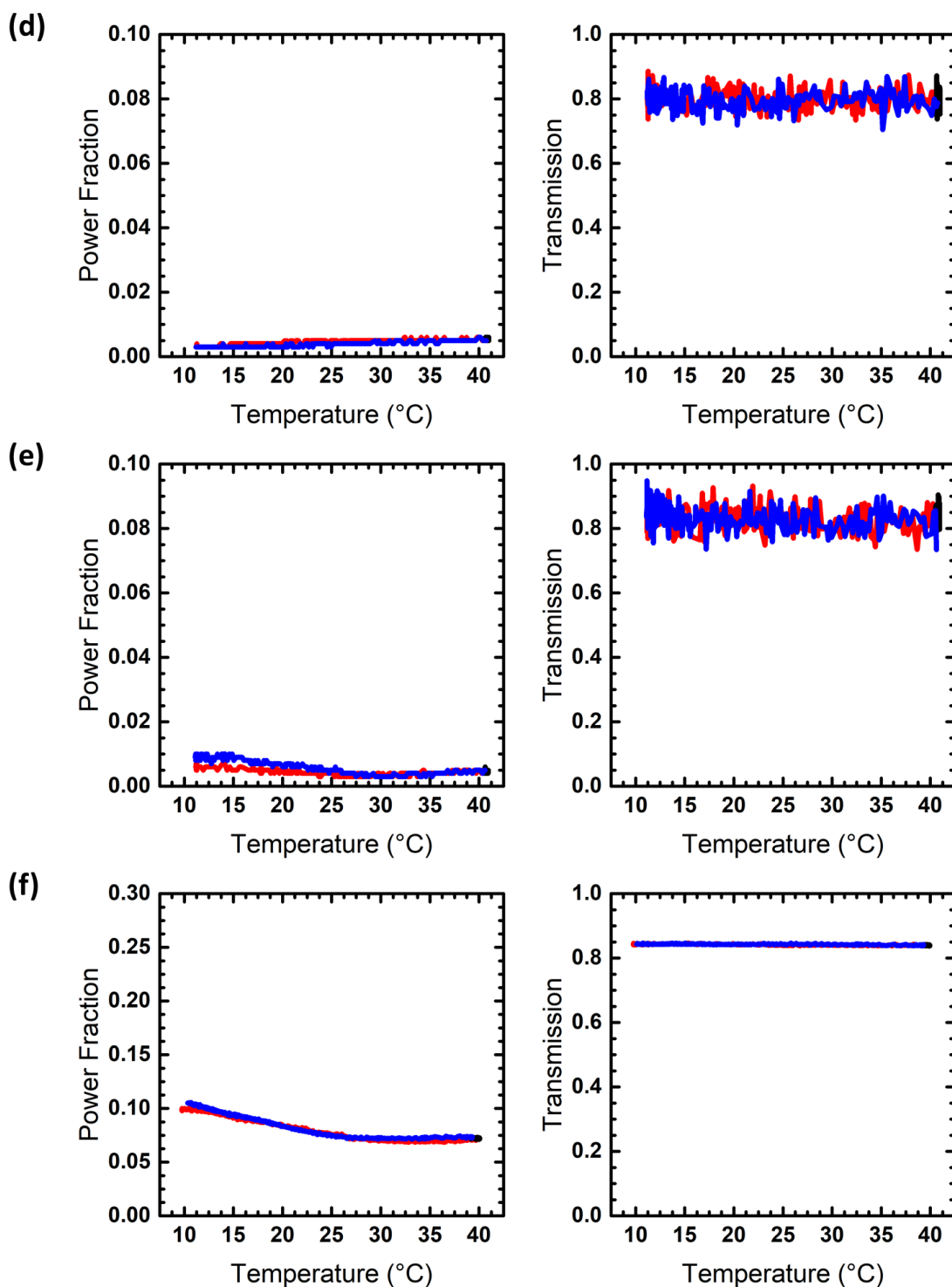


**Figure B-7 d-f.** DPLS and turbidimetry heating/cooling cycles for 2xSP17k at (d) 45 wt.%, (e) 50 wt.%, and (f) 60 wt.%. The red curve represents the heating cycle, and the blue curve represents the cooling cycle. The black curve represents the 10-minute equilibration at the end of the heating cycle before cooling.

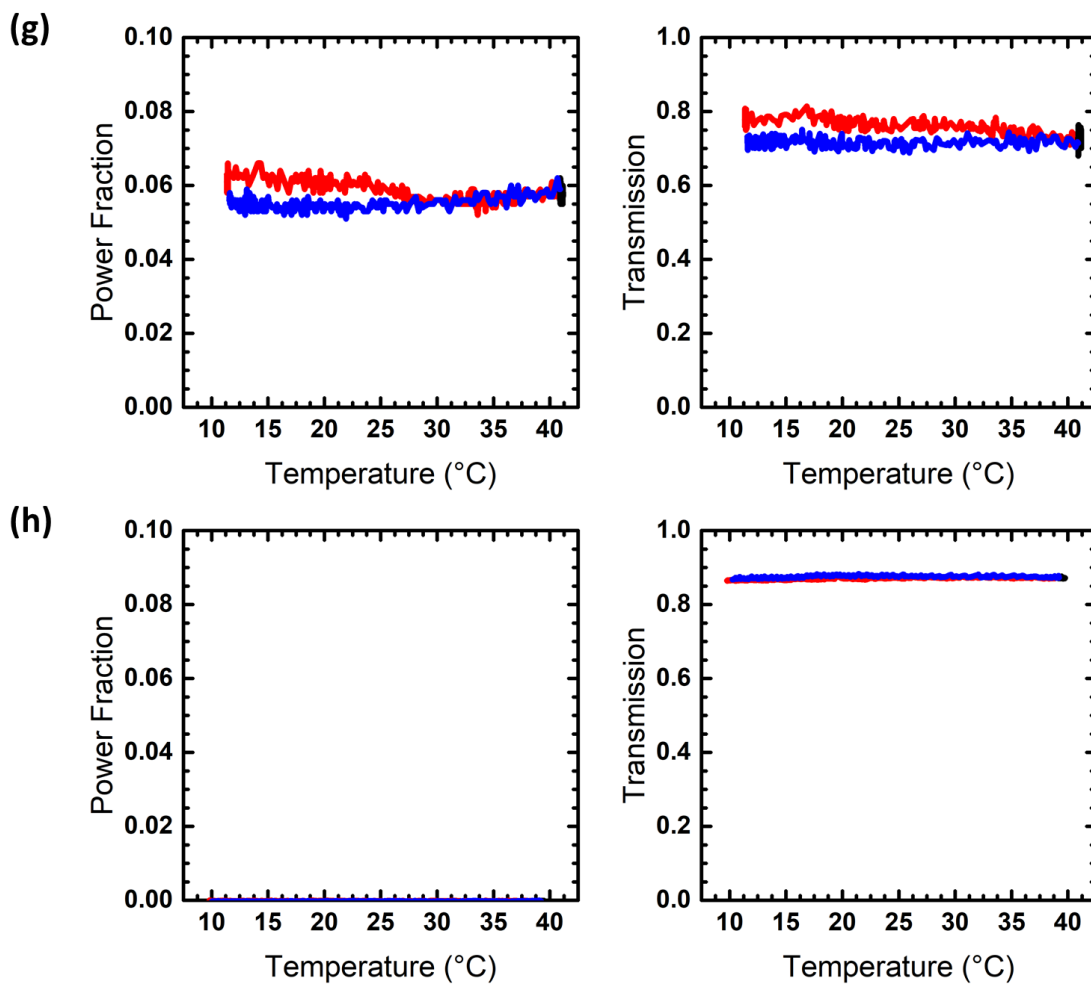


**Figure B-7 g-h.** DPLS and turbidimetry heating/cooling cycles for 2xSP17k at (g) 70 wt.% and (h) 100 wt.%. The red curve represents the heating cycle, and the blue curve represents the cooling cycle. The black curve represents the 10-minute equilibration at the end of the heating cycle before cooling. For the 100 wt.% sample, power fraction is zero under all measured conditions.

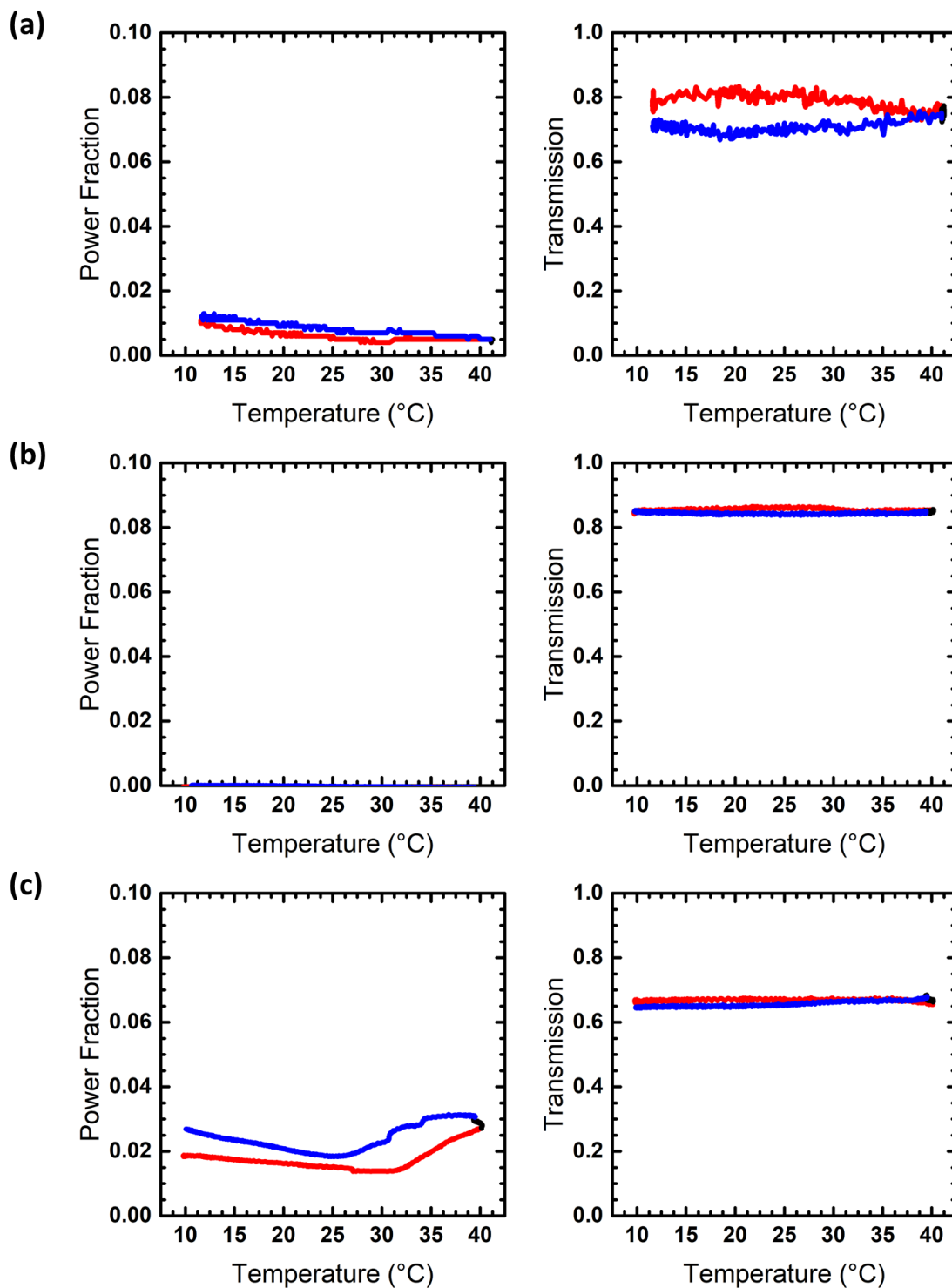


**Figure B-8 a-c.** DPLS and turbidimetry heating/cooling cycles for 3xSP25k at (a) 30 wt.%, (b) 35 wt.%, and (c) 40 wt.%. The red curve represents the heating cycle, and the blue curve represents the cooling cycle. The black curve represents the 10-minute equilibration at the end of the heating cycle before cooling. For the 35 wt.% sample, power fraction is zero under all measured conditions.

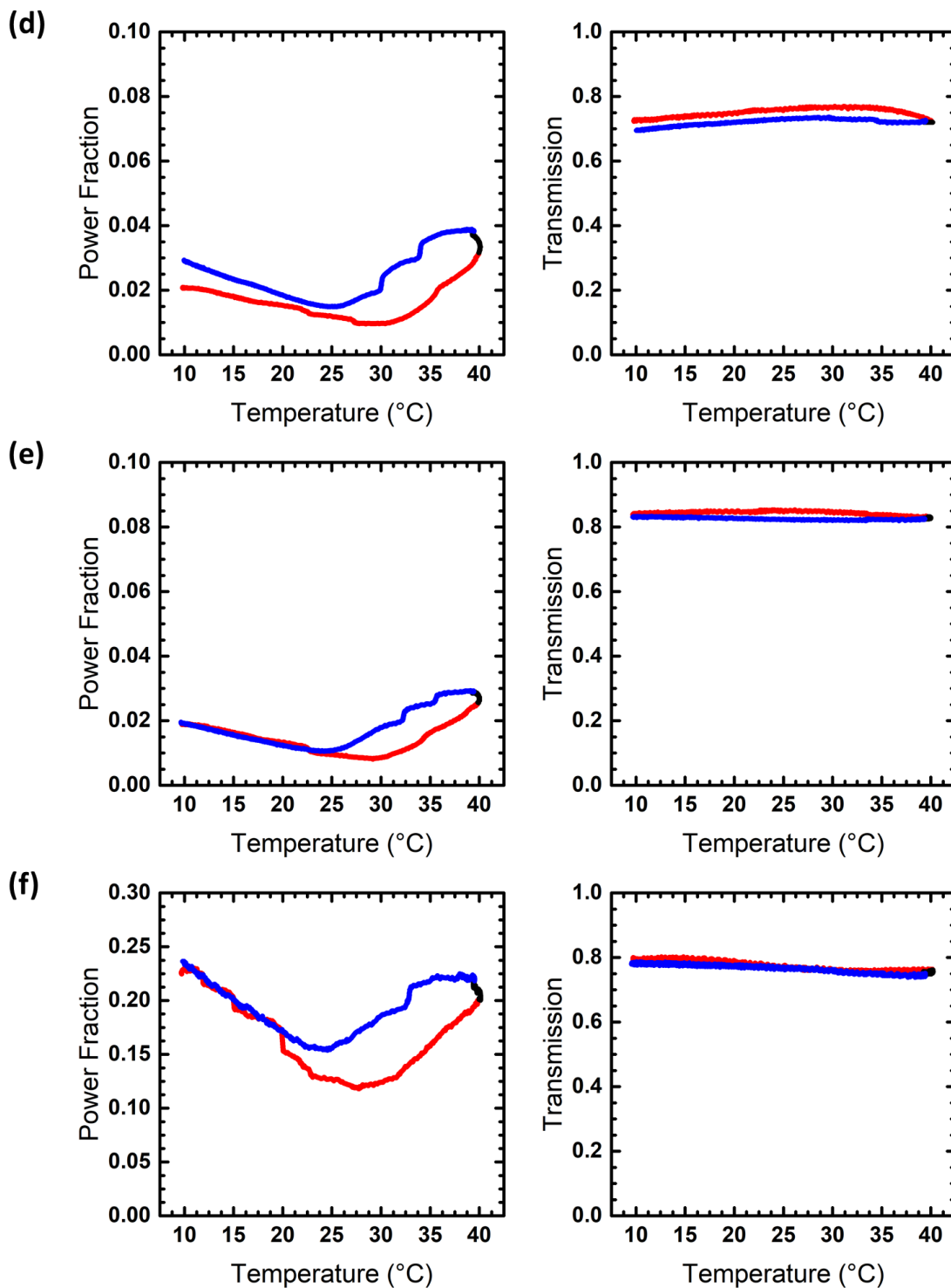


**Figure B-8 d-f.** DPLS and turbidimetry heating/cooling cycles for 3xSP25k at (d) 45 wt.%, (e) 50 wt.%, and (f) 60 wt.%. The red curve represents the heating cycle, and the blue curve represents the cooling cycle. The black curve represents the 10-minute equilibration at the end of the heating cycle before cooling.

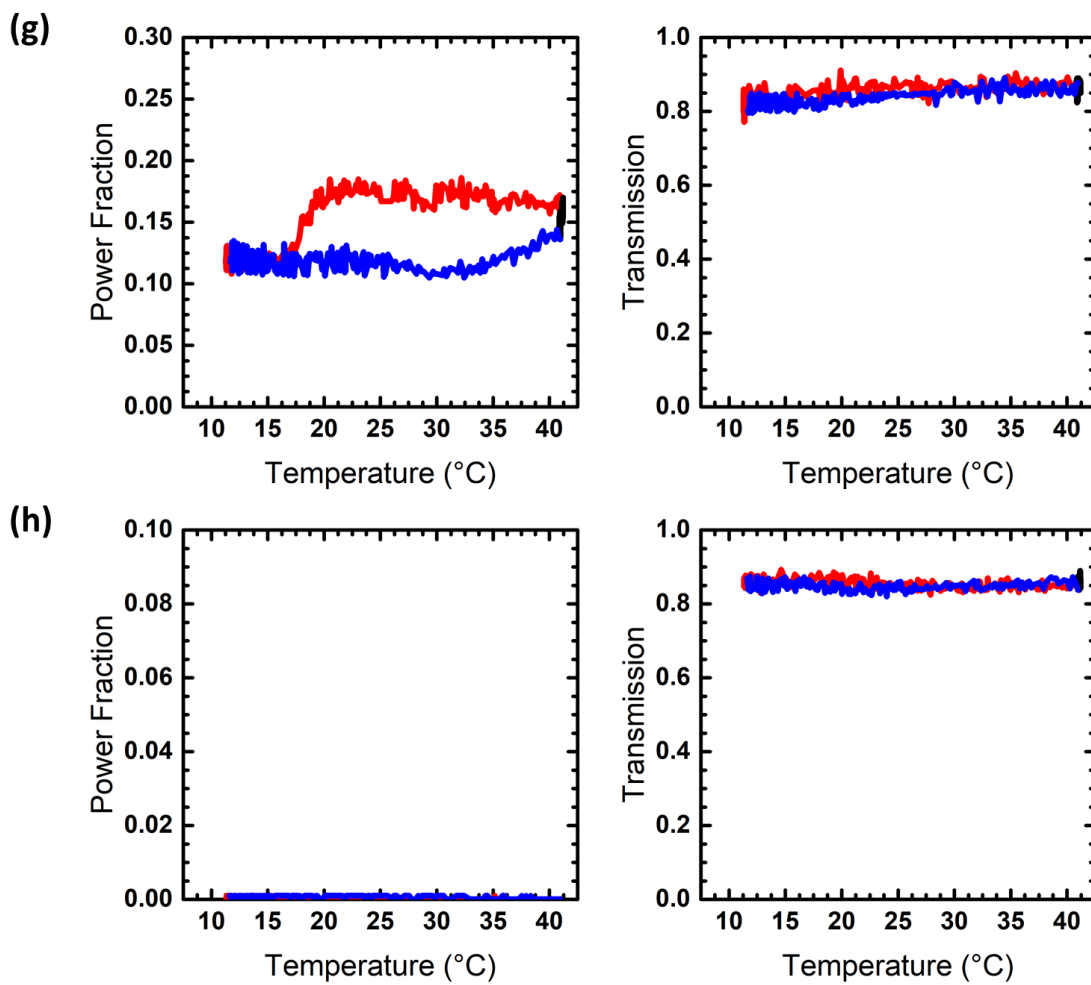


**Figure B-8 g-h.** DPLS and turbidimetry heating/cooling cycles for 3xSP25k at (g) 70 wt.% and (h) 100 wt.%. The red curve represents the heating cycle, and the blue curve represents the cooling cycle. The black curve represents the 10-minute equilibration at the end of the heating cycle before cooling.

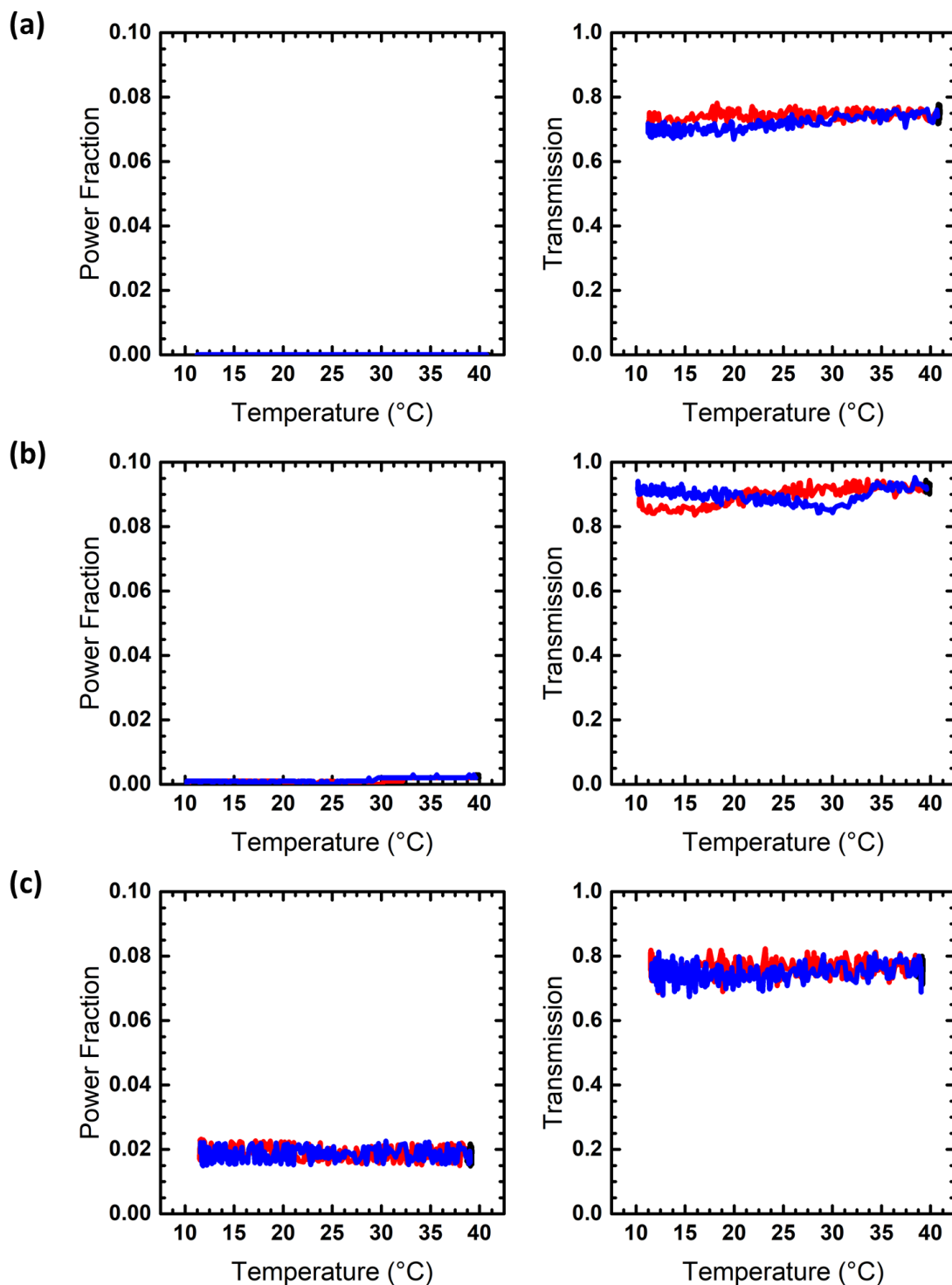


**Figure B-9 a-c.** DPLS and turbidimetry heating/cooling cycles for 4xSP30k at (a) 30 wt.%, (b) 35 wt.%, and (c) 40 wt.%. The red curve represents the heating cycle, and the blue curve represents the cooling cycle. The black curve represents the 10-minute equilibration at the end of the heating cycle before cooling. For the 30 wt.% sample, power fraction is zero under all measured conditions.

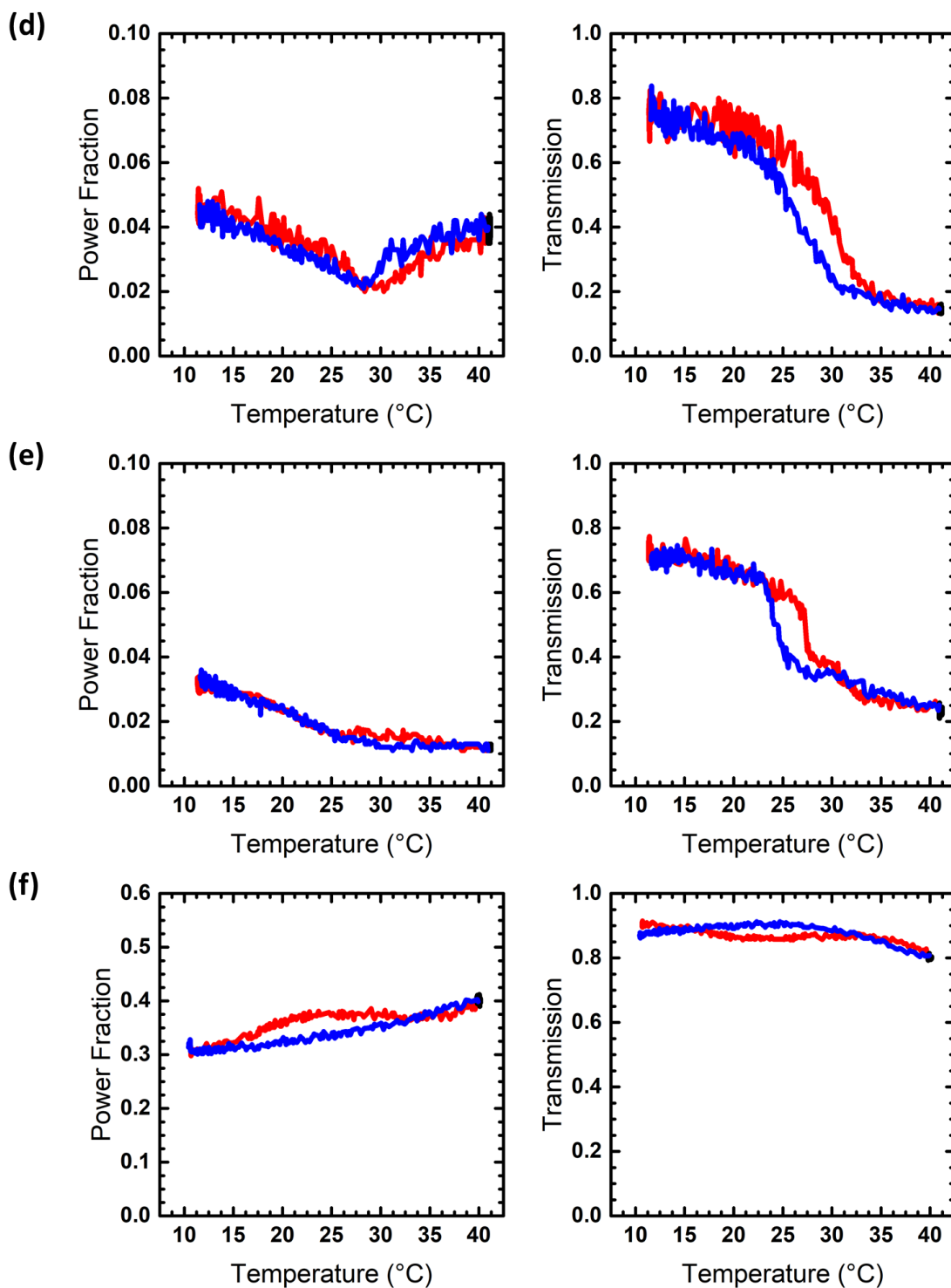


**Figure B-9 d-f.** DPLS and turbidimetry heating/cooling cycles for 4xSP30k at (d) 45 wt.%, (e) 50 wt.%, and (f) 60 wt.%. The red curve represents the heating cycle, and the blue curve represents the cooling cycle. The black curve represents the 10-minute equilibration at the end of the heating cycle before cooling.

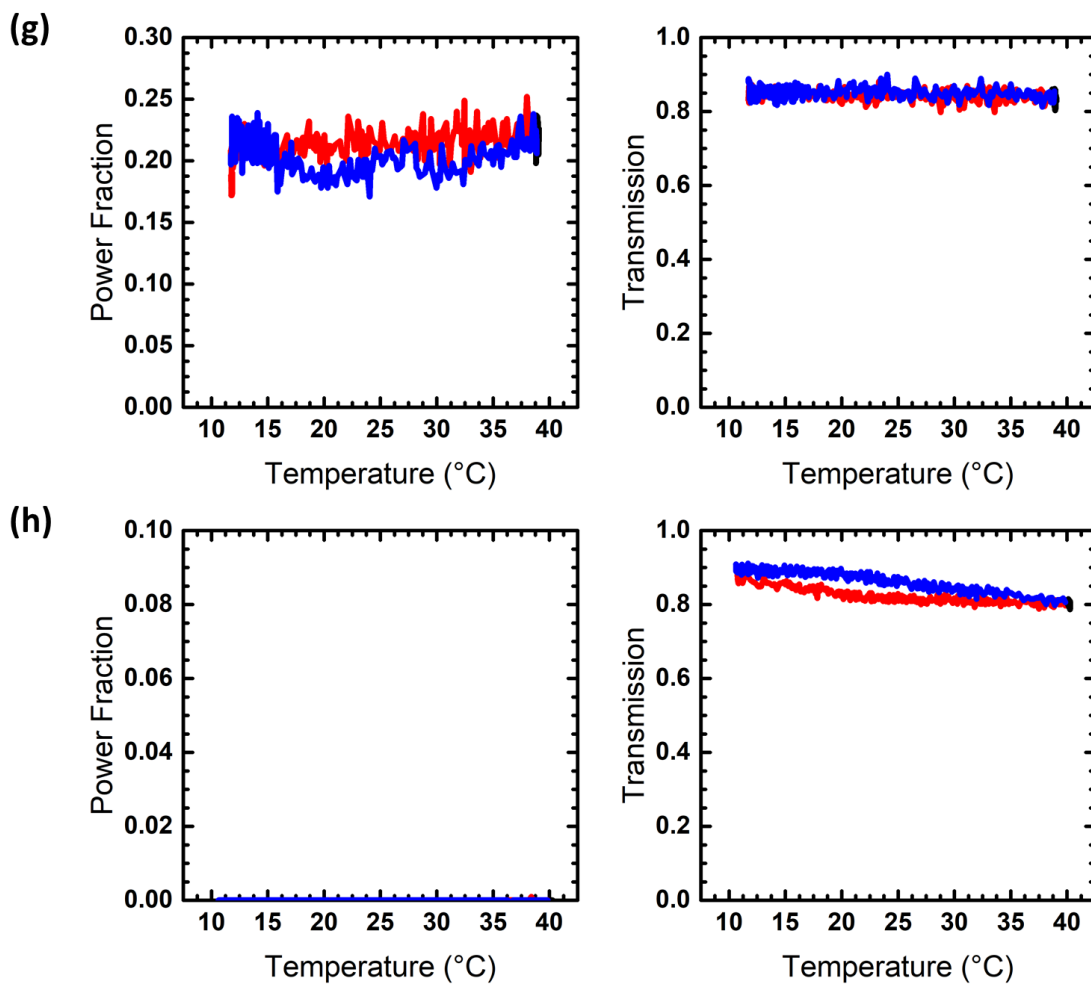


**Figure B-9 g-h.** DPLS and turbidimetry heating/cooling cycles for 4xSP30k at (g) 70 wt.% and (h) 100 wt.%. The red curve represents the heating cycle, and the blue curve represents the cooling cycle. The black curve represents the 10-minute equilibration at the end of the heating cycle before cooling. For the 100 wt.% sample, power fraction is zero under all measured conditions.

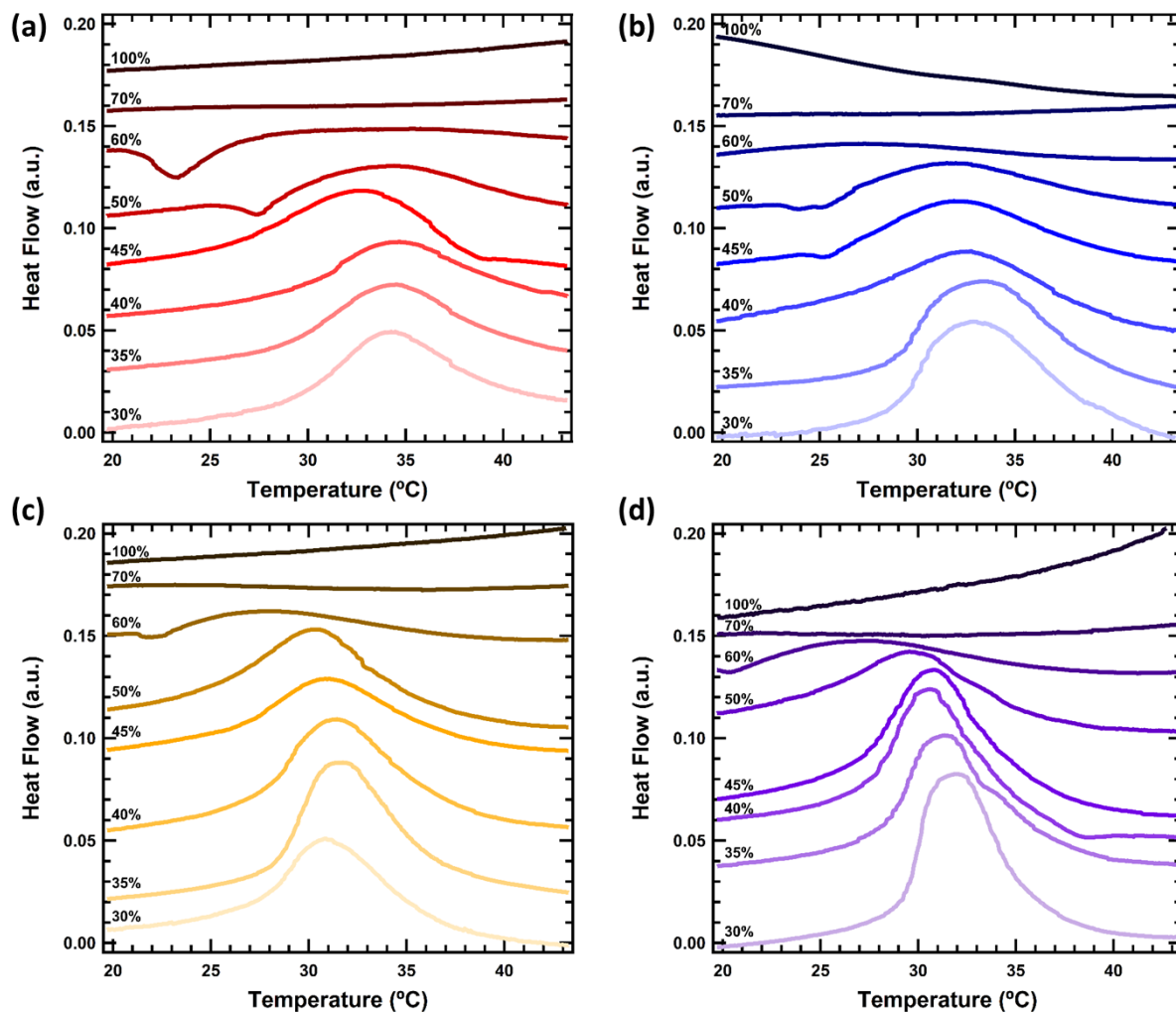


**Figure B-10.** DSC curves of (a) 1xSP9.8k, (b) 2xSP17k, (c) 3xSP25k, and (d) 4xSP30k at varying concentrations. Curves are offset for clarity.

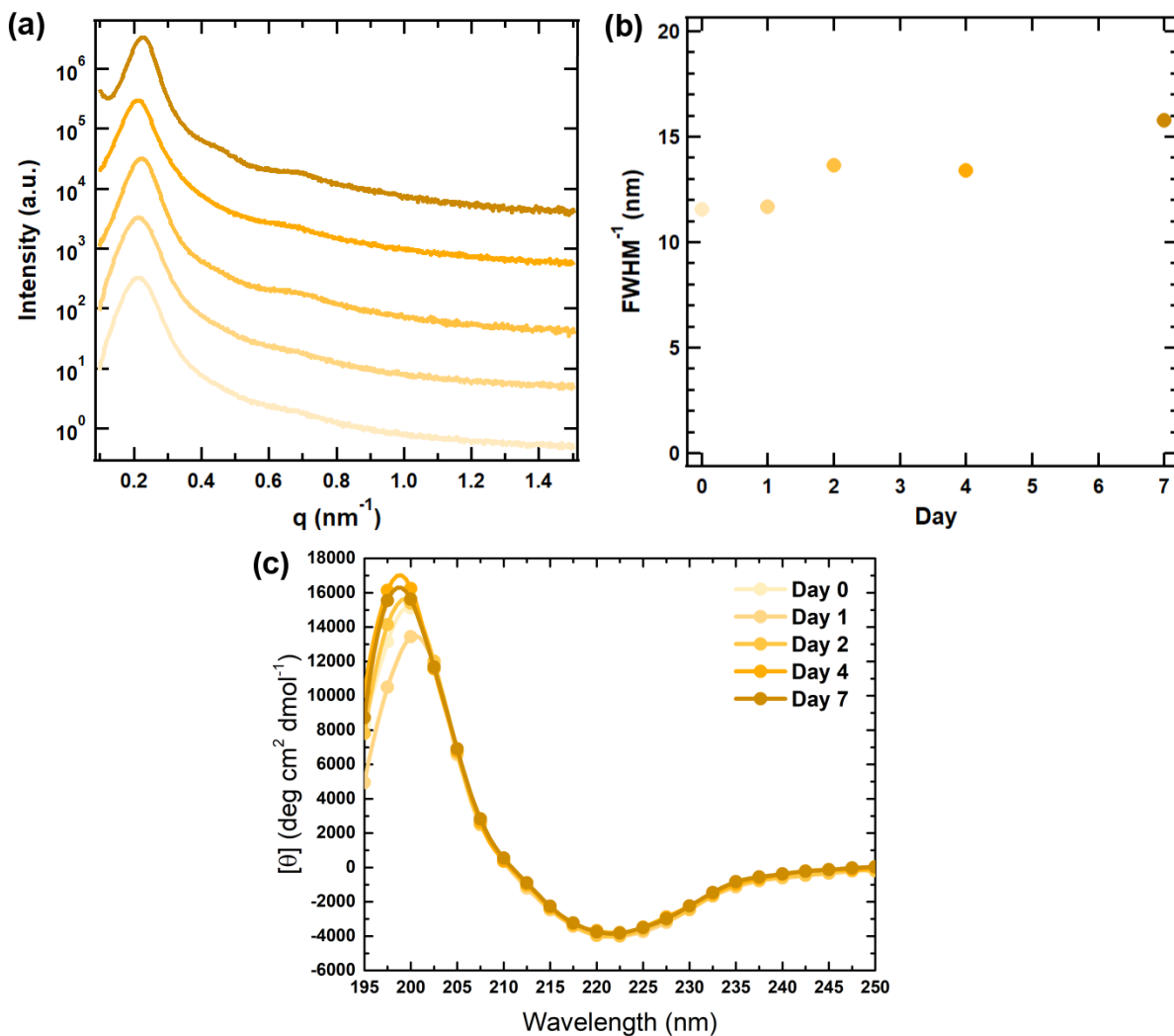


**Figure B-11.** Effect of incubation time on ordering quality in 70 wt.% 3xSP25k samples. (a) SAXS curves for samples incubated at room temperature for 0, 1, 2, 4, or 7 days (bottom to top). (b)  $\text{FWHM}^{-1}$  of the primary scattering peak for samples in (a) indicate a slight improvement in ordering with increasing incubation time. (c) CD spectra of the conjugates reveal that the protein block remains folded during incubation at room temperature. Differences between CD spectra of conjugates in (c) below 205 nm are primarily due to high noise in the CD spectrometer at these wavelengths.

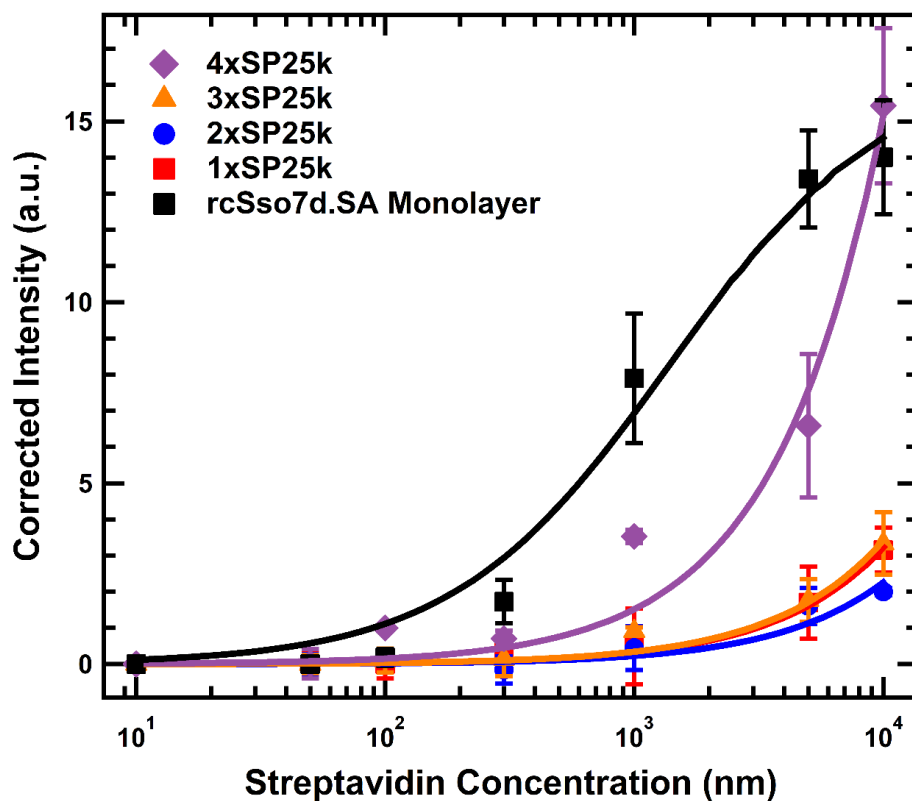


**Figure B-12.** Comparison of binding curves obtained for each considered conjugate and rcSso7d.SA monolayer using streptavidin labeled with Alexa Fluor 647 as the analyte. All curves are shifted to a background signal of 0 for clarity. Thicknesses for the 1xSP9.8k, 2xSP17k, 3xSP25k, and 4xSP30k films are 120, 90, 80, and 135 nm, respectively. Error bars represent the standard deviation of three replicates.

**Table B-1.** Intermediate Values in Calculation of Relative Number of Binding Sites

Thin Film	Weight Fraction <sup>a</sup>	Predicted Ratio <sup>b</sup>	Thickness (nm)	Calculated $[P]_T$ (nM)	Density <sup>c</sup> (mol/cm <sup>2</sup> )	Calculated Ratio <sup>d</sup>
1xSP25k	0.27	1.00	155	3100	4.8	1.00
2xSP25k	0.39	1.43	130	3300	4.3	0.90
3xSP25k	0.47	1.73	150	3900	5.9	1.24
4xSP25k	0.53	1.94	170	3700	6.2	1.31

<sup>a</sup>Calculated as the weight fraction of rcSso7d.SA protein in the conjugate. <sup>b</sup>Ratios of weight fractions relative to the 1xSP25k thin film. <sup>c</sup>Density of binding sites within a cross-sectional area of the film parallel to the surface. <sup>d</sup>Ratios of the product of film thickness and  $[P]_T$  relative to the 1xSP25k thin film.

## References for Appendix B

1. Thomas, C. S.; Glassman, M. J.; Olsen, B. D., Solid-State Nanostructured Materials from Self-Assembly of a Globular Protein–Polymer Diblock Copolymer. *ACS Nano* **2011**, 5 (7), 5697-5707, DOI: 10.1021/nn2013673

## Appendix C. Supporting Information for Chapter 4

**Table C-1.** Activities and thicknesses of 2x and coiled-coil fusion conjugate thin films.

Conjugate	Film Thickness (nm)	Film Activity/Film Thickness (MFI/nm) <sup>a</sup>
2x	151	0.32 ± 0.05
2xZEC	136	6.8 ± 0.3
2xZRC	120	0.8 ± 0.1
2xZEN	111	1.2 ± 0.1
2xZEC-ZRC	204	3.6 ± 0.1
2xZEN-ZRC	172	0.09 ± 0.01

<sup>a</sup>Reported errors represent the standard deviation across three replicates.

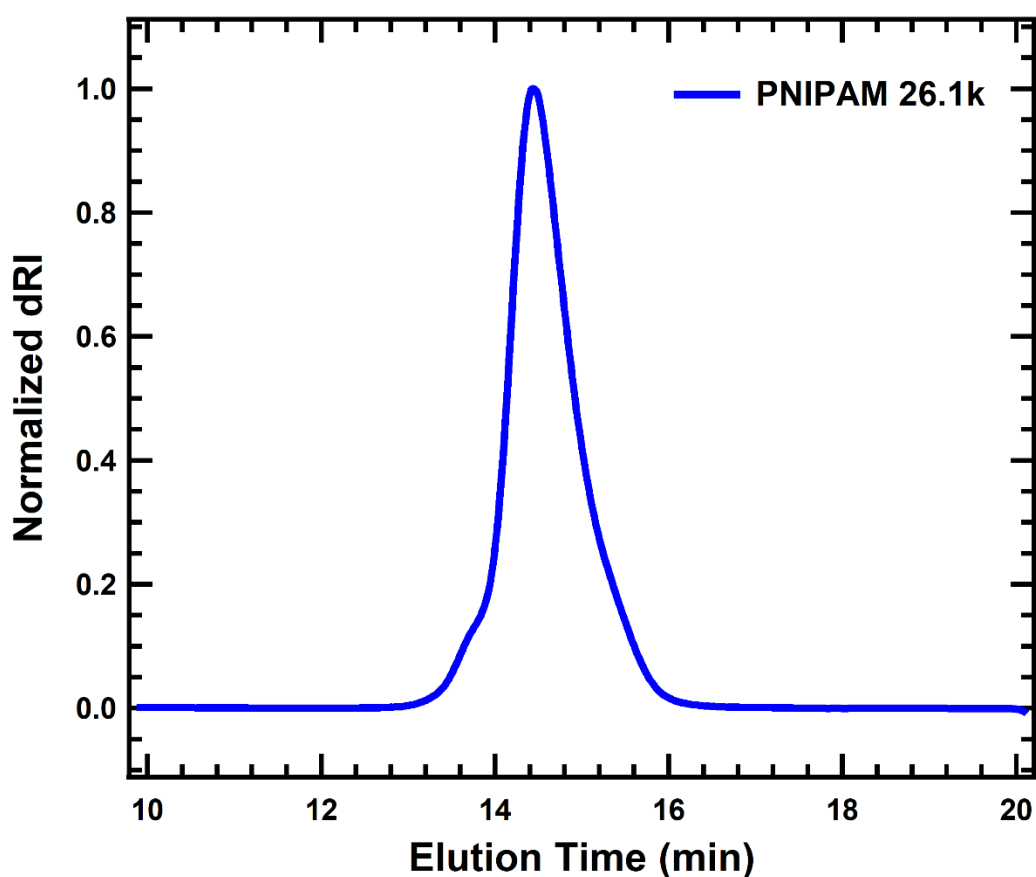


**Figure C-1.** Normalized differential refractive index signal from gel permeation chromatography of the synthesized PNIPAM sample. The small shoulder at an earlier elution time corresponding to twice the peak molecular weight results from slight reactivity of the double bond in the furan-protected maleimide of the CTA, as reported previously.<sup>1</sup>

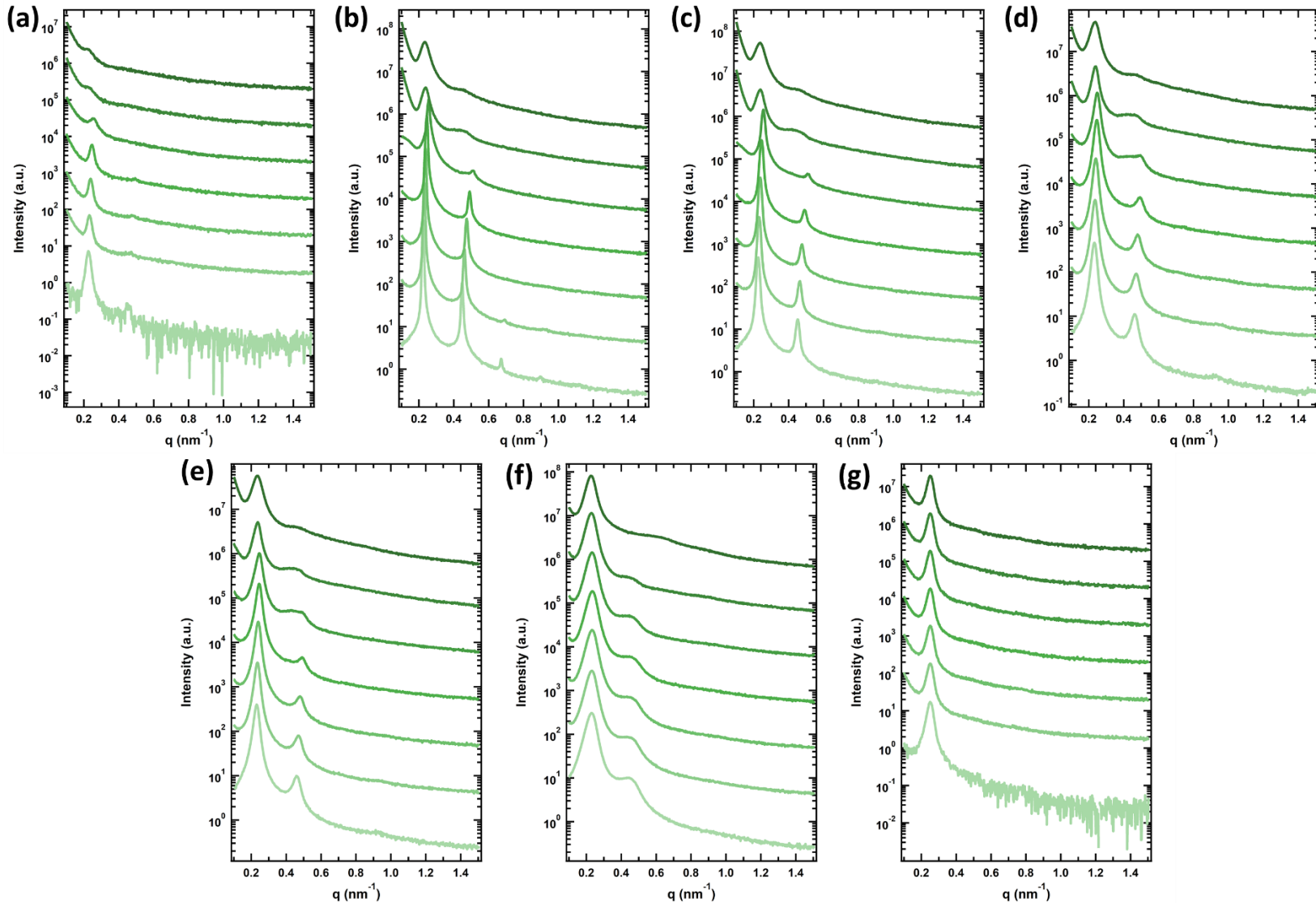


**Figure C-2.** Radially averaged SAXS patterns for 2xZEC conjugates at (a) 30 wt.%, (b) 35 wt.%, (c) 40 wt.%, (d) 45 wt.%, (e) 50 wt.%, (f) 60 wt.%, and (g) 100 wt.%. Curves are offset vertically for clarity. The seven curves in each plot correspond to temperatures of 10 °C to 40 °C in 5 °C intervals, from bottom to top.

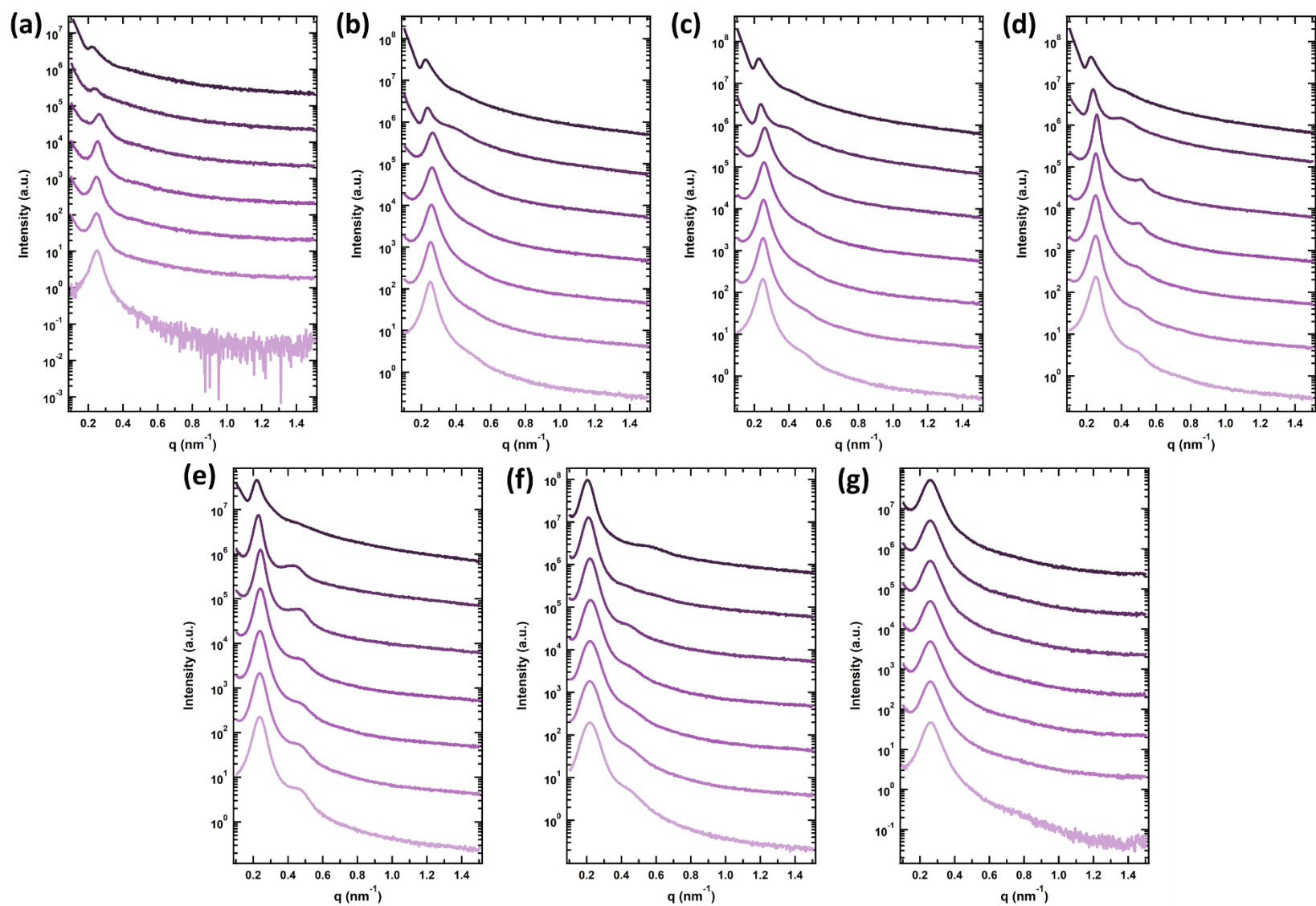


**Figure C-3.** Radially averaged SAXS patterns for 2xZRC conjugates at (a) 30 wt.%, (b) 35 wt.%, (c) 40 wt.%, (d) 45 wt.%, (e) 50 wt.%, (f) 60 wt.%, and (g) 100 wt.%. Curves are offset vertically for clarity. The seven curves in each plot correspond to temperatures of 10 °C to 40 °C in 5 °C intervals, from bottom to top.

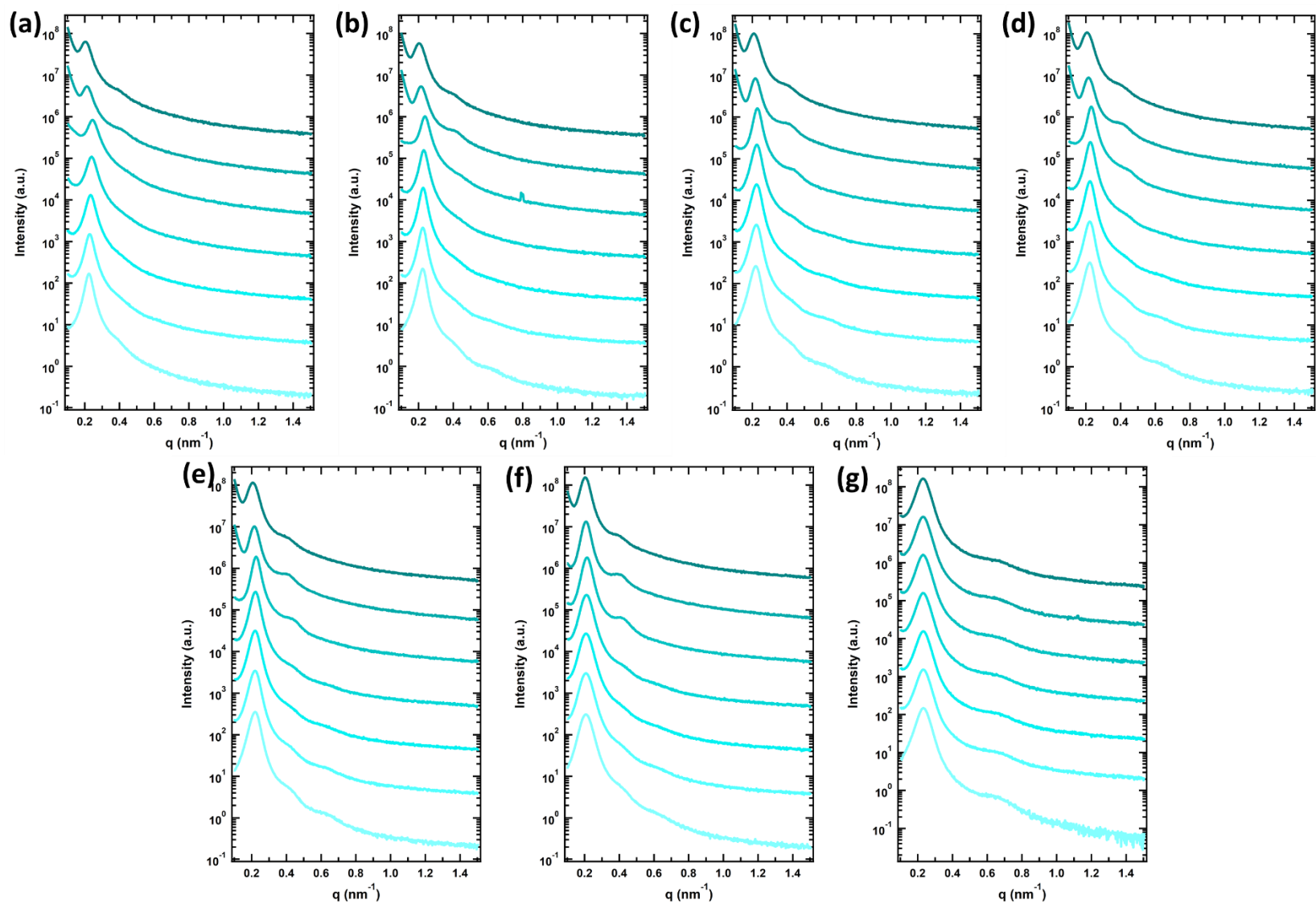


**Figure C-4.** Radially averaged SAXS patterns for 2xZEN conjugates at (a) 30 wt.%, (b) 35 wt.%, (c) 40 wt.%, (d) 45 wt.%, (e) 50 wt.%, (f) 60 wt.%, and (g) 100 wt.%. Curves are offset vertically for clarity. The seven curves in each plot correspond to temperatures of 10 °C to 40 °C in 5 °C intervals, from bottom to top.

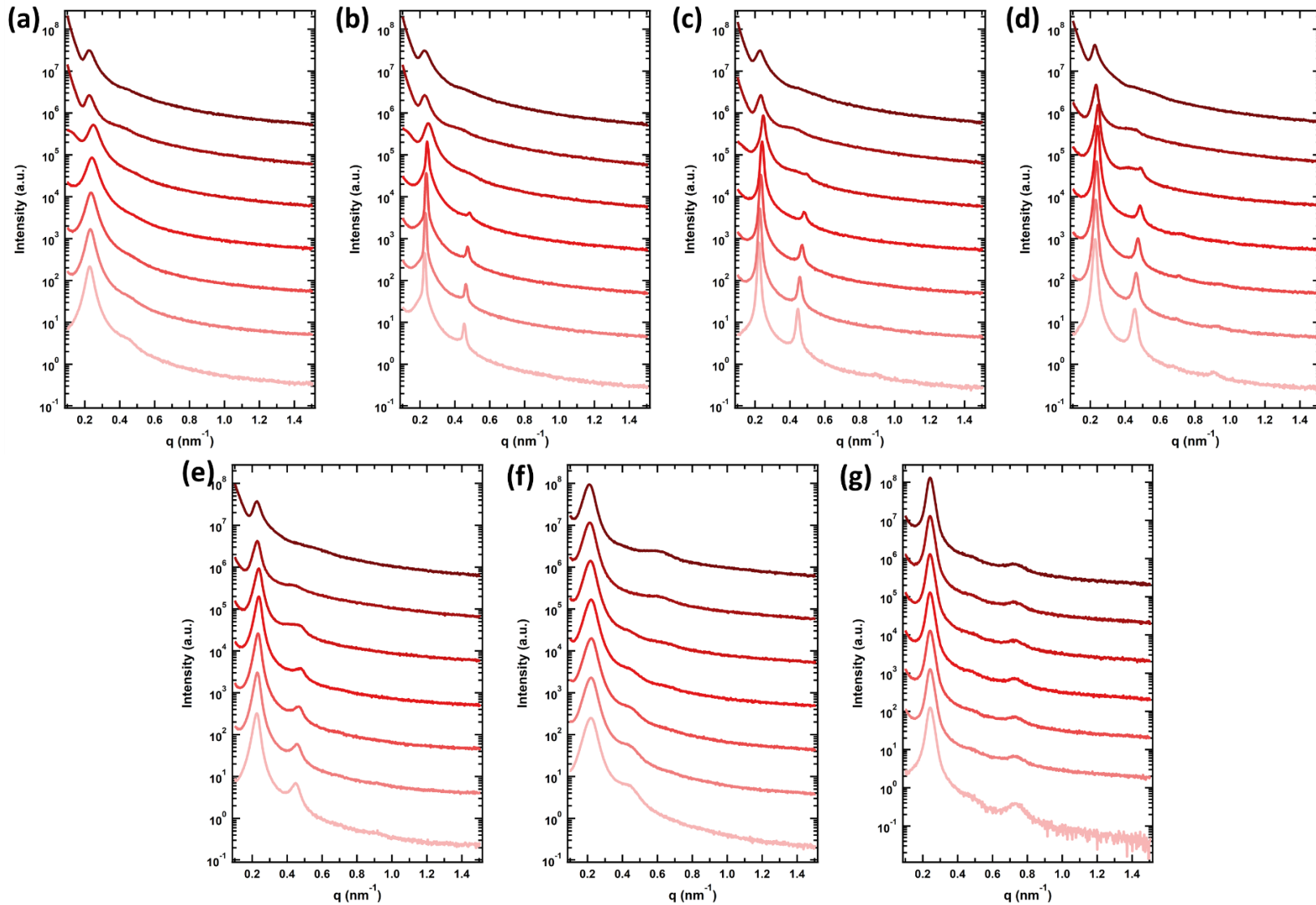


**Figure C-5.** Radially averaged SAXS patterns for 2xZEC-ZRC conjugates at (a) 30 wt.%, (b) 35 wt.%, (c) 40 wt.%, (d) 45 wt.%, (e) 50 wt.%, (f) 60 wt.%, and (g) 100 wt.%. Curves are offset vertically for clarity. The seven curves in each plot correspond to temperatures of 10 °C to 40 °C in 5 °C intervals, from bottom to top.

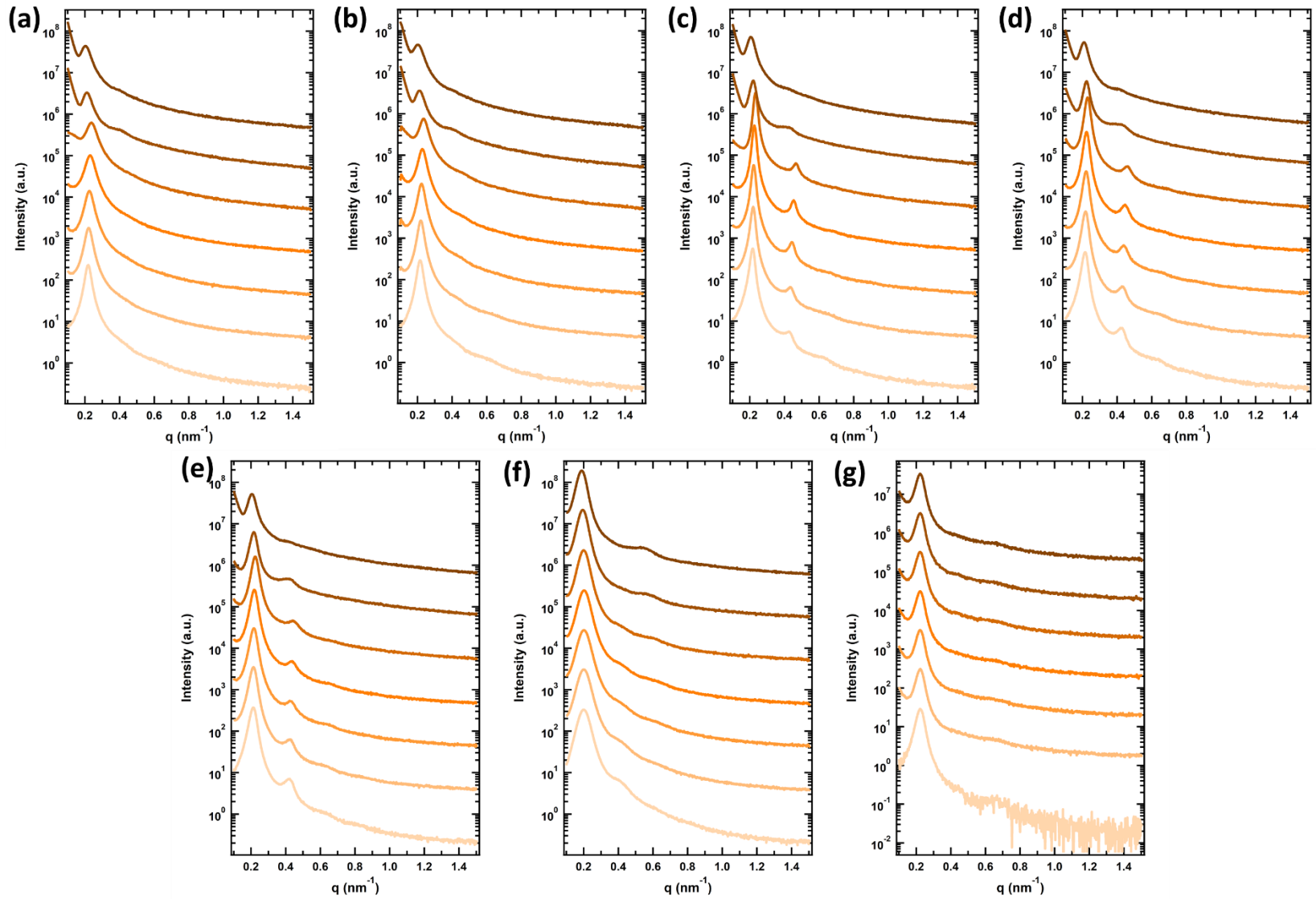


**Figure C-6.** Radially averaged SAXS patterns for 2xZEN-ZRC conjugates at (a) 30 wt.%, (b) 35 wt.%, (c) 40 wt.%, (d) 45 wt.%, (e) 50 wt.%, (f) 60 wt.%, and (g) 100 wt.%. Curves are offset vertically for clarity. The seven curves in each plot correspond to temperatures of 10 °C to 40 °C in 5 °C intervals, from bottom to top.

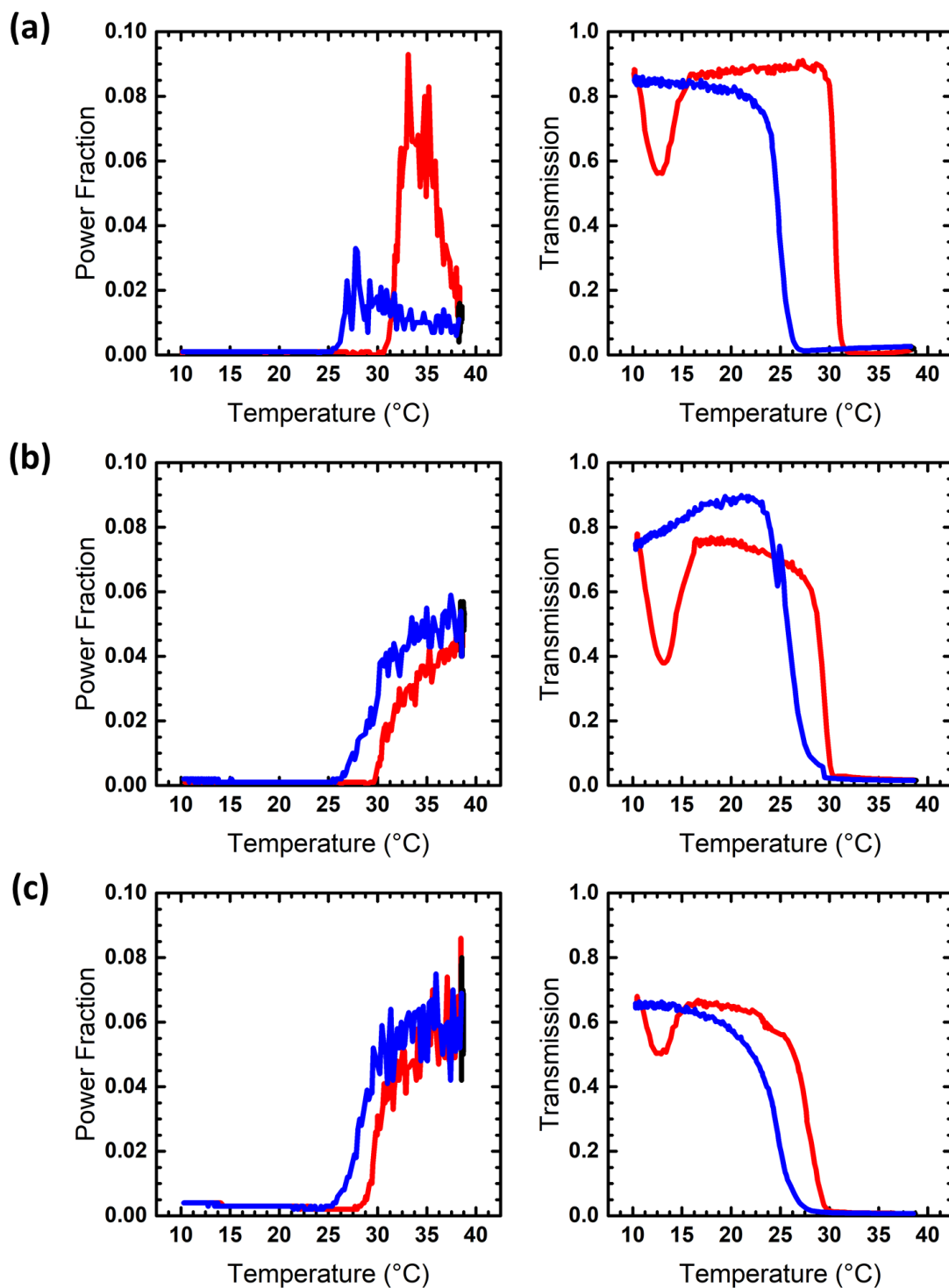


**Figure C-7a-c.** DPLS (left) and turbidimetry (right) heating/cooling cycles for 2xZEC conjugates at (a) 30 wt.%, (b) 35 wt.%, and (c) 40 wt.%. The red curve represents the heating cycle, and the blue curve represents the cooling cycle. The black curve represents the 10-minute equilibration at the end of the heating cycle before cooling.

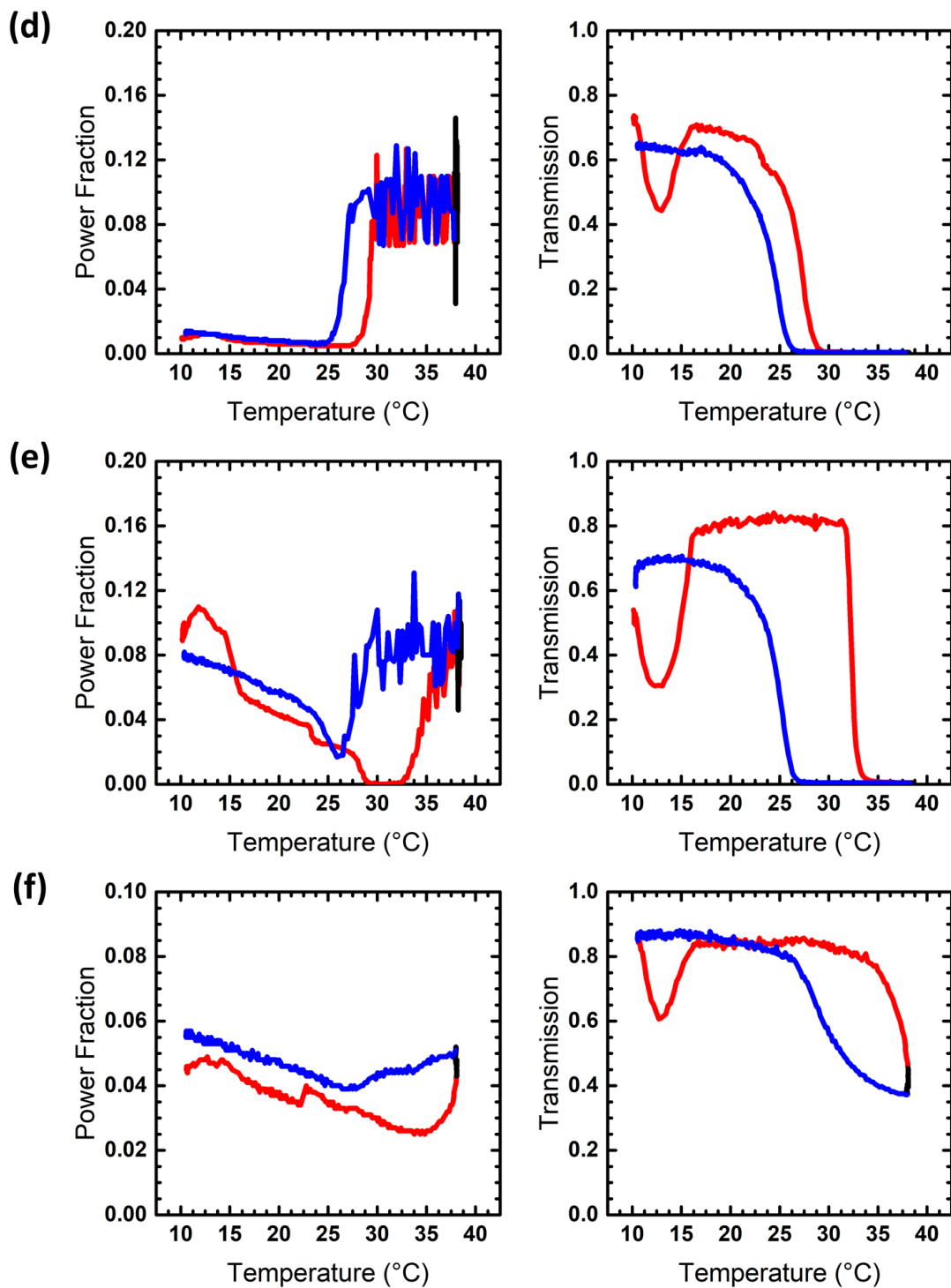


**Figure C-7d-f.** DPLS (left) and turbidimetry (right) heating/cooling cycles for 2xZEC conjugates at (d) 45 wt.%, (e) 50 wt.%, and (f) 60 wt.%. The red curve represents the heating cycle, and the blue curve represents the cooling cycle. The black curve represents the 10-minute equilibration at the end of the heating cycle before cooling.

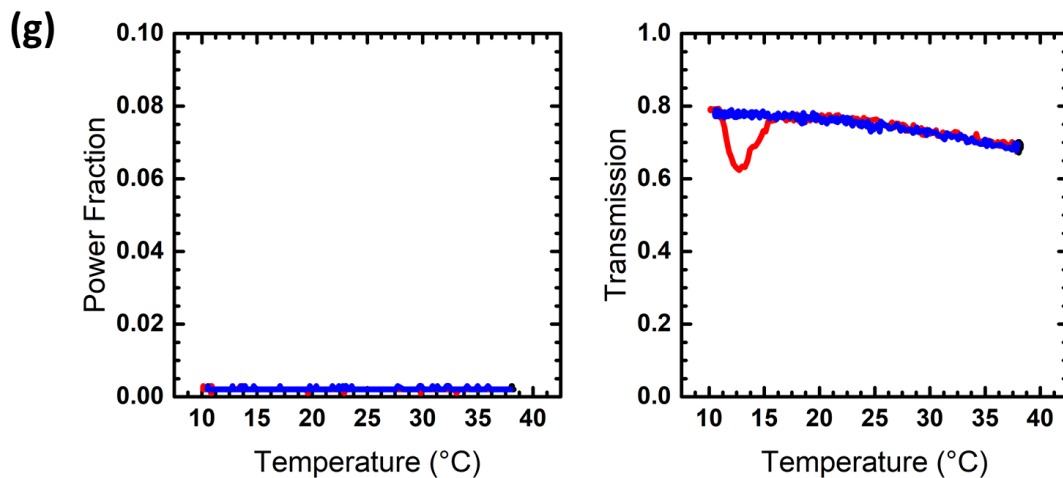


**Figure C-7g.** DPLS (left) and turbidimetry (right) heating/cooling cycles for 2xZEC conjugates at (g) 100 wt.%. The red curve represents the heating cycle, and the blue curve represents the cooling cycle. The black curve represents the 10-minute equilibration at the end of the heating cycle before cooling.

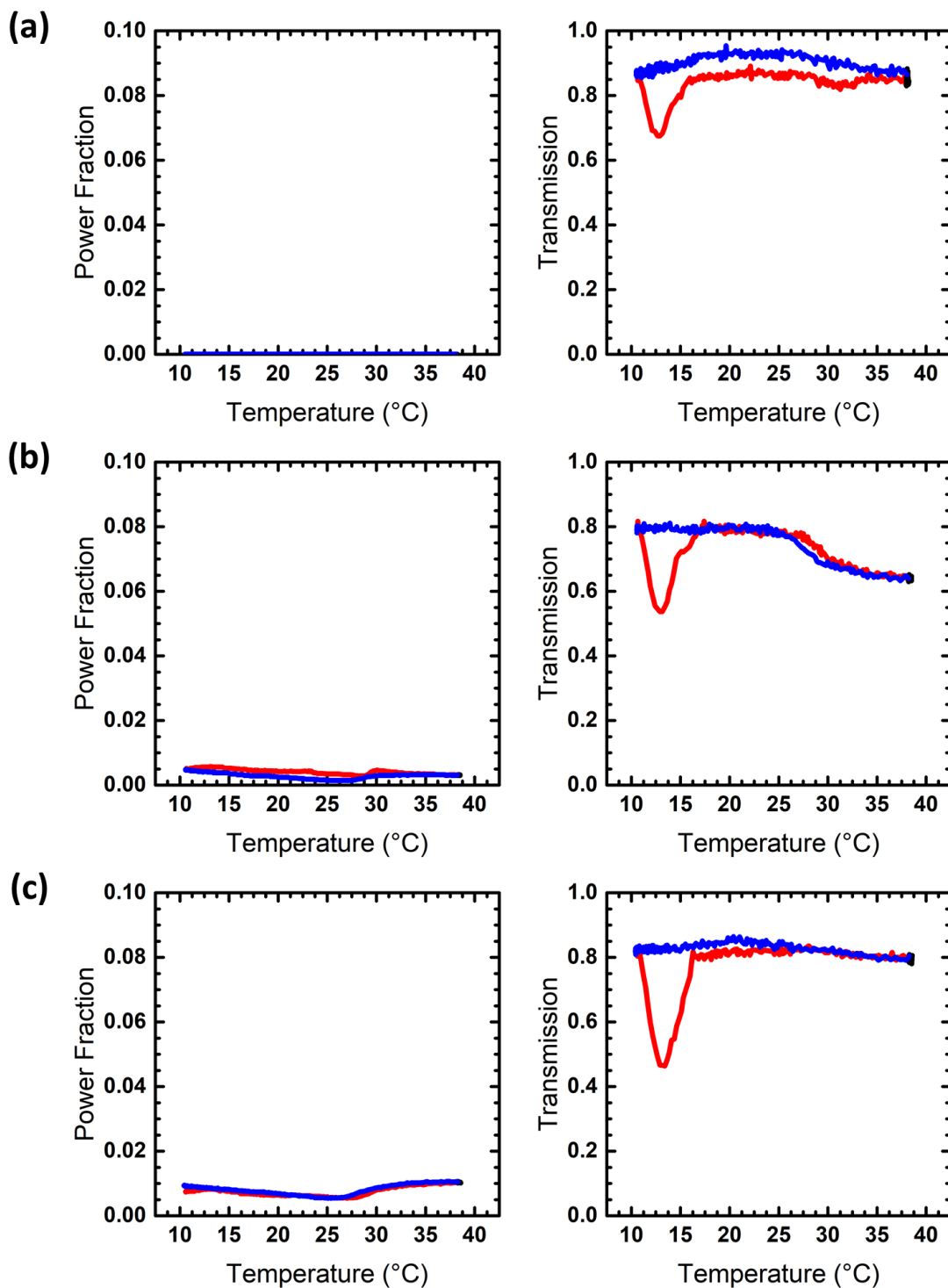


**Figure C-8a-c.** DPLS (left) and turbidimetry (right) heating/cooling cycles for 2xZRC conjugates at (a) 30 wt.%, (b) 35 wt.%, and (c) 40 wt.%. The red curve represents the heating cycle, and the blue curve represents the cooling cycle. The black curve represents the 10-minute equilibration at the end of the heating cycle before cooling.

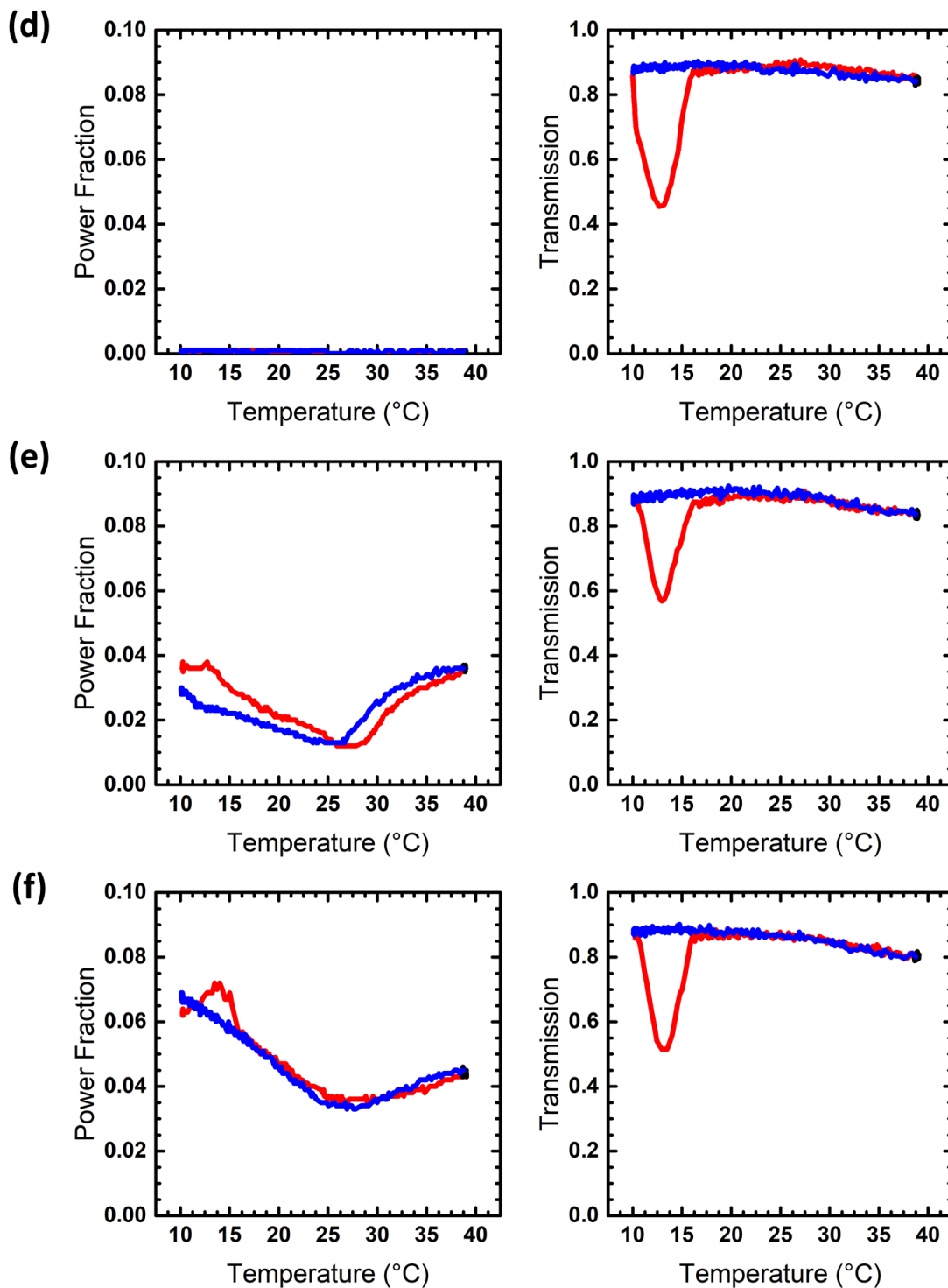


**Figure C-8d-f.** DPLS (left) and turbidimetry (right) heating/cooling cycles for 2xZRC conjugates at (d) 45 wt.%, (e) 50 wt.%, and (f) 60 wt.%. The red curve represents the heating cycle, and the blue curve represents the cooling cycle. The black curve represents the 10-minute equilibration at the end of the heating cycle before cooling.

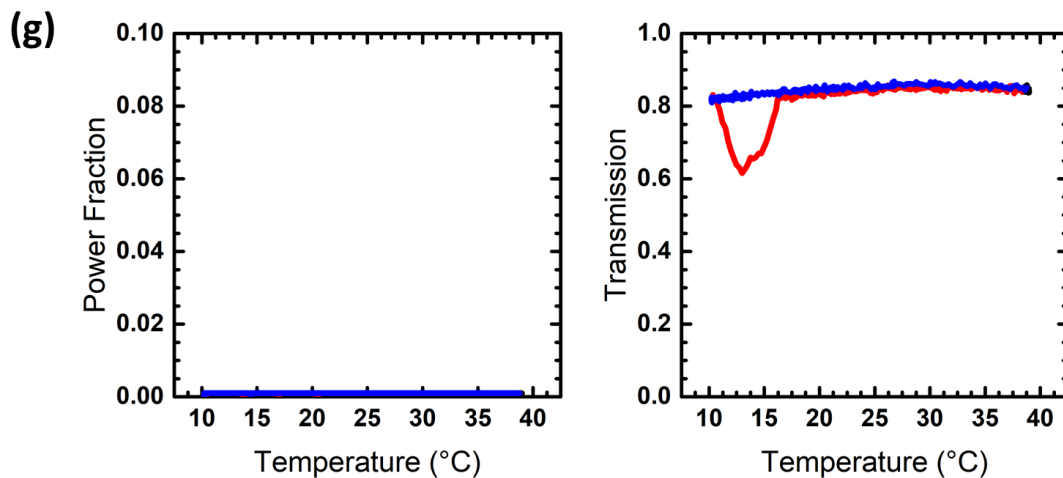


**Figure C-8g.** DPLS (left) and turbidimetry (right) heating/cooling cycles for 2xZRC conjugates at (g) 100 wt.%. The red curve represents the heating cycle, and the blue curve represents the cooling cycle. The black curve represents the 10-minute equilibration at the end of the heating cycle before cooling.

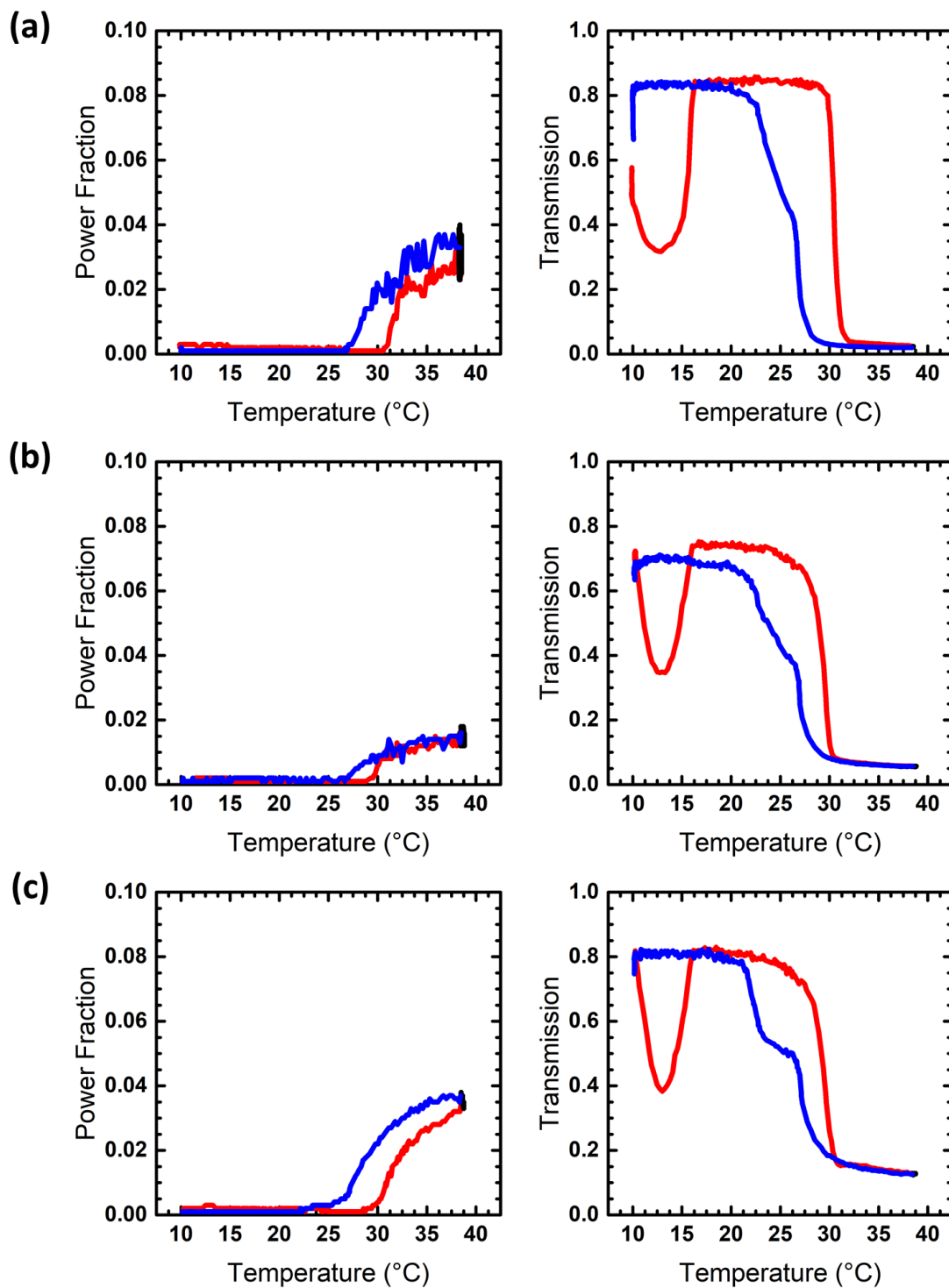


**Figure C-9a-c.** DPLS (left) and turbidimetry (right) heating/cooling cycles for 2xZEN conjugates at (a) 30 wt.%, (b) 35 wt.%, and (c) 40 wt.%. The red curve represents the heating cycle, and the blue curve represents the cooling cycle. The black curve represents the 10-minute equilibration at the end of the heating cycle before cooling.

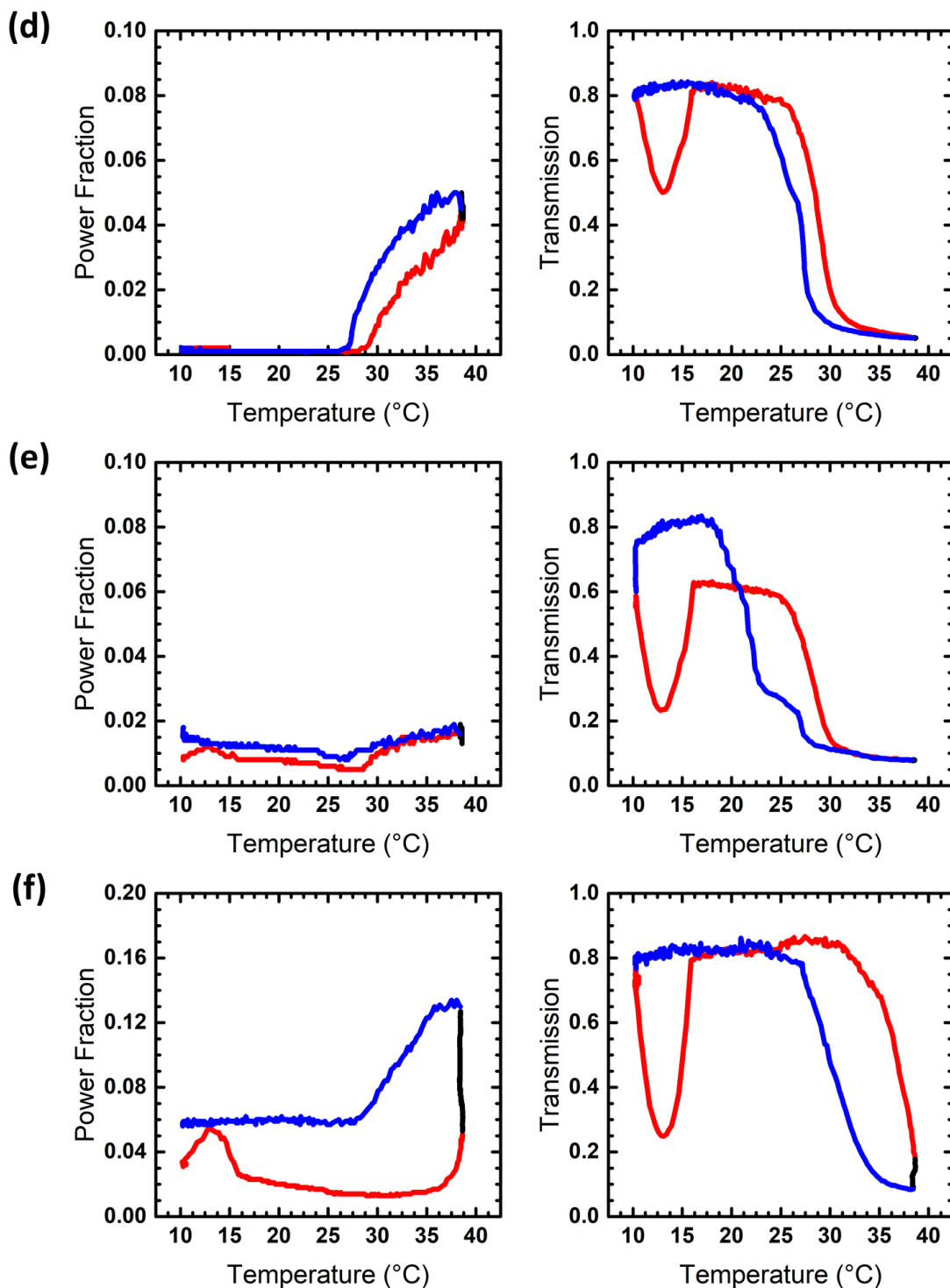


**Figure C-9d-f.** DPLS (left) and turbidimetry (right) heating/cooling cycles for 2xZEN conjugates at (d) 45 wt.%, (e) 50 wt.%, and (f) 60 wt.%. The red curve represents the heating cycle, and the blue curve represents the cooling cycle. The black curve represents the 10-minute equilibration at the end of the heating cycle before cooling.

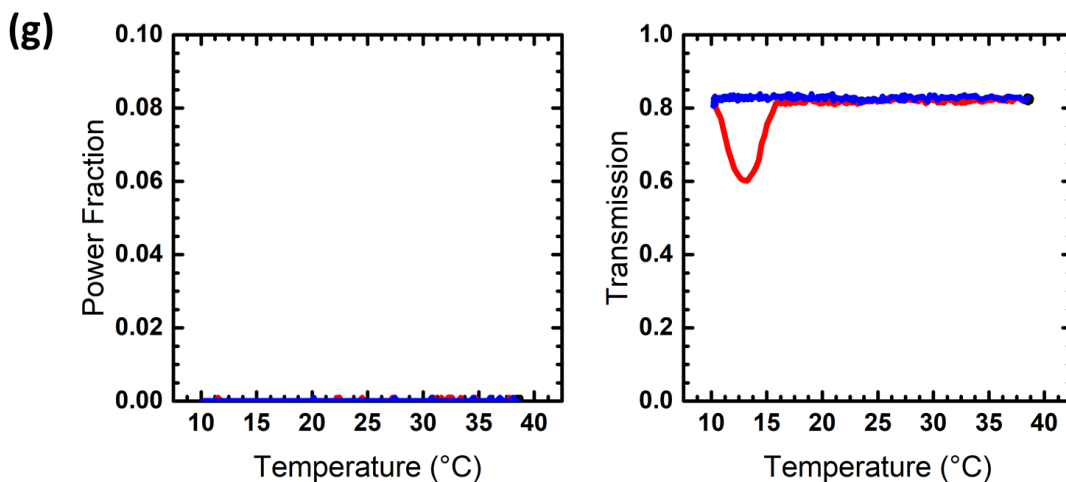


**Figure C-9g.** DPLS (left) and turbidimetry (right) heating/cooling cycles for 2xZEN conjugates at (g) 100 wt.%. The red curve represents the heating cycle, and the blue curve represents the cooling cycle. The black curve represents the 10-minute equilibration at the end of the heating cycle before cooling.

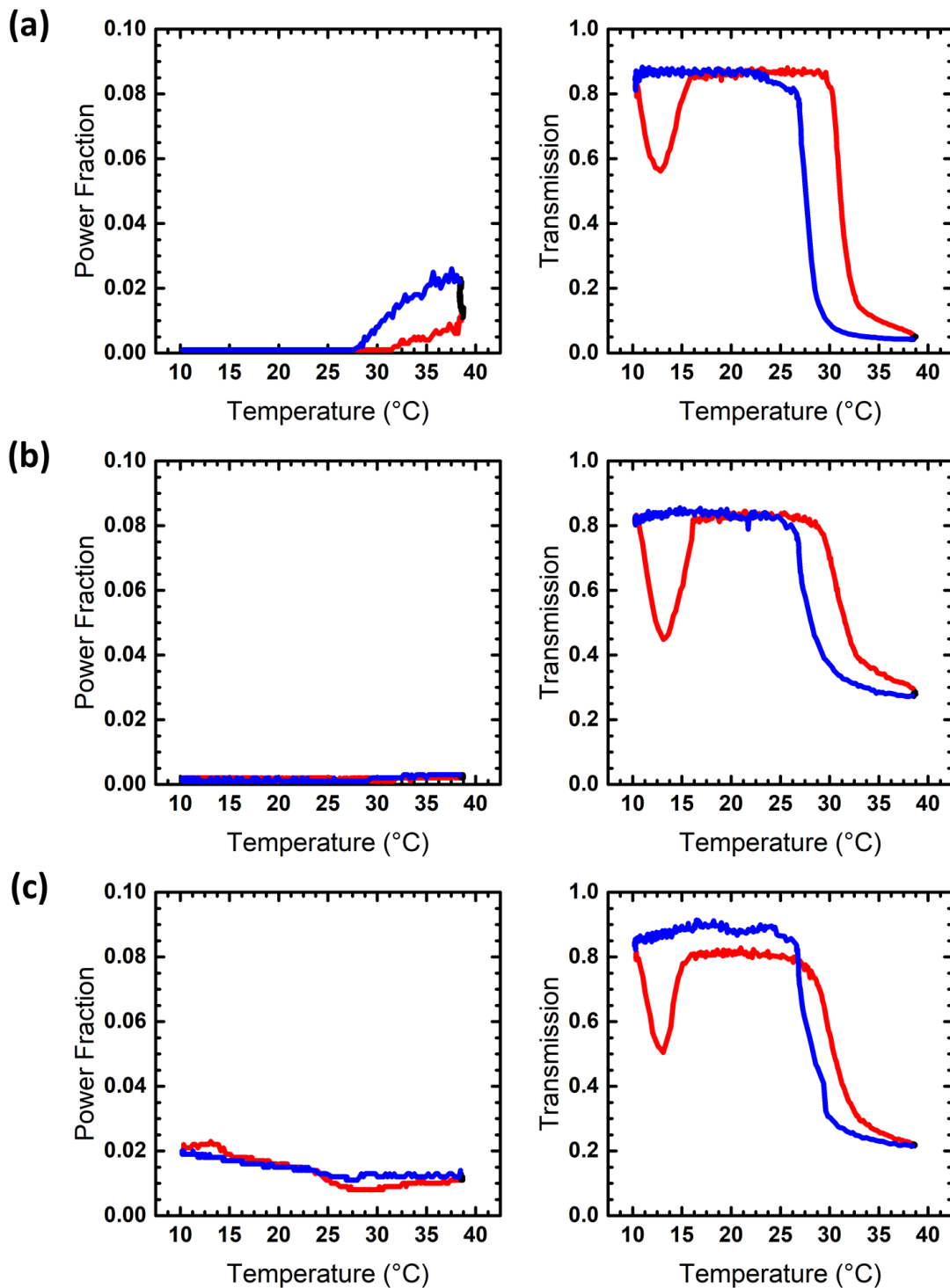


**Figure C-10a-c.** DPLS (left) and turbidimetry (right) heating/cooling cycles for 2xZEC-ZRC conjugates at (a) 30 wt.%, (b) 35 wt.%, and (c) 40 wt.%. The red curve represents the heating cycle, and the blue curve represents the cooling cycle. The black curve represents the 10-minute equilibration at the end of the heating cycle before cooling.

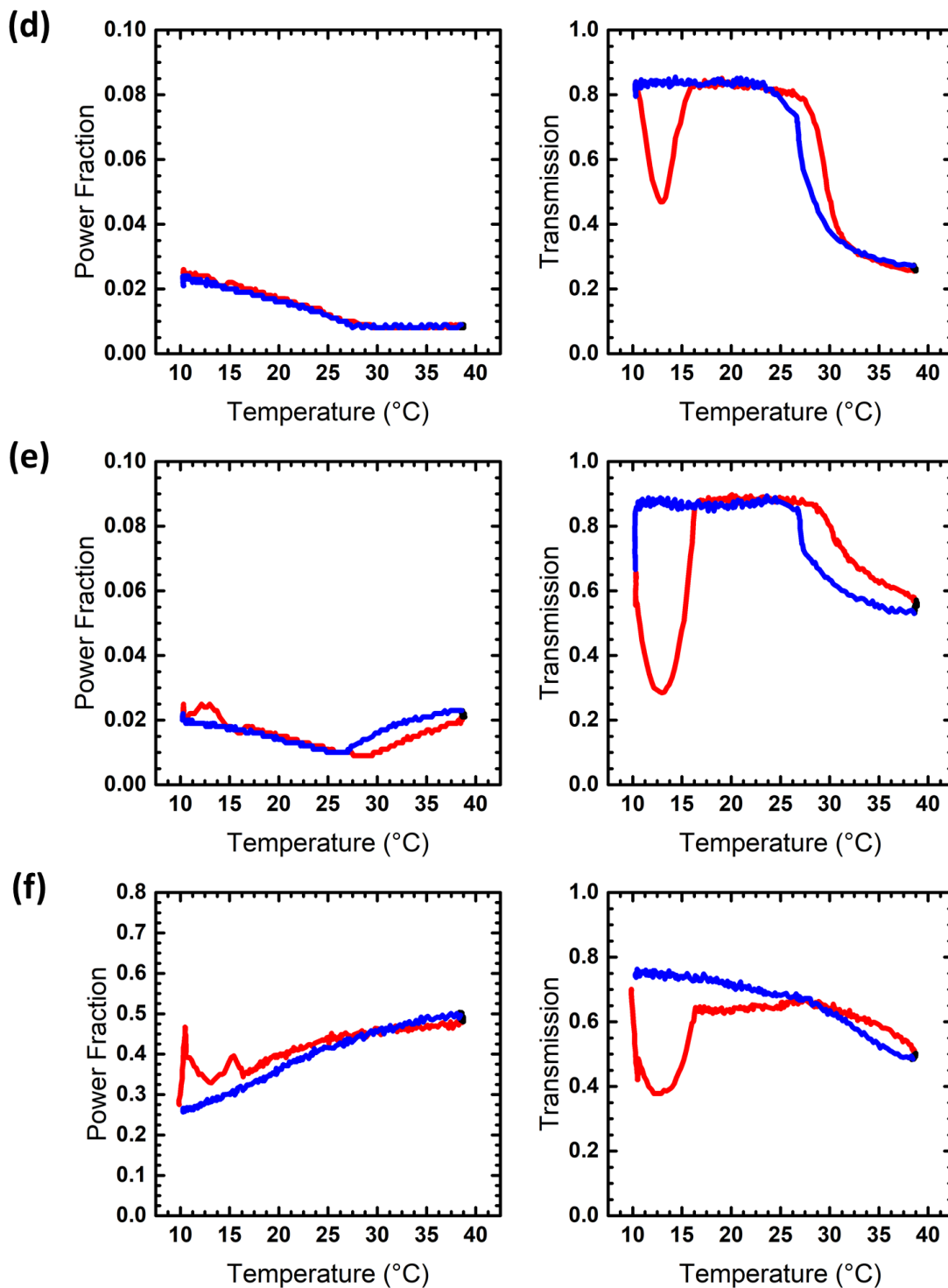


**Figure C-10d-f.** DPLS (left) and turbidimetry (right) heating/cooling cycles for 2xZEC-ZRC conjugates at (d) 45 wt.%, (e) 50 wt.%, and (f) 60 wt.%. The red curve represents the heating cycle, and the blue curve represents the cooling cycle. The black curve represents the 10-minute equilibration at the end of the heating cycle before cooling.

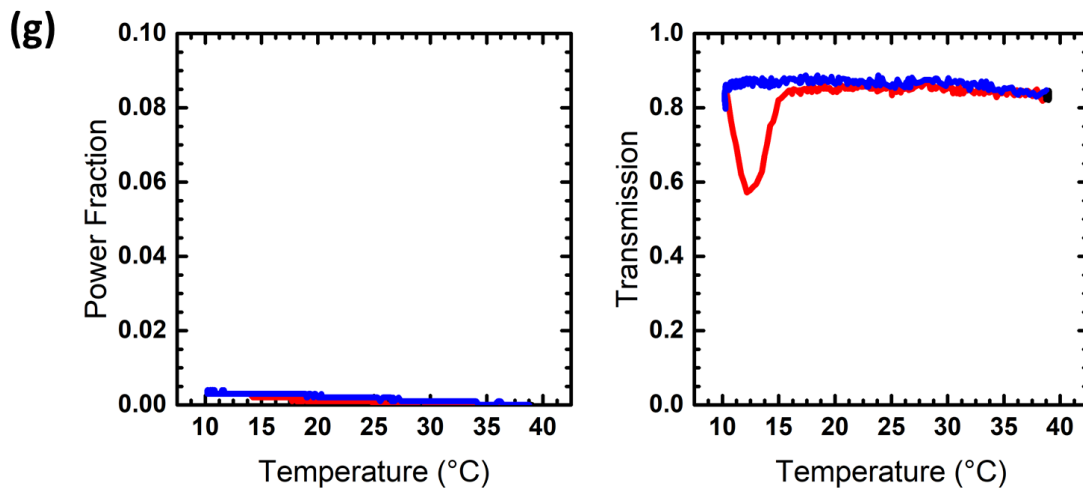


**Figure C-10g.** DPLS (left) and turbidimetry (right) heating/cooling cycles for 2xZEC-ZRC conjugates at (g) 100 wt.%. The red curve represents the heating cycle, and the blue curve represents the cooling cycle. The black curve represents the 10-minute equilibration at the end of the heating cycle before cooling.

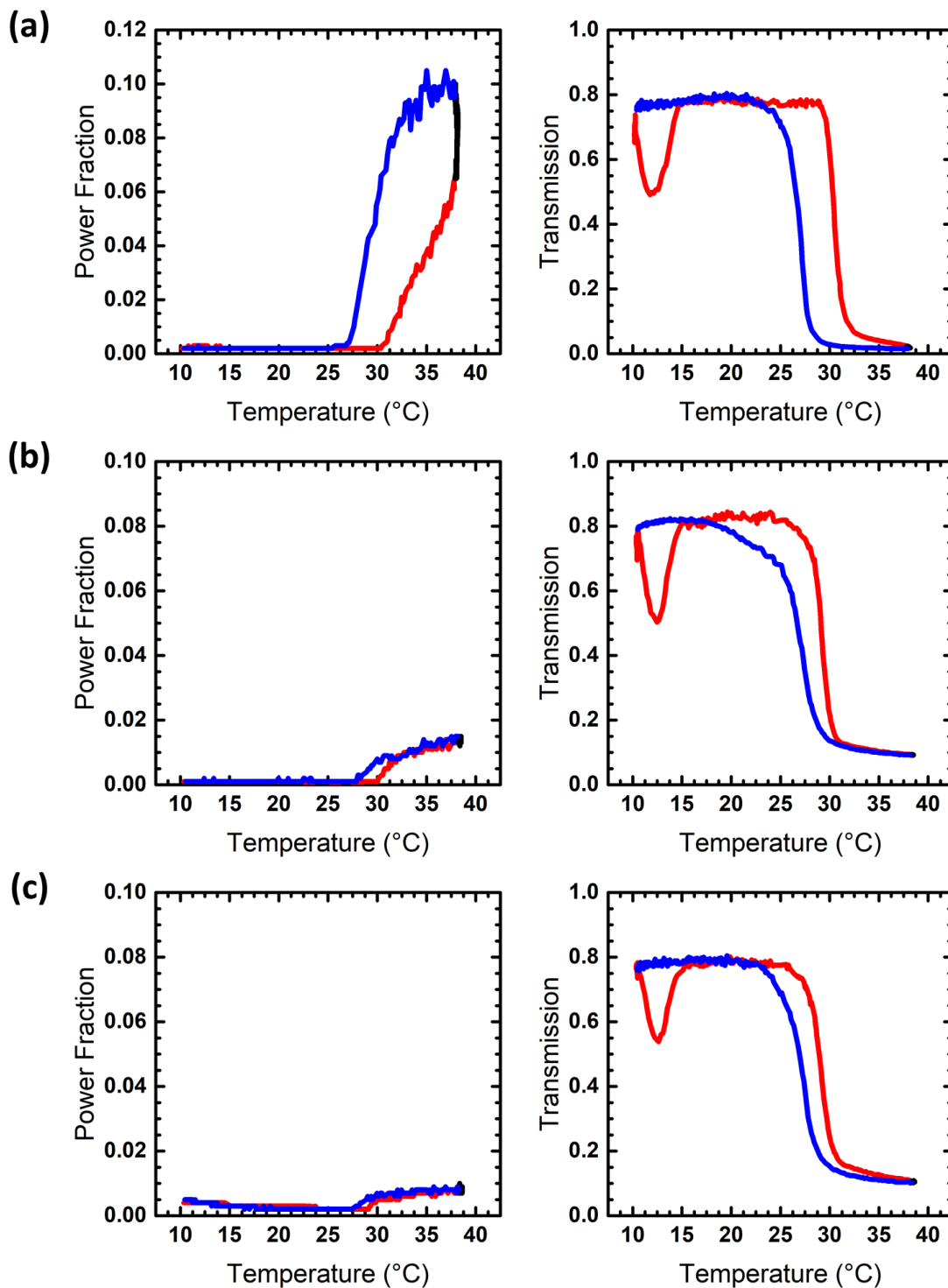


**Figure C-11a-c.** DPLS (left) and turbidimetry (right) heating/cooling cycles for 2xZEN-ZRC conjugates at (a) 30 wt.%, (b) 35 wt.%, and (c) 40 wt.%. The red curve represents the heating cycle, and the blue curve represents the cooling cycle. The black curve represents the 10-minute equilibration at the end of the heating cycle before cooling.

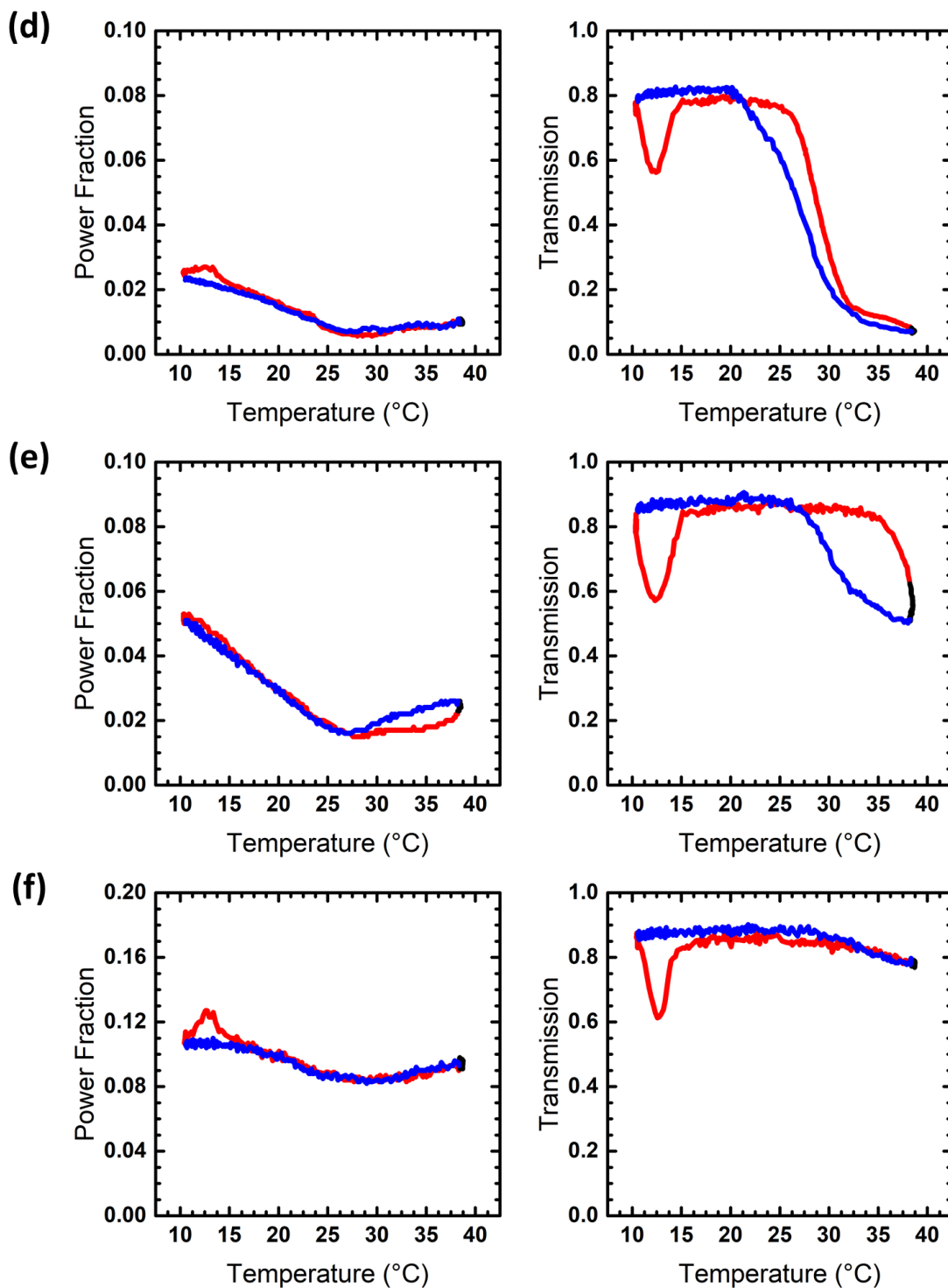


**Figure C-11d-f.** DPLS (left) and turbidimetry (right) heating/cooling cycles for 2xZEN-ZRC conjugates at (d) 45 wt.%, (e) 50 wt.%, and (f) 60 wt.%. The red curve represents the heating cycle, and the blue curve represents the cooling cycle. The black curve represents the 10-minute equilibration at the end of the heating cycle before cooling.

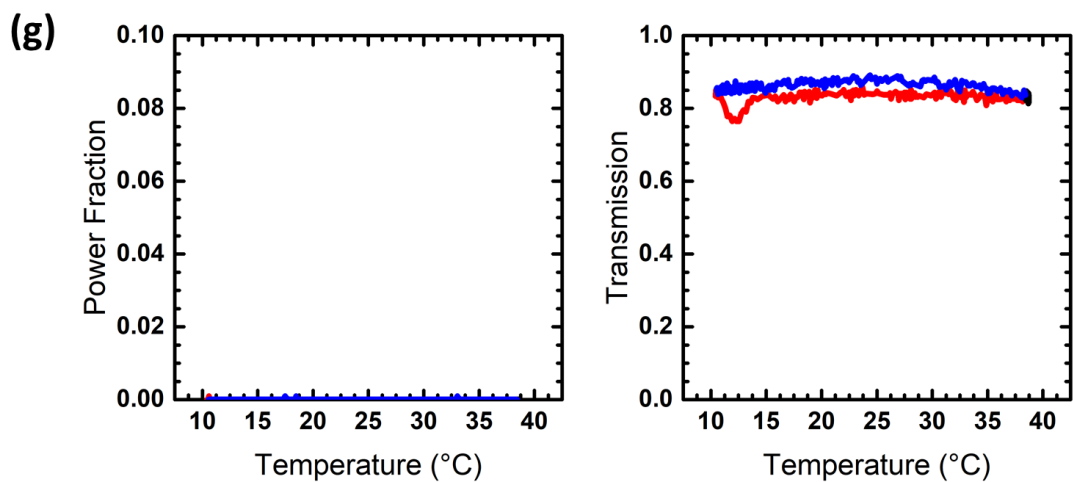


**Figure C-11g.** DPLS (left) and turbidimetry (right) heating/cooling cycles for 2xZEN-ZRC conjugates at (g) 100 wt.%. The red curve represents the heating cycle, and the blue curve represents the cooling cycle. The black curve represents the 10-minute equilibration at the end of the heating cycle before cooling.

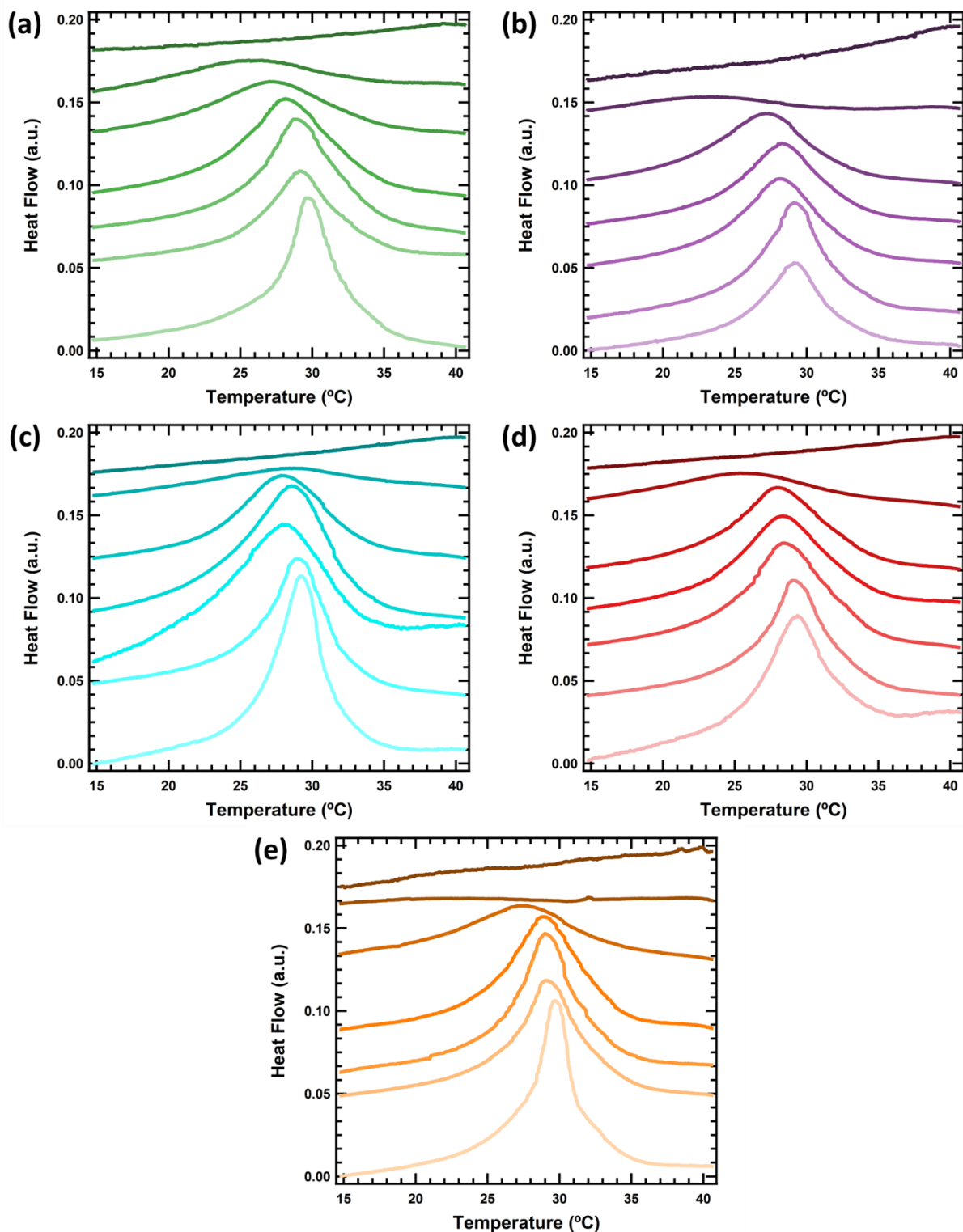


**Figure C-12.** DSC curves of (a) 2xZEC, (b) 2xZRC, (c) 2xZEN, (d) 2xZEC-ZRC, and (e) 2xZEN-ZRC at varying concentrations. Curves are offset for clarity. The seven curves in each plot correspond to concentrations of 30, 35, 40, 45, 50, 60, and 100 wt.%, from bottom to top.

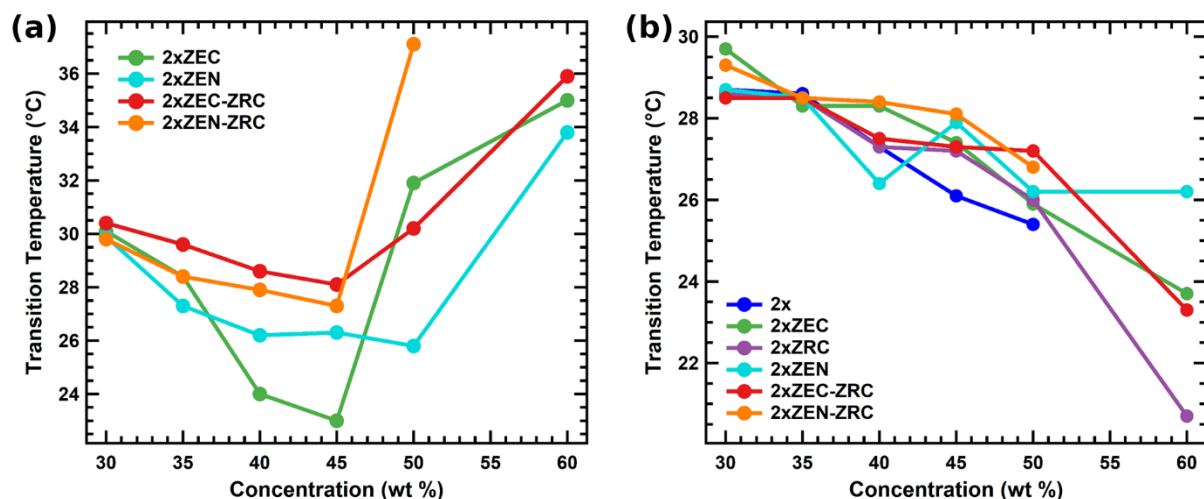


**Figure C-13.** Transition temperatures for (a) macrophase separation and (b) PNIPAM desolvation for the coiled-coil fusion conjugates as a function of concentration. In (a) no macrophase separation was observed in 2x or 2xZRC conjugates.

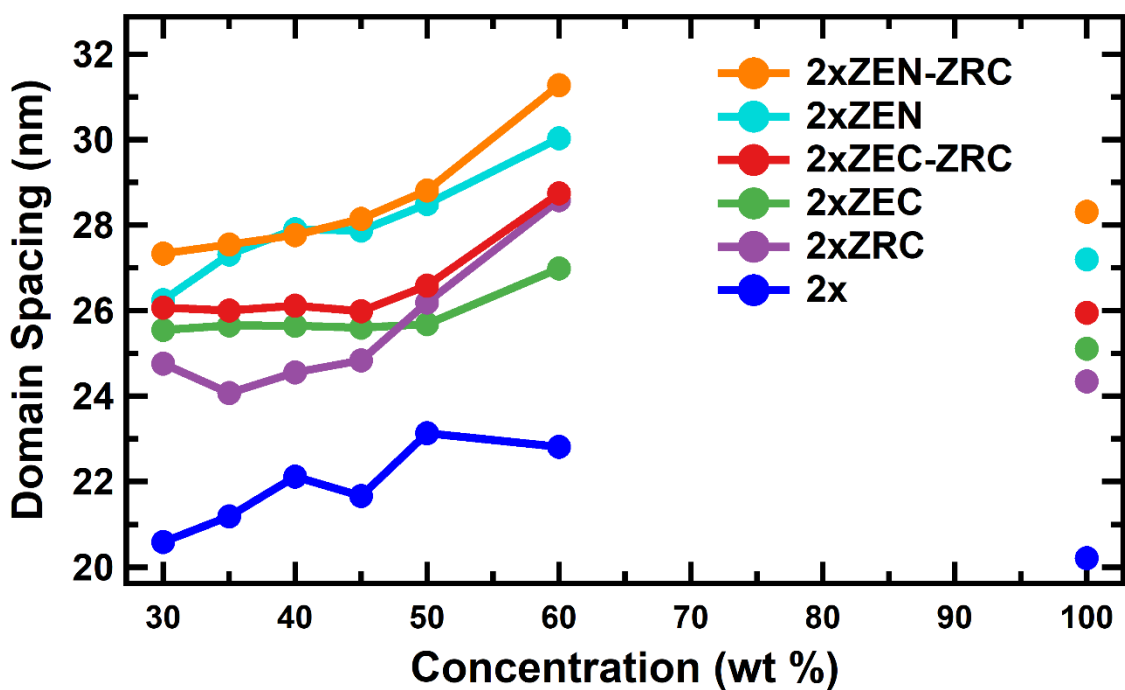


**Figure C-14.** Domain spacings of coiled-coil fusion conjugates in aqueous solution at 25 °C. Bulk data are disconnected from solution-phase data to indicate that the bulk samples are not at equilibrium. Data for 2x are taken from the literature.<sup>2</sup>

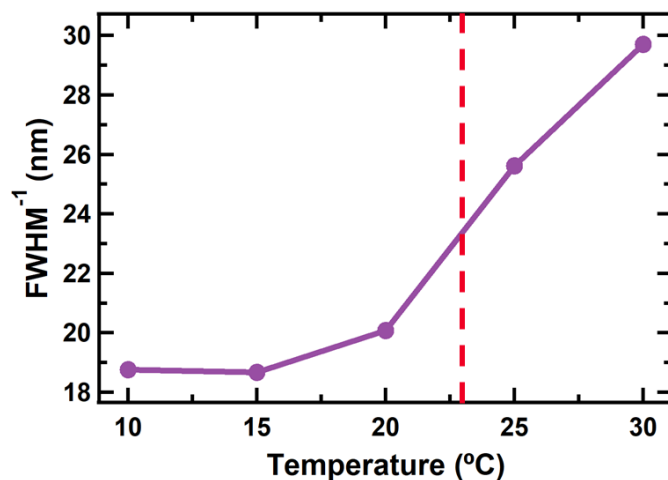


**Figure C-15.** FWHM<sup>-1</sup> of ordered phases in 45 weight percent 2xZRC samples as a function of temperature. The red dashed line represents the measured melting point of 2xZRC homodimerized coiled-coils, 23 °C.

#### References for Appendix C

1. C. S. Thomas, M. J. Glassman and B. D. Olsen, *ACS Nano*, 2011, **5**, 5697-5707.
2. J. M. Paloni, E. A. Miller, H. D. Sikes and B. D. Olsen, *Biomacromolecules*, 2018, **19**, 3814-3824.

Appendix D. Supporting Information for Chapter 5

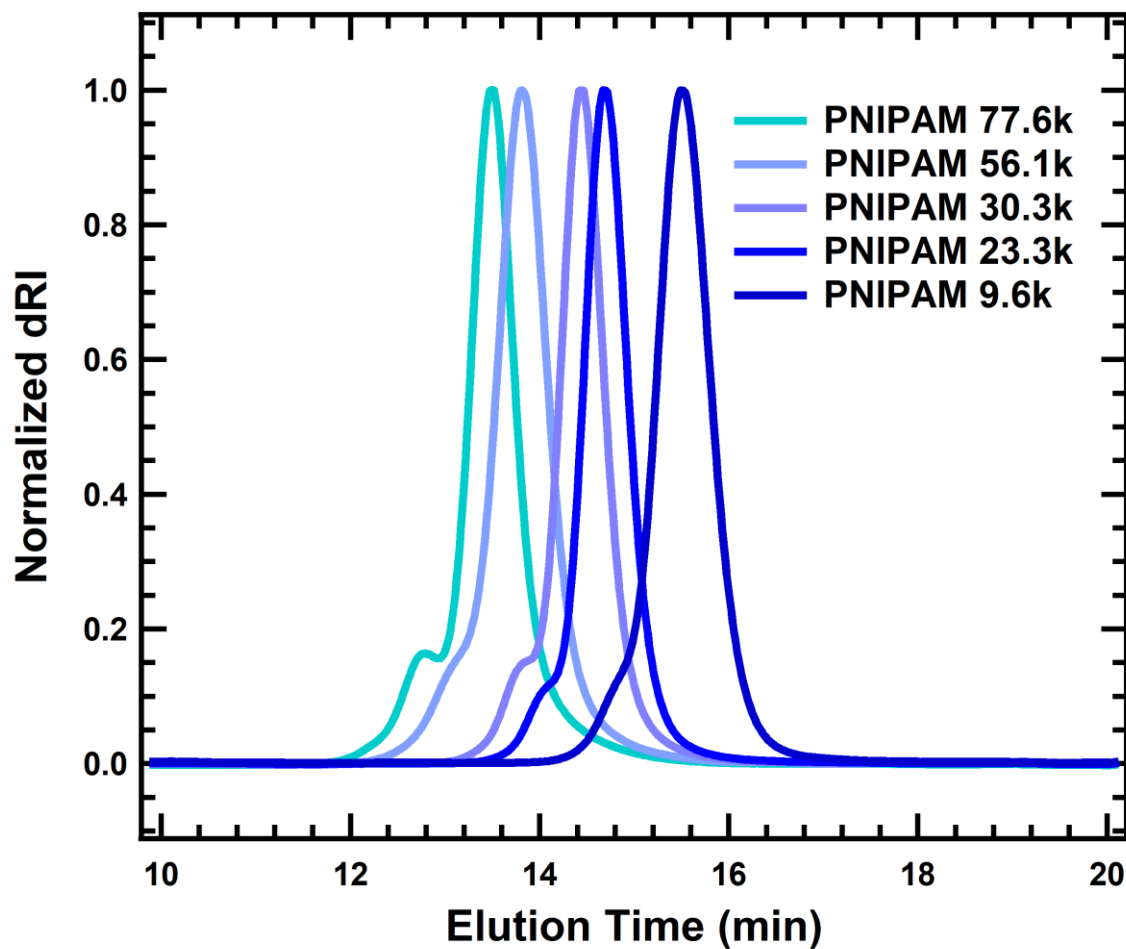


**Figure D-1.** Normalized differential refractive index signals from gel permeation chromatography of PNIPAM samples. The small shoulder at earlier elution times corresponding to twice the peak molecular weight in some samples results from slight reactivity of the double bond in the furan-protected maleimide of the CTA, as reported previously.<sup>1</sup>

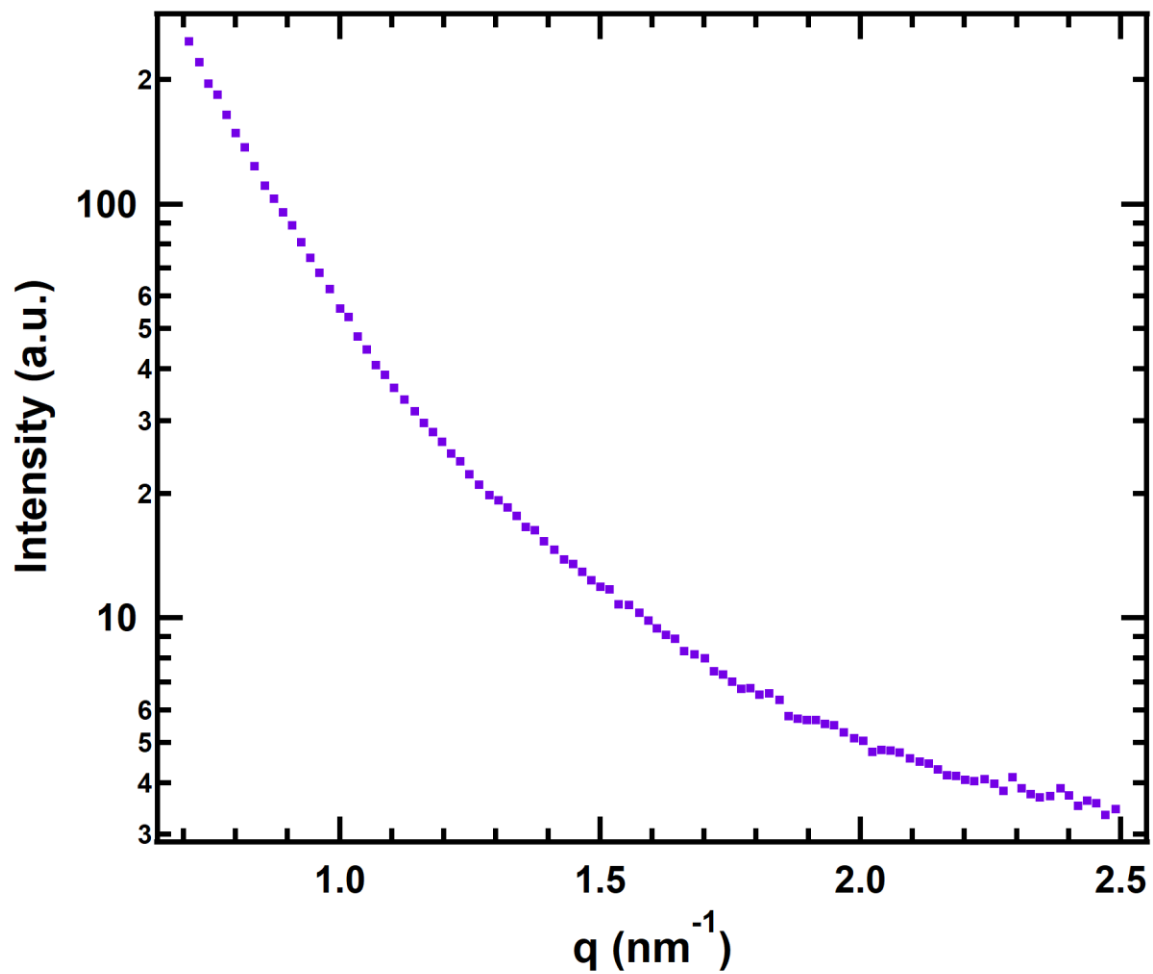


**Figure D-2.** Representative GISAXS vertical linecut from swollen thin films. GISAXS pattern was collected from a 3xSP56.1k thin film at an incident angle of 0.140°.

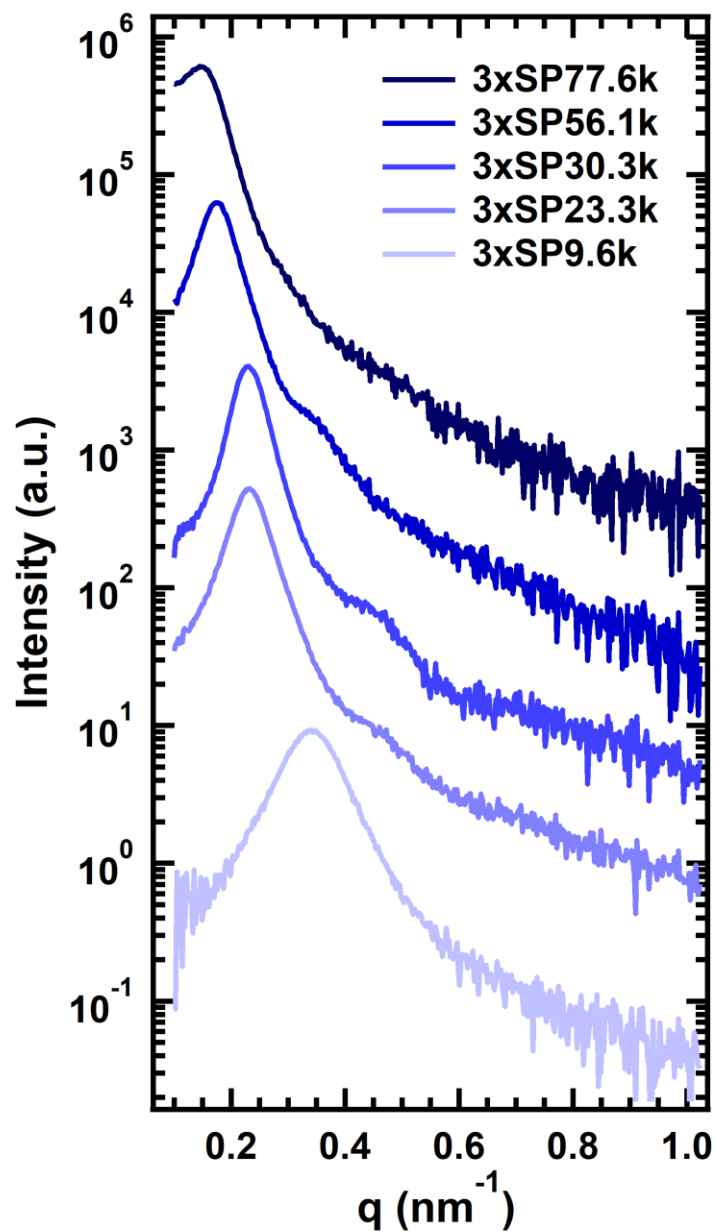


**Figure D-3.** Bulk SAXS curves for synthesized conjugates at ambient conditions.

**Table D-1.** Comparison of Bulk and Thin Film Domain Spacings

Conjugate	Bulk Domain Spacing (nm) <sup>a</sup>	Film Domain Spacing (nm) <sup>b</sup>
3xSP9.6k	18.4	21.9
3xSP23.3k	26.9	30.6
3xSP30.3k	27.5	32.0
3xSP56.1k	35.9	43.5
3xSP77.6k	43.5	53.9

<sup>a</sup>Measured using bulk samples at ambient conditions. <sup>b</sup>Measured at 95% RH.

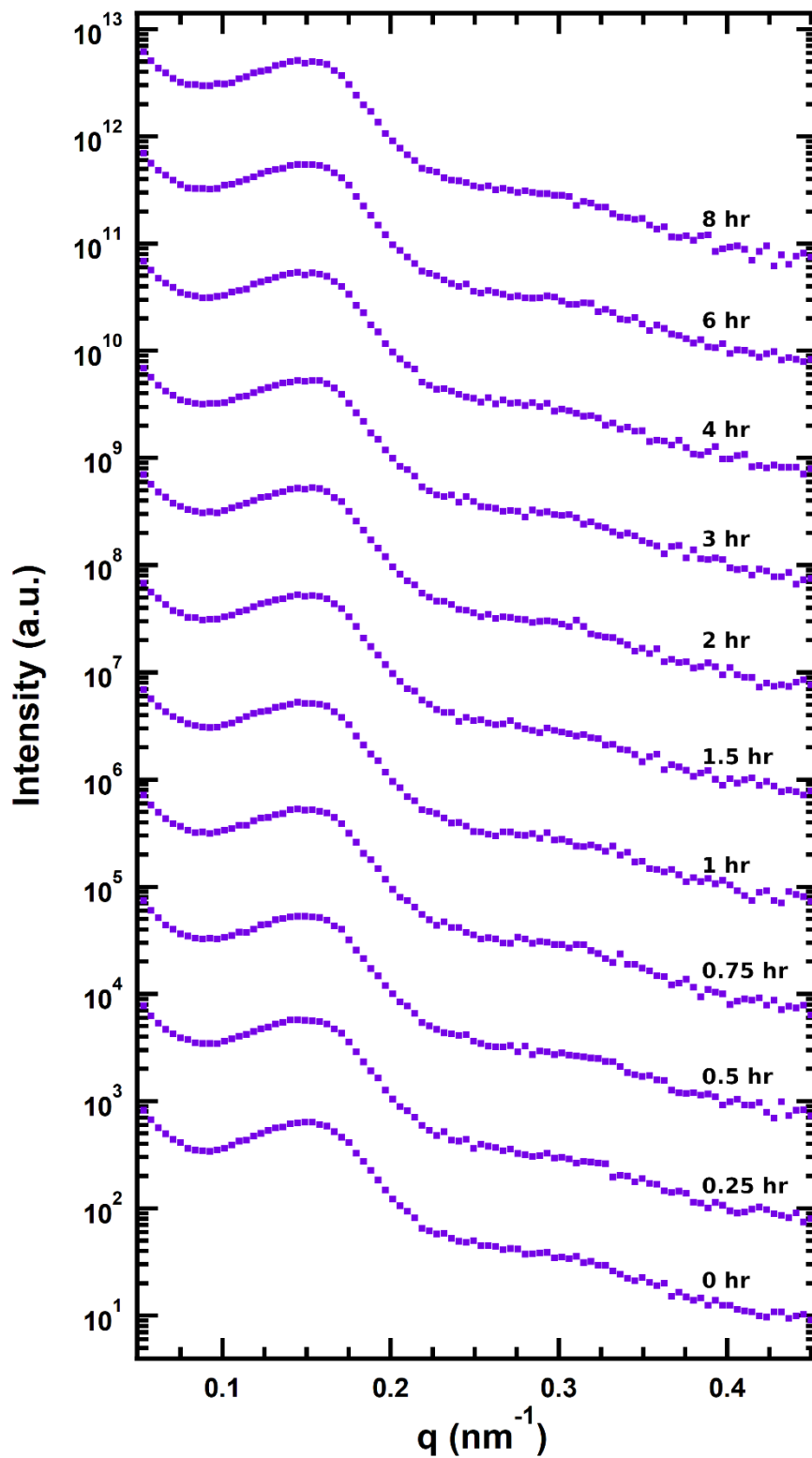


**Figure D-4.** GISAXS horizontal linecuts of a 150 nm 3xSP56.1k film swollen in an environment maintained at 95% RH for different periods of time. GISAXS patterns were collected at an incident angle of  $0.140^\circ$ .

**Table D-2.** Best-fit Parameters for Buffer Binding Curves

<b>Streptavidin Films</b>				
<b>Film</b>	<b>Thickness (nm)</b>	<b><math>\alpha^a</math> (MFI/nM)</b>	<b><math>[P]r^a</math> (nM)</b>	<b><math>K_{d,app}^a</math> (<math>\mu</math>M)</b>
Monolayer	--	$107 \pm 8$	$0.36 \pm 0.03$	$8 \pm 2$
3xSP9.6k, 30 min	173	$100 \pm 10$	$0.08 \pm 0.01$	$60 \pm 10$
3xSP9.6k, 4 h	138	$110 \pm 20$	$0.9 \pm 0.2$	$40 \pm 10$
3xSP77.6k, 30 min	161	$80 \pm 50$	$0.3 \pm 0.2$	$80 \pm 60$
3xSP77.6k, 4 h	121	$123 \pm 6$	$0.41 \pm 0.02$	$17 \pm 2$
3xSP77.6k, 8 h	105	$130 \pm 20$	$0.64 \pm 0.07$	$15 \pm 4$
<b>Monomeric Streptavidin Films</b>				
<b>Film</b>	<b>Thickness (nm)</b>	<b><math>\alpha^a</math> (MFI/nM)</b>	<b><math>[P]r^a</math> (nM)</b>	<b><math>K_{d,app}^a</math> (<math>\mu</math>M)</b>
Monolayer	--	$100 \pm 10$	$0.35 \pm 0.05$	$3 \pm 1$
3xSP9.6k, 30 min	165	$114 \pm 9$	$0.38 \pm 0.03$	$11 \pm 2$
3xSP9.6k, 4 h	138	$100 \pm 20$	$0.7 \pm 0.1$	$3.7 \pm 0.9$
3xSP56.1k, 30 min	202	$129 \pm 7$	$1.17 \pm 0.06$	$33 \pm 4$
3xSP56.1k, 4 h	140	$80 \pm 9$	$3.2 \pm 0.4$	$16 \pm 4$
3xSP56.1k, 8 h	133	$90 \pm 10$	$2.8 \pm 0.4$	$13 \pm 5$

<sup>a</sup>Reported errors represent 95% confidence intervals for the parameter estimate.

**Table D-3.** Best-fit Parameters for Biological Matrix Binding Curves

<b>Streptavidin Films (Urine)</b>				
<b>Film</b>	<b>Thickness (nm)</b>	$\alpha^a$ (MFI/nM)	$[P]_T^a$ (nM)	$K_{d,app}^a$ ( $\mu$ M)
Monolayer	--	150 $\pm$ 10	0.29 $\pm$ 0.02	47 $\pm$ 5
3xSP9.6k	142	80 $\pm$ 20	0.26 $\pm$ 0.05	30 $\pm$ 10
3xSP30.3k	184	80 $\pm$ 20	0.27 $\pm$ 0.06	30 $\pm$ 10
3xSP77.6k	154	160 $\pm$ 30	0.30 $\pm$ 0.06	50 $\pm$ 20
<b>Streptavidin Films (Blood)</b>				
<b>Film</b>	<b>Thickness (nm)</b>	$\alpha^a$ (MFI/nM)	$[P]_T^a$ (nM)	$K_{d,app}^a$ ( $\mu$ M)
Monolayer	--	150 $\pm$ 20	0.28 $\pm$ 0.04	40 $\pm$ 10
3xSP9.6k	123	90 $\pm$ 10	0.27 $\pm$ 0.04	50 $\pm$ 10
3xSP30.3k	159	80 $\pm$ 20	0.23 $\pm$ 0.04	40 $\pm$ 10
3xSP77.6k	133	120 $\pm$ 20	0.6 $\pm$ 0.1	40 $\pm$ 10
<b>Monomeric Streptavidin Films (Urine)</b>				
<b>Film</b>	<b>Thickness (nm)</b>	$\alpha^a$ (MFI/nM)	$[P]_T^a$ (nM)	$K_{d,app}^a$ ( $\mu$ M)
Monolayer	--	119 $\pm$ 3	0.40 $\pm$ 0.01	50 $\pm$ 2
3xSP9.6k	142	128 $\pm$ 5	17.0 $\pm$ 0.7	26 $\pm$ 2
3xSP30.3k	184	120 $\pm$ 20	16 $\pm$ 2	29 $\pm$ 6
3xSP77.6k	154	120 $\pm$ 10	15 $\pm$ 1	31 $\pm$ 5
<b>Monomeric Streptavidin Films (Blood)</b>				
<b>Film</b>	<b>Thickness (nm)</b>	$\alpha^a$ (MFI/nM)	$[P]_T^a$ (nM)	$K_{d,app}^a$ ( $\mu$ M)
Monolayer	--	120 $\pm$ 10	0.40 $\pm$ 0.03	62 $\pm$ 7
3xSP9.6k	123	97 $\pm$ 2	9.4 $\pm$ 0.2	12.2 $\pm$ 0.6
3xSP30.3k	159	111 $\pm$ 4	5.7 $\pm$ 0.2	20 $\pm$ 1
3xSP77.6k	133	110 $\pm$ 10	4.5 $\pm$ 0.5	35 $\pm$ 6

<sup>a</sup>Reported errors represent 95% confidence intervals for the parameter estimate.

**Table D-4.** Linear Range Approximations for Detection of mSA2 in Urine

<b>Film</b>	<b>Approximate Linear Range Concentrations (nM)</b>
Monolayer	5000 – $\geq$ 28000 <sup>a</sup>
3xSP9.6k	10 – $\geq$ 28000 <sup>a</sup>
3xSP30.3k	10 – $\geq$ 28000 <sup>a</sup>
3xSP77.6k	100 – $\geq$ 28000 <sup>a</sup>

<sup>a</sup>The maximum concentration of mSA2 that could be tested was 28000 nM, and the linear range for all 4 films was found to include this concentration.

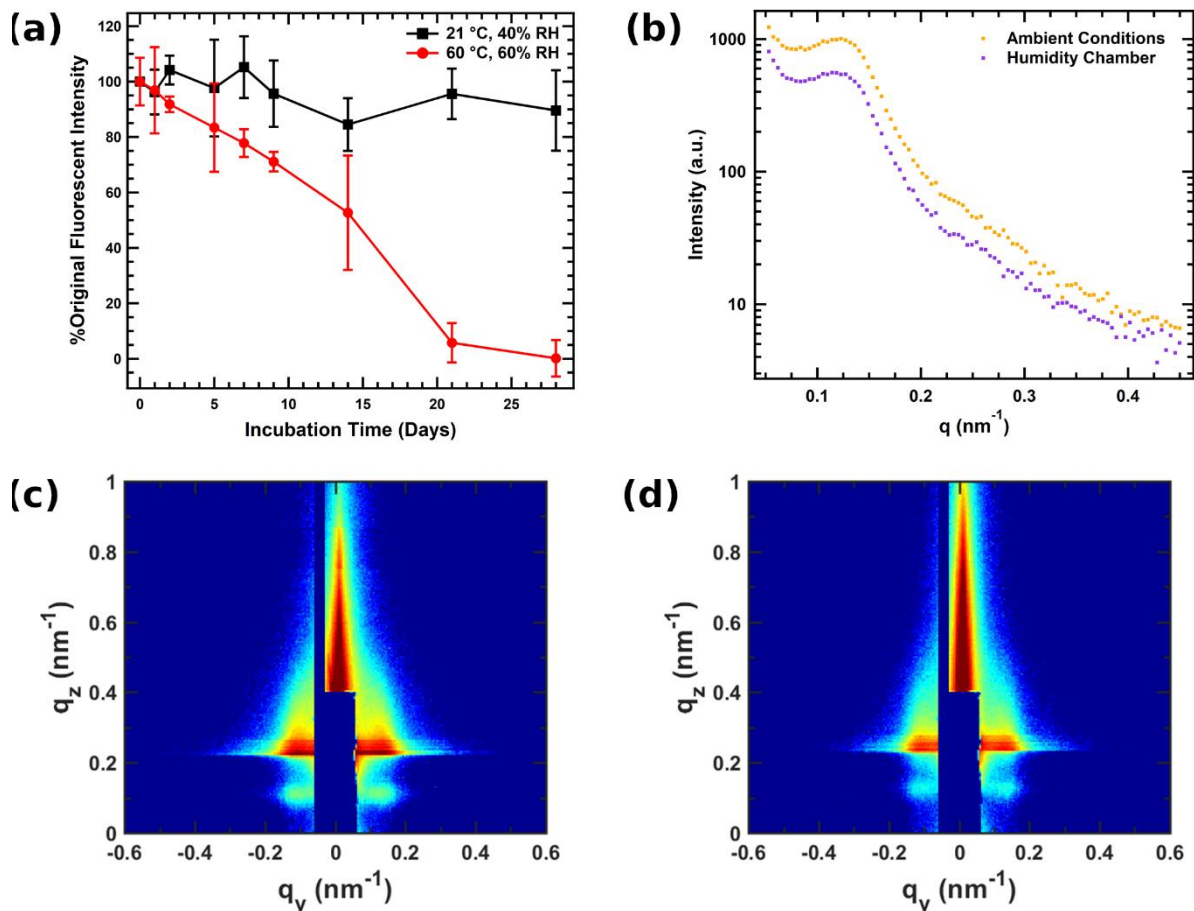


**Figure D-5.** (a) Retention of biosensing capabilities in 3xSP77.6k thin films under different temperature and humidity conditions. (b) GISAXS horizontal linecuts of the films in (a) after 14 days show no significant change in structure. Full GISAXS patterns for films exposed to (c) ambient conditions and (d) high temperature and high humidity from which the linecuts in (b) were generated. All measurements were conducted on sections cut from the same 204 nm film. Films in (a) were exposed to 10  $\mu\text{M}$  solutions of SA for 4 hours. GISAXS patterns were collected at an incident angle of  $0.140^\circ$ . Error bars in (a) represent the standard deviation of three replicates.

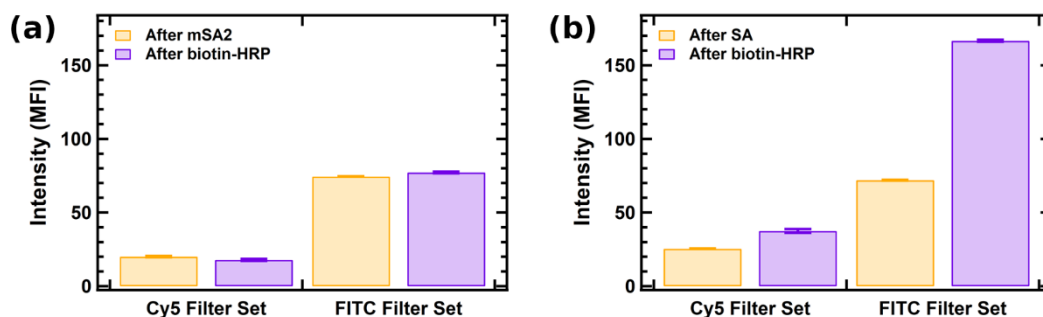


**Figure D-6.** Results of sequential fluorescent binding assays using (a) mSA2 and (b) SA as the analyte. Error bars represent the standard deviation of three replicates. 150 nm 3xSP77.6k thin films were exposed for 4 hours to solutions of either mSA2 or SA (fluorescently labeled with Alexa Fluor 647; similar emission and excitation maxima as Cy5), each with a concentration of 10  $\mu$ M, and imaged using Cy5 and FITC filter sets (orange bars in figure). Films were then exposed to a 200 ng/mL solution of biotin-HRP (fluorescently labeled with Alexa Fluor 488; similar emission and excitation maxima as FITC) for 4 hours and again imaged using Cy5 and FITC filter sets (purple bars in figure). While the film exposed to SA showed significant biotin-HRP binding, almost no biotin-HRP was bound to the film exposed to mSA2. The slight increase in fluorescent signal in the Cy5 filter channel after biotin-HRP binding in (b) is likely due to slight overlap of the Cy5 filter set emission and excitation wavelengths with the emission and excitation spectra for Alexa Fluor 488.

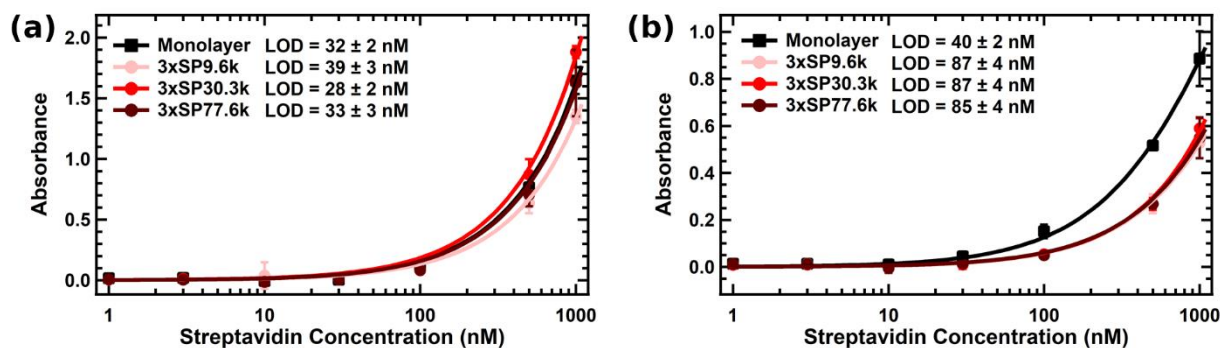


**Figure D-7.** Binding curves for sandwich assays performed with SA in (a) 50% urine and (b) 50% blood serum. Error bars represent the standard deviation of three replicates.

## References for Appendix D

1. Thomas, C. S.; Glassman, M. J.; Olsen, B. D., Solid-State Nanostructured Materials from Self-Assembly of a Globular Protein–Polymer Diblock Copolymer. *ACS Nano* **2011**, *5* (7), 5697-5707, DOI: 10.1021/nn2013673

## Appendix E. Supporting Information for Chapter 6

The entanglement molar mass of PNIPAM at a concentration  $c$  in solution can be calculated from the entanglement molar mass in the melt  $M_e$  as follows:<sup>1-2</sup>

$$M_e(c) = \frac{M_e}{(c/g\text{ cm}^{-3})^{1.3}}$$

Because the density of PNIPAM,  $1.05\text{ g/cm}^3$ ,<sup>3</sup> is close to that of water, a 0.2 volume fraction solution of PNIPAM should have a concentration of approximately  $0.2\text{ g/cm}^3$ . Using an approximate range of 15-30 kDa for the melt entanglement molar mass of PNIPAM,<sup>1</sup> it can be estimated that:

$$M_e(0.2\text{ vol. frac.}) \approx 120 - 230\text{ kDa}$$

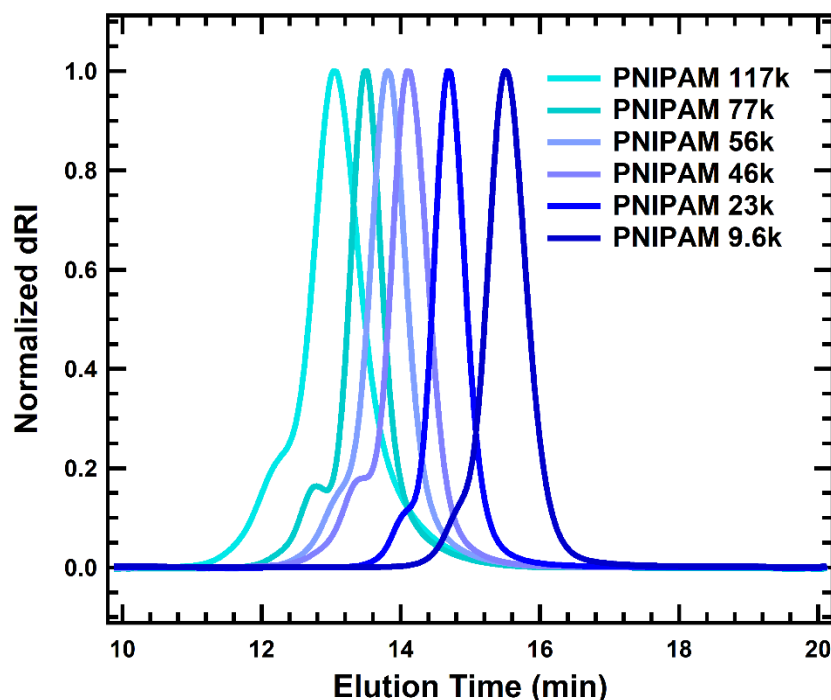


**Figure E-1.** Normalized differential refractive index signals from gel permeation chromatography of PNIPAM samples. The small shoulder at earlier elution times corresponding to twice the peak molecular weight in some samples results from slight reactivity of the double bond in the furan-protected maleimide of the CTA, as reported previously.<sup>4</sup>

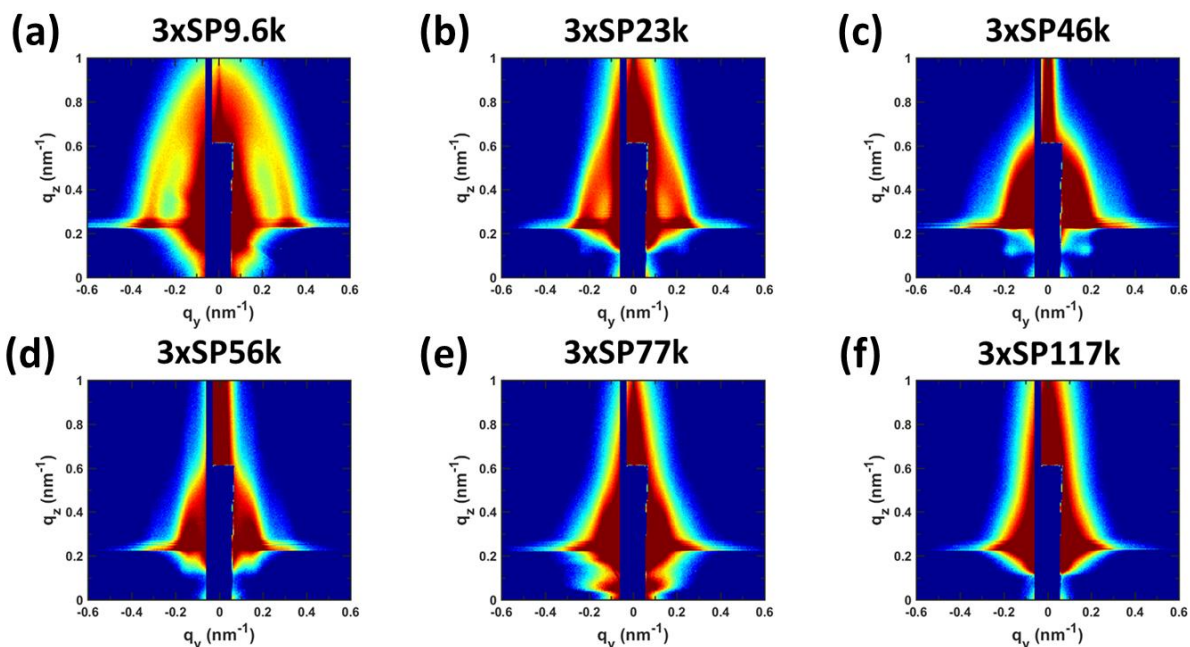


**Figure E-2.** GISAXS patterns of crosslinked thin films of (a) 3xSP9.6k, (b) 3xSP23k, (c) 3xSP46k, (d) 3xSP56k, (e) 3xSP77k, and (f) 3xSP117k at 0% RH.

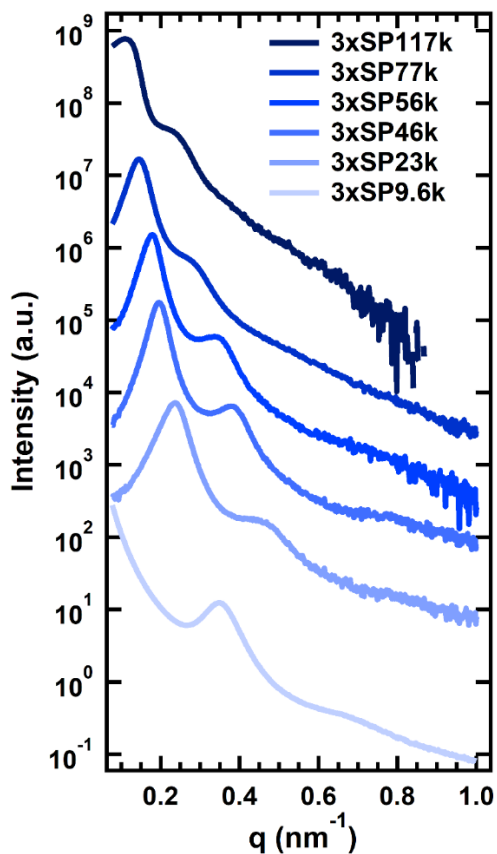


**Figure E-3.** Radially averaged SAXS patterns for 3x rcSso7d.SA conjugates in the bulk state. Curves are offset vertically for clarity. Data were collected at 20 °C.

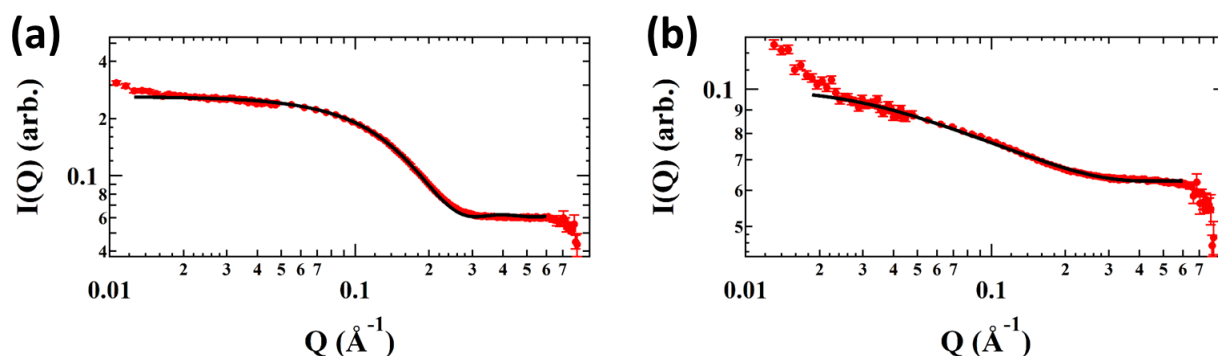


**Figure E-4.** Fits to SANS patterns for (a) CytC and (b) mSA2 in deuterated PBS at 20 °C. The CytC curve was fit using a sphere form factor with a Schultz distribution to account for polydispersity in the radius, and the mSA2 curve was fit using a cylinder form factor with a Schultz distribution to account for polydispersity in the length.

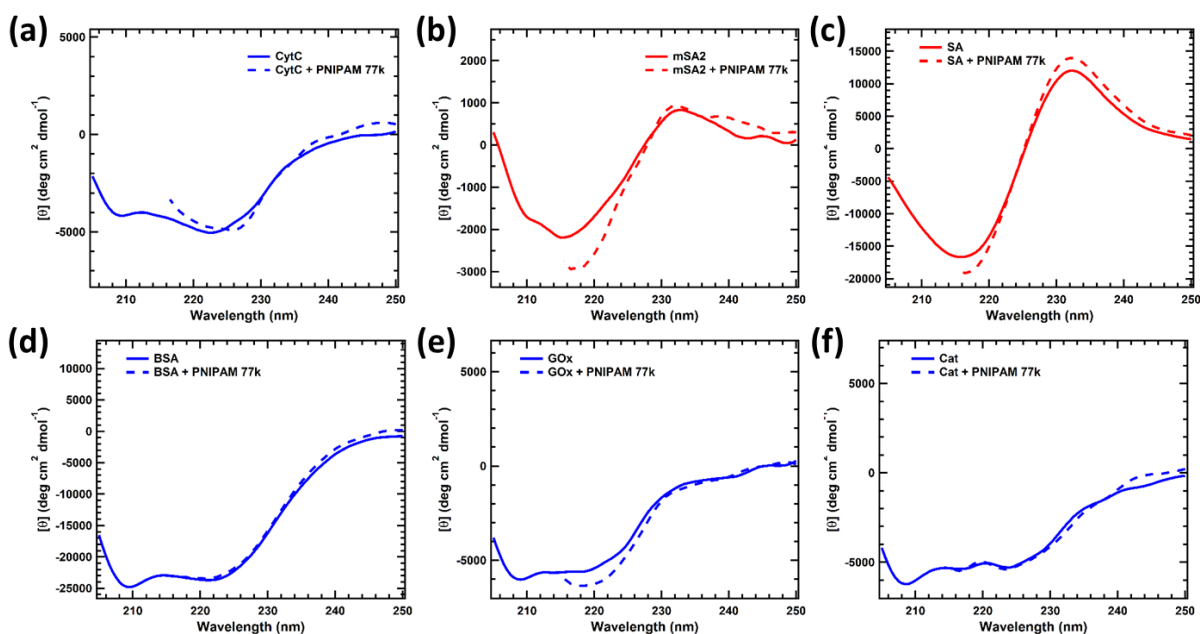


**Figure E-5.** CD curves for proteins in PBS with and without 10 wt.% PNIPAM 77k added at 20 °C. Curves in the presence of PNIPAM are only plotted to 215 nm, as at lower wavelengths the CD signal became noisy due to absorbance from PNIPAM. In all cases, the protein secondary structure shows no significant change when exposed to PNIPAM, suggesting that the polymer is not causing protein unfolding.

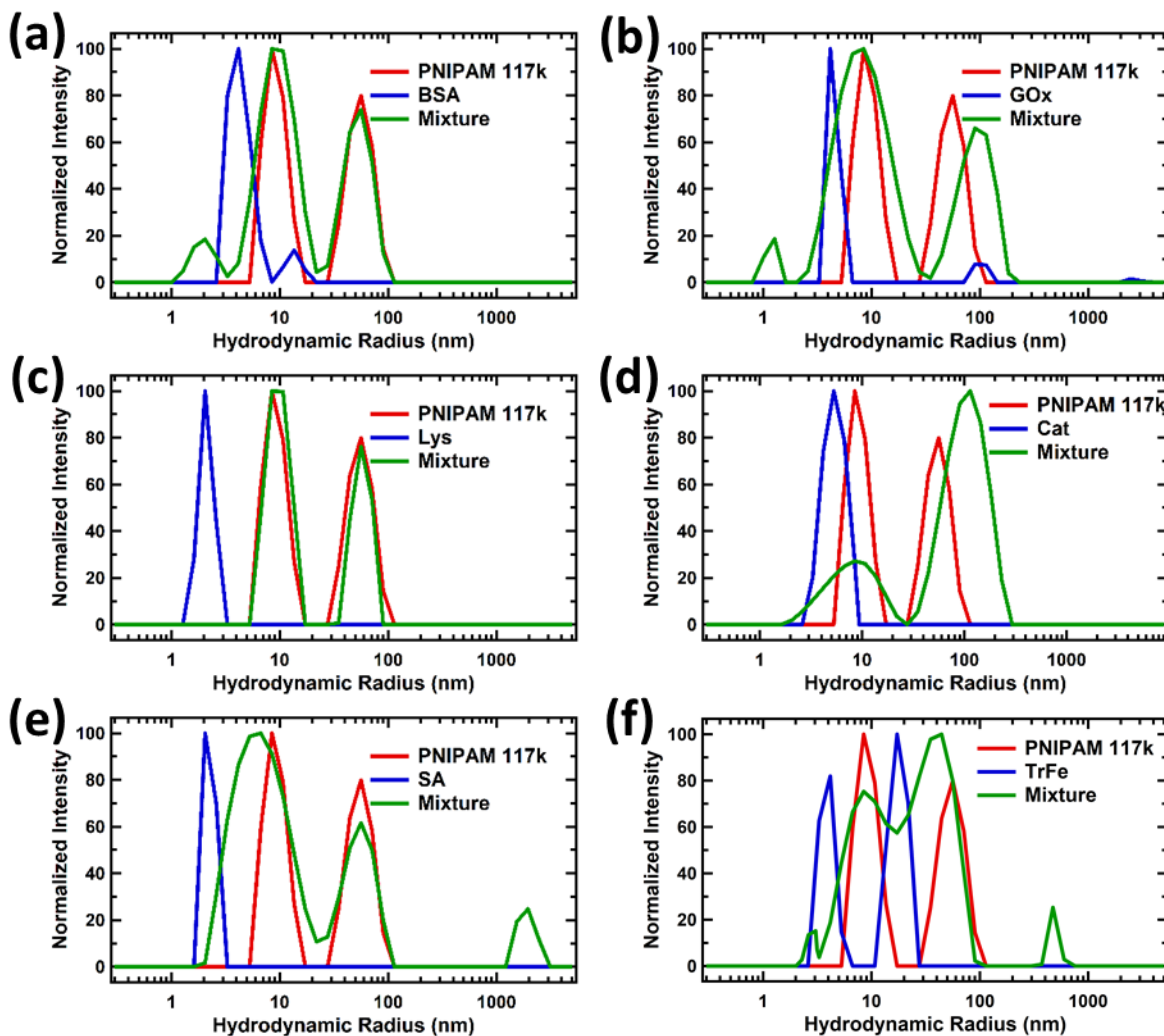


**Figure E-6.** DLS size histograms at 20 °C for PNIPAM 117k in PBS and proteins (~0.4 wt.%) in PBS with and without 1 wt.% PNIPAM 117k added. Graphs show proteins that consistently diffused (a, b) faster than, (c, d) roughly in accordance with, and (e, f) slower than Stokes-Einstein predictions in PNIPAM solutions. Solutions with only PNIPAM 117k show two peaks, corresponding to two populations of relaxation times. Protein solutions generally exhibit a single peak with a smaller mean radius than either of the PNIPAM peaks. When mixed with PNIPAM 117k, the PNIPAM peaks are present in roughly the same positions as in pure PNIPAM solutions while the protein peaks disappear. This disappearance is likely the result of the peaks becoming convoluted with the PNIPAM peaks, as the proteins experience slower diffusion and relaxation times in the presence of PNIPAM. In (a) and (b), a new peak corresponding to fast relaxation times is observed, and in (e) and (f), a new peak corresponding to extremely slow relaxation times is observed. All of these new peaks are consistent with the fast or slow diffusivities compared to Stokes-Einstein predictions that are observed in FRAP experiments.

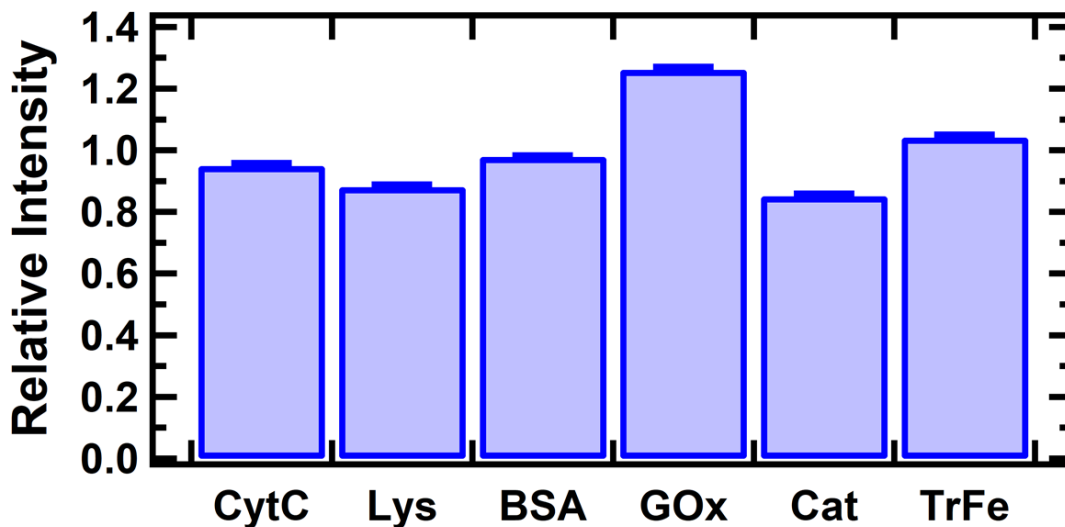


**Figure E-7.** Fluorescence intensities of 1  $\mu\text{M}$  mixtures of fluorescently-labeled mSA2 with 100  $\mu\text{M}$  of the specified protein relative to that of a 1  $\mu\text{M}$  solution of only fluorescently-labeled mSA2.

#### References for Appendix E

1. Biswas, C. S.; Wu, Y.; Wang, Q.; Du, L.; Mitra, K.; Ray, B.; Yan, Z.-C.; Du, B.; Stadler, F. J., Effect of tacticity and molecular weight on the rheological properties of poly(N-isopropylacrylamide) gels in benzyl alcohol. *J. Rheol.* **2017**, *61* (6), 1345-1357, DOI: 10.1122/1.5006807
2. Osaki, K.; Inoue, T.; Isomura, T., Stress overshoot of polymer solutions at high rates of shear. *J. Polym. Sci., Part B: Polym. Phys.* **2000**, *38* (14), 1917-1925, DOI: 10.1002/1099-0488(20000715)38:14<1917::Aid-polb100>3.0.Co;2-6
3. Zhang, L.; Daniels, E. S.; Dimonie, V. L.; Klein, A., Synthesis and characterization of PNIPAM/PS core/shell particles. *J. Appl. Polym. Sci.* **2010**, *118* (5), 2502-2511, DOI: 10.1002/app.31508
4. Thomas, C. S.; Glassman, M. J.; Olsen, B. D., Solid-State Nanostructured Materials from Self-Assembly of a Globular Protein–Polymer Diblock Copolymer. *ACS Nano* **2011**, *5* (7), 5697-5707, DOI: 10.1021/nn2013673